ATOMIC STRUCTURE AND NONELECTRONIC PROPERTIES
OF SEMICONDUCTORS

Optical Absorption and Chromium Diffusion
in ZnSe Single Crystals

Yu. F. Vaksman*^, V. V. Pavlov*, Yu. A. Nitsuk*, Yu. N. Purtov*,
A. S. Nasibov**, and P. V. Shapkin**

*Mechnikov National University, ul. Petra Velikogo 2, Odessa, 65028 Ukraine
^e-mail: Vaksman_yu@farlep.net
**Lebedev Physical Institute, Russian Academy of Sciences, Leninskii pr. 53, Moscow, 117924 Russia
Submitted June 15, 2004; accepted for publication August 9, 2004

Abstract—ZnSe:Cr single crystals were obtained using diffusion-related doping with chromium. The diffusion of chromium was performed in an atmosphere of saturated zinc vapors, and the metallic Cr layer deposited on the crystal surface was used as the source. Lines corresponding to chromium absorption at 2.766, 2.717, and 2.406 eV were observed in the optical-density spectrum at 77 K. The highest chromium concentration in the crystals was determined from infrared absorptance in the region of 0.72 eV and was found to be equal to 8×10^{19} cm^{-3}. It is shown that the diffusion profile of the chromium impurity can be determined by measuring the optical density of the crystals in the visible region of the spectrum. The diffusion coefficients D of chromium in ZnSe crystals at temperatures of 1073–1273 K are calculated. An analysis of the temperature dependence $D(T)$ made it possible to determine the coefficients in the Arrhenius equation: $D_0 = 4.7 \times 10^{10}$ cm^2/s and $E = 4.45$ eV.
© 2005 Pleiades Publishing, Inc.

1. INTRODUCTION

Zinc chalcogenide crystals doped with transition metals are of interest due to the fact that they can be employed as the active media of lasers that emit in the middle infrared (IR) spectral region (1–3 μm). These lasers are used in medicine, biology, and other application-oriented fields.

It is well known [1] that the Cr^{2+} ions in zinc chalcogenides exhibit intracenter radiative transitions of an $^5E \longrightarrow {}^5T_2$ type between the lower excited state (^5E) and the ground state ($^5T_2$). These transitions give rise to IR luminescence with a quantum yield close to unity. Among II–VI semiconductors, zinc selenide is a promising material for the fabrication of a frequency-tuned laser that can lase in a wavelength ranging from 2 to 3 μm at room temperature. Ivanov *et al.* [2] discussed the mechanism for the excitation of laser radiation in ZnSe:Cr in the region of 2.4 μm. At the same time, in order to obtain efficient laser structures based on zinc selenide, the chromium concentration should be no lower than 10^{19} cm^{-3}. The growth of crystals by a method involving the physical transport of vapors in vertical and horizontal configurations was reported in [3]. However, the mechanism of chromium transport in the vapor phase is not yet known. As a result, a reliable technology for the growth of ZnSe:Cr crystals has not yet been developed. Another method for obtaining ZnSe:Cr crystals involves diffusion-related doping of nominally undoped ZnSe crystals with chromium [4]. An appreciable obstacle to this method of doping is the lack of data on both the mechanism of chromium diffu-sion and the value of the diffusion coefficient. This problem has been successfully solved for GaAs:Cr [5]. It was shown that, as a result of chromium diffusion into GaAs, high-resistivity layers are formed. Thus, the thickness of the diffusion layers was determined by measuring the breakdown voltage of a pressed probe at the angle lap of the crystal.

We suggest a contactless method for determining the chromium diffusion coefficient that is based on an analysis of the optical-absorption spectra of ZnSe:Cr in the visible region of the spectrum. We show that the diffusion profile of the impurity can be determined and the chromium diffusion coefficient calculated by measuring the relative optical density of ZnSe:Cr crystals. The objective of this study is to determine both the temperature dependence of the chromium diffusion coefficient and the activation energy of the diffusion process in ZnSe crystals.

2. EXPERIMENTAL

The ZnSe:Cr crystals under study were obtained by doping nominally undoped ZnSe single crystals with chromium by diffusion. The undoped crystals were obtained by free growth on the substrates of ZnSe single crystals with the orientation (111) or (100). This method was described in detail, along with a report of the main characteristics of the obtained crystals, in [6, 7]. The choice of the temperature profiles and design of the growth chamber precluded any contact between the crystal and chamber's walls. The disloca-

D^*, arb. units
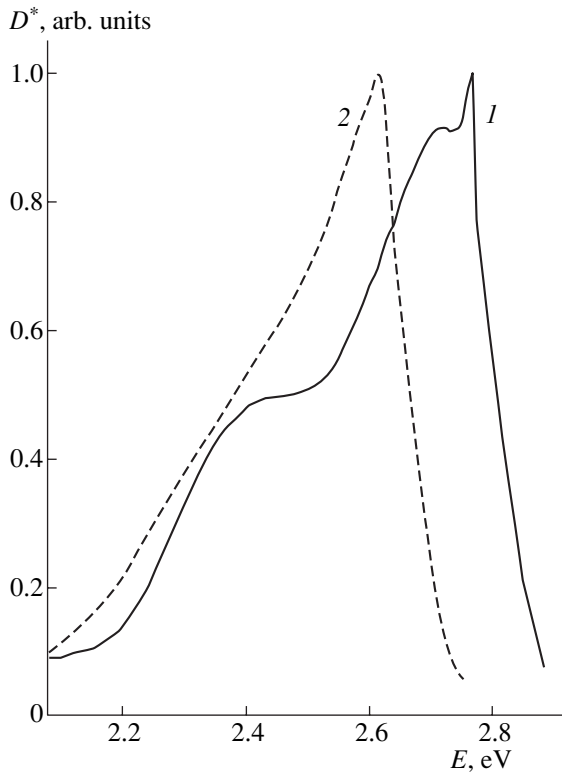
Fig. 1. The optical-density spectra of ZnSe:Cr crystals measured at (*1*) 77 and (*2*) 293 K.

tion density in the crystals under study was no higher than 10^4 cm^{-2}.

The crystals were doped by the diffusion of chromium from the metallic Cr layer deposited onto the surface. The diffusion was performed in an atmosphere of saturated zinc vapors. The crystals were annealed in evacuated quartz cells for 2–30 h at temperatures ranging from 1073 to 1273 K. As a result of the annealing, the crystals acquired a characteristic dark red coloring. This circumstance made it possible to observe the diffusion profile of the impurity using an optical microscope.

The chromium diffusion was carried out under conditions in which the impurity concentration in the source (the metallic chromium layer) remained nearly constant. In this case, a solution to the Fick diffusion equation for one-dimensional diffusion can be written as

$$C(x, t) = C_0\left(1 - \text{erf}\frac{x}{\sqrt{4Dt}}\right), \qquad (1)$$

where C_0 is the activator concentration at the surface and erf denotes the error function (the Gaussian function).

The optical-density spectra in the visible region of wavelengths were measured using an SF-46 grating spectrophotometer. The transmission spectra in the mid-IR region were recorded using an MDR-6 grating monochromator. The optical-density spectra were mea-

sured at the temperatures 77 and 293 K, whereas the transmission spectra were measured at 293 K.

In order to measure the impurity diffusion profile, we cleaved a thin (0.2–0.4 mm) platelet from a ZnSe:Cr crystal in the plane longitudinal to the diffusion-flux direction. The optical-density profile in the ZnSe:Cr crystals was measured using an MF-2 microphotometer. This method made it possible to measure the optical density with a step of 10 µm in the direction of the diffusion flux. The integrated optical density was measured in the spectral range from 440 to 550 nm.

3. OPTICAL ABSORPTION IN ZnSe:Cr IN THE VISIBLE REGION OF THE SPECTRUM

We used the undoped ZnSe crystals as standards when measuring the optical-absorption spectra of ZnSe:Cr. In Fig. 1, we show the optical-density D^* spectra of a crystal doped with chromium at 1073 K. The absorption spectrum of chromium in the ZnSe:Cr crystals is located in the blue–green region of wavelengths. In the spectrum measured at 77 K, the main absorption line located at 2.766 eV and two additional lines located at 2.717 and 2.406 eV are observed. A single line peaked at 2.614 eV is observed in the absorption spectrum measured at room temperature. Thus, the main absorption line shifts from 2.766 to 2.614 eV as the temperature at which the measurements are taken is increased from 77 to 293 K. The magnitude of this shift (8×10^{-4} eV/K) corresponds to a temperature-induced variation in the ZnSe band gap [8]. The result obtained indicates that the processes of absorption in the blue–green region of the spectrum occur with the involvement of transitions between the valence band and chromium levels. This inference is supported by the absence of electron photoconductivity for the case where the ZnSe:Cr crystal is exposed to blue–green light.

4. TRANSMISSION SPECTRA IN THE IR REGION

It is established that the ZnSe:Cr crystals under study exhibit a characteristic transmission minimum at 0.72 eV (Fig. 2). A similar result was reported in [1, 3]. Absorption in the IR region of the spectrum is caused by the $^5T_2 \longrightarrow {}^5E$ intracenter transitions between the ground ($^5T_2$) and the lower excited (^5E) levels of the Cr^{2+} ion states. In [1], It was established that the relation between the absorption coefficient α of ZnSe:Cr crystals in the spectral region 0.72 eV and the chromium-impurity concentration is given by

$$\alpha = 11.34 \times 10^{-19}[\text{Cr}], \qquad (2)$$

where the absorption coefficient is expressed in cm^{-1} and the chromium concentration [Cr] is expressed in cm^{-3}. We used relation (2) to estimate the highest concentration of the chromium impurity in the crystals
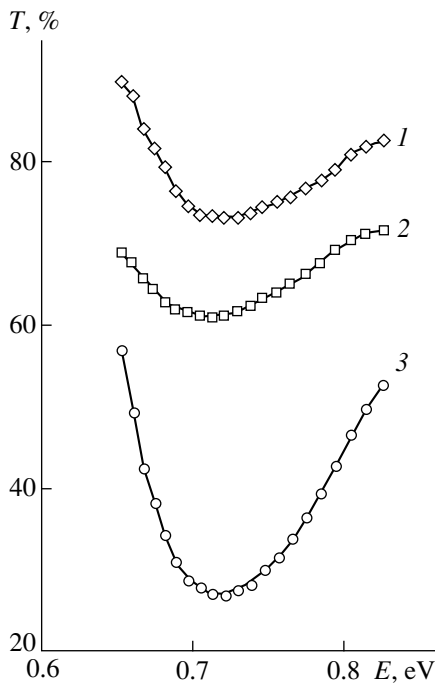
Fig. 2. The transmission spectra of ZnSe crystals doped with chromium at temperatures of (*1*) 1073, (*2*) 1123, and (*3*) 1273 K.
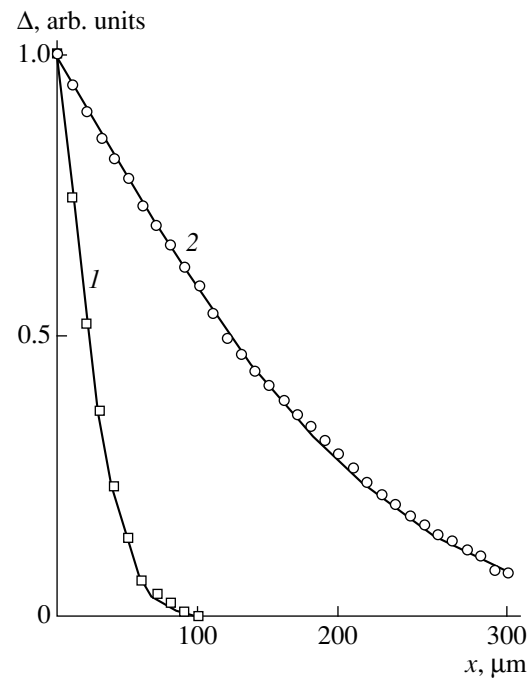
Fig. 3. The profiles of the relative optical density (circles and squares) and the chromium diffusion profiles (solid lines) in ZnSe crystals doped with chromium at temperatures of (*1*) 1073 and (*2*) 1173 K.

under study. The absorption coefficient was calculated using the following expression:

$$T = (1 - R)^2 e^{-\alpha l}. \tag{3}$$

Here, T is the transmission coefficient of light, $R = \dfrac{(n-1)^2}{(n+1)^2}$ is the reflection coefficient, n is the refractive index (equal to 2.45 at a photon energy of 0.72 eV), and l is the thickness of the absorbing layer.

If the diffusion temperature is 1173 K and diffusion duration is 10 h, the thickness of the absorbing chromium layer is $l \approx 200$ μm. Using expressions (2) and (3), we estimated the highest chromium impurity concentration as being equal to 8×10^{19} cm^{-3} in the crystals under study.

5. DIFFUSION PROFILE OF THE IMPURITY

The presence of characteristic chromium-absorption lines in the visible region of the spectrum indicates that it is possible to determine the impurity-diffusion profile by measuring the relative optical density Δ. This quantity is a function of the coordinate x in the direction of the diffusion flux and is defined by the expression

$$\Delta = \frac{D^*(x) - D^*(\infty)}{D^*(0) - D^*(\infty)}, \tag{4}$$

where $D^*(x)$ is the crystal's optical density as a function of the coordinate x, $D^*(0)$ is the optical density of the
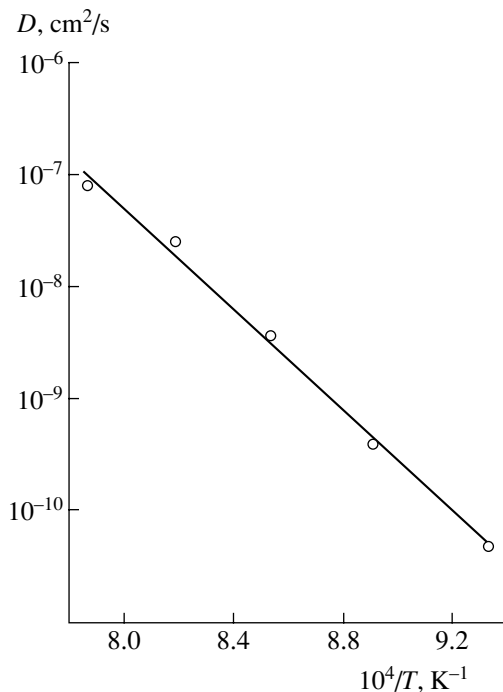
Fig. 4. The temperature dependence of the chromium diffusion coefficient in ZnSe crystals.

crystal in the surface layer with the coordinate $x = 0$, and $D^*(\infty)$ is the optical density of the crystal in the region where the chromium concentration is negligible (the crystal is not doped). The chosen definition of rel-

ative optical density makes it possible to compare the dependence $\Delta(x)$ with the impurity concentration profile $C(x)/C_0$ calculated using formula (1). By choosing the value of the diffusion coefficient in Eq. (1), we managed to obtain good agreement between the relative-optical-density and chromium-concentration profiles in the crystals (Fig. 3). Using this approach, we calculated the coefficients of the chromium diffusion in ZnSe crystals at temperatures of 1073, 1123, 1173, 1223, and 1273 K. The temperature dependence of the diffusion coefficient (see Fig. 4) is described by the Arrhenius equation

$$D(T) = D_0 \exp\left(-\frac{E}{kT}\right), \tag{5}$$

where the factor $D_0 = 4.7 \times 10^{10}$ cm^2/s and the diffusion activation energy $E = 4.45$ eV. The obtained value of the quantity E suggests that chromium diffuses in ZnSe crystals according to a dissociative mechanism. This mechanism is characteristic of the majority of II–VI semiconductor compounds.

6. CONCLUSIONS

We can draw the following conclusions on the basis of the results reported above:

(i) Diffusion-based doping can be used to obtain ZnSe:Cr single crystals with a chromium concentration as high as 8×10^{19} cm^{-3}.

(ii) It is established that the main absorption line of ZnSe:Cr in the blue–green region of the spectrum is caused by optical transitions of electrons from the valence band to the levels of chromium ions.

(iii) It is shown that the diffusion profile of a chromium impurity can be determined by measuring the relative optical density of ZnSe:Cr crystals.

(iv) The diffusion coefficient D of chromium in ZnSe crystals at temperatures of 1073–1273 K is determined for the first time. An analysis of the temperature dependence $D(T)$ made it possible to determine the parameters in the Arrhenius equation: $D_0 = 4.7 \times 10^{10}$ cm^2/s and $E = 4.45$ eV.

REFERENCES

1. J. T. Vallin, G. A. Slack, and S. Roberts, Phys. Rev. B **2**, 4313 (1970).

2. V. Yu. Ivanov, A. A. Shagov, A. Szczerbakow, and M. Godlewski, Physica B (Amsterdam) **308–310**, 942 (2001).

3. Ching-Hua Su, Shari Feth, M. P. Volz, *et al.*, J. Cryst. Growth **207**, 35 (1999).

4. V. I. Konstantinov, V. I. Levchenko, V. N. Yakimovich, *et al.*, J. Cryst. Growth **198–199**, 980 (1999).

5. S. S. Khludkov, O. B. Koretskaya, and A. V. Tyazhev, Fiz. Tekh. Poluprovodn. (St. Petersburg) **38**, 274 (2004) [Semiconductors **38**, 262 (2004)].

6. Yu. V. Korostelin, V. I. Kozlovsky, A. S. Nasibov, and P. V. Shapkin, J. Cryst. Growth **161**, 51 (1996).

7. Yu. V. Korostelin, V. I. Kozlovsky, A. S. Nasibov, and P. V. Shapkin, J. Cryst. Growth **197**, 449 (1999).

8. D. D. Nedeoglo and A. V. Simashkevich, *Electrical and Luminescent Properties of Zinc Selenide* (Shtiintsa, Chisinau, 1980) [in Russian].

Translated by A. Spitsyn

Raman Spectra of the Laser-Irradiated GaSe Single Crystals

A. Baĭdullaeva^, Z. K. Vlasenko, B. K. Dauletmuratov, L. F. Kuzan, and P. E. Mozol'
Lashkarev Institute of Semiconductor Physics, National Academy of Sciences of Ukraine, Kiev, 03028 Ukraine
^e-mail: baidulla@yahoo.com
Submitted June 23, 2004; accepted for publication July 12, 2004

Abstract—The specific features of the crystal structure of the lamellar GaSe crystals of various polytypes are analyzed. The possibility of identifying the phase transitions, which occur as a result of variations in temperature, pressure, and composition, is considered from the standpoint of resonance Raman scattering. The effects of high-temperature thermal annealing and pulsed laser irradiation on Raman spectra is investigated. It is found that pulsed laser radiation gives rise to regions with different polytype composition and regions with residual stress. © 2005 Pleiades Publishing, Inc.

1. INTRODUCTION

Single crystals of gallium selenide, similarly to the entire class of lamellar crystals, exhibit a strongly pronounced structural anisotropy, which leads to a quasi-two-dimensional character of vibrational states. This anisotropy most clearly manifests itself in all properties determined by the phonon subsystem of the crystal. The main and most interesting property of the structure of these crystals, which gives rise to a strong anisotropy of physical properties, is alternation of the packets of atomic planes (layers). These planes are bound together by weak van der Waals forces, while the bonding forces inside the layers are ion–covalent. These specific features of the structure spur interest among researchers concerning the manner and measurement of the effect of weak bonding between the layers on the energy spectra of lamellar crystals, specifically their vibrational spectra.

The main structural unit of GaSe is the elementary layer with two molecules (four atoms) in the unit cell. The atoms are located in the planes normal to the *C* axis in the sequence Se–Ga–Ga–Se. Each GaSe layer thereby consists of two planes of Ga atoms, which are surrounded on two sides by the unit planes of the Se atoms. The location of atoms inside the layer corresponds to the D_{3h}^1 group of point symmetry. In this case, three anions form a tetrahedron along with the metal atom.
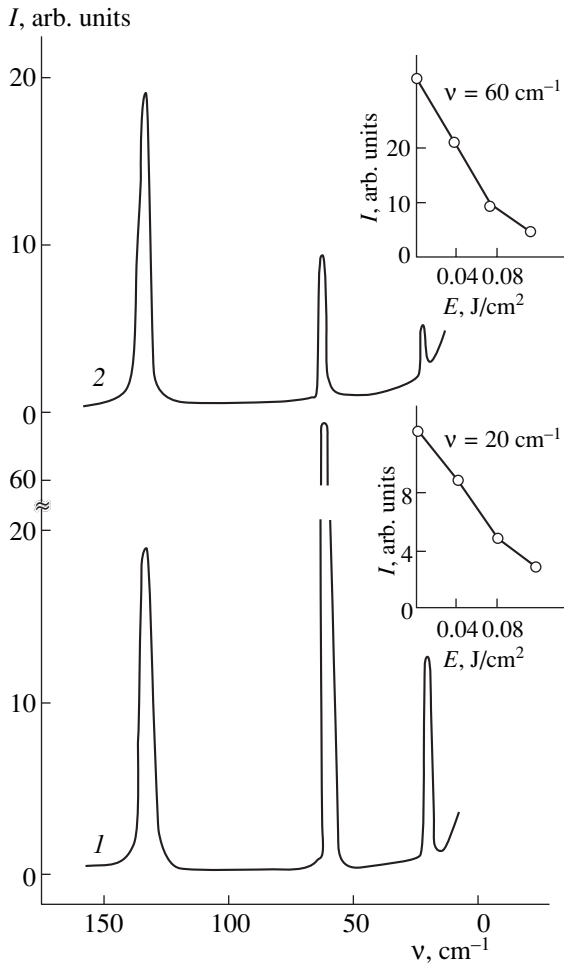
Depending on the package type of separate layers and their amount in the unit cell, GaSe crystals can have a structure that corresponds to various polytype modifications. Four polytypes are known for GaSe (ε, β, γ, and δ) [1–4]. The formation of a particular polytype or a mixture of several polytypes depends substantially on the growth method of single crystals [5, 6].

For example, the Czochralski and Bridgman–Stockbarger methods yield mainly the ε polytype [7]. Gas-transport reactions also yield the ε polytype with a large number of stacking faults [6]. Needle crystals of ε, γ, and δ polytypes are formed by vacuum sublimation [8, 9]. Single crystals of the β polytype are formed only occasionally. They can be found in the mass of needle crystals grown by vacuum sublimation or by gas-transport reactions with a low concentration *J* [10].

Thus, a particular pure GaSe polytype is a rare thing. As a rule, the crystals include a mixture of ε and γ polytypes. In addition, the crystals of all polytypes are formed of identical layers and differ only in the weak forces of interlayer interaction. Therefore, the distinctions in the intensities of polytype lines in the Raman spectra manifest themselves insignificantly, while most modes, which become allowed upon passing from the β polytype to the ε polytype and the γ polytype, are active only slightly.

In certain crystals, the phase transitions are observed at increased hydrostatic pressure. These transitions lead to reconstruction of the phonon and electron subsystems of the crystal. For example, for the absorption spectra of GaSe at a pressure of 5.2 kbar, a drastic change in the shape of the absorption edge is observed with a subsequent change in the sign and magnitude of dE_g/dp [11]. This phenomenon is interpreted as the transformation of one GaSe polytype into another. Analysis of the absorption spectra and interference patterns in the transmission spectra of GaSe in the pressure range of 1–5.53 kbar provides additional proof of the occurrence of polytype transformations. These are the intrapolytype transformation under an increase in pressure from 2.79 to 3.35 kbar and the interpolytype transformation under an increase in pressure from 4.34 to 4.71 kbar [12]. This interpretation is also confirmed by analysis of the energy location of the exciton line as a function of pressure [13]. The study of the resonance Raman scattering in GaSe with the bandgap varied by the effect of the hydrostatic pressure showed that an anomalous behavior of intensities of the resonance Raman bands of nonpolar vibrations, which consists in

Fig. 1. Raman spectra for annealed GaSe crystals (*1*) prior to and (*2*) after irradiation with pulses of the ruby laser. The variation in intensity of the bands at 20 and 60 cm^{-1} versus the laser irradiation dose is shown in insets.

Thus, the complete identification of polytypes is very complicated and requires the use of a combination of methods. However, taking into account that both the phonon and electron subsystems of the crystal are reconstructed during the phase transition, the method of the resonance Raman scattering can be successfully used to identify various polytypes.

Under resonance Raman scattering, when the energy of excitation light attains the energy of the electron transition of the crystal under investigation, the intensities of the bands of the Raman scattering increase. The cross section of the resonant Raman scattering is determined by two factors, namely, by the electron–(exciton)–photon and electron–phonon interactions. The relative intensities of various bands in the spectrum of the resonance Raman scattering of any substance depend on the constants of the electron–phonon interaction.
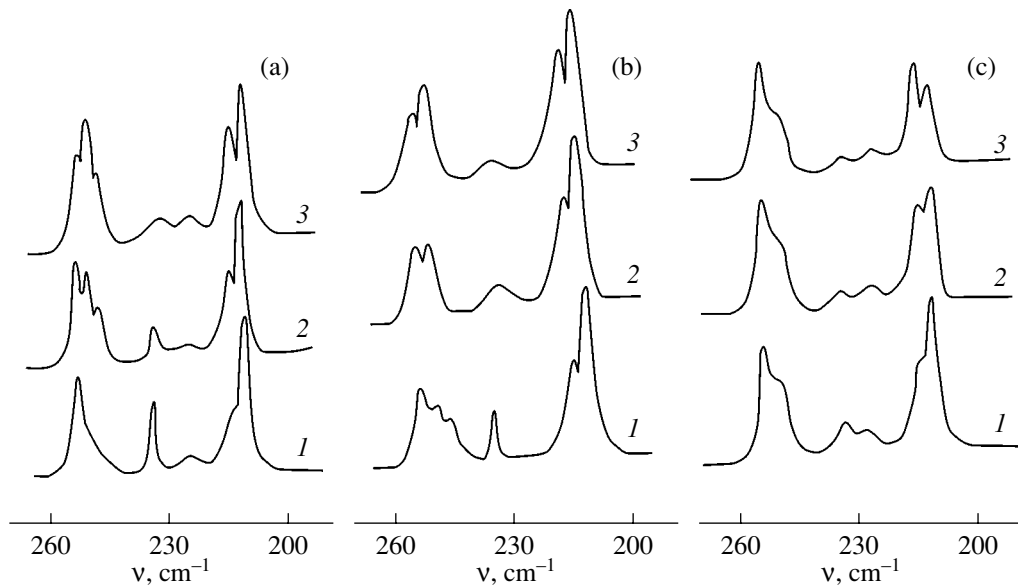
Currently, several methods are used to attain the resonance-excitation conditions for the Raman spectra. In all methods, the function of the electron–phonon interaction is varied as a result of the change in the difference between energies of the electron transition and the excitation photon. Such variations are attained either by frequency tuning of the excitation light or by the energy shift of the electron transition due to variations in temperature, the substance composition, or the hydrostatic pressure.

2. RESULTS AND DISCUSSION

In experiments, we used the ε-GaSe single crystals grown by the Bridgman–Stockbarger method. The Raman spectra were excited by the 6470.2 Å line of a Kr laser and detected using a DFS-24 double monochromator. The scattered light was collected under the right angle to the excitation radiation incident onto a facet of a natural cleavage of the single crystal normally to the *C* axis. All measurements were carried out at room temperature.

The samples were irradiated at room temperature using a multimode ruby laser ($\hbar\omega$ = 1.78 eV) with nanosecond pulses below the sample destruction threshold. The laser emission was homogenized using a quartz diffuser.

Figure 1 shows the resonance Raman spectra of (*1*) the starting ε-GaSe single crystal and (*2*) the crystal subjected to the highest dose of radiation of the multimode ruby laser, which causes no destruction of the crystal surface. As the irradiation dose increases, the intensities of the Raman bands are redistributed. Insets in Fig. 1 show the dynamics of variations in the intensities of the bands at 20 and 60 cm^{-1} with an increase in the radiation dose. We observed a considerable decrease in intensities of the bands at 20 (*E'*) and 60 (*E''*) cm^{-1}; the latter decreases much more rapidly. For example, at the excitation energy density 0.1 J/cm^2, the intensity of the band at 60 (*E'*) cm^{-1} decreased by a fac-

an increase in intensities of separate bands, is caused by phase transitions that occur as the pressure increases [14].

The concentration phase transition in the GaS$_x$Se$_{1-x}$ mixed crystals, which is caused by the variation in their composition, is noteworthy. These compounds have a polymorphic crystal structure that depends on the concentration *x*. The GaS$_x$Se$_{1-x}$ crystals only form the β modification at $x \geq 0.6$, while the mixture of various modifications, preferentially ε and γ, is formed at $x \leq 0.4$. In the concentration range $0.2 < x < 0.3$, the drastic change in the Raman spectra of the mixed crystals is observed. This change is caused by the structural phase transitions ε $\longleftrightarrow$ β, which are accompanied by the change in the crystal symmetry [15]. The measurements of the Raman spectra and the infrared reflection of light [16] as well as the study of X-ray diffraction [17] indicate that two concentration-related phase transitions exist in the GaS$_x$Se$_{1-x}$ alloys, namely β $\longrightarrow$ γ at $x \approx 0.6$ and γ $\longrightarrow$ ε at $x \approx 0.97$.

Fig. 2. Raman spectra for unannealed crystals (a) GaSe, (b) $Ga_{0.95}Se_{1.05}$, and (c) $Ga_{1.05}Se_{0.95}$ (curve *1*) prior to and (curves *2*, *3*) after irradiation with the pulses of the ruby laser at a dose of 0.04 and 0.08 J/cm^2, respectively.

tor of 7, while the intensity of the band at 20 (*E*″) cm^{-1} decreased only by a factor of 4. The intensities of other bands in the resonance Raman spectrum are virtually independent of the laser-radiation intensity. A similar pattern was observed in [13], where the resonance Raman spectra were studied in the case where the band-gap was varied by a hydrostatic pressure. As the pressure increased, the intensity of the band at 60 cm^{-1} decreased drastically, while the band at 20 cm^{-1} weakened to a considerably less extent. At a pressure of 4.35 kbar, the band at 20 cm^{-1} decreased by a factor of 3, while the band at 60 cm^{-1} vanished completely. As a rule, as the energy of an excitation laser line approaches the bottom of the conduction band, either the intensity of the lines in the Stokes region increases with an insignificant variation in the relative intensities, or the cross section of scattering by the longitudinal polar vibrations increases strongly. The classification of all vibrations by symmetry types is well known for GaSe [16, 17]; therefore, it is impossible to explain the variation in band intensities observed in the spectra (Fig. 1) by the conventional behavior of the Raman bands.

The effect of laser radiation is similar to the effect of the hydrostatic pressure; however, the former is irreversible. The character of variation in the intensities of the resonance Raman bands with varying pressure is completely reproducible as the pressure increases and decreases, while the laser radiation forms the residual stress regions in the crystal bulk.

Figure 2 shows the Raman spectra (a) of (*1*) the starting and (*2*, *3*) the irradiated and unannealed GaSe single crystals, as well as the Raman spectra of the single crystals grown with the excess (c) ($Ga_{1.05}Se_{0.95}$) or deficit (b) Se ($Ga_{0.95}Se_{1.05}$) of Ga. The starting samples

have identical spectra that somewhat differ in the regions 210–215 and 247–254 cm^{-1}.

The Raman bands at 247 and 254 cm^{-1} are identified with the modes $A_2''(LO)$ and $E'(LO)$, respectively, whose frequencies can be measured only for phonon propagation along the corresponding symmetry axes. For an arbitrary direction of phonon propagation under an angle Θ to the axis *C* of the crystal, the observed normal mode is a superposition of modes $A_2''(LO)$ and $E'(LO)$ with an intermediate frequency.

Modes $A_2(TO)$ at 235 cm^{-1} and $E'(TO)$ at 215 cm^{-1} can also mix and form a new mode with an intermediate frequency [18]. The bands with frequencies of 211 and 215 cm^{-1} are attributed to modes *E*″ and $E'(TO)$. Their resonance behavior in the *ZZ* configuration, where both these vibrations are forbidden, exhibits a number of specific features. For example, the band at 211 cm^{-1} prevails in the Raman spectrum far from the resonance, while the band at 215 cm^{-1} is unobservable at all. In the *XX*, *YX* configuration, where the band at 211 cm^{-1} is forbidden by the selection rules, the intensities of these bands are approximately equal to each other [18]. As resonance is approached, the intensity of the band at 211 cm^{-1} in the *ZZ* polarization decreases, and the band at 215 cm^{-1} starts to manifest itself. In the resonance state, the Raman spectrum includes only the band at 215 cm^{-1} [17].

Violation of selection rules is caused by the fact that scattering, which depends on the direction of phonon propagation, starts to prevail when the resonance state is attained. The presence of a large number of stacking faults along the *C* axis in GaSe single crystals causes

violation of both the structural periodicity in this direction and the momentum conservation law, which leads to violation of the selection rules. The bands at 247 and 254 cm^{-1} exhibit a similar resonant behavior.

The Raman spectra of the annealed GaSe crystals (Fig. 1, curve *1*) are not characteristic of most of the samples studied. As a rule, these spectra have a shape identical to that shown in Fig. 1 (curve *2*). In this case, the band at 135 cm^{-1} is more intense than that at 60 cm^{-1}. It was previously shown that the intensity of the band at 60 cm^{-1} is inversely proportional to the external hydrostatic pressure or to the local stresses in the crystal. High-temperature thermal treatment reduces the local stresses, which leads to a considerable increase in the intensity of this band (Fig. 1, curve *1*).

Both after irradiation of the GaSe crystals by the radiation pulses of the multimode ruby laser ($\hbar\omega = 1.78$ eV) with the power density below the destruction threshold of the sample surface for the stoichiometric composition and as a result of a deviation from the stoichiometry, the intensity of the band at 60 cm^{-1} varies as for the annealed samples.

Irradiation causes an increase in the intensity of the band at 215 cm^{-1} in the Raman spectra of GaSe and Ga$_{0.95}$Se$_{1.05}$. In this case, no noticeable variations in the intensity of the band at 211 cm^{-1} are observed. The intensity of the band at 249 cm^{-1} increases. After irradiation, it is more intense that the band at 254 cm^{-1} (Fig. 2a, 2b; curves *1–3*).

The intensity of the band at 215 cm^{-1} in the Raman spectra of the Ga$_{1.05}$Se$_{0.95}$ single crystals is unchanged after irradiation. However, the intensity of the band at 211 cm^{-1} considerably decreases, while no noticeable variations are observed in the spectral region of 247–254 cm^{-1} (Fig. 2c, curves *1–3*).

It was shown previously that the band at 249 cm^{-1} is the mixed mode of A(LO) at 247 cm^{-1} and E(LO) at 254 cm^{-1}, while the band at 228 cm^{-1} is formed by the superposition of modes A_2'(TO) at 235 cm^{-1} and E'(TO) at 215 cm^{-1}. An increase in the intensity of mixed vibrations in the regions at 249 and 228 cm^{-1}, which are associated with polar A–E phonons, is caused by variation in the spectral activity of modes A(TO) at 235 cm^{-1} and E(LO) at 254 cm^{-1} on passing from the ε polytype to the γ polytype [4].

3. CONCLUSIONS

Thus, irradiation of ε-GaSe crystals with pulses of the multimode ruby laser with a power density below the destruction threshold of the sample surface causes the following effects. (i) Regions with different polytype composition (γ polytype) are formed in the crystals. This is evidenced by the fact that the intensity of the band at 20 cm^{-1} (the interlayer vibration) decreases, while the intensity of mixed vibrations at 249 and 228 cm^{-1} increases, which is accompanied by a decrease in the intensity of the band at 235 cm^{-1}. (ii) Residual-stress regions are formed in the samples, which is confirmed by a decrease in the intensity of the band at 60 cm^{-1}.

REFERENCES

1. K. Schubert and E. Dorre, Naturwissenschaften **40**, 604 (1953).
2. F. Jellinek and H. Hahn, Z. Naturforsch. **166**, 713 (1961).
3. A. Kuhn, R. Chevalier, and A. Rimsky, Acta Crystallogr. B **81**, 2841 (1975).
4. K. Schubert, E. Dorre, and M. Kluge, Z. Naturforsch. **46**, 216 (1955).
5. J. C. Terhell and R. M. Leith, Phys. Status Solidi A **5**, 719 (1971).
6. A. Kuhn, A. Chevy, and R. Chevalier, Phys. Status Solidi A **31**, 469 (1975).
7. A. I. Balitskiĭ, A. S. Krochuk, I. M. Stakhira, and A. V. Franiv, Fiz. Tverd. Tela (Leningrad) **24**, 76 (1982) [Sov. Phys. Solid State **24**, 42 (1982)].
8. J. C. Terhell and R. M. Lieth, J. Cryst. Growth **16**, 54 (1972).
9. A. Polian, K. Kunk, and A. Kuhn, Solid State Commun. **19**, 1079 (1976).
10. F. Auticn, J. L. Brebner, and E. Maser, Phys. Status Solidi **31**, 129 (1969).
11. V. V. Panfilov, S. I. Subbotin, L. F. Vereshchagin, *et al.*, Phys. Status Solidi B **72**, 823 (1975).
12. S. I. Subbotin, V. V. Panfilov, and R. T. Molchanova, Phys. Status Solidi A **39**, 357 (1977).
13. G. L. Belen'kiĭ, É. Yu. Salaev, R. A. Suleĭmanov, and É. I. Mirzoev, Fiz. Tverd. Tela (Leningrad) **22**, 3153 (1980) [Sov. Phys. Solid State **22**, 1842 (1980)].
14. E. A. Vinogradov, G. N. Zhizhin, N. N. Mel'nik, and S. I. Subbotin, Fiz. Tverd. Tela (Leningrad) **22**, 2240 (1980) [Sov. Phys. Solid State **22**, 1305 (1980)].
15. E. M. Gamarts, B. S. Zadokhin, and A. N. Starukhin, Fiz. Tverd. Tela (Leningrad) **20**, 3721 (1978) [Sov. Phys. Solid State **20**, 2153 (1978)].
16. N. M. Gasanly, A. F. Goncharov, N. N. Melnik, and A. S. Ragimov, Phys. Status Solidi B **120**, 137 (1983).
17. N. M. Gasanly, N. N. Melnik, V. I. Tegirov, and A. A. Yushin, Phys. Status Solidi B **135**, K107 (1986).
18. R. M. Holf and J. C. Irwin, Phys. Rev. B **10**, 3464 (1974).

Translated by N. Korovin

ELECTRONIC AND OPTICAL PROPERTIES
OF SEMICONDUCTORS

The Electrical and Optical Properties of InAs Irradiated with Electrons (~2 MeV): The Energy Structure of Intrinsic Point Defects

V. N. Brudnyĭ*^, S. N. Grinyaev*, and N. G. Kolin**^^

Kuznetsov Physicotechnical Institute at the Tomsk State University, pl. Revolyutsii 1, Tomsk, 634034 Russia
^*e-mail: brudnyi@mail.tsu.ru*
***State Research Center at the Karpov Physicochemical Institute (Obninsk Branch), Obninsk, Kaluga oblast, 249033 Russia*
^^*e-mail: fci@meteo.ru*
Submitted May 13, 2004; accepted for publication August 9, 2004

Abstract—The results of experimental studies of the electrical and optical properties of *n*- and *p*-InAs crystals irradiated with electrons at an energy of ~2 MeV and doses as high as $D = 1 \times 10^{19}$ cm^{-2} are reported. Specific features of the annealing (at temperatures as high as 800°C) of radiation defects are also reported. The electronic structure of nonrelaxed V_{As}, V_{In}, As_{In}, In_{As} defects is calculated. A relation between the electrical properties and the Fermi level position in irradiated InAs on the one hand and the electronic structure of the intrinsic defects and special features of the energy-band spectrum of InAs on the other hand is discussed. © 2005 Pleiades Publishing, Inc.

1. INTRODUCTION

Indium arsenide (InAs) occupies a particular place among Group IV semiconductors and III–V binary compounds, owing to special features of the variations in the electrical properties of InAs resulting from irradiation with high-energy particles (electrons, ions, and neutrons). Compensation of initial conductivity and pinning of the Fermi level within a crystal's band gap as a result of irradiation with high-energy particles are characteristic of the majority of semiconductors [1]. In contrast to this behavior, as radiation defects are introduced into InAs at an initial electron concentration of lower than 10^{18} cm^{-3}, an increase in the free-electron concentration and a shift of the Fermi level to the region of allowed energies in the conduction band are invariably observed. For many years, the behavior of InAs has been related to special features of radiation-defect formation in this compound, specifically, to a preferential buildup of hydrogen-like donor defects [2]. Only studies of heavily doped n^+-InAs (with an electron concentration of 2×10^{19} cm^{-3}) [3] have shown that acceptor-type defects are also introduced into InAs as a result irradiation. This finding made it possible to suggest that the effect of the donor (or acceptor) defects introduced during irradiation on the electrical properties of InAs and, possibly, on the efficiency of the formation of these defects depends, to a great extent, on the doping level and conductivity type of the initial material.

In this paper, we report the results of studying the electrical and optical properties of bulk InAs samples irradiated with electrons; in addition, the annealing of radiation defects in this material is studied. These results complement those of previous studies concerned with InAs irradiated with fast neutrons and protons [3, 4]. We conducted the first study of the effect of irradiation with electrons on the electrical parameters of InAs doped using neutron-induced nuclear transmutations and InAs doped with an isovalent Sb impurity. We also report the results of theoretical calculations of the electronic structure of the V_{As}, V_{In}, As_{In}, and In_{As} defects that are presumably responsible for the observed variations in the properties of InAs subjected to irradiation with electrons.

2. EXPERIMENTAL

In our studies, we used Czochralski grown *n*- and *p*-InAs crystals that were nominally undoped; InAs doped with Te, Sn, or Zn during growth; and also InAs doped simultaneously with Sn and Sb. As is well known, isovalent impurities are used to enhance the electrical homogeneity and structural quality of semiconductors [5]. It is therefore important to study the effect of these impurities on the production of radiation defects. As the base material for obtaining transmutation-doped InAs crystals, we used nominally undoped *n*-InAs (grown by the Czochralski method) with the initial electron concentration $n_0 = (1–2) \times 10^{16}$ cm^{-3}. The neutron-transmutation doping of InAs was carried out by irradiation of this material with neutrons in a water-cooled and water-moderated reactor at the Research Center of the Karpov Physicochemical Institute (Obninsk Branch) and subsequent annealing for 20 min at $T_{ann} = 800–900$°C. It is well known that Sn atoms are efficiently introduced into In-containing semiconduc-
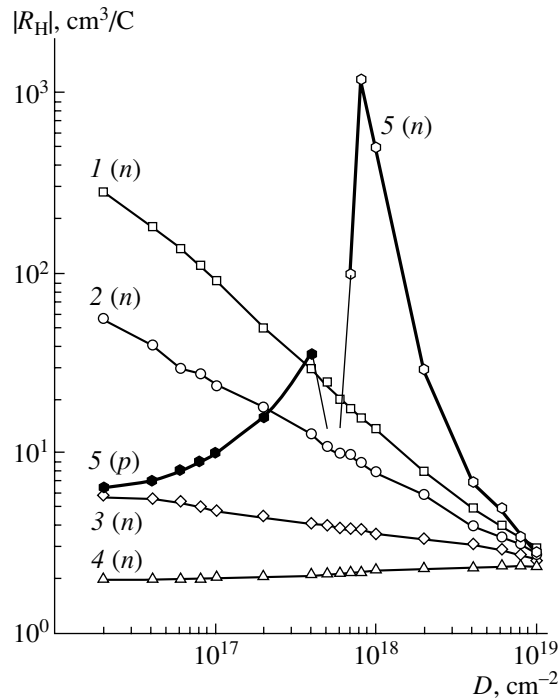
Fig. 1. Variations in the Hall coefficient $|R_H|$ in InAs resulting from irradiation with electrons. The electron energy is equal to ~2 MeV, and the temperature of the measurements $T = 77$ K. Numbers at the curves correspond to the numbers of the samples in Table 1. The conductivity type is indicated.
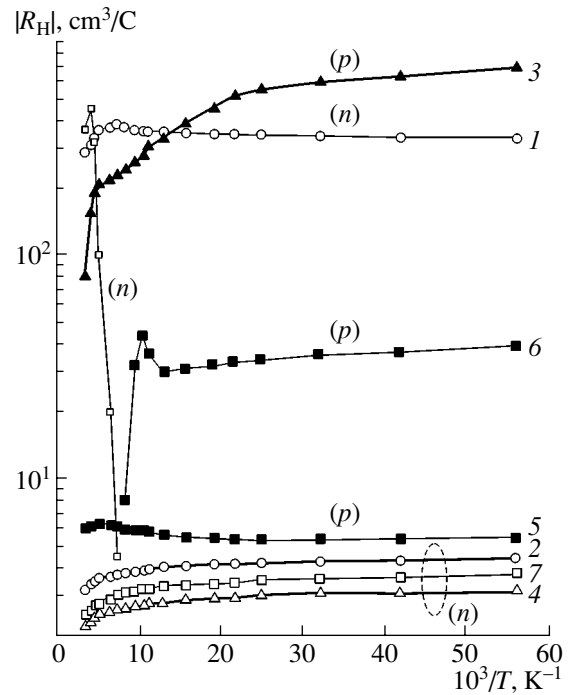
Fig. 2. Temperature dependences of the Hall coefficient $|R_H|$ in the InAs samples: (*1, 2*) correspond to sample 1; (*3, 4*), to sample 12; and (*5–7*), to sample 11. Curves *1, 3,* and *5* were obtained before irradiation and curves *2, 4, 6,* and *7* were obtained after irradiation with electrons at an energy of ~2 MeV and the dose $D = $ (*6*) 9×10^{17} and (*2, 4, 7*) 1×10^{19} cm^{-2}. The conductivity type is indicated.

tors as a result of irradiation with integrated-spectrum reactor neutrons (the main reaction is ^{115}In(n, γ), ^{116}In $\longrightarrow$ ^{116}Sn). The concentration of these atoms can be estimated from the expression $N_{Sn} \approx 2.9 D_{tn}$, where D_{tn} is the integrated flux of thermal neutrons [6, 7]. Irradiation with electrons was performed using an ÉLU-4 accelerator at temperatures in the vicinity of 295 K under the following conditions: the electron energy $E_e \approx 2$ MeV, the electron-current density $\langle j \rangle \approx (5–9) \times 10^{-6}$ A/cm^2, the electron-pulse width was 4.5×10^{-6} s, and the pulse-repetition frequency was 250 Hz. The highest integrated radiation flux was $D = 1 \times 10^{19}$ cm^{-2}, which exceeded all the corresponding values obtained so far in experiments with InAs by more than an order of magnitude. The thickness of the InAs samples irradiated with electrons was ~(0.6–0.8) mm. In order to preclude heating of the samples during irradiation, they were cooled by a flow of gaseous nitrogen. Before any measurements were taken, the samples were aged for a period lasting from one to several weeks. Isochronous annealing (for 10 min) was performed in vacuum for temperatures as high as $T_{ann} = 400°$C, while, at $T_{ann} > 450°$C, the annealing was carried out at the equilibrium pressure of As vapors.

The electrical parameters were calculated in the three-band approximation, taking into account the fact that the conduction band is not parabolic. We used the following values for the parameters in numerical estimations: the temperature dependence of the band gap $E_g(T) = [0.426 – \gamma T^2/(93 + T)]$ eV, where $\gamma = 3.158 \times 10^{-4}$ eV/K and the temperature T is expressed in K; effective masses in the vicinity of the band edges are given by $m_n/m_0 = 0.0245$ for electrons and $m_p/m_0 = 0.6$ for holes; the spin–orbit splitting $\Delta_{s0} = 0.38$ eV [8]; and the ratio between the electron and hole mobilities $\mu_n/\mu_p = 80$.

3. ELECTRICAL MEASUREMENTS

In Fig. 1, we show the variation in the Hall coefficient R_H (at the temperature $T = 77$ K) resulting from irradiation with electrons ($E_e \approx 2$ MeV) for the InAs samples whose parameters are listed in Table 1. The results of corresponding studies show that bombardment with electrons inevitably gives rise to n^+-InAs and to a shift of the Fermi level F to the allowed energies in the conduction band (Fig. 1, Table 1). The specific features of the variation in the temperature dependences of R_H in the samples with n- and p-type conductivity produced as a result of irradiation are also indicative of the transition of InAs to the degenerate state of n^+-type conductivity (Fig. 2). It is worth noting that the extent

**Table 1.** The electrical parameters of InAs samples before (0) and after (D) irradiation with electrons

Sample	Doping	$R_H(0)$, cm^3/C	$R_H(D)$, cm^3/C	$\sigma(0)$, Ω^{-1} cm^{-1}	$\sigma(D)$, Ω^{-1} cm^{-1}	$F(0)$, eV	$F(D)$, eV
1	Undoped	−284	−2.5	88.8	1560	0.31	0.51
2	Sn	−312	−2.7	70.5	1425	0.31	0.51
3	Sn + Sb (~10^{18} cm^{-3})	−78	−2.6	241	1311	0.34	0.51
4	Te	−56	−2.0	314	1350	0.36	0.52
5	Sn	−8.9	−2.6	1541	1307	0.46	0.51
6	Te	−6.1	−2.3	2017	1435	0.45	0.52
7	TD (800°C, 20°C)	−6.2	−2.0	1938	1525	0.45	0.53
8	TD (900°C, 20°C)	−5.2	−2.4	2283	1208	0.46	0.52
9	Te	−2.2	−2.4	4227	1237	0.53	0.52
10	Zn	+1.9	−3.9	63.2	718	0.03	0.49
11	Zn	+6.2	−2.5	22.6	1040	0.06	0.51
12	Zn	+80	−2.1	2.56	1050	0.12	0.53
13	Zn	+300	−2.3	0.83	1348	0.16	0.52

Note: The electron energy $E_e \approx 2$ MeV, the integrated flux $D = 1 \times 10^{19}$ cm^{-2}, the annealing temperature $T_{ann} \approx 200$°C, and the temperature of the measurements $T = 295$ K. The Fermi energy level is measured from the valence-band top (the level Γ_{8V}), σ designates the electrical conductivity, and TD stands for transmutation-doped.

of the effect of the donor radiation defects on the electrical properties of InAs is reduced as both the free-electron concentration in the initial material and the radiation dose increase. Under the conditions of a high-dose irradiation of InAs, where the concentration of radiation defects exceeds that of the initial chemical doping impurities, limiting values of the free-electron concentration $n_{lim} \approx (2–3) \times 10^{18}$ cm^{-3} are attained and, in the vicinity of the limiting position $F_{lim} \approx E_V + (0.52–0.55)$ eV, Fermi level pinning takes place in the temperature range $T = 77–295$ K for all the samples considered in this study. These experiments show that the efficiency of the donors and acceptors introduced into InAs as a result of irradiation is controlled by the Fermi level position in the band gap in relation to its limiting position F_{lim} in irradiated InAs. In general, the variations in the InAs electrical characteristics resulting from irradiation with electrons are qualitatively similar to the corresponding data obtained for InAs irradiated with fast neutrons or protons [3, 4]. This observation indicates that the electrical properties of irradiated InAs are independent of the type of crystal-lattice radiation damage; moreover, these properties are almost the same in the case of both the point defects produced as a result irradiation with electrons and the cluster-type defects produced by fast neutrons.

As a result of the irradiation of InAs crystals with high doses D of electrons, the Hall electron mobility $\mu_H = |R_H|\sigma$ becomes lower than the mobility in InAs doped with hydrogen-like impurities in a melt and has the same free-electron concentration. In Fig. 3, we show the dependences of μ_H measured at 77 and 295 K in the nominally undoped material (*n*-InAs, sample 1)
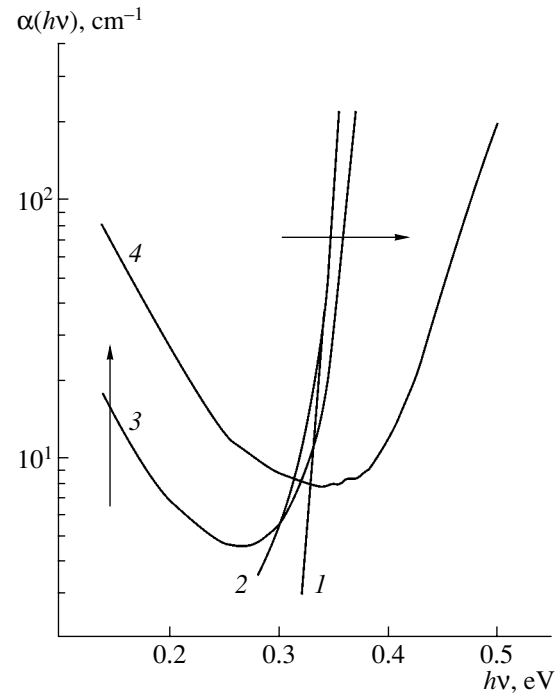
with the compensation factor $K \approx 0.10–0.15$ on the free-electron concentration n specified by irradiation of the crystal with high-energy electrons (here, $n \propto D$). The calculated values of $\mu_H(n)$ (dashed lines) at 295 and 77 K in the case of free-electron scattering by impurities in the absence of compensation are also shown in Fig. 3, with the nonparabolicity of the InAs conduction band taken into account [9]. It follows from the data shown in Fig. 3 that, in the region of high doses (when $n(D) > 10^{18}$ cm^{-3}), a drastic decrease in $\mu_H(n)$ is observed while the free-electron concentration varies only slightly. It is noteworthy that the most pronounced effect is observed in the region of $n \approx n_{lim}$, in which the free-electron concentration remains nearly constant as the irradiation dose increases, while the radiation defects continue to be introduced into the crystal lattice. The dependences $\mu_H(n)$ for *n*-InAs (sample 1) irradiated with 10-MeV protons at the highest dose used, $D_{max} = 2 \times 10^{16}$ cm^{-2}, are also shown in Fig. 3. These dependences indicate that the variations in $\mu_H(n)$ in the case of irradiation with protons at doses as high as $D_{max} = 2 \times 10^{16}$ cm^{-2} are similar to those induced by irradiation with electrons, although these variations are larger in the case of protons. For the highest doses of electrons ($D = 10^{19}$ cm^{-2}) and protons ($D = 2 \times 10^{16}$ cm^{-2}), the experimental values of μ_H are smaller than the results of the calculations by factors of ~1.5 and ~3 for the electron and proton irradiation, respectively; the values of μ_H are close to those for InAs doped during growth with hydrogen-like impurities at a concentration as high as ~$(2–3) \times 10^{19}$ cm^{-3} [6].
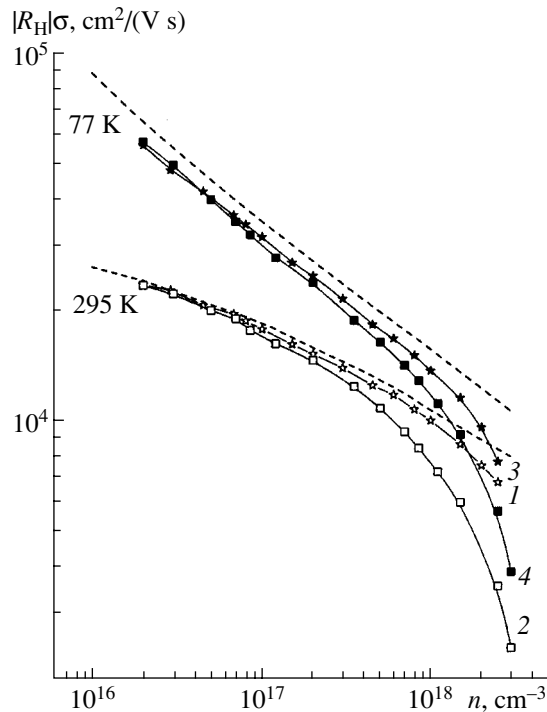
Fig. 3. Dependences of the Hall mobility of the electrons, $\mu_H = |R_H \sigma|$, on their concentration n ($n \propto D$) for as-grown n-InAs (sample 1) irradiated with (*1*, *3*) electrons at an energy of ~2 MeV and with (*2*, *4*) 10-MeV protons at $T = 295$ and 77 K. The dashed lines represent the result of the calculation of $\mu_H(n)$ in the case of the scattering of free electrons by impurity ions in the absence of compensation [9].

Fig. 4. Spectra of the optical-absorption coefficient of n-InAs (sample 1) irradiated with electrons at an energy of ~2 MeV and with the integrated fluxes $D = $ (*1*) 0, (*2*) 1 × 10^{17}, (*3*) 1 × 10^{18}, and (*4*) 1 × 10^{19} cm^{-2}. The temperature of the measurements was 295 K.

4. THE OPTICAL-ABSORPTION SPECTRA

Figure 4 illustrates the variations in the spectra of the optical-absorption coefficient $\alpha(h\nu)$ of nominally undoped n-InAs (sample 1) resulting from irradiation with electrons. The main features of the observed variations in the optical spectrum are the appearance of long-wavelength extrinsic absorption in the curves $\alpha(h\nu)$, a shift of the short-wavelength region of the spectrum to higher photon energies $h\nu$, and a variation in the slope of the $\alpha(h\nu)$ curves in this region as the dose of incident electrons increases. The trends of the variations in the absorption spectra for the short- and long-wavelength regions resulting from irradiation with electrons are indicated by arrows. The observed effects are caused by the transition, resulting from irradiation with electrons, of the initial undoped InAs to a degenerate n^+ state, which is in general agreement with the results of the electrical measurements. Estimation of the cross section S_n of the optical absorption by free charge carriers at the photon energy $h\nu \approx 0.14$ eV for the sample irradiated with the electron dose $D = 1 \times 10^{19}$ cm^{-2} yields $S_n \approx 4 \times 10^{-17}$ cm^2, which is close to the corresponding values for InAs doped with shallow-level donor impurities (the free-electron concentration is ~(2–3) × 10^{18} cm^{-3}). No features related to deep radiation-defect states were observed in the curves $\alpha(h\nu)$ in the optical spectra of the irradiated samples.

5. DISCUSSION

In contrast to other III–V semiconductor compounds in which the Fermi level shifts to the band gap as a result of irradiation, the Fermi level in irradiated InAs is always pinned in the region of allowed energies in the conduction band. Therefore, InAs can be used as a test material in order to verify the corresponding theoretical models describing the pinning of the Fermi level in semiconductors with a high defect concentration. According to these models, the limiting position of the Fermi level F_{lim} in an irradiated semiconductor can be identified with the position of the "neutral" point in a semiconductor (the branching point of a complex energy-band structure). A change in the donor–acceptor properties of the defect-related (gap) states in a semiconductor occurs in the vicinity of this point. The point is calculated either as the position of the charge (local) neutrality for the defect-related states in the crystal [10, 11] or as the energy position of the most localized (deepest) defect-related state in the semiconductor under consideration in the energy range near the band gap [12]. Estimations of the aforementioned energy position in InAs using these models [4] yield $E_V + (0.50–0.55)$ eV, which is in satisfactory agreement with both the results of this study (Table 1) and the data of

previous studies concerned with the irradiation of InAs with neutrons and protons [3, 4].

If the Fermi level is pinned, an irradiated semiconductor is considered as a material in which the concentration of the charge bound to the radiation defects is much higher than that of the free charge carriers, i.e., as a semiconductor with a low concentration of free electrons (holes). This assumption is apparently justified for materials where, after irradiation, the Fermi level is pinned deep within the band gap, particularly for the case of semiconductors with a wide band gap (Si, GaAs, GaP, SiC, and so on), since the limiting charge-carrier concentrations $n_{lim}(p_{lim})$ in this case are close (within an order of magnitude) to the intrinsic concentrations of free electrons (holes) n_i. At the same time, the limiting concentration of free electrons in InAs after irradiation is as high as $\sim(2–3) \times 10^{18}$ cm^{-3}, which corresponds to the pronounced degeneracy of the material. However, the results of the corresponding calculations of the quantity F_{lim} in the context of theoretical models [10–12] are in good agreement with the experimental data for both InAs and other semiconductors. This circumstance suggests that the concentration of radiation defects in irradiated InAs (as in other semiconductors) exceeds n_{lim} when the Fermi level is pinned at the limiting position. As a result, irradiated InAs can also be considered as a material with a low concentration of free electrons. These conclusions are supported by the corresponding numerical estimates. For example, assuming that the hole removal rate ~ 5 cm^{-1} under the irradiation of p^+-InAs (samples 12 and 13) with electrons ($E_e \approx 2$ MeV) is equal to the production rate for radiation-induced donors and extrapolating this value to the dose 1×10^{19} cm^{-2}, we obtain the concentration $N_{RD} \approx 5 \times 10^{19}$ cm^{-3} for these donors. The corresponding estimation for the radiation-induced acceptors in InAs with $n^+ = 2 \times 10^{19}$ cm^{-3} irradiated with fast neutrons yields $N_{RA} \approx 1.7 \times 10^{19}$ cm^{-3} when the Fermi level is pinned [3]. It then follows that, in heavily irradiated InAs, the concentrations of radiation-induced donors N_{RD}^+ and acceptors N_{RA}^- exceed the value of n_{lim} and are close to each other; as a result, this material exhibits a compensation factor almost equal to unity. In this case, the electroneutrality equation

$$(n_{lim}^2 - n_i^2)/n_{lim} = N_{RD}^+ - N_{RA}^-$$

can be replaced by the following condition for the charge neutrality of radiation defects:

$$N_{RA}^- \approx N_{RD}^+,$$

as it can in the irradiated wide-gap semiconductors. The above estimates show that irradiated InAs exhibits the properties of a degenerate semiconductor with n^+-type conductivity and, at the same time, is a material for which the condition $(N_{RD} - N_{RA})/N_{RD} \approx n_{lim}/N_{RD} \ll 1$ is satisfied.

Since the enthalpy of the formation of intrinsic defects in a semiconductor depends on their charge state and decreases as the value of the difference $|F - F_S|$ increases [13–16], the donor-type defects should be predominantly produced in the case of irradiation of p^+-InAs, whereas the acceptor-type defects should be predominantly formed when n^+-InAs is irradiated. Here, F is the Fermi level position in the initial crystal and F_S is a certain characteristic position of this level in the semiconductor (F_S is identical to F_{lim} [17]). When the Fermi level is pinned in the vicinity of F_{lim}, the efficiencies of the production of the radiation-induced donors and acceptors should be close to each other, which is, in general, confirmed by the experimental data.

6. ELECTRONIC STRUCTURE OF THE INTRINSIC LATTICE DEFECTS IN INDIUM ARSENIDE

The high concentration of free electrons in InAs after irradiation makes experimental studies of the radiation-defect spectrum difficult. As a result, there is a lack of reliable data in this field and only general assumptions concerning the nature of the radiation defects can be forwarded.

It is evident that defects of a dangling-bond type are responsible for the pinning of the Fermi level in irradiated semiconductors. The simplest defects of this type in InAs are the antisite defects As_{In} and In_{As}; the vacancies V_{As} and V_{In}; and the complexes $As_{In}–In_{As}$, $As_{In}–V_{As}$, and $In_{As}–V_{In}$. Taking into account the high mobility of interstitial atoms, these defects are typically disregarded. The most likely defects in binary semiconductors at room temperature are antisite defects that exhibit a low enthalpy of formation and a high thermal stability. Vacancies can also exist in binary semiconductors, since the complex structure of the compounds is conducive to the thermal stability of these defects. The data reported so far and obtained from measurements of the electron spin resonance in certain irradiated (at $T \approx 295$ K) III–V semiconductors confirm the presence of both antisite defects and (tentatively) vacancies [18–20]. As these studies show, the production efficiency for radiation defects in InAs at 295 K is only a factor of 1.8 lower than that at 20 K [21]. This circumstance means that the majority of radiation defects in InAs are immobile at 295 K.

Taking into account the above reasoning, we consider that the nonrelaxed vacancies (V_{As} and V_{In}) and antisite defects (In_{As} and As_{In}) are the most important defects in InAs irradiated with electrons. The levels of the vacancies and antisite defects were calculated by the pseudopotential and expanded unit-cell ($8 \times 8 \times 8$) methods in accordance with Brudnyi et al. [22]. Since the energies of the deep levels in narrow-gap semiconductors are especially sensitive to fine features of the energy-band structure, we calculated these energies using a more accurate model of nonlocal pseudopotentials that takes into account the spin–orbit interaction [23].

Table 2. Energy levels of neutral intrinsic defects

V_{In} (3)	V_{As} (1)	In_{As} (4)	As_{In} (2)
$\sim\Gamma_{15V}$ (T_2)R	0.57 (T_2)R	0.20 (T_2)	0.82 (A_1)R
$\leq\Gamma_{8V}$ (E', G')R	0.56 (E')R, 0.57 (G')R	−0.08 (E')R, 0.15 (G')	0.69 (E')R
−2.84 (A_1)R	−6.54 (A_1)	−2.83 (A_1)R	0.50 (A_1)
−2.97 (E')R	−6.67 (E')	−2.96 (E')R	0.37 (E')
		−6.90 (A_1)	−9.39 (A_1)
		−7.03 (E')	−9.52 (E')
			−13.55 (A_1)
			−13.68 (E')

Note: The energies are measured from the level Γ_{15V} (Γ_{8V}) in the ideal InAs crystal and are expressed in eV. The number of electrons at the levels is indicated in the brackets near the designation of the defect type, the results of the calculations with the spin–orbit interaction disregarded are listed in the upper row, and the results obtained taking into consideration the spin–orbit interaction are given in the lower row. Resonance states are designated by R.

The Bloch functions of an ideal InAs crystal were determined using the basis of ~70 plane waves. Due to the fact that the model pseudopotentials are "soft," an increase in the number of plane waves only slightly affects the spectra of the ideal and defect-containing crystals. In order to reduce the volume of computations involved in calculating the deep levels of the defects, we disregarded (in contrast to [23]) the additional waves consistent with Levdin's perturbation theory; however, we changed the parameters of the pseudopotentials somewhat in order to ensure better agreement with the experimental optical spectra. The obtained values of the ion pseudopotentials for the local portion (V_0, R_m) of corrections related to the d-caused nonlocality (A_d), the energy dependence (β), and the spin–orbit coupling (λ) were found to be equal to (in atomic units, where $h = m = e = 1$) $V_0(In) = -0.6$, $R_m(In) = 3.5$, $\beta(In) = 40$, $A_d(In) = 0.5$, $\lambda(In) = 3.0$, $V_0(As) = -3.15$, $R_m(As) = 3.34$, $\beta(As) = 12$, $A_d(As) = 4$, and $\lambda(As) = 3.2$. The lowest interband-transition energies calculated using these parameters are in satisfactory agreement with the experimental values at low temperatures (given in brackets): $E_0(\Gamma_{6C} - \Gamma_{8V}) = 0.42$ (0.42) eV, $\Delta_{so}(\Gamma_{8V} - \Gamma_{7V}) = 0.38$ (0.38) eV, $E_{\Gamma X}(X_{6C} - \Gamma_{8V}) = 1.86$ (1.87) eV, and $E_{\Gamma L}(L_{6C} - \Gamma_{8V}) = 1.55$ eV.

The wave functions of a defect-containing crystal were represented as a superposition of symmetrized combinations composed of 30–50 lower Bloch states of the ideal crystal in order to ensure a satisfactory convergence (~0.1 eV) of the deep-level energies. The potentials of the neutral point defects were composed of the local parts of the pseudopotentials, in a similar manner to [24, 25]. For the antisite defects, these potentials were chosen as the difference between the local pseudopotentials of substituted ions screened by the valence electrons in the Thomas–Fermi model, with corrections for the exchange and an electron concentration equal to that in the ideal crystal. The potentials of the defects with deeper levels (vacancies) were taken as being equal (with the opposite sign) to the pseudopotential of the removed atoms screened by electrons with the local density $(Z_v - Z_d)/\Omega_0$, where $Z_v = 8$, Z_d is the number of the valence electrons in an atom residing in the vacancy, and Ω_0 is the volume of the unit cell in the ideal crystal. The above choice of potential for the defects yields results that are close to those of the self-consistent calculations. Furthermore, the spin–orbit interaction with the core p-state atoms and defects in the expanded unit cell was taken into account using perturbation theory with the involvement of the ~30 states closest to the deep levels (see, also, [24, 25]). Following from an analysis of the electron density, the localized and resonance states of the defects were identified with the energy-band states of the superlattice for the wave vector $\mathbf{k} = 0$. The wave functions of the deep levels are localized near the defects, mainly within a sphere with its radius equal to the spacing between the nearest neighbors $R = (\sqrt{3}/4)a_0$ (a_0 is the lattice constant). Therefore, in order to describe the charge states of the deep-level centers, we added an additional potential produced by a homogeneously charged sphere with the radius R and screened by electron gas according to the Thomas–Fermi model to the Hamiltonian operator of the ideal crystal.

The calculated energies of the deep levels of the neutral defects V_{As}, V_{In}, In_{As}, and As_{In} are listed in Table 2. Since the majority of theoretical calculations of the defect levels in III–V compounds have so far been performed disregarding the spin–orbit interaction, we list the values of defect levels obtained by both taking into account and disregarding the spin–orbit interaction. The states E' and G' are transformed according to the two-valued representations of the tetrahedron point group; here, E' is a doubly degenerate state and G' is a fourfold degenerate state. We first consider the results of the calculations for the neutral states of the aforementioned defects. It follows from the calculation that the repulsive potential for the most important intrinsic defect V_{As} gives rise to the donor resonance state T_2 in the conduction band if the spin–orbit interaction is disregarded. The wave function of this state is highly localized in the vicinity of the defect. The potential of the spin–orbit interaction V_{so} is localized in the region of atomic cores. Since this potential is equal to zero for a vacancy, the level T_2 experiences only a slight split (~0.006 eV) into the levels E' and G', owing to a slight overlap of the defect's wave function with the potentials V_{so} of the neighboring atoms, if the spin–orbit interaction is taken into account. A single electron resides at the lower level E', while the upper level G' is unoccupied. In addition, a vacancy V_{As} introduces a localized state E' into the valence-band gap. An indium vacancy exhibits a weaker repulsive potential, which gives rise to resonance states in the vicinity of the

valence-band top. The antisite defect In_{As} introduces the deep level T_2 into the band gap. This level is mainly formed from Γ_{15V} states. As a consequence, the splitting of this level (0.23 eV) is close to that of the valence-band top Δ_{so} if the spin–orbit interaction is taken into account. As a result of the splitting, the lower state with the E' symmetry becomes a resonance-type state and is located within the valence-band continuum, whereas the upper state with the G' symmetry is located in the band gap and is half-occupied by two electrons. Therefore, the defect In_{As} acts as a doubly charged acceptor. In addition, this defect introduces the resonance and localized states with the E' symmetry into the valence band. The defect As_{In} gives rise to an attractive potential that splits off a single deep level E' from the conduction band. This level is completely occupied by electrons and has an energy of 0.37 eV (with respect to a Γ_{8V} level). The defect As_{In} acts as a doubly charged donor. In addition, it gives rise to two localized states in the valence band and a single resonance level E' unoccupied by electrons in the conduction band. The calculated level energies of the neutral intrinsic defects in InAs are in satisfactory agreement with the results obtained using the tight-binding approximation [26, 27].

The results of the numerical evaluation of the deep levels related to neutral intrinsic defects in InAs and located within the conduction band and the band gap are shown in Fig. 5. The data indicate that the neutral vacancies do not introduce localized states into the band gap of InAs; however, the antisite defects form the donor (As_{In}) and acceptor (In_{As}) states. In addition, a specific feature of InAs is the fact that point defects form resonance-type states in the region of allowed energies in the conduction and valence bands. States of this type are observed fairly often in narrow-gap semiconductors, for example, in IV–VI semiconductor compounds [28].

Since the charge state of the defects depends on the mutual location of their levels in relation to the Fermi level and can vary in the course of irradiation, we also calculated the levels of the charged states of the vacancies and antisite defects for the energy interval in the vicinity of the InAs band gap (Fig. 5). The energies of these states have previously been assessed only semiempirically for InAs [27, 29]; it is noteworthy that the results obtained in [27] and [29] differ from each other considerably. The shifts of the deep levels for the negatively charged states of the In_{As} defects [29] are close to the results obtained in this study.

Only the triply charged state $(G')^{---}$ occupied by four electrons (the state completely occupied by electrons) for V_{In} is split off from the valence band and becomes a localized state with the energy $E = E_V + 0.02$ eV, whereas the neutral, singly charged, and doubly charged states form resonances in the valence band. In contrast, the neutral resonance state of V_{As} becomes a localized state located in the band gap and has the energy $E = E_V + 0.34$ eV after ionization.
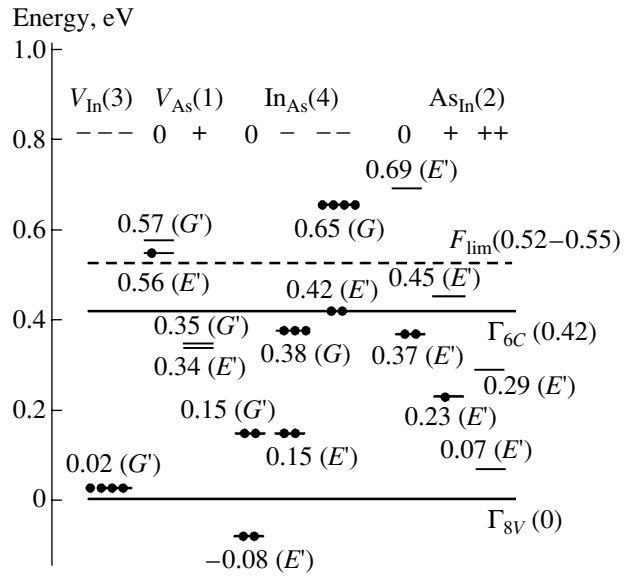
Fig. 5. The energy spectrum of the nonrelaxed defects V_{As}, V_{In}, As_{In}, and In_{As} in InAs, which was calculated taking into account the spin–orbit splitting. Positions of the levels of the neutral and charged defects in the band gap and in its vicinity are shown. The energy is measured from the level Γ_{8V}; the values of the energy are measured at $T \approx 0$ K and are expressed in eV.

The majority of the charged states of the As_{In} defect are located within the band gap, whereas, for the In_{As} defect, the state $(G')^{--}$ is doubly negatively charged, completely occupied by electrons, pushed into the conduction band ($E = E_V + 0.65$ eV), and becomes a resonance state. Using the single-electron energies of the point-defect states, we can particularly identify the level F_{lim} with the energy $E(-/--) = 0.51$ eV for the In_{As} antisite defect and the energy $E(-/--) = 0.46$ eV for the arsenic vacancy V_{As}. In general, this identification is consistent with the conclusions forwarded in [29, 30], which were concerned with the particular role of deep levels of defects in the anionic sublattices of III–V compounds in the phenomenon of the pinning of the Fermi level. This relation is not accidental since the defects under consideration give rise to strong perturbation potentials and highly localized wave functions. Thus, the states of these defects are at their deepest in a semiconductor and, as was shown in [12, 22], their energy levels are highly resistant to disordering of the crystal lattice. In terms of the parameters in the tight-binding approximation, the special feature of the defects under consideration is related to the fact that the positions of the In_{As} and V_{As} levels only differ due to a interatomic matrix element that exhibits little variation for different III–V semiconductors. Defects of this type accumulate in the course of irradiation and can become dominant among the defects responsible for the Fermi level pinning in irradiated semiconductors. Thus, we further developed the defect model [31] to show that the Fermi level position in an electron-irradiated InAs crystal
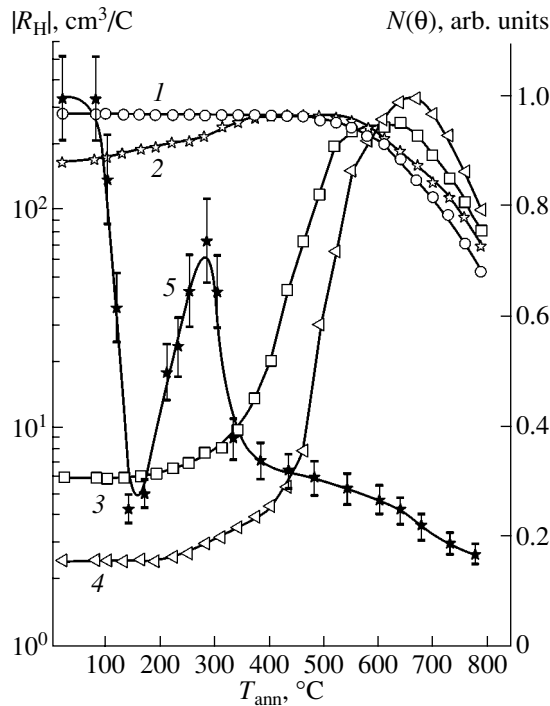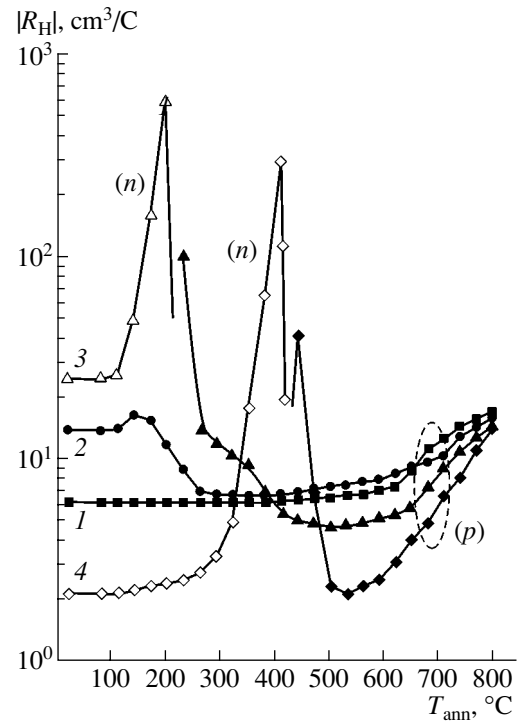
Fig. 6. Dependences of the Hall coefficient $|R_H|$ on the temperature of isochronous annealing (for 10 min) for *n*-InAs (sample 1) irradiated with electrons at an energy of ~2 MeV and with the integrated fluxes $D = $ (*1*) 0, (*2*) 4×10^{17}, (*3*) 5×10^{18}, and (*4*) 1×10^{19} cm^{-2}. Curve *5* illustrates the variation in the count rate of annihilation γ-ray photons in the region of small angles $N(\theta \approx 0)$ as a result of the isochronous annealing (for 10 min) of sample 1 after irradiation with electrons at the dose $D = 5 \times 10^{18}$ cm^{-2}. The temperature of the measurements $T = 295$ K.

Fig. 7. Dependences of the Hall coefficient $|R_H|$ on the temperature of isochronous annealing (for 10 min) for *p*-InAs (sample 11) irradiated with electrons at an energy of ~2 MeV and with the integrated fluxes $D = $ (*1*) 0, (*2*) 2×10^{17}, (*3*) 3×10^{18}, and (*4*) 1×10^{19} cm^{-2}. The temperature of the measurements was $T = 295$ K. The conductivity type is indicated.

within the allowed energies in the conduction band evidently correlates with the states of separate intrinsic defects in the anionic sublattice V_{As} and the antisite defects In_{As}. Almost the same assumptions were used in previous publications [32, 33] where the formation of n^+-type conductivity channels at a cleaved or thermally treated InAs surface was related to the presence of V_{As} resonance states.

To conclude this section, we can note that an InAs crystal irradiated with electrons is a material with n^+-type conductivity in which the Fermi level is pinned above the conduction-band top. This pinning of the Fermi level is a result of the mutual compensation of the entire ensemble of the donor and acceptor states of radiation defects; as a consequence, the F_{lim} level is located between the levels of the radiation defects with the highest concentrations.

7. ANNEALING OF RADIATION DEFECTS

In Figs. 6 and 7, we show the results of studying the isochronous annealing of InAs crystals irradiated with electrons. Heating of the initial samples to temperatures

higher than 450°C leads to the formation of quenched-in donors, which is especially noticeable for lightly doped InAs. This phenomenon is well known for InAs [4, 34]; therefore, the annealing of radiation defects in this study was performed at temperatures no higher than 800°C. In the initial *n*-type samples irradiated with electrons, the radiation defects are annealed off in a wide temperature range, from 80 to 800°C, which indicates that the concentration of donor-type radiation defects decreases (Fig. 6). Furthermore, it follows from studies of the positron annihilation that clusterization of the radiation defects (in addition to annealing) occurs as the annealing temperature is increased. For example, if the samples are annealed in the temperature range 150–300°C, an increase in the capture rate of positrons is observed in the region of small angles $N(\theta \approx 0)$, which indicates that clusters of vacancy-type defects are formed (Fig. 6). Such phenomena are characteristic of the annealing of III–V semiconductors with a high concentration of radiation defects (see, e.g., [35]). Subsequent decomposition of these defect-containing clusters in InAs occurs at annealing temperatures T_{ann} higher than 300°C; however, residual defects are still observed in irradiated InAs annealed at $T_{ann} \approx$ 800°C.

The recovery of R_H in the initial samples with p-type conductivity is illustrated in Fig. 7, using an initial heavily doped sample (sample 11) as an example. The presence of a reverse-annealing stage is observed in lightly doped InAs at temperatures of ~(100–150)°C, which indicates that either the radiation-induced acceptors are annealed out or donor-type defects are formed. For the heavily irradiated samples, an "overannealing" of the value of R_H is observed, which indicates that residual acceptors are present in this material and are not annealed out, even after heat treatment at temperatures close to 600°C. As in the initial samples with n-type conductivity, the efficiency of the annealing of radiation defects in p-InAs is reduced both as the electron dose increases and as the initial level of doping of InAs decreases.

8. CONCLUSIONS

Irrespective of the type of radiation (electrons, protons, or fast neutrons) and also the parameters and history of the initial InAs material, the curves $F(D)$ always exhibit a tendency towards leveling off in the region of $E_V + (0.51–0.55)$ eV at $T = 77–295$ K, which corresponds to the limiting free-electron concentration $n_{lim} \approx (2–3) \times 10^{18}$ cm^{-3}. These unusual properties of are caused by the character of the energy spectrum of an ideal crystal rather than by special features of the formation of radiation defects in this compound. The low position of the level Γ_{6C} in the InAs dielectric gap compared to in Group IV semiconductors and III–V compounds causes a fraction of the radiation defects (V_{As} and In_{As}) to form resonance-type states in the region of allowed energies in the conduction band, and it is these states that control the electrical properties of irradiated InAs.

In InAs, as in other Group IV semiconductors and III–V compounds, radiation defects of both the donor and acceptor types are produced as a result of irradiation; the extent of the effect of these defects on the electrical properties of InAs depends on the level of doping and the conductivity type of the initial material. At $n > n_{lim} \approx (2–3) \times 10^{18}$ cm^{-3}, the radiation-induced acceptors are more effective, whereas radiation-produced donors play the most important role if $n < n_{lim} \approx (2–3) \times 10^{18}$ cm^{-3}. In general, the response of InAs (and other semiconductors) to irradiation with high-energy particles can be described as the phenomenon of radiation-induced self-compensation (compensation of the electrical activity of the initial material) and the transition of a semiconductor to a state corresponding to $K \approx 1$. We did not observe any special features relating to changes of the electrical properties of transmutation-doped InAs and InAs:Sb subjected to irradiation with electrons compared to the InAs crystals doped with hydrogen-like impurities in the course of growth.

In irradiated InAs, the position of the Fermi level F_{lim} is close to that at the metal–semiconductor boundary and in the surface n^+-type layer inevitably formed at the cleaved surface when InAs is kept under atmospheric conditions. This position of the Fermi level is characteristic of InAs and is independent of the type of intrinsic lattice defect; consequently, it is also independent of the irradiation conditions. These data, as in the case of other Group IV semiconductors and III–V compounds, once again verify the fundamental character of the parameter F_{lim} and indicate that there is a unified mechanism of the Fermi level pinning observed both in bulk defect-containing InAs after irradiation and at the InAs surface and metal–InAs boundary.

REFERENCES

1. V. N. Brudnyĭ, Izv. Vyssh. Uchebn. Zaved., Fiz. **29** (8), 84 (1986).
2. M. Soukiassian, J. K. Albany, and M. Vandevyver, Inst. Phys. Conf. Ser., No. 31, 395 (1977).
3. N. G. Kolin, V. B. Osvenskiĭ, N. S. Rytova, and U. S. Yugova, Fiz. Tekh. Poluprovodn. (Leningrad) **21**, 521 (1987) [Sov. Phys. Semicond. **21**, 320 (1987)].
4. V. N. Brudnyĭ, N. G. Kolin, and A. I. Potapov, Fiz. Tekh. Poluprovodn. (St. Petersburg) **37**, 408 (2003) [Semiconductors **37**, 390 (2003)].
5. V. V. Karataev, E. S. Yurova, M. G. Mil'vidskiĭ, *et al.*, Neorg. Mater. **21**, 1631 (1985).
6. N. G. Kolin, V. B. Osvenskiĭ, N. S. Rytova, and E. S. Yurova, Fiz. Tekh. Poluprovodn. (Leningrad) **20**, 822 (1986) [Sov. Phys. Semicond. **20**, 519 (1986)].
7. N. G. Kolin, Izv. Vyssh. Uchebn. Zaved., Fiz. **46** (6), 12 (2003).
8. Yang June Jung, Byund Ho Kim, and Hyang Jae Lee, Phys. Rev. B **26**, 3151 (1982).
9. V. V. Karataev, M. G. Mil'vidskiĭ, N. S. Rytova, and V. I. Fistul', Fiz. Tekh. Poluprovodn. (Leningrad) **11**, 1718 (1977) [Sov. Phys. Semicond. **11**, 1009 (1977)].
10. V. N. Brudnyĭ and S. N. Grinyaev, Fiz. Tekh. Poluprovodn. (St. Petersburg) **32**, 315 (1998) [Semiconductors **32**, 284 (1998)].
11. V. N. Brudnyi, S. N. Grinyaev, and V. E. Stepanov, Physica B (Amsterdam) **212**, 429 (1995).
12. V. N. Brudnyĭ, S. N. Grinyaev, and N. G. Kolin, Materialovedenie **3** (72), 17 (2003).
13. T. W. Dobson and J. F. Wager, J. Appl. Phys. **66**, 1997 (1989).
14. W. Walukiewicz, Appl. Phys. Lett. **54**, 2094 (1989).

15. N. V. Agrinskaya and T. V. Mashovets, Fiz. Tekh. Poluprovodn. (St. Petersburg) **28**, 1505 (1994) [Semiconductors **28**, 843 (1994)].

16. S. B. Zhang, S. H. Wei, and A. Zunger, Phys. Rev. Lett. **84**, 1232 (2000).

17. V. N. Brudnyĭ, Doctoral Dissertation (Tomsk State Univ., Tomsk, 1993).

18. H. J. Bardeleben, Solid State Commun. **57**, 137 (1986).

19. N. D. Wilsey and T. A. Kennedy, in *Proceedings of the Symposium on Microscopic Identification of Electronic Defects in Semiconductors, San Francisco, 1985* (Pittsburg, PA, 1985), p. 309.

20. R. C. Newman, in *Proceedings of 13th International Conference on Defects in Semiconductors, Coronado, California, 1984* (Metallurgical Soc. of AIME, Warrendale, PA, 1985), p. 84.

21. M. Ladjemi, Le Titre de Docteur Ingenieur (Univ. Paris-Sud, Centre D'Orsay, Paris, 1982).

22. V. N. Brudnyĭ, S. N. Grinyaev, and N. G. Kolin, Fiz. Tekh. Poluprovodn. (St. Petersburg) **37**, 557 (2003) [Semiconductors **37**, 537 (2003)].

23. V. A. Chaldyshev and S. N. Grinyaev, Izv. Vyssh. Uchebn. Zaved., Fiz. **26** (3), 38 (1983).

24. S. N. Grinyaev and V. A. Chaldyshev, Izv. Vyssh. Uchebn. Zaved., Fiz. **39** (8), 13 (1996).

25. S. N. Grinyaev and G. F. Karavaev, Fiz. Tekh. Poluprovodn. (St. Petersburg) **31**, 545 (1997) [Semiconductors **31**, 460 (1997)].

26. S. Das Sarma and A. Madhukar, Phys. Rev. B **24**, 2051 (1981).

27. W. Kuhn, R. Strehlow, and M. Hanke, Phys. Status Solidi A **141**, 541 (1987).

28. V. I. Kaĭdanov and Yu. I. Ravich, Usp. Fiz. Nauk **145**, 51 (1985) [Sov. Phys. Usp. **28**, 31 (1985)].

29. M. S. Daw and D. L. Smith, J. Vac. Sci. Technol. **17**, 1028 (1980).

30. W. Potz and D. K. Ferry, Phys. Rev. B **31**, 968 (1985).

31. W. E. Spicer, P. W. Chye, P. R. Skeath, *et al.*, J. Vac. Sci. Technol. **16**, 1422 (1979).

32. M. A. Bunin and Yu. A. Matveev, Fiz. Tekh. Poluprovodn. (Leningrad) **19**, 2018 (1985) [Sov. Phys. Semicond. **19**, 1241 (1985)].

33. V. V. Karataev, M. I. Reznikov, and V. I. Tal'yanskiĭ, Poverkhnost, No. 4, 57 (1986).

34. V. V. Karataev, G. A. Nemtsova, N. S. Rytova, and T. G. Yugova, Fiz. Tekh. Poluprovodn. (Leningrad) **11**, 1670 (1977) [Sov. Phys. Semicond. **11**, 982 (1977)].

35. V. N. Brudnyi, S. A. Verobiev, and A. A. Tsoi, Phys. Status Solidi A **72**, 529 (1982).

Translated by A. Spitsyn

ELECTRONIC AND OPTICAL PROPERTIES
OF SEMICONDUCTORS

The Transport and Thermoelectric Properties of Semiconducting Rhenium Silicide

A. B. Filonov*^, A. E. Krivosheev*^, L. I. Ivanenko*^^, G. Behr**, J. Schumann**, D. Souptel**, and V. E. Borisenko*

*Belarusian State University of Informatics and Radioelectronics, Minsk, 220013 Belarus
^e-mail: anton@nano.bsuir.edu.by
^^e-mail: ivanenko@nano.bsuir.edu.by
**Leibniz Institute of Solid State and Materials Research, PF2701 16, D-01171 Dresden, Germany
Submitted June 9, 2004; accepted for publication August 9, 2004

Abstract—The transport and thermoelectric properties of semiconducting rhenium silicide $ReSi_{1.75}$ are comprehensively studied both experimentally and theoretically. Single-crystal samples of undoped and aluminum-doped $ReSi_{1.75}$ are grown by floating-zone melting using optical heating. The temperature dependences of the resistivity, Hall coefficient, and Seebeck coefficient (thermoelectric power) are measured in the range 77–800 K. At room temperature, the charge-carrier concentration for the undoped rhenium silicide is 10^{19} cm^{-3} and the carrier mobility is 30 cm^2/(V s). The theoretical study of the transport and thermoelectric properties includes ab initio calculation of the band structure; estimation of the carrier effective masses; simulation of the electron and hole mobility, taking into account classical scattering mechanisms; and calculation of the Seebeck coefficient. The results of the simulation and the experimental data are in good agreement. © 2005 Pleiades Publishing, Inc.

1. INTRODUCTION

Recently, a great deal of attention has been paid to the study of the transport properties of various modifications of silicide systems with the purpose of increasing their thermoelectric efficiency $Z = S^2/\rho\chi$, where S is the Seebeck coefficient, ρ is the resistivity, and χ is the thermal conductivity. The major problem regarding this line of research is to produce a material with the largest possible ratio S^2/ρ. A potential candidate for thermoelectric application is semiconducting rhenium silicide $ReSi_{1.75}$ [1–3].

The decisive role in the estimation of S^2/ρ, and, hence, the thermoelectric efficiency of a material as a whole, is played by carrier mobility. A report indicating a high carrier mobility in $ReSi_{1.75}$ single crystals (up to 370 cm^2/(V s) at 300 K [4]) initiated active studies of the transport properties of this material. At the same time, it was shown that the room-temperature hole mobility does not exceed 150 cm^2/(V s) for epitaxial films [5] and 30 cm^2/(V s) for single crystals [6].

The main objective of this paper is a comprehensive experimental and theoretical study of the transport properties of semiconducting rhenium silicide for the purpose of estimating the thermoelectric efficiency of this compound and the prospects for its application to thermoelectricity.

2. EXPERIMENTAL

Perfect single-crystal samples of undoped and aluminum-doped semiconducting rhenium silicide were grown by floating-zone melting using optical heating. The setup is described in detail in [7]. The polycrystalline feed rods were made of high-purity materials: 99.99%-pure rhenium (Goodfellow), 99.9999%-pure silicon (Alfa), and 99.9998%-pure aluminum (Goodfellow). The aluminum concentration in the feed rods was 1.5 at %. The grown single crystals were cylinder-shaped and had a length and diameter of 70 and 6 mm, respectively. The composition, microstructure, and structural quality of the crystals were determined using X-ray diffraction, optical metallography, and electron probe microanalysis. The crystal orientation was determined using Laue backscattering. Samples 10 mm in diameter and 1 mm thick were cut from the grown crystals for transport measurements. The sample resistivity was measured using a four-probe method and was performed simultaneously with the Seebeck coefficient measurement in the temperature range 77–800 K. The carrier concentration and mobility were determined from the Hall coefficient measurements.

An X-ray diffraction analysis showed that the as-grown samples represent a triclinic phase of rhenium silicide $ReSi_{1.75}$ with the lattice parameters $a = 0.3138$ nm, $b = 0.3120$ nm, $c = 0.7670$ nm, and $\alpha = 89.9°$. The Laue method confirmed the single-crystal perfection of samples and the absence of twin crystals.
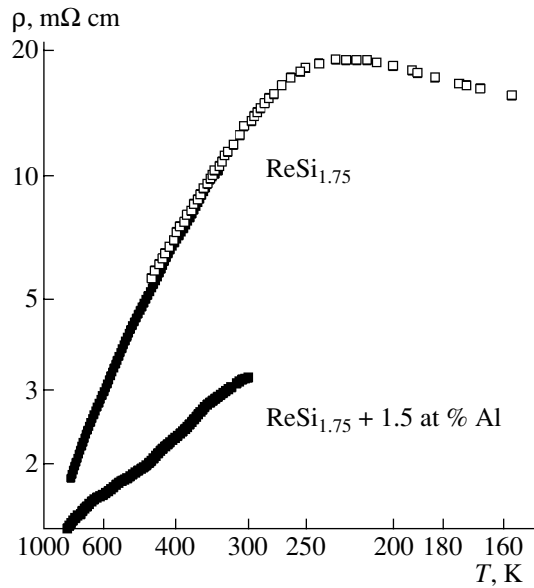
Fig. 1. Temperature dependences of the resistivity of the undoped and Al-doped $ReSi_{1.75}$ single crystals.

Fig. 2. Temperature dependences of the Seebeck coefficient for the undoped and Al-doped $ReSi_{1.75}$ single crystals: (a) experimental and (b) calculated data.

According to the temperature dependence of the resistivity (Fig. 1), the $ReSi_{1.75}$ band gap is 0.14 eV, which is in good agreement with the experimental data of [4, 6] and the results of our previous calculations [8]. Doping with aluminum, when compared to the undoped sample, decreased the resistivity by a factor of 3. The room-temperature carrier concentration in the undoped silicide was relatively high, 10^{19} cm^{-3}, and the carrier mobility was 30 cm^2/(V s).
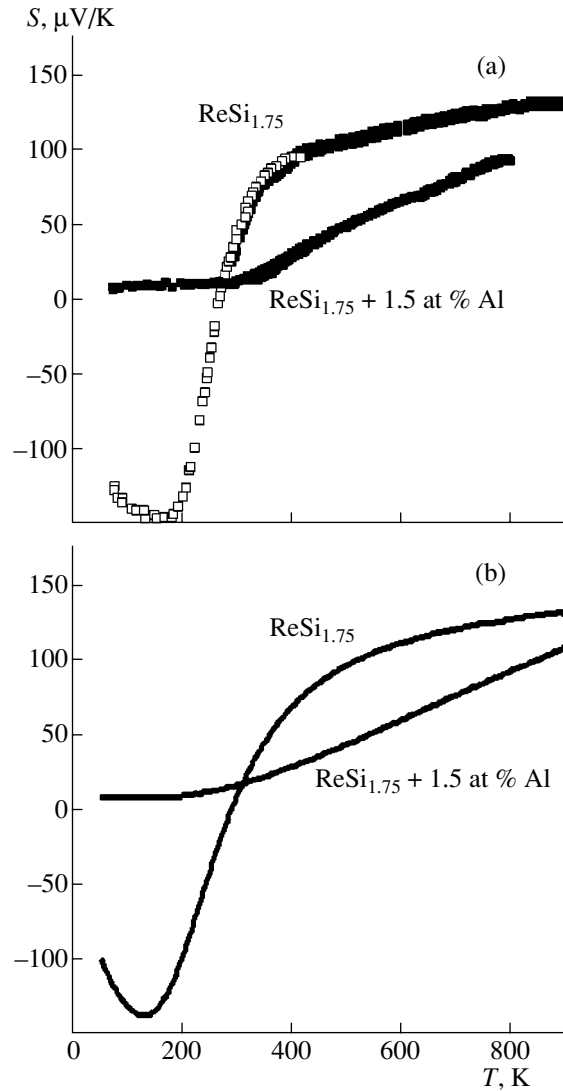
The experimental data obtained when measuring the Seebeck coefficient suggest that the as-grown undoped crystals of semiconducting rhenium silicide contain carriers of both types (Fig. 2a). We can see that rhenium silicide exhibits *n*- and *p*-type conductivity at temperatures below and above 270 K, respectively.

The temperature dependence of the Seebeck coefficient can be conventionally subdivided into three regions.

(i) 77 K $\leq T \leq$ 150 K: the Seebeck coefficient magnitude increases with temperature and peaks at 150 K, which is obviously caused by the effect of the low-temperature donor levels.

(ii) 150 K $< T \leq$ 400 K: beginning from 150 K, the effect of the donor levels decreases and ionized acceptor centers begin to have an increasing effect. These centers rapidly compensate the electron conductivity. As a result, the hole conductivity becomes more dominant than the electron conductivity above 270 K, due to the higher concentration of acceptor centers, and the Seebeck coefficient increases with temperature.

(iii) $T >$ 400 K: the acceptor levels are saturated, which results in an insignificant linear increase in the Seebeck coefficient as the temperature rises.

The highest Seebeck coefficient for the undoped $ReSi_{1.75}$ crystals is 130 µV/K. For the aluminum-doped $ReSi_{1.75}$ crystals (Fig. 2a), the Seebeck coefficient is positive in the entire temperature range under consideration and peaks (100 µV/K) at ~800 K. This observation suggests that the hole conductivity is dominant in the entire temperature range under study.

3. SIMULATION

The rhenium silicide $ReSi_{1.75}$ lattice belongs to the space group $P1$ and has a triclinic structure with the lattice parameters a = 0.3138, b = 0.3120, c = 0.7670 nm, and α = 89.9°. Due to a slight deviation from a tetragonal structure ($C11b$), two of the Si atom sites are not completely occupied (the occupation probability is 0.75) [4]. However, since the *c*-axis tilt angle α to the

ab plane deviates very little from a right angle and cannot significantly affect the calculated results, we consider this lattice as a simple orthorhombic one (without any modification of the atomic sites). In order for the periodic structure under study to contain an integer number of atoms of every type, the primitive cell was increased twofold along directions *a* and *b*. To promote convergence of the calculated results, empty spheres were introduced in place of the two atomic sites free of silicon.

The ReSi$_{1.75}$ band structure was simulated using the WIEN97 software package [9], which is based on a method of linear augmented plane waves. Expansion of the wave functions in lattice harmonics for the partial waves used inside atomic spheres was carried out up to $l = 10$. Integration over the Brillouin zone was obtained using the tetrahedron method. Self-consistency cycles were completed when the determination error of the system total energy was 0.0001 Ry/atom.

Figure 3 shows a fragment of the obtained band structure along the high-symmetry direction of the Brillouin zone. The band gap is 0.16 eV, and rhenium silicide exhibits an indirect transition between the points Γ (the valence-band top) and S (the conduction-band bottom).

Then, based on the data on the band structure, the carrier (electron and hole) effective masses were estimated. The determined components of the effective mass tensor are listed in the table. We noted a significant difference between the hole effective masses for directions *a*, *b*, and *c*, which is caused by an almost plane valence band in the Γ–Z direction (Fig. 3). This difference, in turn, can cause significant anisotropy of the ReSi$_{1.75}$ transport properties. Such anisotropy was, in part, experimentally observed in [4].

Let us consider the carrier mobility using the relation

$$\mu^{-1} = \mu_{AC}^{-1} + \mu_{NPO}^{-1} + \mu_{PO}^{-1} + \mu_{I}^{-1}, \qquad (1)$$

where μ_{AC}, μ_{NPO}, μ_{PO}, and μ_{I} are the mobilities for scattering by acoustic phonons (AC), polar (PO) and nonpolar (NPO) optical phonons, and ionized impurity atoms (I), respectively. In the case of a nondegenerate semiconductor with parabolic bands for every individual scattering mechanism, we have (see [10])

$$\mu_i = \frac{4e}{3m^*(kT)^{5/2}\sqrt{\pi}}\int_0^\infty E^{3/2}\tau_i\exp\left(-\frac{E}{kT}\right)dE, \qquad (2)$$

where m^* and E are the averaged carrier effective mass and energy, T is the temperature, and τ_i is the relaxation time for the *i*th scattering mechanism.

In the case of scattering by acoustic phonons, the relaxation time is written as (see [11])

$$\tau_{AC} = \frac{\pi\hbar^4 e^2\rho v_s^2}{\sqrt{2m^{*3}E}\,\Xi_{AC}kT}, \qquad (3)$$
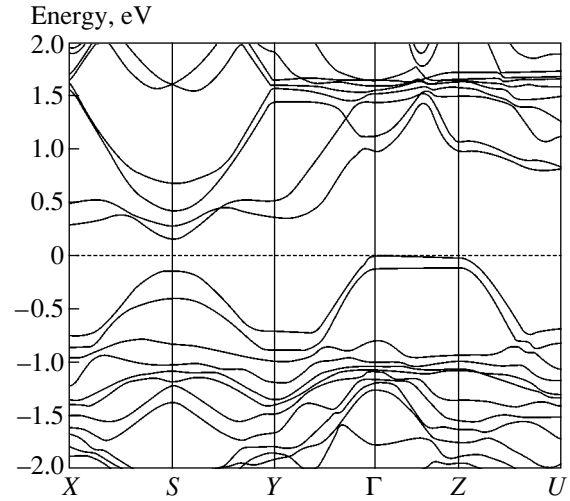
Energy, eV

Fig. 3. The band structure of semiconducting rhenium silicide.

where ρ is the material density (10.66 g/cm^3), v_s is the longitudinal velocity of sound in the material (3.7 × 10^5 cm/s), and Ξ_{AC} is a constant defined by the components of the deformation potential tensor. Typically, for semiconductors, this constant varies from 5 to 15 eV. In the case under consideration, we assume that $\Xi_{AC} = 5$ eV.

In addition, the formula suggested in [11] for the relaxation time for scattering by nonpolar optical phonons can be rewritten as

$$\tau_{NPO} = \tau_{AC}[C(1 + k\theta/E)^{1/2} + \exp(\theta/T)(1 - k\theta/E)^{1/2}]^{-1}, \qquad (4)$$

where θ is the Debye temperature (580 K), $C = \eta/2(\theta/T)[\exp(\theta/T) - 1]^{-1}$, and $\eta = (\Xi_{NPO}/\Xi_{AC})^2$. The latter quantity is the parameter of the suggested model.

Let us consider the relaxation time associated with scattering by polar optical phonons in the following form (see [11]):

$$\tau_{PO} = \sqrt{\frac{2^5 E}{m^*}}\frac{\pi\hbar\varepsilon_p}{e^2\omega_0}\left\{n(\omega_0)\sqrt{1 + \frac{\hbar\omega_0}{E}} + n(\omega_0 + 1)\right.$$

$$\times\sqrt{1 - \frac{\hbar\omega_0}{E}} + \frac{\hbar\omega_0}{E}\left[n(\omega_0 + 1)\text{arcsinh}\left(\sqrt{\frac{E}{\hbar\omega_0} - 1}\right)\right. \qquad (5)$$

$$\left.\left. - n(\omega_0)\text{arcsinh}\left(\sqrt{\frac{E}{\hbar\omega_0} - 1}\right)\right]\right\}^{-1}.$$

Components of the tensor of carrier effective masses

	m_a	m_b	m_c
Electrons	0.35	0.32	0.37
Holes	0.27	0.27	11.82
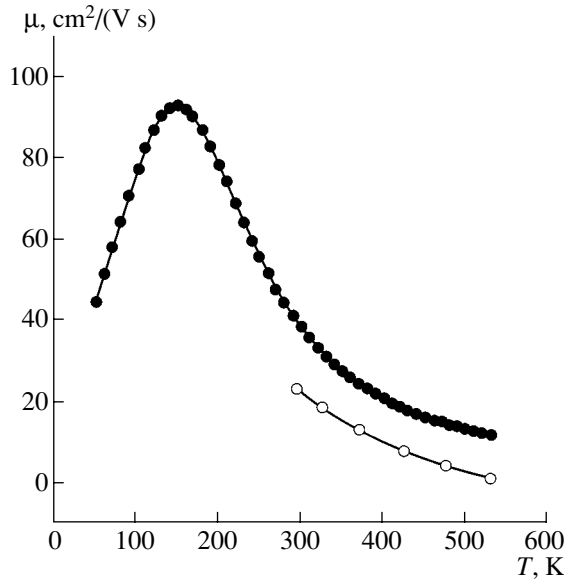
Fig. 4. Experimental (open circles) and calculated (closed circles) temperature dependences of the hole mobility in ReSi$_{1.75}$.

Here, $1/\varepsilon_p = 1/\varepsilon_\infty - 1/\varepsilon_0$, ε_0, and ε_∞ are the static and high-frequency permittivities (30.0 and 3.0, respectively [12]); ω_0 is the optical phonon frequency defined by the Debye temperature θ ($\omega_0 = k\theta/\hbar$); and the number of phonons is defined as $n(\omega_0) = [\exp(h\omega_0/kT) - 1]^{-1}$.

Currently, there are many models describing scattering by ionized impurities. The Brooks–Herring model [11] is most appropriate for the objective of this study,

$$\tau_I = \frac{\sqrt{2m^*E}}{\pi e^4 N_i \varphi(x)} \varepsilon_0, \tag{6}$$

where N_i is the concentration of ionized impurities or defects (10^{19} cm^{-3}),

$$\varphi(x) = \ln(1 + x) + \frac{x}{(1 + x)}, \quad x = \frac{8m^*E\Gamma_0}{\hbar^2},$$

$$\Gamma_0 = \frac{\sqrt[3]{\pi/3n}\,\varepsilon_0\hbar^2}{4m^*e^2},$$

and n is the charge-carrier concentration.

Furthermore, for doped rhenium silicide, we took into consideration the additional mechanism of scattering by a neutral impurity (see [11]),

$$\tau_0 = e^2 m^{*2}(20\varepsilon_0 h^2 N_0)^{-1}, \tag{7}$$

where N_0 is the neutral-impurity concentration (the model parameter in the case under consideration).

To illustrate the efficiency of the suggested model for calculating the carrier mobility in semiconducting rhenium silicide, Fig. 4 shows the calculated and experimental temperature dependences of the hole mobility

in ReSi$_{1.75}$. It should be noted that we succeeded in reproducing the distinctive features of the experimental dependence in a certain temperature range both qualitatively and quantitatively.

Since both carrier types should be taken into account for semiconducting rhenium silicide in a wide temperature range, the formula for the Seebeck coefficient in the case under consideration is written as (see [13])

$$\begin{aligned}
S(T) = \frac{k}{\sigma}\Bigg\{ &n\mu_n\left[A + \ln\frac{2(2\pi m_n^* kT)^{3/2}}{h^3 n}\right] \\
&-p\mu_p\left[A + \ln\frac{2(2\pi m_p^* kT)^{3/2}}{h^3 p}\right]\Bigg\},
\end{aligned} \tag{8}$$

where σ is the electrical conductivity; n, p, $\mu_{n,p}$, and $m_{n,p}^*$ are the electron and hole concentrations, mobilities, and effective masses, respectively; and A is a constant that depends on the scattering mechanism.

The calculated dependences of the Seebeck coefficient (Fig. 2b) for both the doped and undoped rhenium silicide are consistent with the experimental data not only qualitatively but also quantitatively, which once again confirms the high accuracy of the developed mobility model and the chosen approach for simulating the thermoelectric properties of semiconducting rhenium silicide.

4. CONCLUSION

Floating-zone melting was used to grow single-crystal samples of rhenium silicide ReSi$_{1.75}$ and silicide doped with aluminum. The temperature dependences, resistivity, and Seebeck coefficient were studied in a wide temperature range. The room-temperature concentration of majority carriers (holes) for the undoped silicide was found to be high, 10^{19} cm^{-3}. An analysis including calculation of the band structure and the Seebeck coefficient, estimation of the carrier effective masses, and simulation of the electron and hole mobility was carried out, taking into account classical scattering mechanisms. The results obtained were in good agreement with the experimental data.

The largest Seebeck coefficient for the ReSi$_{1.75}$ crystals was 130 µV/K. This figure provides good stimulation for the further study of this material in relation to the aim of its application to thermoelectricity.

REFERENCES

1. L. Ivanenko, H. Lange, and A. Heinrich, in *Semiconducting Silicides*, Ed. by V. E. Borisenko (Springer, Berlin, 2000), Chap. 5, p. 243.

2. C. A. Kleint, A. Heinrich, H. Griessmann, *et al.*, in *Proceedings of MRS Fall Meeting on Thermoelectric Materials, 1998* (Boston, USA, 1998); Mater. Res. Soc. Symp. Proc. **545**, 165 (1999).

3. A. Heinrich, C. Kleint, H. Griessmann, *et al.*, in *Proceedings of XVIII International Conference on Thermoelectrics* (Baltimore, USA, 1999), p. 161.

4. U. Gottlieb, B. Lambert-Andron, F. Nava, *et al.*, J. Appl. Phys. **78**, 3902 (1995).

5. I. Ali, P. Muret, and A. Haydar, Semicond. Sci. Technol. **16**, 966 (2001).

6. L. Ivanenko, V. L. Shaposhnikov, A. B. Filonov, *et al.*, Microelectron. Eng. **64** (1–4), 225 (2002).

7. D. Souptel, G. Behr, L. Ivanenko, *et al.*, J. Cryst. Growth **244**, 296 (2002).

8. A. B. Filonov, D. B. Migas, V. L. Shaposhnikov, *et al.*, Europhys. Lett. **46**, 376 (1999); Microelectron. Eng. **50**, 249 (2000).

9. P. Blaha, K. Schwarz, P. Sorantin, and S. B. Trickey, Comput. Phys. Commun. **59**, 399 (1990).

10. V. L. Bonch-Bruevich and S. G. Kalashnikov, *Physics of Semiconductors*, 2nd ed. (Nauka, Moscow, 1990) [in Russian].

11. B. Ridley, *Quantum Processes in Semiconductors* (Clarendon, Oxford, 1982; Mir, Moscow, 1986), p. 143.

12. T. Siegrist, F. Hulliger, and G. Travaglini, J. Less-Common Met. **92**, 119 (1983).

13. A. F. Ioffe, *Physics of Semiconductors* (Akad. Nauk SSSR, Leningrad, 1957; Infosearch, London, 1960).

Translated by A. Kazantsev

The Effect of the Charge State of Nonequilibrium Vacancies on the Nature of Radiation Defects in *n*-Si Crystals

T. A. Pagava

Georgian Technical University, Tbilisi, 0175 Georgia
e-mail: tpagava@gtu.edu.ge
Submitted June 21, 2004; accepted for publication August 9, 2004

Abstract—The aim of this study is to gain insight into the effect of the charge state of nonequilibrium vacancies on the processes that occur during irradiation and annealing in silicon crystals. *n*-Si floating-zone crystals with an electron concentration of $N = 6 \times 10^{13}$ cm^{-3} are irradiated with 25-MeV protons at 300 K. The irradiated crystals are then studied by the Hall method at temperatures ranging from 77 to 300 K. It is shown that the nature and energy spectrum of radiation defects in *n*-Si crystals are mainly controlled by the charge state of nonequilibrium vacancies. © 2005 Pleiades Publishing, Inc.

1. INTRODUCTION

A method combining local irradiation with subsequent measurements of the bulk photovoltage over the irradiated area was previously used in [1–3] to show that primary radiation defects in *p*-Si crystals are positively charged at 300 K. In *n*-Si crystals, self-interstitials are positively charged, whereas vacancies are negatively charged.

In the course of irradiation, nonequilibrium vacancies enter into quasi-chemical reactions with doping impurities (phosphorus or boron), with background impurities (oxygen or carbon), and with each other. As a result, secondary radiation defects are formed. These defects feature a high thermal stability and control the physical properties of an irradiated crystal up to 600°C (secondary radiation defects are completely annealed out at this temperature) [4].

The objective of this study was to gain insight into the effect of the charge state of the primary radiation defects (in particular, vacancies) on the nature and energy spectrum of the secondary radiation defects.

2. EXPERIMENTAL

n-Si floating-zone crystals with an electron concentration of $N = 6 \times 10^{13}$ cm^{-3} were studied. The concentrations of background impurities (oxygen N_O and carbon N_C) were determined from the spectra of infrared absorption and were found to be equal to $N_O \approx N_C \approx 2 \times 10^{16}$ cm^{-3}. The growth-dislocation density was determined from the etch-pit density and did not exceed 10^3–10^4 cm^{-2}. The samples under study had an area of $1 \times 3 \times 10$ mm^3 and thickness of 1 mm and were irradiated with 25-MeV protons. The proton-flux density was $\varphi = 10^{11}$ cm^{-2} s^{-1}. The electron concentration N was measured by a compensation method in a magnetic field of 10 kOe in the temperature range $T = 77$–300 K. The

defect-level energies ΔE were determined from the slope of the curves $N = f(10^3/T)$ in the highly compensated samples. The error in the determination of the concentration and energy did not exceed 10%.

3. RESULTS

In the initial samples, the dependence $N = f(1/T)$ in the range $T = 77$–300 K corresponded to a complete ionization of the shallow donors (the phosphorus P atoms): $N \approx \text{const} = 6 \times 10^{13}$ cm^{-3} (see figure, curve *1*). After irradiation with protons at a dose of $\Phi = 2.7 \times 10^{12}$ cm^{-2}, the temperature dependence of the electron concentration corresponded to a depletion of the acceptor centers with $E_c - (0.17 \pm 0.01)$ eV (see figure, curve *6*). As a result of irradiation of the crystals at a dose of $\Phi = 8.1 \times 10^{12}$ cm^{-2}, a linear portion was observed in the curve $N = f(1/T)$; this portion corresponds to a depletion of the acceptor centers with $E_c - (0.41 \pm 0.02)$ eV (see figure, curve *3*). Otherwise, a portion related to the existence of acceptor centers with the level $E_c - (0.54 \pm 0.02)$ eV was observed (see figure, curve *2*). As is well known [5, 6], the acceptor level $E_c - 0.17$ eV is related to *A* centers, the level $E_c - 0.41$ eV is related to *E* centers or divacancies V_2, and the level $E_c - 0.54$ eV is related to an unknown center. It is worth noting that the relation of the last level to V_2 was disputed in [7]. In the figure, curves *4* and *5* correspond to a depletion of the *A* centers. These curves were obtained for the samples irradiated with the proton dose $\Phi = 8.1 \times 10^{12}$ cm^{-2} and subjected to a subsequent annealing at the temperatures $T_{\text{ann}} = 150$ and 300°C.

4. DISCUSSION

In the *n*-Si crystals irradiated with 2-MeV electrons, the formation efficiency of the *E* centers η_E is higher than that of the *A* centers η_A by a factor of 1.3, in spite

N, cm^{-3}
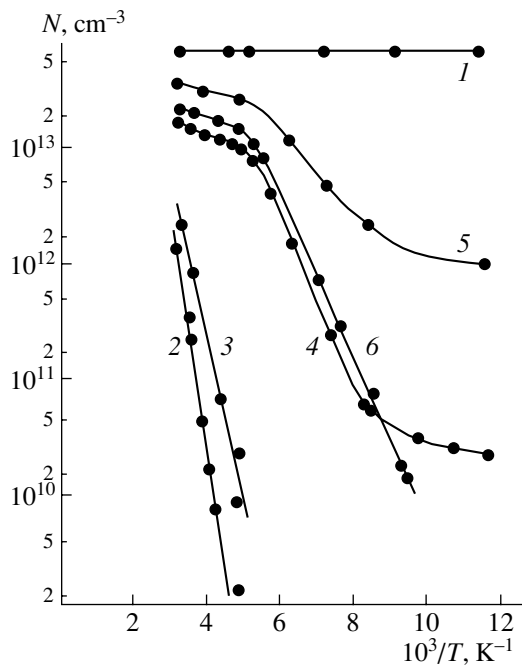
Temperature dependences of the electron concentration in n-Si crystals (1) before irradiation and (2–6) after irradiation with 25-MeV protons. The radiation dose Φ was (2–5) 8.1×10^{12} and (6) 2.7×10^{12} cm^{-2}. The samples were subjected to postirradiation annealing at $T_{\text{ann}} = $ (4) 150 and (5) 300°C.

of the fact that N_{O} is about three orders of magnitude larger than the phosphorus concentration N_{P}. It is believed [8] that the high efficiency of E-center production at 300 K is caused by the effect of the charge state of the vacancies on their migration rate and also by the Coulomb interaction between an electron captured by a vacancy and a positively charged donor $\mathbf{P}^+$.

We may conclude, on the basis of the above reasoning, that the charge state of the primary radiation defects controls the processes that occur in the n-Si crystals in the course of irradiation or subsequent isochronous annealing.

As is well known, the A centers are produced according to the following reaction in the course of irradiation at 300 K:

$$V^- + O \longrightarrow A^0 + e.$$

The level at $E_A = E_c - 0.17$ eV corresponds to the A centers. At 300 K, these centers are in an electroneutral state and can enter into the following quasi-chemical reaction with V^-: $A^0 + V^- \longrightarrow (V_2 + O)^-$. The latter center exhibits the energy level $E_{V_2 + O} = E_c - 0.5$ eV. These centers are negatively charged at 300 K; as a result, their involvement in the reaction with V^- is unlikely, owing to the ensuing electrostatic repulsion.

Since the E centers are negatively charged at room temperature (the level energy $E_E = E_c - 0.41$ eV), the

formation of a divacancy complex with an attachment of V^- is infeasible.

The attachment of V^- to V_2 is also hindered by the fact that $E_{V_2} = E_c - 0.39$ eV. Furthermore, the V_2 centers are negatively charged at 300 K. It is worth noting that the formation of divacancies V_2 from negative monovacancies via a diffusion-related mechanism is unlikely in the course of irradiation at 300 K. Apparently, divacancies are produced as primary defects.

Indeed, as can be seen from the figure, the A and E centers, divacancies, and $V_2 + O$ complexes are formed in the floating-zone n-Si crystals in the course of irradiation with protons at 300 K. We failed to detect the level at $E_c - 0.5$ eV that corresponds to the $V_2 + O$ complex, although the existence of this defect can be deduced from the increase in the electron concentration at 250 K occurring as a result of postirradiation isochronous annealing in the temperature region $T_{\text{ann}} \geq$ 500°C [8].

5. CONCLUSIONS

Thus, the nature and energy spectrum of secondary radiation defects in n-Si crystals depend on the charge state of nonequilibrium vacancies; in turn, this state depends on the radiation dose and temperature of the irradiated samples under study.

ACKNOWLEDGMENTS

REFERENCES

1. L. S. Milevskiĭ and V. S. Garnyk, Fiz. Tekh. Poluprovodn. (Leningrad) **13**, 1369 (1979) [Sov. Phys. Semicond. **13**, 801 (1979)].
2. T. A. Pagava, Z. V. Basheleĭshvili, V. S. Garnyk, *et al.*, Ukr. Fiz. Zh. **48**, 576 (2003).
3. Z. V. Basheleĭshvili and T. A. Pagava, Fiz. Tekh. Poluprovodn. (St. Petersburg) **33**, 924 (1999) [Semiconductors **33**, 845 (1999)].
4. V. V. Emtsev and T. V. Mashovets, *Impurities and Point Defects in Semiconductors* (Radio i Svyaz', Moscow, 1981), Part 1, Chap. 2, p. 82 [in Russian].
5. I. D. Konozenko, A. K. Semenyuk, and V. I. Khivrich, *Radiation Effects in Silicon* (Naukova Dumka, Kiev, 1974), Part 1, Chap. 2, p. 35 [in Russian].
6. P. F. Lugakov and V. V. Lukyanitsa, Phys. Status Solidi A **84**, 457 (1984).
7. V. S. Vavilov, V. F. Kiselev, and B. N. Mukashev, *Defects in Silicon and on Its Surface* (Nauka, Moscow, 1990), Chap. 3, p. 76 [in Russian].
8. L. S. Milevskiĭ and T. A. Pagava, Fiz. Tekh. Poluprovodn. (Leningrad) **10**, 1287 (1976) [Sov. Phys. Semicond. **10**, 763 (1976)].

Translated by A. Spitsyn

SEMICONDUCTOR STRUCTURES, INTERFACES, AND SURFACES

Photoconversion in *n*-ZnO:Al/Pd*Pc*/*p*-CuIn₃Se₅ Structures

I. V. Bodnar'*, E. S. Dmitrieva*, S. E. Nikitin**, V. Yu. Rud'***^,
Yu. V. Rud'**, and E. I. Terukov**

*Belarussian State University of Informatics and Radioelectronics, ul. Brovki 17, Minsk, 220027 Belarus
**Ioffe Physicotechnical Institute, Russian Academy of Sciences, Politekhnicheskaya ul. 26, St. Petersburg, 194021 Russia
***St. Petersburg State Technical University, ul. Politekhnicheskaya 29, St. Petersburg, 195251 Russia
^e-mail: rudvas@spbstu.ru
Submitted June 15, 2004; accepted for publication June 30, 2004

Abstract—*n*-ZnO:Al/Pd*Pc*/*p*-CuIn₃Se₅ photosensitive structures have been proposed and fabricated for the first time by vacuum sublimation of palladium phthalocyanine on the surface of wafers of the ternary semiconductor compound CuIn₃Se₅ and by magnetron sputtering of *n*-ZnO:Al films on the surface of palladium phthalocyanine films. The current–voltage characteristics and spectra of the photoconversion quantum efficiency of the obtained structures are investigated. It is shown that these structures can be used as multiband white-light converters. © *2005 Pleiades Publishing, Inc.*

Thin-film photoconversion structures have been fabricated using I–III–VI₂ ternary compounds, chosen due to the fact that they are the closest analogs of II–VI binary semiconductors. These structures have unprecedently high quantum efficiency (≈19%) and radiation resistance as compared with the thin-film solar cells known at present [1, 2]. It has also recently been demonstrated that light converters can be developed in which the active region is formed as a result of bringing diamond-like semiconductors into contact with organic semiconductors [3]. Synthetic phthalocyanines from various metals were used as the organic semiconductors in these structures [4, 5].

In this study, we analyzed the photosensitive properties of the structure formed when palladium phthalocyanine (Pd*Pc*) film comes into contact with the ternary semiconductor compound CuIn₃Se₅. The latter is formed in the quasi-binary section Cu₃Se–In₂Se₃ and provides new opportunities to control the fundamental properties of complex phases without the introduction of impurities [6].

1. The photosensitive structures were fabricated based on *p*-CuIn₃Se₅ crystals grown by planar crystallization from a stoichiometric melt. The boat was in a horizontal position and the selenium vapor pressure was controlled. The composition of the grown crystals was determined by X-ray microprobe analysis on a Cameca-SX 100 system. The content of copper, indium, and selenium corresponded to the chemical formula of this compound. The diffraction patterns of samples cut from different portions of the ingot corresponded to a defect chalcopyrite structure. The unit-cell parameters calculated by the least-squares method from reflections measured at angles of 2θ > 60° were *a* =

5.766 ± 0.001 Å and *c* = 11.499 ± 0.005 Å, which are consistent with the known data for this compound. According to the thermopower sign, the grown crystals had *p*-type conductivity and the resistivity ρ = 10⁷– 10⁸ Ω cm at *T* = 300 K. In the temperature range 280–380 K, their resistivity obeyed the Arrhenius law

$$\rho = \rho_0 \exp(E_a/kT), \qquad (1)$$

where *k* is the Boltzmann constant. The activation energy $E_a = 0.51 \pm 0.03$ eV, on the assumption of strong compensation of deep acceptor levels, can be related to the presence of acceptor centers in these crystals. The nature of these centers has still to be ascertained. However, the dependence of ρ on the crystallization conditions suggests that the ternary compound CuIn₃Se₅ is a typical representative of phases possessing a variable composition, whose properties are determined by their deviations from stoichiometry.

Wafers of *p*-CuIn₃Se₅, with an average size of about $0.1 \times 5 \times 10$ mm³, were first ground and then underwent mechanical and chemical polishing. Thin (~1 μm) Pd*Pc* films were deposited onto the wafers by vacuum sublimation of Pd*Pc* powder. The deposited phthalocyanine films had a uniform interference color in white light, mirror-smooth surface, and good adhesion to the CuIn₃Se₅ surface. Then, thin ($d = 0.5$–1 μm) *n*-ZnO:Al films were deposited on the Pd*Pc* surface by magnetron sputtering in an argon atmosphere. The deposited *n*-ZnO:Al films had the electron concentration $n \approx 10^{20}$ cm⁻³ at *T* = 300 K, a mirror-smooth surface, and good adhesion to the Pd*Pc* films.

2. One specific feature of the steady-state current–voltage (*I–V*) characteristics of all the *n*-ZnO:Al/Pd*Pc*/*p*-

CuIn$_3$Se$_5$ structures fabricated in this study is relatively poor rectification. The rectification factor (the ratio of currents at different polarities of a bias of fixed amplitude) was generally about 1.5 for the best structures. The fabrication of other types of structures (In/CuIn$_3$Se$_5$ and ZnO/CuIn$_3$Se$_5$) on such crystals did not lead to an increase in the rectification. The forward direction of the current in n-ZnO:Al/PdPc/p-CuIn$_3$Se$_5$ structures always corresponds to a positive bias on CuIn$_3$Se$_5$.

The initial portion of the forward I–V characteristics of the structures under consideration (Fig. 1) is described by the equation [7]

$$I = I_s[\exp(eU/nkT) - 1], \qquad (2)$$

where the saturation current $I_s = (5$–$8) \times 10^{-8}$ A and the diode factor $n \approx 10$, which suggests the possibility of a tunneling recombination mechanism for the current transport in ZnO/PdPc/CuIn$_3$Se$_5$ structures. Similar values of n were also observed for the forward portion of the I–V characteristics of the structures formed on crystalline Si substrates [3].

As can be seen in Fig. 1, in a wide range of forward ($U = 0.5$–100 V) and reverse ($U = 0.1$–100 V) biases, the current through the structures under study follows the power dependence $I \propto U^m$. Note that the exponent m for reverse and forward currents at biases of $U \leq 35$ V is close to unity (Fig. 1b), which is generally attributed to the tunneling of charge carriers or the limitation of the current by the space charge in the velocity saturation mode [8]. In the range of forward and reverse biases 35 V $< U < 100$ V (Fig. 1b, curves 1 and 2), the exponent $m \approx 1.6$, which corresponds to the Lide–Langmuir law. This fact is attributed to the limitation of currents by the space charge in the ballistic mode [8, 9].
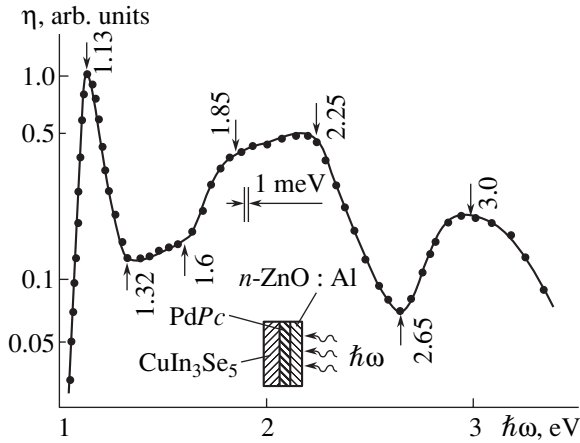
3. Illumination of the n-ZnO:Al/PdPc/p-CuIn$_3$Se$_5$ structures induces a photovoltage, whose sign is positive for the p-CuIn$_3$Se$_5$ substrate. This photovoltage polarity is consistent with the rectification direction. Under the illumination of the structures by an incandescent lamp with an intensity of ~10 mW/cm^2 from the side of the ZnO film, the photovoltaic effect reaches a maximum. In the best structures, the open-circuit photovoltage and short-circuit current are as high as ~30 mV and ~0.1 μA, respectively, at $T = 300$ K. The highest photovoltaic sensitivity for the n-ZnO:Al/PdPc/p-CuIn$_3$Se$_5$ structures is ~30 V/W, which is comparable with the data for structures formed on KDB-0.01 (p-Si:B, $\rho = 0.01$ Ω cm) substrates [3].

Figure 2 shows a typical spectral dependence of the relative photoconversion quantum efficiency $\eta(\hbar\omega)$ for an n-ZnO:Al PdPc/p-CuIn$_3$Se$_5$ structure in unpolarized light at 300 K and a schematic representation of the photodetection. It can be seen that, under the illumination of these structures from the ZnO side, photosensi-
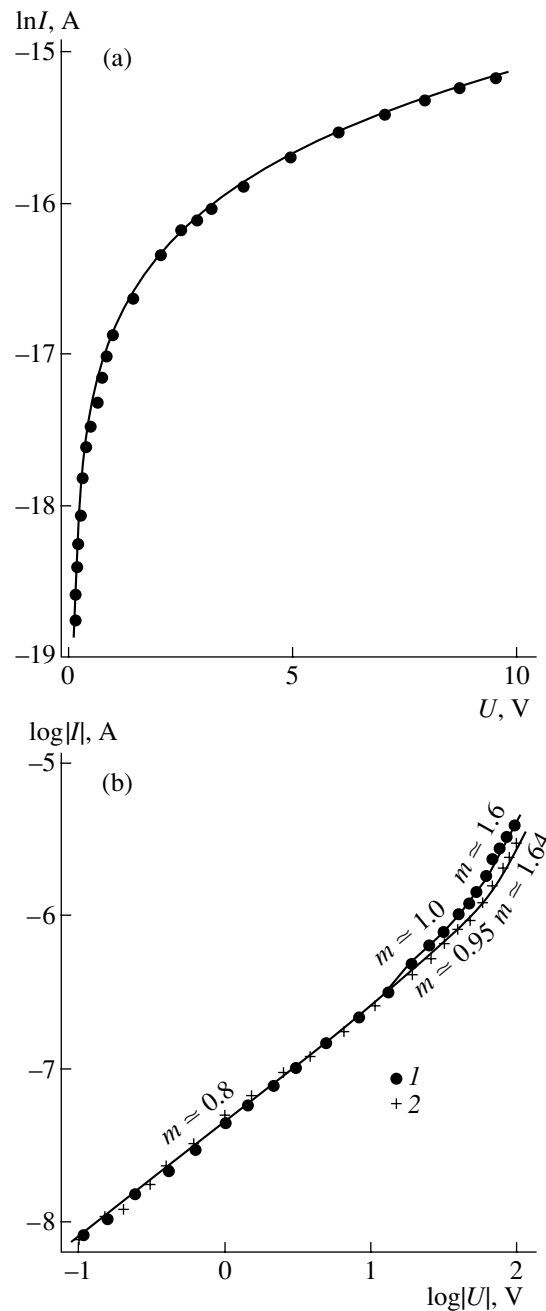
Fig. 1. The steady-state I–V characteristic of an n-ZnO:Al/PdPc/p-CuIn$_3$Se$_5$ structure at $T = 300$ K: (a) the forward portion at the semilogarithmic coordinates $\ln I = f(U)$ and (b) the forward (1) and reverse (2) portions in the double logarithmic scale. A positive bias is applied to the p-CuIn$_3$Se$_5$ substrate.

tivity is observed in a wide spectral range: 1.1–3.4 eV. The long-wavelength increase in the photosensitivity at photon energies of >1 eV is linear at the $(\eta \cdot \hbar\omega)^2$–$\hbar\omega$ coordinates (Fig. 3) and the extrapolation $(\eta \cdot \hbar\omega)^2 \longrightarrow 0$ yields the value of the cutoff energy ~1.12 eV. According to the theory of interband optical absorption in semiconductors [10], the validity of the quadratic law

Fig. 2. The spectrum of the relative photoconversion quantum efficiency of an *n*-ZnO:Al/Pd*Pc*/*p*-CuIn₃Se₅ structure at $T = 300$ K. Illumination is by unpolarized light from the *n*-ZnO:Al film. The inset shows a schematic representation of the photodetection.

indicates that the interband transitions in CuIn₃Se₅ are direct and the band gap $E_g^{dir} \approx 1.12$ eV at $T = 300$ K. The long-wavelength photosensitivity limit for the obtained structures is observed at $\hbar\omega > 3.2$ eV. This value is close to the band gap width of ZnO [11]; therefore, the long-wavelength limit can be related to an increase in the light absorption in the wide-gap component of the structures. A distinctive feature of the photosensitivity spectra $\eta(\hbar\omega)$ of the *n*-ZnO:Al/Pd*Pc*/*p*-CuIn₃Se₅ structures is the presence of three bands in the high-photosensitivity range from 1.0 to 3.4 eV (Fig. 2). These bands manifest themselves as three pronounced peaks: a rather narrow long-wavelength peak at $\hbar\omega_1^{max} \approx$ 1.13 eV with the full width at half-maximum $\delta_1 \approx$ 0.1 eV, a wide intermediate peak at $\hbar\omega_2^{max}$ in the range from 1.85 to 2.25 eV ($\delta_2 \approx 0.65$ eV), and the shortest wavelength peak at $\hbar\omega_3^{max} \approx 3$ eV ($\delta_3 \approx 0.58$ eV). The photosensitivity spectra of the *n*-ZnO:Al/Pd*Pc*/*p*-CuIn₃Se₅ structures also show characteristic dips with the minimum energies $\hbar\omega_1^{min}$ in the range 1.3–1.6 eV and $\hbar\omega_2^{min} \approx 2.65$ eV. The occurrence of these features can be related to the discreteness of the optical absorption spectra of phthalocyanines [5], which leads to the difference between the $\eta(\hbar\omega)$ spectra of structures fabricated on the basis of organic semiconductors and the spectra of conventional heterojunctions between inorganic semiconductors, with a pronounced window effect in the interval between the band gap widths of the semiconductors in contact [10, 12]. The presence of the bands in the photosensitivity spectra of the *n*-ZnO:Al/Pd*Pc*/*p*-CuIn₃Se₅ structures can be used in
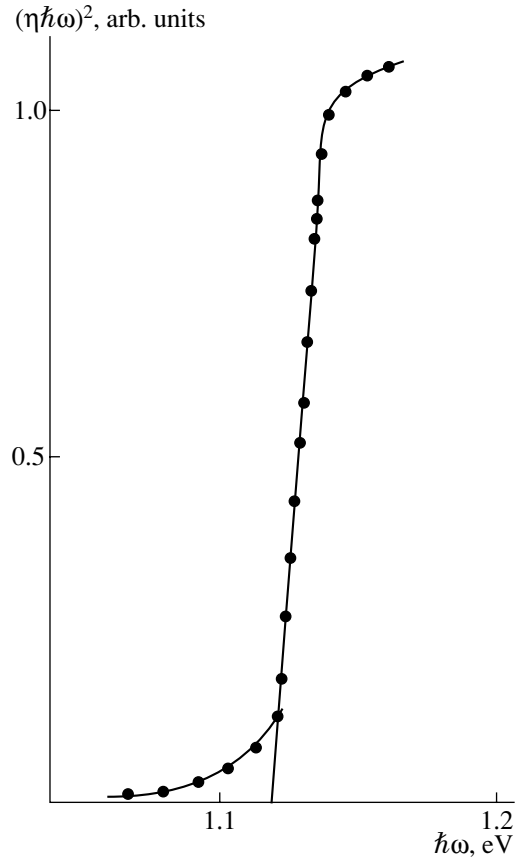
Fig. 3. The dependence of $(\eta \cdot \hbar\omega)^2$ on $f(\hbar\omega)$ for an *n*-ZnO:Al/Pd*Pc*/*p*-CuIn₃Se₅ structure.

the development of multiband photodetectors, which would then be photosensitive only in certain ranges of broadband background radiation.

Thus, due to the use of organic semiconductors (with the example of palladium phthalocyanine) and ternary semiconductor compounds (CuIn₃Se₅), we obtained the first photosensitive *n*-ZnO:Al/Pd*Pc*/*p*-CuIn₃Se₅ structures with multiband photosensitivity spectra in the range 1.0–3.5 eV. These structures are suitable for application in the development of a new generation of light converters.

REFERENCES

1. H.-W. Schock and A. Shah, in *Proceedings of 14th European Photovoltaic Solar Energy Conference* (Barcelona, Spain, 1997).

2. G. Lundberg, M. Edoff, and L. Stolt, in *Abstracts of Solar World Congress ISES 2003* (Goteborg, Sweden, 2003), p. 57.

3. G. A. Il'chuk, N. V. Klimova, O. I. Kon'kov, *et al.*, Fiz. Tekh. Poluprovodn. (St. Petersburg) **38**, 1056 (2004) [Semiconductors **38**, 1018 (2004)].

4. D. D. Eley, Nature **162**, 819 (1948).

5. A. T. Vartanyan, Zh. Tekh. Fiz. **22**, 819 (1948).

6. I. V. Bodnar', V. F. Gremenok, V. Yu. Rud', and Yu. V. Rud', Fiz. Tekh. Poluprovodn. (St. Petersburg) **33**, 805 (1999) [Semiconductors **33**, 740 (1999)].

7. S. Sze, *Physics of Semiconductor Devices*, 2nd ed. (Wiley, New York, 1981; Mir, Moscow, 1984).

8. M. A. Lampert and P. Mark, *Current Injection in Solids* (Academic, New York, 1970; Mir, Moscow, 1973).

9. E. Hernandes, Cryst. Res. Technol. **33**, 285 (1998).

10. Zh. I. Alferov, V. M. Andreev, and N. N. Ledentsov, in *Ioffe Institute: 1918–1998. Development and Research Activities* (Physicotechnical Inst., St. Petersburg, 1998).

11. *Physicochemical Properties of Semiconductors: A Handbook*, Ed. by A. V. Novoselova and V. B. Lazarev (Nauka, Moscow, 1979) [in Russian].

12. A. G. Milnes and D. L. Feucht, *Heterojunctions and Metal–Semiconductor Junctions* (Academic, New York, 1972; Mir, Moscow, 1975).

Translated by Yu. Sin'kov

Edge Photoluminescence of Single-Crystal Silicon at Room Temperature

E. G. Gule^, E. B. Kaganovich, I. M. Kizyak, E. G. Manoilov, and S. V. Svechnikov

Lashkarev Institute of Semiconductor Physics, National Academy of Sciences of Ukraine, Kiev, 03028 Ukraine
^e-mail: dept_5@isp.kiev.ua
Submitted July 20, 2004; accepted for publication September 9, 2004

Abstract—The edge photoluminescence of single-crystal silicon (c-Si) with a peak at ~1.09 eV at room temperature is observed for structures that consist of nanocrystalline silicon (nc-Si) and c-Si. The structures are obtained by pulsed-laser deposition of an nc-Si film onto a c-Si substrate. The photoluminescence signal increases as both the density of surface states at the nc-Si/c-Si boundary and the scattering of the edge emission from c-Si in the nc-Si film decreases. © 2005 Pleiades Publishing, Inc.

1. INTRODUCTION

One line of research directed at the development of emitters based on silicon involves a return to the intrinsic luminescence of single-crystal silicon (c-Si) [1–12]. The fabrication of silicon light-emitting diodes (LEDs) emitting in the region of band-to-band recombination with an energy-conversion efficiency of 1% at temperatures close to 295 K was reported in 2001. These results were attributed to optimization of the emission yield and the suppression of nonradiative recombination due to the confinement of charge carriers in the active region [1, 2]. These data on electroluminescence (EL) in Si-based LEDs produced a renewed interest in the edge photoluminescence (PL) of c-Si [7–9]. At room temperature, the external quantum yield of PL was as high as 6.1% on a textured and SiO_2-passivated c-Si surface. An increase in the probability of radiative recombination (disregarding a decrease in the surface-recombination velocity of charge carriers) was stimulated by the formation of dislocation structures introduced by various methods, e.g., plastic deformation, implantation of heavy ions with subsequent annealing, melting of the surface layer by laser radiation, and so on [2]. Local fields limiting the charge-carrier diffusion to nonradiative recombination centers are related to dislocations. Emel'yanov *et al.* [8] established a correlation between the density of surface states (N) at the c-Si/SiO_2 interface and the intensity of PL with a peak at 1.15 µm. The structures were annealed in a hydrogen atmosphere in order to decrease the values of N and were irradiated with γ photons to increase N.

It was shown, in our previous publications [13, 14] on the spectra of the electronic states in structures consisting of nanocrystalline Si (nc-Si) and c-Si (nc-Si/c-Si), that the densities of the interface electronic states at the nc-Si/c-Si boundary and those of the traps of nonequilibrium charge carriers at this boundary can be reduced by choosing appropriate conditions for both the deposition

of the nc-Si film on the c-Si substrate and the doping of this film with metallic impurities. It was hypothesized that the fundamental edge PL of c-Si could be observed in the structures under study. It is also worth noting that Belyaev *et al.* [15] observed a band of edge c-Si EL (in addition to other bands) with a peak at 1.05 eV (1.18 µm) at room temperature in studies of EL in structures with porous silicon (por-Si/c-Si) in contact with an electrolyte. The aforementioned results provided the impetus for us to initiate a study whose aim was to clarify the conditions needed to observe interband PL in c-Si at room temperature in nc-Si/c-Si structures formed by a deposition induced by pulsed laser radiation.

2. EXPERIMENTAL

We used p-Si:B wafers with orientation (100) and a resistivity of 10 Ω cm as substrates. Films of nanocrystalline silicon (nc-Si) were formed on these substrates using a deposition induced by pulsed laser radiation. These films were nanocomposites that consisted of silicon nanocrystals with dimensions of 1–5 nm in the SiO_x matrix ($1 < x \leq 2$). The p-Si target was subjected to radiation pulses from a YAG:Nd^{3+} laser that operated in the Q-switched mode (a wavelength of 1.06 µm, pulse energy of 0.2 J, pulse duration of 10 ns, and pulse-repetition frequency of 25 Hz). Type I films were deposited onto the substrate using a direct flux of high-energy particles from an erosion plume; the substrate was spaced 30 mm apart from the source by the normal. The deposition was performed in a residual gas atmosphere in a vacuum chamber with the addition of oxygen at a pressure of 6.5 Pa. Type II films were deposited onto the substrate using a reverse flux of low-energy particles from the erosion plume in an argon atmosphere at a pressure of ~13 Pa; the substrate was positioned in the target plane. Some of the films were doped with Au, In, Al, Fe, Er, and other metals in the course of

their formation [13, 14]. For comparison, the *nc*-Si films were also deposited onto other substrates, for example, mica. The *por*-Si/*c*-Si structures were also formed using the selective chemical etching of *c*-Si.

In this paper, we use the results from our previous studies of the structural, optical, photoluminescent, and electronic properties of *nc*-Si films. These studies were initiated in order to clarify the nature of PL in *nc*-Si films in the visible region of the spectrum in the photon-energy range 1.4–3.0 eV (see [13, 14] and the references therein).

The PL spectra were measured at room temperature in the photon-energy range 0.9–1.3 eV. The PL was excited by radiation from an LGN-402 argon laser with a wavelength of 514.5 nm and power of ~100 mW. We used an MDR-23 monochromator, and the spectral width of the slit was ~40 Å. A cooled FD-315 germanium diode was used as a photodetector. The signal from the photodetector was fed to a selective amplifier and was recorded using synchronous detection.

Photoluminescence spectra of the *nc*-Si/*c*-Si structures with *nc*-Si films of type II: (*1*) undoped film and (*2*–*6*) the films doped with (*2*) In, (*3*) Er, (*4*) Fe, (*5*) Au, and (*6*) Al.

3. RESULTS AND DISCUSSION

The PL of *c*-Si in the photon-energy range 0.95–1.25 eV (the wavelength range 1.3–1 μm) is caused by radiative band-to-band transitions of charge carriers and the annihilation of free excitons with the involvement of phonons. The involvement of phonons is demonstrated by the peaks in the spectral curves (these peaks are typically distinct at temperatures below 295 K) and on the logarithmic scale of the PL intensity [7–9]. In addition to the PL bands in the visible region of the spectrum at 1.4–3.2 eV, we observed a PL band with a peak at 1.09 eV for the *nc*-Si/*p*-Si structures under study. The measured PL spectra in this mid-IR region of the spectrum were similar to those typically reported in the case of the linear intensity scale for *c*-Si edge PL at a temperature of 300 K [7] (see figure). This PL signal was only observed for some of the samples.

Edge *c*-Si PL with a peak at 1.09 eV was typically observed for the structures with the type II films deposited from a low-energy flux of particles from the erosion plume. This signal exhibited a lower energy density of the surface states *N* at the *nc*-Si/*c*-Si interface [13, 14]. The doping of these films with metallic impurities brought about an increase in the PL-signal intensity; however, we failed to ascertain what the effect of the impurity type on this intensity was. The shape of the spectrum was almost independent of the impurity type.

The edge PL of *c*-Si was not observed for the structures with the type I films deposited using a flux of high-energy particles from the erosion plume. This signal had a high density of surface states at the *nc*-Si/*c*-Si interface [13, 14]. The *c*-Si PL signal was not observed if the initial *c*-Si substrates had a natural surface oxide SiO$_x$, which led to highly efficient nonradiative recombination. Hence, it follows that, in order to observe edge PL in *c*-Si structures obtained using pulsed laser
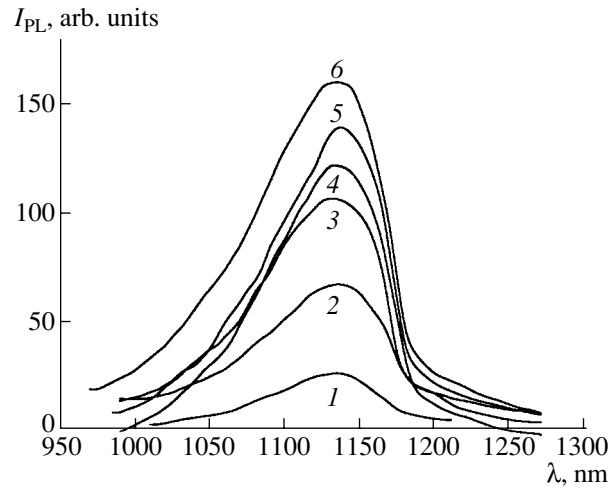
deposition, it is necessary to (i) deposit the *nc*-Si films from a reverse particle flux of the erosion plume and (ii) dope the films with metallic impurities.

The *c*-Si edge PL can be related not only to the *c*-Si substrate but also to the presence of large silicon nanocrystals in the film. These large nanocrystals are present in *nc*-Si (in addition to small-sized nanocrystals in which quantum-mechanical effects exist) due to the large spread of nanocrystal sizes. However, test experiments show that the *c*-Si edge PL signal is not observed for all the *nc*-Si films deposited on mica substrates. This circumstance indicates that the PL signal is indeed related to the *c*-Si substrate.

The *por*-Si/*c*-Si structures exhibited a low-intensity edge-PL signal. This behavior is evidently caused by the scattering of radiation at the highly developed *por*-Si surface. It is worth noting that the type I films deposited from a direct flux of particles exhibit a large spread of nanocrystal sizes. The surface of these films includes clusters with sizes that amount to hundreds of nanometers, with a large spread of heights. At the same time, the type II films exhibit a much higher homogeneity, a smaller spread of nanocrystal sizes, and a much larger uniformity of their surface profile. The lower magnitude of radiation scattering in these films also gives rise to the increased intensity of the *c*-Si PL signal.

4. CONCLUSION

Thus, in this study, we observed the *c*-Si edge photoluminescence signal in structures composed of nanocrystalline Si (*nc*-Si) and single-crystal Si (*c*-Si) at room temperature for the first time. It is shown that, if the *nc*-Si film is deposited onto the *c*-Si substrate using pulsed laser sputtering, one can satisfy the conditions for suppression of the nonradiative recombination at the *nc*-Si/*c*-Si interface and reduce the losses of the *c*-Si

edge emission by choosing an appropriate deposition mode and by doping the *nc*-Si films with metallic impurities in the course of the film formation.

REFERENCES

1. M. A. Green, J. Zhao, A. Wang, *et al.*, Nature **412**, 805 (2001).

2. W. L. Ng, M. A. Lourenco, R. M. Gwillian, *et al.*, Nature **410**, 192 (2001).

3. M. S. Bresler, O. B. Gusev, B. P. Zakharchenya, and I. N. Yassievich, in *Proceedings of Meeting on Nanophotonics* (Nizhni Novgorod, Russia, 2003), Vol. 1, p. 59.

4. J. M. Sun, T. Decorsy, W. Skorupa, *et al.*, Appl. Phys. Lett. **83**, 3885 (2003).

5. A. M. Emel'yanov, N. A. Sobolev, T. M. Mel'nikova, and S. Pizzini, Fiz. Tekh. Poluprovodn. (St. Petersburg) **37**, 756 (2003) [Semiconductors **37**, 730 (2003)].

6. A. V. Sachenko, A. P. Gorban', and V. P. Kostylev, Fiz. Tekh. Poluprovodn. (St. Petersburg) **38**, 570 (2004) [Semiconductors **38**, 550 (2004)].

7. T. Trupke, J. Zhao, A. Wang, *et al.*, Appl. Phys. Lett. **82**, 2996 (2003).

8. A. M. Emel'yanov, N. A. Sobolev, and S. Pizzini, Fiz. Tekh. Poluprovodn. (St. Petersburg) **36**, 1307 (2002) [Semiconductors **36**, 1225 (2002)].

9. T. Trupke, M. A. Green, P. Würfel, *et al.*, J. Appl. Phys. **94**, 4930 (2003).

10. A. M. Emel'yanov, N. A. Sobolev, and E. I. Shek, Fiz. Tverd. Tela (St. Petersburg) **46**, 44 (2004) [Phys. Solid State **46**, 40 (2004)].

11. N. A. Sobolev, A. M. Emel'yanov, E. I. Shek, and V. I. Vdovin, Fiz. Tverd. Tela (St. Petersburg) **46**, 39 (2004) [Phys. Solid State **46**, 35 (2004)].

12. M. S. Bresler, O. B. Gusev, E. I. Terukov, *et al.*, Fiz. Tverd. Tela (St. Petersburg) **46**, 18 (2004) [Phys. Solid State **46**, 13 (2004)].

13. É. B. Kaganovich, I. M. Kizyak, S. I. Kirillova, *et al.*, Fiz. Tekh. Poluprovodn. (St. Petersburg) **36**, 1105 (2002) [Semiconductors **36**, 1027 (2002)].

14. E. B. Kaganovich, S. I. Kirillova, E. G. Manoilov, *et al.*, Semicond. Phys.: Quantum Electron. Optoelectron. **5**, 125 (2002).

15. L. V. Belyaev, D. N. Goryachev, D. I. Kovalev, *et al.*, Fiz. Tekh. Poluprovodn. (St. Petersburg) **29**, 1288 (1995) [Semiconductors **29**, 667 (1995)].

Translated by A. Spitsyn

SEMICONDUCTOR STRUCTURES, INTERFACES, AND SURFACES

Fabrication and Photoelectric Properties of *n*-ZnO:Al/Pd*Pc*/*p*-Si Structures

G. A. Il'chuk*, S. E. Nikitin*, Yu. A. Nikolaev*, V. Yu. Rud'**^, Yu. V. Rud'*, and E. I. Terukov*

*Ioffe Physicotechnical Institute, Russian Academy of Sciences, Politekhnicheskaya ul. 26, St. Petersburg, 194021 Russia
**St. Petersburg State Technical University, ul. Politekhnicheskaya 29, St. Petersburg, 195251 Russia
^e-mail: rudvas@spbstu.ru
Submitted August 10, 2004; accepted for publication September 9, 2004

Abstract—Photosensitive *n*-ZnO:Al/Pd*Pc*/*p*-Si structures were fabricated by vacuum sublimation of palladium phthalocyanine with subsequent magnetron sputtering of ZnO:Al films on *p*-Si substrates. The current transport mechanisms and the photosensitivity of the structures obtained were investigated. It is shown that structures based on Pd*Pc* films are promising for photosensitive devices based on contacts between organic and inorganic semiconductors. © *2005 Pleiades Publishing, Inc.*

Semiconducting properties of a wide class of synthetic phthalocyanines of various metals have been known for a long time [1]. However, only in recent years has the potential of these materials found application in the development of new generation optoelectronic devices [2–4]. Recently, we ascertained the possibility of using a heterocontact of copper phthalocyanine (Cu*Pc*) with an inorganic semiconductor (by the example of Si) in broadband light converters [5]. In this study, which continues this promising line of development, we report the results of the first study of the photoelectric properties of heterocontacts of Si with thin films of another representative of organic semiconductors of this class: palladium phthalocyanine (Pd*Pc*).

The structures were prepared by vacuum sublimation of Pd*Pc* powder. Palladium phthalocyanine films were deposited on the polished (111) surface of KDB-0.03 wafers (*p*-Si:B, $\rho = 0.03\ \Omega$ cm) kept during sublimation at a temperature of about 50°C. Due to the optimization of the sublimation conditions, the films grown had uniform dark blue color when passed under the light of an incandescent lamp. The films had a mirror-smooth surface. The adhesion of the obtained Pd*Pc* films to the silicon surface was sufficiently good and stable in time. The thickness of the Pd*Pc* films was $d \approx$ 0.5 μm and could be easily controlled by varying the sublimation time.

After sublimation, high-resistivity transparent *n*-ZnO:Al films were deposited on the postgrowth surface of the Pd*Pc* films by magnetron sputtering of an undoped ZnO target in an argon atmosphere in the presence of pure aluminum. The deposited films had a free electron concentration of $n \approx 10^{20}$ cm^{-3} at $T = 300$ K. The deposition time of *n*-ZnO:Al films with thicknesses up to ~1 μm was 4 h at a temperature of the Pd*Pc*/Si substrate of about 50°C and an argon pressure of 0.5 Pa. The quality of the surface of the *n*-ZnO:Al

films grown under such conditions was similar to that of Pd*Pc* films, which served as substrates for ZnO films in this case. The adhesion of the ZnO films to the surface of Pd*Pc* was also rather good.

Measurement of the steady-state current–voltage (*I–V*) characteristics of the *n*-ZnO:Al/Pd*Pc*/*p*-Si structures obtained here clearly demonstrated the presence of the rectification effect in them, like in the *n*-ZnO:Al/Cu*Pc*/*p*-Si structures studied in [5]. Figure 1 shows a typical steady-state *I–V* characteristic of one of
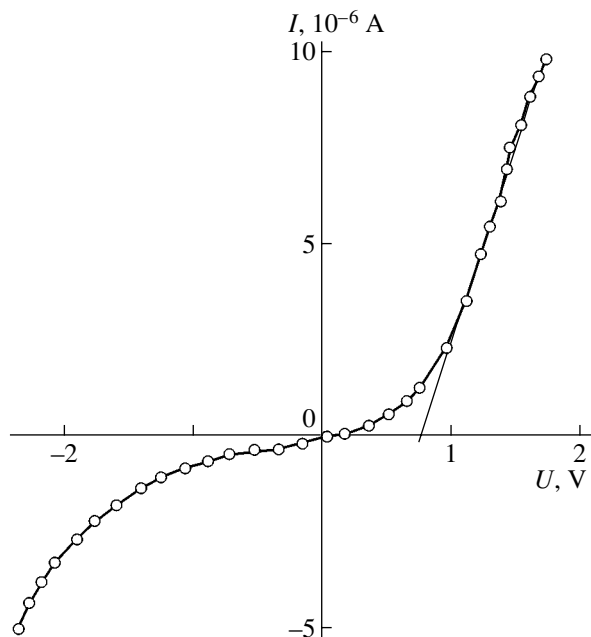
Fig. 1. Steady-state *I–V* characteristic of an *n*-ZnO:Al/Pd*Pc*/*p*-Si structure at $T = 300$ K. The forward direction corresponds to a positive bias applied to the *p*-Si substrate (KDB-0.03).
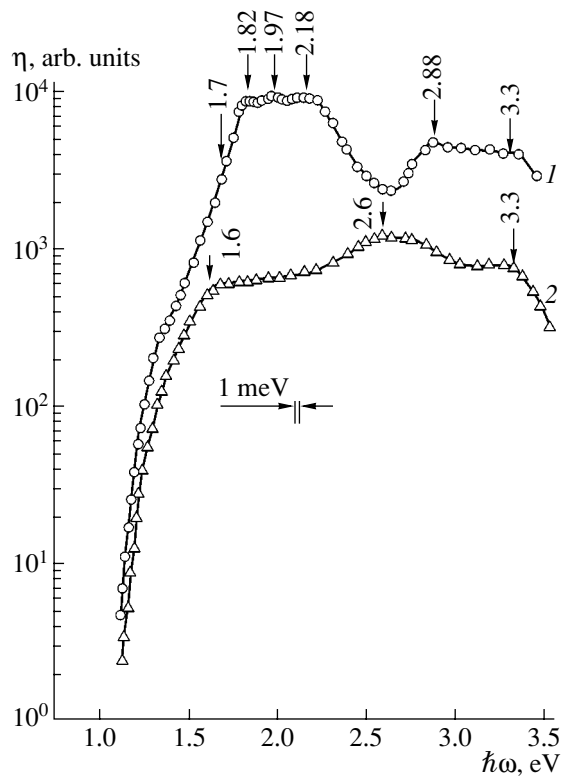
Fig. 2. Spectra of relative photoconversion quantum efficiency for (*1*) *n*-ZnO:Al/Pd*Pc*/*p*-Si and (*2*) *n*-ZnO:Al/Cu*Pc*/*p*-Si structures at $T = 300$ K. The structures are exposed to white light from the side of the *n*-ZnO:Al layer. The spectra are shifted along the ordinate. Arrows indicate the positions of specific spectral features.

the structures, in which the forward direction corresponds to a negative bias on the *n*-ZnO:Al film. The rectification factor *K* of the first *n*-ZnO:Al/Pd*Pc*/*p*-Si structures, determined as the ratio of the forward to the reverse current at a bias of $U = 2$ V, generally does not exceed ~5–8, which is much smaller than the rectification factor of the *n*-ZnO:Al/Cu*Pc*/*p*-Si structures obtained in a similar way [5]. This difference may be related to the differences in the chemical structure of molecules of phthalocyanines of different metals [1, 6].

Investigation of the *I–V* characteristics showed that at forward biases of $U \leq 0.2$ V, the dark current through the *n*-ZnO:Al/Pd*Pc*/*p*-Si structures is described by the diode equation [7]

$$I = I_s \exp\left(\frac{eU}{nkT} - 1\right), \qquad (1)$$

where the saturation current $I_s \cong 10^{-9}$ A and the diode factor $n \cong 3.7$ at $T = 300$ K. Large values of *n* suggest that the tunnel recombination mechanism of current transport manifests itself in the structures obtained here, as in the *n*-ZnO:Al/Cu*Pc*/*p*-Si structures based on Cu*Pc* films [5].

Figure 1 shows that in the forward-bias region at $U > 1$ V the dark current linearly depends on *U*:

$$I = \frac{U - U_0}{R_0}, \qquad (2)$$

where the cutoff voltage $U_0 \cong 0.7$–0.8 V and the residual resistance $R_0 \cong 2 \times 10^5$ Ω.

With increasing voltage in the range $U = 0.1$–2.5 V, the reverse current through the *n*-ZnO:Al/Pd*Pc*/*p*-Si structures under consideration follows a power dependence: $I \propto U^m$. The exponent *m* increases with increasing *U*: $m \approx 0.8$ at $U \leq 0.5$ V and $m \approx 2.3$–2.4 at $U > 1.5$ V. Taking into account the results of [8, 9], we can suggest that at voltages $U < 0.5$ V the reverse current is determined by the tunneling of carriers or the limitation by the space charge in the velocity saturation mode, whereas the increase in the exponent *m* to 2.3–2.4 requires taking into consideration the continuous exponential energy distribution of traps [9]. The forward current in structures at $U > 0.3$ V is also described by a power dependence with values of $m \approx 1.5$ in the range $U = 0.2$–2.5 V, whereas in the range $U = 2.5$–10 V, the exponent increases to 2.8. Hence, with due regard to the data of [8, 9], the observed power dependence $I \propto U^m$ and the values of the exponent *m* indicate that the forward current at $U < 2.5$ V is limited by the space charge in the mobility mode and the increase in *m* at $U > 2.5$ V may indicate the dominant effect of continuous energy distribution of traps.

Illumination of the *n*-ZnO:Al/Pd*Pc*/*p*-Si structures is accompanied by the generation of a photovoltage, whose sign (minus on the *n*-ZnO:Al layer) is independent of the light intensity, the photon energy, and the location of the excitation probe (~0.4 mm in diameter) on the surface of the structures studied. A negative bias on the *n*-ZnO:Al layer corresponds to the forward current direction through the structures. The highest photovoltaic sensitivity for the best structures was $S_U^m = 2$ V/W. Figure 2 shows a typical spectrum of the relative photoconversion quantum efficiency η for one of the *n*-ZnO:Al/Pd*Pc*/*p*-Si structures obtained in this study (curve *1*) in comparison with an *n*-ZnO:Al/Cu*Pc*/*p*-Si structure (curve *2*).

The main features of the η spectra of the structures based on films of two different phthalocyanines consist in the following. Under illumination from the side of the thin-film wide-gap ZnO:Al component (the same for these structures), the photosensitivity spectra are broadband. The long-wavelength increase in η for these structures begins at $\hbar\omega \geq 1.1$ eV and is adequately approximated by the law characteristic of indirect interband transitions [10, 11]:

$$\eta\hbar\omega = A'(\hbar\omega - E_G)^2. \qquad (3)$$

Here, *A'* is the proportionality factor and E_G is the bandgap of the semiconductor. In this case, the extrapolation $(\eta\hbar\omega)^{1/2} \longrightarrow 0$ for the structures under comparison

yields almost the same value, $E_G = 1.1$ eV at $T = 300$ K, which corresponds to crystalline Si [10, 12]. Therefore, the long-wavelength edge of the η spectrum of the structures based on films of phthalocyanines of different metals (Cu and Pd) is determined by the bandgap of their common narrow-gap component (p-Si). As can be seen in Fig. 2 (curves 1 and 2), the short-wavelength decay of the photosensitivity in the structures under comparison also begins at almost the same photon energy ($\hbar\omega \approx 3.3$ eV), which, in turn, corresponds to the bandgap of ZnO [12]. Therefore, there are grounds to assign the short-wavelength edge to direct interband transitions in the ZnO film. Finally, the maximum photosensitivity of the structures under comparison is implemented in the interval between the bandgap widths of the "input window" material (ZnO) and the Si substrate, which, in general, is characteristic of ideal heterojunctions [13].

It can also be seen in Fig. 2 that the shape of the $\eta(\hbar\omega)$ spectrum in the interval between the bandgap widths of ZnO and Si is significantly different for the structures based on Pd and Cu phthalocyanines. This may be primarily related to the differences in the fundamental properties of CuPc and PdPc. The photosensitivity spectrum of the structure with a PdPc film (curve 1) contains two pronounced bands: a long-wavelength band with maximum photosensitivity in the range $\Delta_1 \approx 1.8$–2.2 eV and a short-wavelength band with high photosensitivity in the range $\Delta_2 \approx 2.88$–3.35 eV, which a separated by a pronounced minimum at $\hbar\omega = 2.6$ eV. The η spectrum of the structure with a CuPc film (curve 2) contains only one absolute maximum $\hbar\omega_1 = 2.6$ eV. Most likely, these differences in the $\eta(\hbar\omega)$ spectra can be attributed to the discreteness of the optical absorption spectra, which is typical of such organic semiconductors [1]. For conventional heterostructures based on inorganic semiconductors, the dips in the photosensitivity spectra in the fundamental absorption region (far from the edge) of their widegap component, similar to those found for the n-ZnO:Al/PdPc/p-Si structures (Fig. 2, curve 1), have not yet been observed. This circumstance is due to the continuous character of their fundamental absorption spectrum.

In our opinion, the η spectra of photosensitive structures based on films of phthalocyanines of different metals [1] can be characterized by the full width at half maximum (FWHM) of η bands. In this case, we have $\delta_1 = 0.64$ eV for the long-wavelength band and $\delta_2 = 0.9$ eV for the short-wavelength band in the η spectrum of the n-ZnO:Al/PdPc/p-Si structures (Fig. 2, curve 1). Obviously, control of the PdPc film thickness would

make it possible to control the shape of the η spectrum of such structures. As can be seen in Fig. 2 (curve 2), in going to the n-ZnO:Al/CuPc/p-Si structures, the FWHM of the photosensitivity band significantly increases: $\delta = 1.63$ eV. The reason for this effect is that the discreteness of the absorption spectrum of CuPc manifests itself in the absorption spectrum on the structures based on CuPc films, whereas the photosensitivity peak at $\hbar\omega^m \geq 2.6$ eV may be due to the presence of an optical transparency band in the transmission spectrum of CuPc.

Thus, we obtained for the first time photosensitive structures n-ZnO:Al/PdPc/p-Si, which can find application in the development of photoelectron devices with a controlled profile of maximum photosensitivity. It is also obvious that the use of phthalocyanines of various metals opens new opportunities for controlling the parameters of light converters.

REFERENCES

1. A. T. Vartyanyan, Zh. Fiz. Khim. **22**, 769 (1948).

2. S. S. Leznoff and A. B. P. Lever, *Phthalocyanine, Properties and Application* (VCH, Cambridge, 1989), p. 1.

3. N. B. Mckrown, *Phthalocyanine. Materials—Syntesis, Structure and Function* (Cambridge Univ. Press, Cambridge, 1998), p. 2.

4. P. Penmans and S. R. Forrest, Appl. Phys. Lett. **79**, 126 (2001).

5. G. A. Il'chuk, N. V. Klimova, O. I. Kon'kov, *et al.*, Fiz. Tekh. Poluprovodn. (St. Petersburg) **38**, 1056 (2004) [Semiconductors **38**, 1018 (2004)].

6. Yi-Qun Wu, Dong-Hong Gu, Fu-Xi Gan, *et al.*, Chin. Phys. Lett. **19**, 1700 (2002).

7. S. M. Sze, *Physics of Semiconductor Devices*, 2nd ed. (Wiley, New York, 1981; Mir, Moscow, 1984).

8. E. Hernandez, Cryst. Res. Technol. **33**, 285 (1998).

9. M. A. Lampert and P. Mark, *Current Injection in Solids* (Academic, New York, 1970; Mir, Moscow, 1973).

10. A. N. Pikhtin, *Physical Fundamentals of Quantum Electronics and Optoelectronics* (Vysshaya Shkola, Moscow, 1983) [in Russian].

11. K. V. Shalimova, *Physics of Semiconductors* (Énergiya, Moscow, 1976) [in Russian].

12. *Physicochemical Properties of Semiconductors: A Handbook*, Ed. by A. V. Novoselova and V. B. Lazarev (Nauka, Moscow, 1979) [in Russian].

13. A. G. Milns and J. J. Feucht, *Heterojunctions and Metal–Semiconductor Junctions* (Academic, New York, 1972; Mir, Moscow, 1975).

Translated by Yu. Sin'kov

<center>

LOW-DIMENSIONAL
SYSTEMS

</center>

Effects of Spatial Reproduction as a Result of the Interference of Electron Waves in Two-Dimensional Semiconductor Nanostructures with Parabolic Quantum Wells

V. A. Petrov and A. V. Nikitin

Institute of Radio Engineering and Electronics, Russian Academy of Sciences, ul. Mokhovaya 18, Moscow, 101999 Russia
Submitted April 8, 2004; accepted for publication June 28, 2004

Abstract—Effects of spatial nonuniformity for the probability flux density $j_x(x, z)$ (or for the density of the quantum-mechanical current $ej_x(x, z)$, where e is the elementary charge) are studied. These effects arise in two-dimensional semiconductor nanostructures that consist of thin rectangular and wide parabolic quantum wells that are consecutively arranged in the direction of the electron-wave propagation (the x axis) and are oriented along the dimensional-quantization axis z. A nonuniform distribution of $j_x(x, z)$ arises as a result of interference of electron waves that propagate simultaneously in a wide quantum well over different quantum-dimensional subbands. Particular attention is paid to the effects of the spatial reproduction of electron waves in the nanostructures under consideration. It is shown that the transverse distribution $j_x(0, z)$ existing at the entry to the wide quantum well is reproduced to a certain accuracy at a distance of X_1 from the entry. In addition, the initial distribution $j_x(0, z)$ is reproduced periodically in the sections $X_q = qX_1$ (coefficients q are integers). The results of numerical calculations of magnitudes of these effects in the structures that are symmetric with respect to the z axis are reported; a modification of the effects under consideration in asymmetric nanostructures is considered. © *2005 Pleiades Publishing, Inc.*

1. INTRODUCTION

At present, advances in nanotechnology have made it possible to fabricate semiconductor nanostructures in which linear dimensions of one-dimensional (1D) or two-dimensional (2D) conducting channels in the direction of the electron-wave propagation are smaller than the mean free path of an electron. In such a channel, particles move ballistically, which makes it possible to study the effects of ballistic transport in the aforementioned structures; in particular, various electron-interference effects can be studied. The theoretical foundations of these effects, as well as an analysis of the most important experimental data in this field, were reported in a number of monographs [1–3]. At the same time, the majority of theoretical results in this field were represented by original publications in which the effects under consideration were studied for various types of nanostructures. In particular, a great number of theoretical publications are concerned with studies of the ballistic transport of electrons in the 1D and 2D nanostructures whose common specific feature is the presence (in quantum-mechanical channels) of regions with a drastic (nonadiabatic) change in either the channel configuration or the potential profile in the channel. Scattering of electron waves within these regions of inhomogeneity results in mixing of electron modes in the channel and appearance of electron-interference effects. The quantum-mechanical transport in the structures under consideration was studied theoretically in the 1D channels with rectangular [4] and parabolic [5]

profiles that connect the 2D electron reservoirs, and also in quantum-mechanical point contacts of various types connecting the aforementioned reservoirs [6], in tee-shaped channels [7, 8], channels with sharp kinks and channels with curved shape [9–11], channels with a δ-shaped scattering center inside [12], crossed channels [13], separate geometrically inhomogeneous channels with portions of different width [14–17], and in geometrically homogeneous 1D and 2D nanostructures with portions with a sharp variation in the potential profile that is controlled by the transverse constant electric field [18]. The role of damped modes in quantum-mechanical point contacts was considered previously [12, 19, 20].

Scattering within a region with a sharp inhomogeneity of the electron wave propagating over a single (for example, the lowest) dimensional subband gives rise to reflected and transmitted waves with both the real (undamped waves) and imaginary (damped waves) quasi-momenta in other subbands. It is important that a specific wave function of transverse quantization corresponds to each subband. It can be shown that, in the case of the scattering under consideration, the component of quantum-mechanical current density in the direction of the wave propagation (for example, ej_x, where e is the elementary charge and j_x is the probability-flux density) exhibits the coordinate dependence on the longitudinal coordinate x and on a single (in 2D structures) or two (in 1D structures) transverse coordinates; the above component is obtained as a result of summa-

tion over all dimensional subbands. We are reminded that j_x is independent of coordinates for a free particle [21]. In theoretical publications concerned with the effects of ballistic transport of electrons in the channels with sharp inhomogeneities, the dependences of the quantum-mechanical coefficient T of transmission through the structure on the energy of propagating particle, the configuration and parameters of the structure, and external fields have been studied as a rule. The structure's conductance G [22] and its temperature dependence are calculated when needed. It is worth noting that, in order to determine the above quantities, it is necessary to calculate the total current of particles in the quantum-mechanical channel, which can be accomplished by integrating the coordinate-dependent density of the quantum-mechanical current over the channel cross section. We show in what follows that the spatially inhomogeneous effects for the density of the quantum-mechanical current disappear as a result of the above-described procedure.

The main objective of this study was to theoretically analyze the effects of spatial inhomogeneity for the probability-flux density j_x (or the density of the quantum-mechanical current ej_x). These effects arise in 2D semiconductor nanostructures that consist of two quantum wells (QWs) arranged sequentially in the direction of the electron-wave propagation (the x axis); the first QW is narrow and rectangular, and the second QW is wide and parabolic along the z axis (the latter corresponds to the axis of dimensional quantization). We will show that a nonuniform distribution $j_x(x, z)$ arises owing to the interference of electron waves that propagate in a wide QW along several quantum-mechanical channels simultaneously. It will be shown that the transverse distribution $j_x(0, z)$ existing at the entry to the wide QW is reproduced to within a certain accuracy at a distance X_1 from the entry and is reproduced periodically in the sections $X_q = qX_1$ (the values of q are integers). We will also show that the multiplication effects that are clearly pronounced in the structures with rectangular QWs of various widths are much less pronounced in the QWs with a parabolic profile. We will report the results of numerical evaluation of the effects under consideration in symmetric structures and the modification of these effects in nanostructures asymmetric with respect to the z axis. In particular, we will show that an inverse and nonmonotonic dependence of the probability that a particle is found in a quantum-dimensional subband in the wide QW on the subband number is possible in asymmetric structures.

It is worth noting that the effect of spatial reproduction was predicted earlier and was partially confirmed experimentally for electromagnetic waves in waveguides [23]. In this study, we use an analysis of simple phase relations between electromagnetic waves propagating in a waveguide with different phase velocities to show that, for waveguides of a specific type (in particular, for a planar or a rectangular waveguide with the thickness A), the situation where the monochromatic wave beam that

has a characteristic size $a \ll A$ (for example, a beam coming from the narrow waveguide) and is incident on the waveguide entry reproduces to within a certain accuracy the structure of the electromagnetic field at the waveguide entry at some distance from the entry. The physical cause of this effect is the fulfillment of certain phase relations between the waves that include various eigenmodes and propagate along the waveguide. However, it is evident that complete generalization of the results obtained for electromagnetic waves in waveguides to electron waves in semiconductor nanostructures is incorrect to a great extent. The causes of possible distinctions are related to the presence of charge and mass at an electron, limitations existing in practice that are imposed on the geometrical parameters of nanostructures as a result of the necessity for simultaneous fulfillment of the conditions for dimensional quantization and ballistic transport of charge carriers in the nanostructure, the temperature limitations in electron-transport problems, specific features of the charge-carrier scattering in solids, and so on. Thus, a comprehensive study is necessary of the possibility of nanostructures existing in electronic analogues to the waveguide effects that are observed for electromagnetic waves.

The possibility of existence of a reproduction effect for the electron wave in the potential channel was discussed briefly in [24]. It was shown previously that the effects of reproduction and multiplication for the density flux of probability j_x (or ej_x) can exist in semiconductor nanostructures [25]. In continuation and development of the study reported in [25], we performed a detailed numerical analysis of the above effects for 2D semiconductor nanostructures formed of the sequence of a narrow rectangular QW and a wide parabolic QW with specific geometric parameters based on the GaAs–GaAlAs system. As far as we know, no such analysis of the effects of the spatial distribution of ej_x and possible accompanying effects in the 1D and 2D semiconductor nanostructures has been carried out previously.

2. MODEL AND CALCULATION METHOD

We describe first the model and the calculation method. Let us consider a symmetric (Fig. 1a) (or asymmetric, Fig. 1b) 2D nanostructure composed of two QWs arranged sequentially along the x axis: QW_1 with the potential $U_1(z)$ (region 1, $x < 0$) and QW_2 with the potential $U_2(z)$ (region 2, $x > 0$); these QWs localize a particle in reference to the z axis that is normal to the QW planes. We also assume that the motion along the y axis is separate and free and that the potential energy within each of the regions is independent of x and changes abruptly at the point of the QW's joint ($x = 0$). The particles' effective masses m^* are assumed to be isotropic and the same in both regions. The Schrödinger
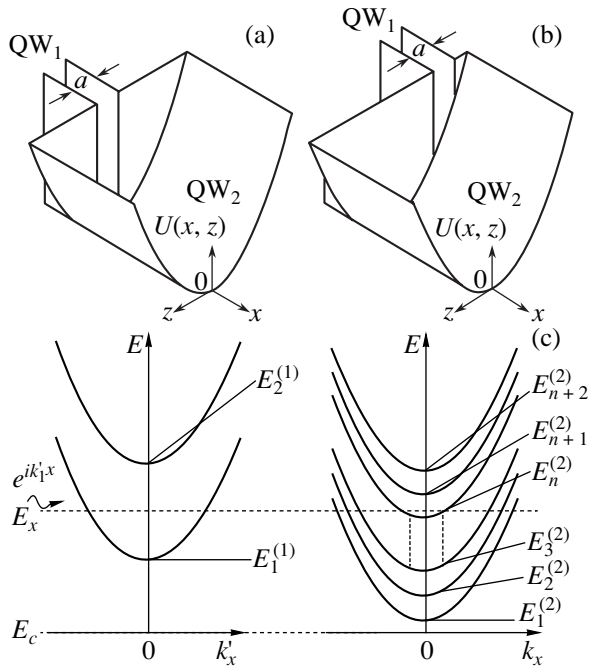
Fig. 1. Schematic representation of (a) symmetric and (b) asymmetric 2D nanostructures based on the sequence of a narrow rectangular (QW$_1$) and a wide parabolic (QW$_2$) quantum wells; the panel (c) shows the energy-band scheme of these nanostructures. The designations $E_1^{(1)}$ and $E_2^{(1)}$ represent the bottoms of the first and second quantum-dimensional subbands in QW$_1$; $E_1^{(2)}$, $E_2^{(2)}$ ... $E_n^{(2)}$, and $E_{n+1}^{(2)}$ correspond to the bottoms of the subbands in QW$_2$; $E_m^{(1)}(k_x')$ and $E_n^{(2)}(k_x)$ represent the dispersion relations of electrons in the QW$_1$ and QW$_2$, respectively; E_c is the position of the bottom of the conduction band in the bulk semiconductor; and E_x is the energy of an injected electron with the wave vector $\mathbf{k}_{1x}'$ in the QW$_1$.

equations that describe the motion of particles along the z axis can be then written as

$$-\frac{\hbar^2}{2m^*}\frac{d^2\chi_j(z)}{dz^2} + U_1(z)\chi_j(z) = E_j\chi_j(z), \qquad (1)$$

$$-\frac{\hbar^2}{2m^*}\frac{d^2\varphi_n(z)}{dz^2} + U_2(z)\varphi_n(z) = E_n\varphi_n(z). \qquad (2)$$

Here, E_j and E_n are the eigenvalues and $\chi_j(z)$ and $\varphi_n(z)$ are the eigenfunctions of Eqs. (1) and (2) in regions 1 and 2, respectively. The total energy of a particle $E = E_{x,y} + E_y$, where $E_y = \hbar^2 k_y^2/2m^*$ is the energy that corresponds to the free motion along the y axis. Let us now consider the situation where, from left to right (from region 1 to region 2) a monochromatic electron wave with the unit amplitude propagates over the quantum-

mechanical subband m in region 1. We assume that the QWs localizing the particle along the z axis have infinitely high potential barriers; i.e., the energy spectra for both QWs are completely discrete along this direction. The particle's wave functions $\phi^{(1)}(x, z)$ and $\phi^{(2)}(x, z)$ in regions 1 and 2 can be then represented as

$$\phi^{(1)}(x, z) = \chi_m(z)\exp(ik_m'x)$$
$$+ \sum_j B_j\chi_j(z)\exp(-ik_j'x), \qquad (3)$$

$$\phi^{(2)}(x, z) = \sum_n C_n\varphi_n(z)\exp(ik_nx). \qquad (4)$$

Here, B_j and C_n are constant coefficients defining the amplitudes of the waves that are reflected in region 1 over the subbands E_j and passed to region 2 through the subbands E_n; and k_j' and k_n are the wave numbers that correspond to the motion of the particle along the x axis in these regions: $k_j' = [2m^*(E - E_j - E_y)]^{1/2}/\hbar$ and $k_n = [2m^*(E - E_n - E_y)]^{1/2}/\hbar$. The reflection and transformation of electron waves in such structure occurs at the potential step $U_0 = E_1^{(1)} - E_1^{(2)}$, where $E_1^{(1)}$ and $E_1^{(2)}$ are the bottoms of the low quantum-dimensional subbands in the QW$_1$ and QW$_2$, respectively. It is noteworthy that, if $E - E_y > E_j$ (and E_n), the quantities k_j' and k_n are real so that the corresponding waves are propagating; in contrast, if the inequality is opposite, the quantities k_j' and k_n are imaginary and the waves are damped with the characteristic attenuation lengths $l_j = |k_j'|^{-1}$ and $l_n = |k_n|^{-1}$. For the structures under consideration with an abrupt transition between the first and second regions, the coefficients B_j and C_n are determined from the following system of equations that is based on the boundary conditions for the wave functions and their derivatives at the point $x = 0$:

$$\phi^{(1)}(x = 0, z) = \phi^{(2)}(x = 0, z),$$

$$\nabla_x\phi^{(1)}(x = 0, z) = \nabla_x\phi^{(2)}(x = 0, z), \qquad (5)$$

$$\chi_m(z) + \sum_j B_j\chi_j(z) = \sum_n C_n\varphi_n(z),$$

$$k_m'\chi_m(z) - \sum_j k_j'B_j\chi_j(z) = \sum_n k_nC_n\varphi_n(z). \qquad (6)$$

Multiplying from the left Eq. (5) by $\varphi_p^*(z)$ and Eq. (6) by $\chi_p^*(z)$ and integrating the obtained expressions with respect to z, we derive the following system of linear

algebraic equations for determining the coefficients B_j and C_n:

$$t_{p,m} + \sum_j B_j t_{p,j} = C_p, \qquad (7)$$

$$k'_m \delta_{pm} - k'_p B_p = \sum_n k_n C_n f_{p,n}. \qquad (8)$$

Here, $t_{p,m} = \int \varphi_p^*(z) \chi_m(z) dz$ and $f_{p,n} = \int \chi_p^*(z) \varphi_n(z) dz$ are the nonorthogonality coefficients for the eigenfunctions in regions 1 and 2; it is noteworthy that $f_{p,m} = t_{m,p}^*$. For structures that are symmetric along the z axis, in which case the potentials $U_1(z)$ and $U_2(z)$ localizing a particle within regions 1 and 2 satisfy the conditions $U_1(z) = U_1(-z)$ and $U_2(z) = U_2(-z)$ (the point $z = 0$ is located on the symmetry axis of the structure), the eigenfunctions $\chi_i(z)$ and $\varphi_n(z)$ in regions 1 and 2 can be classified according to the parity of these functions. In this case, the nonorthogonality coefficients are equal to zero for the functions with differing parities. It is noteworthy that system of Eqs. (7) and (8) is then separated into two independent subsystems: a subsystem of inhomogeneous linear equations containing only the coefficients B_j and C_n with the indices of the same parity as the number of subband (m) over which the wave propagates from region 1 to region 2 and a subsystem of homogeneous linear equations for the coefficients B_j and C_n with the indices that are opposite in parity to the parity of m. It is easy to show that the determinant of the second subsystem is always nonzero, which ensures that all the coefficients B_j and C_n with indices j and n that have the parity opposite to the parity of m are equal to zero.

In what follows, we will be interested in the coordinate dependence of the probability-density flux $j_x(x, z)$ along the x axis in region 2 (or in the component of the quantum-mechanical current density along the x axis); as is well known [21],

$$j_x(x, z) = \frac{\hbar}{2m^*} \{ \phi^{(2)}(x, z) \nabla_x [\phi^{(2)}(x, z)]^* \\ - [\phi^{(2)}(x, z)]^* \nabla_x \phi^{(2)}(x, z) \}. \qquad (9)$$

Substituting the particle's wave function in region 2 (4) into (9), we obtain

$$j_x(x, z) = \frac{\hbar}{2m^*} \sum_{n,t} C_n C_t^* \varphi_n(z) \varphi_t^*(z) \\ \times (k_n + k_t^*) \exp[i(k_n - k_t^*)x]. \qquad (10)$$

For further analysis, it is convenient to divide (10) into the sum of three terms $j_x = j_{x1} + j_{x2} + j_{x3}$, where the sums over various combinations of the real and imaginary wave vectors k are separated. In the model of a QW with infinitely high potential barriers, a finite number N of lower subbands with real values of k exist in region 2

at a given energy E of an incident electron, whereas all the upper subbands have imaginary wave vectors. Let us separate the first term j_{x1} in (10) taking into account the summation only over the N lower subbands with real values of k in this term and assuming that both C_n and $\varphi_n(z)$ are complex quantities; as a result, we obtain

$$j_{x1}(x, z) = \frac{\hbar}{m^*} \sum_{n=1}^{N} |C_n|^2 |\varphi_n(z)|^2 k_n + \frac{\hbar}{2m^*} \\ \times \sum_{n,t=1; n \neq t}^{N} C_n C_t^* \varphi_n(z) \varphi_t^*(z)(k_n + k_t) \exp[i(k_n - k_t)x]. \qquad (11)$$

If we restrict ourselves only to the equations with real values of k in the system of Eqs. (7) and (8) for determining the coefficients C_n, then all C_n are found to be real. If we include the subbands with imaginary wave vectors k into calculation, the coefficients C_n become complex. In the further analysis of other terms in (10), we take into account that the quantities $\varphi_n(z)$ are real in the problem under consideration. We represent the purely imaginary wave vectors k as $k_j = i\,\text{Im}(k_j)$ and the complex coefficients C_j as $C_j = C_{j1} + iC_{j2}$, where $C_{j1} = \text{Re}(C_j)$ and $C_{j2} = \text{Im}(C_j)$. Here, $\text{Re}(C_j)$ is the real part of C_j, while $\text{Im}(C_j)$ and $\text{Im}(k_j)$ are the imaginary parts of C_j and k_j, respectively. As a result, the expression for j_{x2} in which the summation is performed over the indices that correspond to the real and imaginary wave vectors k (the cross terms) can be written as

$$j_{x2}(x, z) = \frac{\hbar}{m^*} \sum_{t=1}^{N} \sum_{n=N+1} \varphi_n(z) \varphi_t^*(z) \\ \times \{ [(C_{n1}C_{t1} + C_{n2}C_{t2})k_t \\ + (C_{n1}C_{t2} - C_{n2}C_{t1})\text{Im}(k_n)] \cos(k_t x) \qquad (12) \\ + [(C_{n1}C_{t1} + C_{n2}C_{t2})\text{Im}(k_n) - (C_{n1}C_{t2} - C_{n2}C_{t1})k_t] \\ \times \sin(k_t x) \exp[-\text{Im}(k_n)x] \}.$$

The expression for j_{x3} in which the summation is carried out over the indices that correspond only to imaginary wave vectors k_j is represented as

$$j_{x3}(x, z) = \frac{\hbar}{m^*} \sum_{n,t=N+1; n \neq t} \varphi_n(z) \varphi_t(z) \\ \times [\text{Im}(k_n) - \text{Im}(k_t)] \qquad (13) \\ \times (C_{n1}C_{t2} - C_{n2}C_{t1}) \exp\{-[\text{Im}(k_n) + \text{Im}(k_t)]x\}.$$

In expression (13), there are no terms with $n = t$ since these terms are equal to zero. It follows from (11)–(13) that the coordinate dependence on x in the expression for j_x is inherent to all terms that contain the products $\varphi_n(z) \varphi_t(z)$ of the functions with $n \neq t$; this inference refers to the second term in (11) and to the sums in (12) and (13). We call attention to the radically different

behavior of j_{x1}, which contains the terms with real wave vectors k and of the components j_{x2} and j_{x3} that contain the terms with imaginary values of k as x increases. As follows from (11)–(13), the current densities j_{x2} and j_{x3} are damped out exponentially as $x \longrightarrow \infty$, whereas j_{x1} oscillates in this range of variation in x. It is noteworthy that the total probability-flux density along the x axis $J_x = \int j_x(x, z)dz$ (and, consequently, the total quantum-mechanical current) does not exhibit a coordinate dependence on x owing to orthonormality of the functions $\{\varphi_n(z)\}$; therefore, only the terms with $n = t$ remain in (10). It is important that the terms corresponding to the subbands with $E_{n,t} > E$ and imaginary $k_{n,t}$ are equal to zero, so that J_x is defined by the expression

$$ J_x = \frac{e\hbar}{m*}\sum_n |C_n|^2 k_n. \tag{14} $$

In (14), summation is performed only over the subbands with $E_n < E$, i.e., over all subbands that belong to region 2 and feature the real wave vectors k_n; unattenuated propagation of electron waves occurs over these subbands. It is worth noting that the conductance G of the structure is also independent of x. It follows from expressions (11)–(13) that the coordinate dependence $j_x(x, z)$ arises owing to the interference terms with $n \neq t$ in expression (10). It is evident that the presence of at least two subbands with unattenuated propagation of electron waves in region 2 is necessary for the appearance of the above coordinate dependence. Thus, expression (10), in combination with both the eigenfunctions $\chi_i(z)$ and $\varphi_n(z)$ obtained from solution of Eqs. (1) and (2) and the coefficients B_j and C_n obtained by solving the system of Eqs. (7) and (8), yields the complete solution of the problem on the distribution of the probability-flux density $j_x(x, z)$ (or the quantum-mechanical current density) in region 2.

Let us study in more detail the coordinate dependence $j_{x1}(x, z)$ (see (11)), which does not contain the damped terms with imaginary wave vectors k. It is easily seen that, if all differences $k_n - k_t$ in the index of the exponential function in the second term of sum (11) can be represented simultaneously for all n and t as

$$ (k_n - k_t) = p_{n,t}\Delta, \tag{15} $$

where $p_{n,t}$ is an integer, then we obtain $j_{x1}(X_1, z) = j_{x1}(x = 0, z)$ for the cross section at $X_1 = 2\pi/|\Delta|$. In this ideal case, the transverse profile $j_{x1}(x = 0, z)$ along the z axis (this profile exists at the entry to region 2, at the point $x = 0$) is reproduced accurately in the sections $X_p = pX_1$ ($p = 1, 2, \dots$). It is evident that this condition is not satisfied to a full extent in the general case as a result of the root dependences of k_n and k_t on E_n and E_t. However, this situation can be realized approximately in the case where the kinetic energy of a particle in region 2 along the x axis is much higher than the energies of the bottoms of the quantum-dimensional sub-

bands over which the unattenuated propagation of electron waves in this region takes place (i.e., we have the condition $E_x \gg E_{n,t}$). Indeed, expanding $k_{n,t}$ in series in a small parameter $E_{n,t}/E_x \ll 1$ and restricting ourselves to the second term in the expansion, we obtain

$$ (k_n - k_t) \approx (m*/2E_x)^{1/2}(E_t - E_n)/\hbar. \tag{16} $$

In this case, the effects of reproduction for j_{x1} can be observed (in the aforementioned approximations) in a number of nanostructures of a certain type if the differences $E_t - E_n$ are proportional to integers, i.e., if $k_n - k_t$ can be represented in the form given by (15).

All the 2D nanostructures of the above-mentioned type exhibit a common special feature. They consist of two QWs that are arranged sequentially along the x axis and have appreciably different effective width. In what follows, we consider a situation where a monochromatic electron wave propagates from the thin rectangular QW_1 (region 1) to the wide parabolic QW_2 (region 2); we assume that, for this wave, $E_y = 0$, so that the total kinetic energy of the particle $E = E_x$. The interference effects we are interested in take place in the wide QW_2. In this paper, we consider two nanostructures based on the sequence of these QWs: symmetric (Fig. 1a) and asymmetric (Fig. 1b) nanostructures. In Fig. 1c, we show the energy diagrams of these structures.

At present, parabolic QWs in 2D nanostructures are obtained experimentally; various physical effects are studied in these QWs. In the approximation of infinitely high potential walls, the eigenfunctions of a particle in a parabolic QW coincide with the harmonic-oscillator functions; in addition, the part of the particle's electron spectrum quantized along the z axis with the potential $U_2(z) = m*\omega_0^2 z^2/2$ in Eq. 2 is represented as $E_n = \hbar\omega_0(n + 1/2)$, where $n = 0, 1, 2, \dots$. The frequency $\omega_0 = (K/m*)^{1/2}$ is controlled by the curvature of the parabola K; this curvature depends on the parameters of the nanostructure. In this case, the difference $E_t - E_n = \hbar\omega_0(t - n)$ in expression (16), where $t - n$ is always an integer; the profile of the initial distribution $j_{x1}(0, z)$ at the entry to the parabolic QW is reproduced in this QW on the x axis at the points $X_p = pX_1$, where X_1 is given by

$$ X_1 = (4\pi/\omega_0)[(E - E_y)/2m*]^{1/2}. \tag{17} $$

For a nanostructure that is symmetric with respect to the z axis in which case the eigenfunctions in regions 1 and 2 can classified according to the parity, only the coefficients $C_{n,t}$ are nonzero in Eqs. (7) and (8) at odd-valued t and n if a particle exits from the QW_1 and is incident on the subbands with odd-valued m (the even solutions). For even-valued m (the odd-valued solutions), only the coefficients $C_{n,t}$ with the odd-valued n and t are nonzero. Therefore, in the symmetric structure, the synphase sections are found twofold as often as in an asymmetric structure; i.e.,

$$ X_1 = (2\pi/\omega_0)[(E - E_y)/2m*]^{1/2}. \tag{18} $$

Thus, in the context of the approximations that we used, the distribution of the undamped component of the probability-flux density $j_{x1}(0, z)$ (or the density of the quantum-mechanical current) at the entry to the parabolic QW_2 is reproduced in synphase sections at the points pX_1. If the damped terms j_{x2} (12) and j_{x3} (13) are disregarded, the total flux density $j_x \approx j_{x1}$ and the initial distribution $j_x(0, z)$ is further reproduced in the same sections.
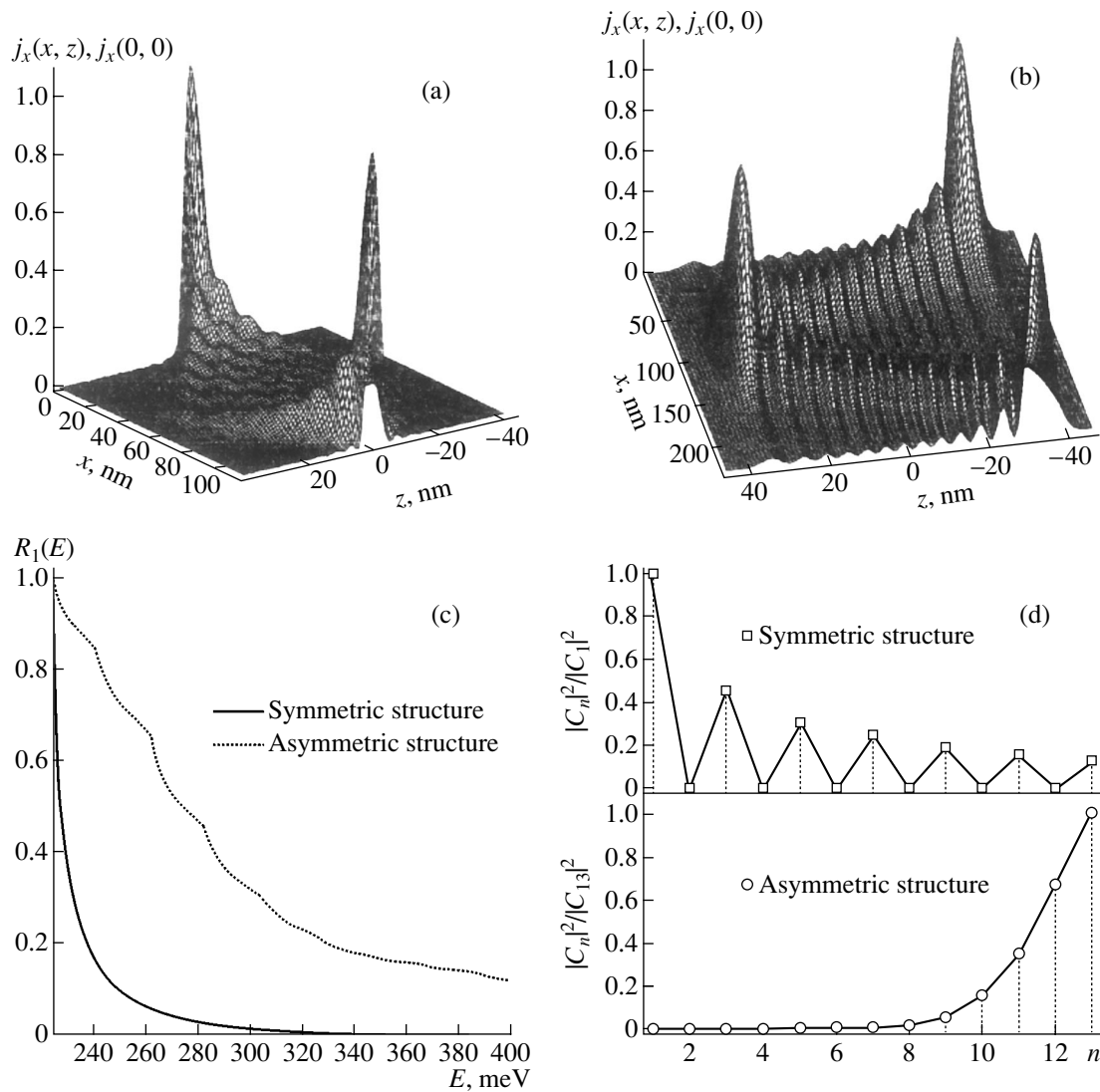
3. RESULTS AND DISCUSSION

In this section, we report the results of numerical calculation of the effects of spatial reproduction for $j_x(x, z)$ in a 2D nanostructure with specified parameters. We considered the problem on the scattering of a monochromatic electron wave that propagated from a narrow rectangular QW_1 (the thickness $a = 50$ Å) over the lower quantum-dimensional subband ($m = 1$) at the abrupt transition from the narrow QW_1 to the wide QW_2 with parabolic profile for two 2D nanostructures with GaAs parameters ($m^* = 0.067m_0$, where m_0 is the free-electron mass); one of these nanostructures is symmetric with respect to the z axis (Fig. 1a) and the other is asymmetric in which case the symmetry axis of the narrow QW_1 is shifted by 34.8 nm with respect to symmetry axis of the wide QW_2.

The calculation was performed in a model of QWs with infinitely high walls. In both cases, the particle's energy measured from the conduction-band bottom E_c in a bulk semiconductor was 270 meV that corresponded to the particle's kinetic energy $E_{x1}^{(1)} = 45.5$ meV for the first subband in QW_1 at $E_{y1}^{(1)} = 0$ (the energies of the bottoms of two lower subbands in QW_2 $E_1^{(1)} = 224.5$ meV and $E_2^{(1)} = 898.0$ meV). Since the motion along the y axis is separate in the structures under consideration, $E_{y, n}^{(2)} = 0$ in QW_2. Spacings between the bottoms of the quantum-dimensional subbands in the parabolic QW_2 were the same due to the equidistant structure of the spectrum and were assumed to be equal to 21 meV in the calculations. It is important that the kinetic energy of a particle in QW_2 was equal to $E_{x1}^{(2)} = 259.5$ meV for the first subband and decreased as the subband number increased. Only a single lower subband with real wave vectors k exists in the narrow QW_1 for the structures with the above parameters in the context of the model under consideration. In contrast, unattenuated propagation of electron waves is possible over 13 subbands with real values of k_{xn} in QW_2 for the particle's energy chosen. In Fig. 1c, we show the energy diagrams for the narrow and wide QWs; these diagrams are identical for symmetric and asymmetric nanostructures. From here on, all necessary information is given in the figure captions.

We determined the coefficients B_j and C_n for the symmetric and asymmetric nanostructures by solving the system of Eqs. (7) and (8), which involves a single subband with real quasi-momenta k'_{xj} and 20 subbands with imaginary quasi-momenta in the QW_1 and also 13 subbands with the real k_{xn} (indexing of the subbands in the parabolic QW starts with $n = 0$) and 8 subbands with imaginary k_{xn} in the QW_2. We restricted ourselves to the above number of equations in the system of Eqs. (7) and (8) since a further increase in the number of equations did not eventually affect the values of the coefficients.

Using this approach, we calculated the spatial distribution of the probability-flux density $j_x(x, z)$ in the parabolic QW_2 in the approximation of the expanded and real values of k_x for both structures. In Fig. 2, we show the spatial distributions of normalized probability-flux density $j_x(x, z)/j_x(0, 0)$ in the wide QW_2 in the plane x–z for a symmetric 2D nanostructure. One can see the effect of reproduction in the section at $x = X_1$ in the above-described approximations (Fig. 2a); a modification of this effect in an asymmetric structure is also illustrated (Fig. 2b). In Fig. 2c, we show the dependences of the reflection coefficients $R_1(E)$ on the energy of a particle that is incident on, and reflected within, the lowest quantum-confinement level in the narrow QW_1 for the symmetric and asymmetric structures in the energy range $E_1^{(1)} < E < E_2^{(1)}$. The energy in Fig. 2c is measured from the bottom of the conduction band E_c in the bulk semiconductor. The calculation shows that the reflection coefficients for the symmetric and asymmetric structures are small ($R_1(E) \leq 0.1$) in the range of the particle's kinetic energies we are interested in. This basically makes it possible to disregard the terms that contain the reflection coefficients in Eqs. (7) and (8), simplify appreciably the calculations, and find nevertheless the main specific features of the coordinate dependence $j_x(x, z)$. We also studied the dependences of the probabilities $|C_n|^2$ of finding the particle in the nth subband in the wide QW_2 on the subband number for the symmetric and asymmetric nanostructures. The dependences of the normalized probabilities $|C_n|^2/|C_1|^2$ (for the symmetric nanostructure) and $|C_n|^2/|C_{13}|^2$ (for an asymmetric structure) on the subband number n in the parabolic QW_2 are different for these cases (see Fig. 2d). In the symmetric structure, the nonzero coefficients $|C_n|^2$ decrease monotonically as the subband number increases, which is caused by a decrease (with the subband number increasing) in the nonzero integrals of overlap of the particle's z-dependent transverse wave function in the lower subband of the narrow QW_1 with the eigenfunctions of subbands in the wide QW_2. It is worth recalling that the coefficients C_n are equal to zero if the subbands in the wide QW_2 have a parity that differs from the parity of the first subband in the narrow QW_1 (the even-valued transverse wave function) and if

$j_x(x, z), j_x(0, 0)$

(a)

$j_x(x, z), j_x(0, 0)$

(b)

$R_1(E)$

(c)

—— Symmetric structure
········· Asymmetric structure

(d)

□ Symmetric structure

○ Asymmetric structure

$|C_n|^2/|C_1|^2$

$|C_n|^2/|C_{13}|^2$

Fig. 2. Spatial distribution of the normalized probability-flux density $j_x(x, z)/j_x(0, 0)$ in the parabolic QW$_2$ for a symmetric 2D nanostructure with GaAs parameters; the effect of reproduction in the section at $x = X_1$ in this nanostructure can be seen in (a), and a modification of this effect in an asymmetric 2D nanostructure is illustrated in (b). Panel (c) represents the dependences of the reflection coefficient on the energy $R_1(E)$ of the particle that is incident on and reflected from the lower quantum-dimensional level in the QW$_1$ for the symmetric and asymmetric structures in the energy range $E_1^{(1)} < E < E_2^{(1)}$. The panel (d) shows the dependences of the ratios $|C_n|^2/|C_1|^2$ for the symmetric and $|C_n|^2/|C_{13}|^2$ for the asymmetric 2D nanostructures on the subband number n in the parabolic QW$_2$. The quantities $|C_n|^2$ control the occupancies of subbands in the QW$_2$. The quantity $a = 50$ Å refers to the QW$_1$; the spacing between the bottoms of the subbands in the parabolic QW$_2$ $\hbar\omega_0 = 21$ meV.

we assume that the electron wave propagates from QW$_1$ to QW$_2$ in the symmetric structure. However, the situation is opposite for an asymmetric structure: inverse behavior of probabilities of finding a particle in the nth subband of the wide QW$_2$ is observed; i.e., an increase in $|C_n|^2$ is observed as the subband number increases. In an asymmetric structure, this effect is caused by a drastic decrease in the integrals of overlap of the wave function of the lower subband in the QW$_1$ with the eigenfunctions of the lower subbands in the QW$_2$.

We also constructed the two-dimensional topograms of the dependences $j_x(x, z)/j_x(0, 0) = $ const in the plane x–z for a number of sections in the range (0–1) for the nanostructures under consideration. In Fig. 3a, we show the topogram calculated in the approximation of the expanded and real k_x for a nanostructure that is symmetric with respect to the z axis; the effects of reproduction for electron waves in various sections can be seen. In Fig. 3b, we show the topogram for an asymmetric 2D structure in the same approximations; this topogram

indicates that the above effects are modified appreciably. As can be seen from Figs. 2b and 3b, the initial profile $j_x(0, z)$ in an asymmetric structure is reproduced in the synphase sections X_q that twice exceed those in the symmetric structure; this behavior is consistent with formula (17). In addition to this effect, additional peaks of $j_x(x, z)$ arise in the asymmetric structure; these peaks have the same amplitude as that at the entry to the wide QW$_2$ but are located in the sections X_q asymmetrically with respect to the entry point of the electron wave.

Evidently, the effects of spatial nonuniformity of $j_x(x, z)$ under consideration are the result of the interference of electron waves in the wide QW$_2$ and are related to the well-known classical effect, i.e., the electron-wave interference at two (or several) slits that are separated in the coordinate space [26]. Recently, the electron-interference effects were studied experimentally in a solid-state analogue of a system with two slits (a system with a double-path interferometer); this analogue was realized in a system with a 2D electron gas that was composed of high-mobility electrons [27]. In the structures considered here, the role of the above slits is played by the quantum-dimensional subbands in the wide QW$_2$ that are separated in the energy space. As a result, the transverse distribution $j_x(x, z)$ that is nonuniform along the z axis and is caused by interference is formed eventually in each section perpendicular to the x axis; however, these distributions exhibit clearly pronounced minima and maxima only for some of the sections.

Undoubtedly, the initial distribution of the probability-flux density (or the quantum current density) cannot be reproduced faithfully in the synphase sections. The main causes of this behavior consist in the finite number of terms in sum (10) (this number is restricted by the requirement that the wave vectors $k_{n, t}$ be real) and the inaccuracy in the condition for the sections to be synphase; this inaccuracy is related to the discarded higher order terms in the expansion of the quasi-momenta (16). Analysis also shows that a modification of the spatial distribution $j_x(x, z)$ due to the contribution of the terms j_{x2} (12) and j_{x3} (13), which are exponentially damped as the coordinate x increases and include imaginary wave vectors $k_{n, t}$, to the sum in (10) exists in the wide parabolic QW$_2$ only at a distance of several tens of angstroms from the entry to this QW. This circumstance is caused by small values of attenuation length l_n for the subbands under consideration. For example, the attenuation length in the QW$_2$ $l_n = |k_n|^{-1}$ is equal to 64.9 Å for first subband with imaginary values of k_n ($n = 13$) in the structure under consideration at the particle energy $E = 270$ meV; as n increases, l_n decreases and attains the value of 19 Å at $n = 20$, which corresponds to the last subband that is included in the calculation and belongs to the parabolic QW$_2$. Needless to say, the value of l_n is even smaller for higher subbands. Thus, fulfillment of the inequality $l_n \ll X_1$ makes it possible to disregard the terms $j_{x2}(x, z)$ and $j_{x3}(x, z)$ in calculating $j_x(x, z)$ and to obtain spatial distribution
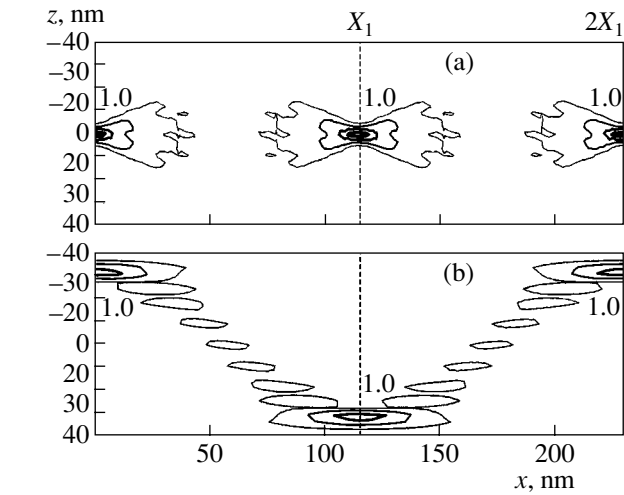
Fig. 3. Topograms of the spatial distribution (in the x–z plane) of the normalized probability-flux density $j_x(x, z)/j_x(0, 0)$ in the parabolic QW$_2$ for the (a) symmetric and (b) asymmetric nanostructures. The symmetry axis of the narrow QW$_1$ is shifted by $\Delta z = 348$ Å from the symmetry axis of the structure. The values of 1.0 represent the amplitudes of the peaks in relative units. The calculation was carried out in the approximation of the real and expanded wave vectors k_x. (a) The lines that have decreasingly smaller thickness correspond to the sections at the heights of 0.8, 0.5, 0.2, and 0.1, respectively; (b) the similar lines correspond to the sections at the heights of 0.8, 0.5, and 0.3.

$j_x(x, z) \approx j_{x1}(x, z)$ that is eventually unattenuated as the coordinate x is further increased.

As is well known, the ballistic transport of electrons in a nanostructure is required for the formation of an interference pattern. The processes of inelastic scattering by phonons and the electron–electron scattering violate the phase coherence. The typical time of inelastic scattering is equal to ~40 ps at $T \sim 1$ K. In this case, the mean electron velocity is ~2.5×10^7 cm/s and the mean free path for inelastic scattering is ~10 μm [28]. However, the situation is more severe for hot electrons, represented by particles injected into the wide QW$_2$. Nevertheless, estimations show that, in the case under consideration as well, the interference pattern can be retained, at least at a distance corresponding to several reproduction events. The particle's velocity is ~1.2×10^8 cm/s if the kinetic energy of the particle in the QW$_2$ is ~260 meV, as was chosen. In this case, the time of the particle's flight to the point of the first reproduction $X_1 \sim 115$ nm in the symmetric structure is $\tau \approx 9.6 \times 10^{-14}$ s. This value is smaller by almost an order of magnitude than the characteristic electrons' energy-relaxation times τ_ε related to the scattering by longitudinal optical (LO) phonons in GaAs, where $\tau_\varepsilon \sim 10^{-12}$ s. As is well known, it is this relaxation mechanism that mainly limits the phase coherence of hot electrons and, thus, destroys the interference pattern.

It is worth noting that the actual beam of particles injected into the wide QW_2 is not exactly monoenergetic. If the spread of the particles' energies in the beam about the value of E_{x0} is $\pm\Delta E_{x0}$, this, as follows from expression (18), leads, in the first approximation, to broadening (on the x axis) of the peaks that correspond to the exact reproduction of the initial distribution $j_x(0, z)$ at the points X_q; this broadening amounts to $\pm\Delta X_q = \pm X_q(\Delta E_{x0}/2E_{x0})$. For example, if the energy width of the injected electron beam is 10 meV, the first reproduction peak at $x = X_1$ in the structure under consideration is broadened by 22 Å. At present, there are methods for injecting the quasi-monoenergetic electron beams in 2D nanostructures. For example, Rauch *et al.* [29] studied ballistic transport over minibands in a superlattice based on a GaAlAs–GaAs system by injecting a quasi-monoenergetic beam of hot electrons into the superlattice.

It is noteworthy that the effects under consideration can be controlled using a constant transverse (directed along the z axis) electric field. The field applied in the region of the wide QW_2 brings about a decrease in the effective width of this QW and also gives rise to asymmetry along the z axis in the symmetric structure. All these effects lead to a modification of the initial (in the absence of a field) spatial distribution $j_x(x, z)$.

In this study, we assumed that the potential step U_0 at the abrupt transition from the narrow QW_1 to the wide QW_2 is equal to the difference between the energy positions of the bottoms of the lower subbands in these QWs: $U_0 = E_1^{(1)} - E_1^{(2)}$. It is evident that one can form an additional built-in potential step by combining the percentage content of Al in the QWs in regions 1 and 2.

In this study, we considered only structures based on a combination of a narrow rectangular quantum well and a wide parabolic quantum well. At the same time, it is evident that the effects considered are fairly general and should exist in structures with QWs with other profiles. We studied a number of such situations, including modifications of the effects under consideration in 1D nanostructures. The results of those studies will be reported in our next publication. It is also worth noting that the pattern of the spatial distribution j_x can be changed in a wide range by varying the structure's parameters (the QW effective width, the ratio between the widths of the narrow and wide QWs, the particle's energy, the degree of the structure's asymmetry, and the structure's material).

REFERENCES

1. Y. Imry, *Introduction to Mesoscopic Physics* (Oxford Univ. Press, Oxford, 1997).
2. D. K. Ferry and S. M. Goodnick, *Transport in Nanostructures* (Cambridge Univ. Press, Cambridge, 1997).
3. S. Datta, *Electronic Transport in Mesoscopic Systems* (Cambridge Univ. Press, Cambridge, 1995).
4. G. Kircenow, Phys. Rev. B **39**, 10452 (1989).
5. G. Kircenow, Solid State Commun. **68**, 715 (1988).
6. E. Tekman and S. Ciraci, Phys. Rev. B **43**, 7145 (1991).
7. F. Sols, M. Macucci, U. Ravaioli, and K. Hess, J. Appl. Phys. **66**, 3892 (1989).
8. H. Tachibana and H. Totsuji, J. Appl. Phys. **79**, 7021 (1996).
9. Hua Wu, D. W. L. Sprung, and J. Martorell, J. Appl. Phys. **72**, 151 (1992).
10. A. Namiranian, M. R. H. Khajehpour, Yu. A. Kolesnichenko, and S. N. Shevchenko, Physica E (Amsterdam) **10**, 549 (2001).
11. O. Olendski and L. Mikhailovska, Phys. Rev. B **66**, 035331 (2002).
12. P. F. Bagwell, Phys. Rev. B **41**, 10354 (1990).
13. Y. Takagaki and D. K. Ferry, Phys. Rev. B **44**, 8399 (1991).
14. T. Itoh, N. Sano, and A. Yoshii, Phys. Rev. B **45**, 14131 (1992).
15. P. Singha Deo, B. C. Gupta, A. M. Jayannavar, and F. M. Peeters, Phys. Rev. B **58**, 10784 (1998).
16. K. Nicolic and R. Sordan, Phys. Rev. B **58**, 9631 (1998).
17. G. J. Jin, Z. D. Wang, A. Hu, and S. S. Jiang, J. Appl. Phys. **85**, 1597 (1999).
18. V. A. Petrov and I. M. Sandler, Mikroélektronika **23**, 3 (1994).
19. K. F. Berggren and Z. Ji, Phys. Rev. B **43**, 4760 (1991).
20. K. F. Berggren and Z. Ji, Phys. Rev. B **45**, 6652 (1992).
21. L. D. Landau and E. M. Lifshitz, *Course of Theoretical Physics*, Vol. 3: *Quantum Mechanics: Non-Relativistic Theory*, 4th ed. (Nauka, Moscow, 1989; Pergamon, Oxford, 1977).
22. R. Landauer, Z. Phys. B **68**, 217 (1978).
23. L. A. Rivlin and V. S. Shil'dyaev, Izv. Vyssh. Uchebn. Zaved., Radiofiz. **11**, 572 (1968).
24. L. A. Rivlin, Kvantovaya Élektron. (Moscow) **6**, 1087 (1979).
25. V. A. Petrov and V. L. Bratman, Phys. Status Solidi B **221**, 459 (2000).
26. R. P. Feynman, R. B. Leighton, and M. Sands, *The Feynman Lectures on Physics* (Addison-Wesley, Reading, Mass., 1963 and 1965; Mir, Moscow, 1978).
27. E. Buks, R. Schuster, M. Heiblum, *et al.*, Nature **391**, 871 (1998).
28. S. Datta, Superlattices Microstruct. **6**, 83 (1989).
29. C. Rauch, G. Strasser, K. Unterrainer, *et al.*, Physica E (Amsterdam) **2**, 282 (1998).

Translated by A. Spitsyn

<div align="center">

LOW-DIMENSIONAL
SYSTEMS

</div>

Effective Mass Anisotropy of Γ Electrons in a GaAs/(AlGa)As Quantum Well

E. E. Vdovin^ and Yu. N. Khanin

Institute of Microelectronics Technology and High-Purity Materials, Russian Academy of Sciences,
Chernogolovka, Moscow oblast, 142432 Russia
^e-mail: vdovin@ipmt-hpm.ac.ru

Abstract—Measurements of the electron transport in double-barrier AlAs/GaAs/AlAs heterostructures grown on (001)- and (311)-oriented substrates are carried out. The results obtained provide information on the anisotropy of the electron subbands in the GaAs quantum wells (QWs) of these heterostructures. The in-plane dispersion relation $E(k_\parallel)$ is determined using magnetotunneling spectroscopy with a magnetic field B applied parallel to the QW layer (i.e., normally to the tunneling current). The amplitudes and bias positions of the resonance peaks in the tunneling current are found to be sensitive both to the magnitude and orientation of the magnetic field with respect to the crystallographic axes in the QW plane. Insertion of an InAs monolayer at different positions in the GaAs QW enables the modification of electron wave functions, which is used to study the nature of electron-subband anisotropy in this type of QW. © 2005 Pleiades Publishing, Inc.

1. INTRODUCTION

The exact shape of the GaAs band structure near the Γ point of the Brillouin zone is a subject that has seen renewed interest in connection with studies of the stripe phase of the quantum Hall effect [1]. In most of these experimental studies, the effective mass of electrons confined in (AlGa)As/GaAs/(AlGa)As quantum wells (QWs) was measured as a function of the QW width (see, e.g., [2]). However, these experiments were not sensitive to mass anisotropy. Nevertheless, anisotropy of the electron subbands in the plane of the QW can lead to anisotropy in the electrical properties. In recent studies [3–6], the in-plane electron-energy dispersion $E(k_\parallel)$ was probed by a magnetotunneling spectroscopy technique with a magnetic field **B** applied parallel to the QW layer (i.e., normally to the tunneling current). The samples investigated were resonance-tunneling double-barrier AlAs/GaAs/AlAs heterostructures grown on (001)-oriented substrates. Due to the effect of the Lorentz force caused by the application of the magnetic field, the electrons tunneling into the QW acquire additional quasi-momentum in the direction normal to the field. Since the quasi-momentum is conserved in the tunneling process, this results in a shift of the positions of the peaks in the tunneling current towards higher bias voltages, which is proportional to $E(k_\parallel)$. It was found that the amplitude of the tunneling current is also sensitive to both the magnitude and orientation of the magnetic field with respect to the crystallographic axes. Thus, by carrying out measurements with different orientations of the magnetic field in the plane of the QW, it is possible to examine the anisotropy of the electron subbands in this plane.

It has been observed [3, 5, 6] that anisotropy of the tunneling current along the [110] and [$\bar{1}$10] axes exists and that the anisotropy direction rotates by 90° when the sign of the bias voltage changes. This anisotropy was explained in terms of the difference in the electron-subband mixing at the GaAs/(AlGa)As and (AlGa)As/GaAs interfaces on opposite sides of a GaAs QW. In order to understand the experimentally observed anisotropy, it is essential that the Al–As (or Ga–As) chemical bonds at the normal (AlAs/GaAs) and inverted (GaAs/AlAs) interfaces of the GaAs QW lie in the two orthogonal planes. The arrangement of Ga, As, and Al atoms in the vicinity of the normal AlAs/GaAs interface is shown schematically in Fig. 1.

Without a bias applied, the directions [110] and [$\bar{1}$10] can be considered as equivalent (assuming that the interfaces are ideal). However, because of the polar character of the chemical bonds, the application of an electric field breaks the symmetry. For example, at one interface, the field pushes electrons towards the first plane of Ga atoms and pulls them away from the plane of As atoms in the barrier. At the other interface, where the direction of the chemical bonds is different, electrons are pushed towards the plane of As atoms. Thus, the electric field induces anisotropy as a result of the polarization of the chemical bonds. Furthermore, the shift in the maximum of the electron wave function in the QW towards one of the interfaces depends on the sign of the applied bias voltage. Thus, the observed anisotropy depends both on the sign and the absolute value of the bias [5].

In this paper, we report the results of a further study of the effective mass anisotropy of Γ electrons in
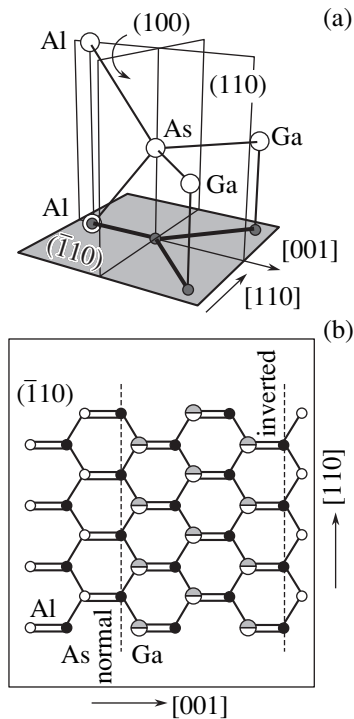
Fig. 1. (a) Arrangement of atomic planes in the vicinity of the normal AlAs/GaAs interface (GaAs grown on AlAs). The Al–As and Ga–As bonds are aligned in the planes (110) and ($\bar{1}$10), respectively; at the opposite interface, these planes are inverted. (b) Projection of the Al–As and Ga–As chemical bonds in an AlAs/GaAs/AlAs QW onto the ($\bar{1}$10) plane.

(AlGa)As/GaAs/(AlGa)As QWs. In the series of samples investigated, the position of the maximum of the wave function in the QW is controlled by placing a monolayer of InAs at different locations within the GaAs QW of the resonance-tunneling diode. The possibility of modifying the electron wave functions was

Composition of structures B and C

Layers	Structure B	Structure C	Doping level, cm^{-3}
GaAs	0.3 μm	0.3 μm	3×10^{18}
GaAs	50 nm	50 nm	2×10^{17}
GaAs	50 nm	50 nm	Undoped
Al$_{0.4}$Ga$_{0.6}$As	8.3 nm	8.3 nm	Undoped
GaAs	1 nm	5.5 nm	Undoped
InAs	0.3 nm	0.3 nm	Undoped
GaAs	10 nm	5.5 nm	Undoped
Al$_{0.4}$Ga$_{0.6}$As	8.3 nm	8.3 nm	Undoped
GaAs	50 nm	50 nm	Undoped
GaAs	50 nm	50 nm	2×10^{17}
GaAs	0.3 μm	0.3 μm	3×10^{18}
GaAs	Substrate	Substrate	3×10^{18}

used to study the origin of the electron-subband anisotropy in this QW. In a reference sample grown on a (001)-oriented substrate, we observed (in agreement with the results of [3, 5]) anisotropy of the tunneling current along the [110] and [$\bar{1}$10] axes, with the anisotropy direction rotating by 90° when the sign of the bias voltage changed. When the InAs layer is placed at the center of the QW, the electron localization occurring there becomes stronger and, thus, the effect of the interfaces is reduced. In this sample, we observed a fourfold anisotropy along the ⟨100⟩ axes, which corresponds to the effective mass anisotropy of Γ electrons in bulk GaAs. When the InAs layer is placed near one of the interfaces, the electron wave function in the QW concentrates in the vicinity of this interface, whatever the sign of the bias voltage, and a twofold anisotropy along the [110] direction is observed both for positive and negative bias voltages. Thus, we could vary the conditions for band mixing at the GaAs/(AlGa)As interfaces by placing the InAs monolayer at different locations within the GaAs QW. In addition, we studied samples similar to those described above but grown on substrates with the (113) orientation. For structures of this type, we observed a twofold anisotropy along the [$\bar{3}\bar{3}$2] axis, independent of the polarity of the applied bias both for the reference samples and the samples with an InAs monolayer at the center of the QW.
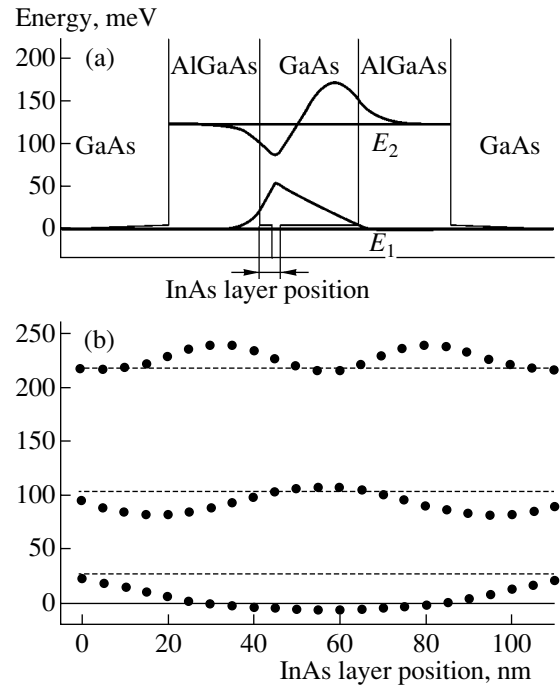
2. SAMPLES

The samples under study were (AlGa)As/GaAs/(AlGa)As resonance-tunneling diodes grown by molecular-beam epitaxy (MBE) on heavily doped n^+-GaAs substrates with (100) and (311)B orientations. Silicon was used as a dopant, and the doping level in the substrate was 2×10^{18} cm^{-3}. Five types of structures, referred to below as A, B, C, D, and E, were investigated. Structure A (a reference sample) was a conventional resonance-tunneling diode with an 11.2-nm-wide GaAs QW placed between two 8.3-nm-thick Al$_{0.4}$Ga$_{0.6}$As barriers. The barriers were separated from the contact regions by 50-nm-thick undoped GaAs layers. Structure B differed from the reference sample in that it included a thin layer of InAs grown within the GaAs QW near the (AlGa)As/GaAs interface. The thickness of this layer (approximately one monolayer) is smaller than the critical value necessary for the formation of self-organized InAs quantum dots [7]. In structure C, the InAs monolayer was placed at the center of the GaAs QW. All three structures (A, B, and C) were grown on (001)-oriented substrates. Structures B and C are described in detail in the table. Structure D was identical to reference structure A and structure E was identical to C, with the exception that they were grown on (311)-oriented substrates. Ohmic contacts were prepared by a successive deposition of AuGa/Ni/Au layers and subsequent annealing at
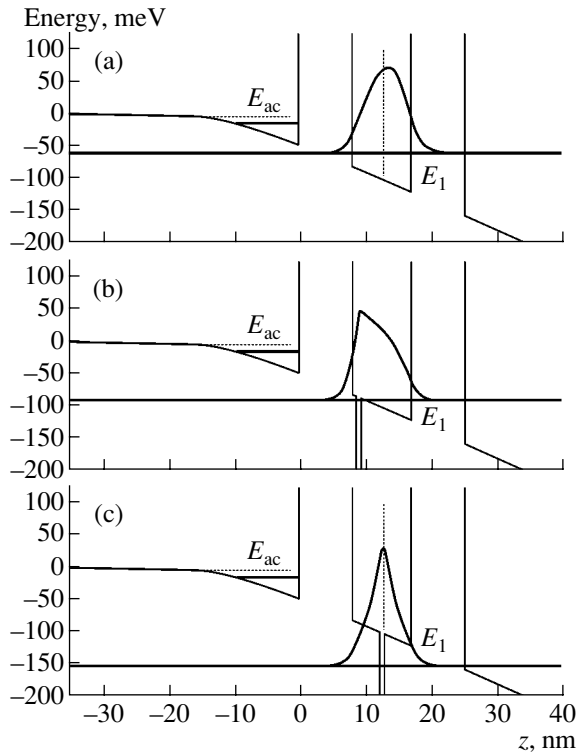
Fig. 2. The profile of the conduction band edge and probability density $|\psi|^2$ for the wave function of the ground state E_1 of the QW (a) in reference sample A, (b) in sample B with an InAs monolayer near the (AlGa)As/GaAs interface, and (c) in sample C with an InAs monolayer at the center of the QW. The calculations are carried out for the bias voltage $V = 300$ mV. The quantum-confinement level E_{ac} in the accumulation layer and the level E_1 in the GaAs QW are also shown.

Fig. 3. (a) The profile of the conduction band edge and wave functions of the ground state E_1 and the first excited state E_2 in a QW of width 11.2 nm. (b) Calculated dependences of the energies of the first three energy levels in an 11.2-nm-wide QW on the position of the InAs monolayer in the QW. The dashed lines indicate the energy levels in the reference sample without an InAs layer.

400°C. Mesa structures with the diameters 50–200 µm were fabricated using conventional chemical etching.

The calculated profiles of the conduction band edge in structures A, B, and C under a bias voltage of $V = 300$ mV are shown in Fig. 2. This bias is sufficient for the formation of a two-dimensional electron accumulation layer in the vicinity of the $Al_{0.4}Ga_{0.6}As$ barrier, and, thus, electron tunneling takes place between this accumulation layer and the two-dimensional subbands in the GaAs QW. The results of self-consistent calculations of the probability density $|\psi|^2$ for the electron ground state in the GaAs QW are also shown in Fig. 2; these calculations were carried out using a numerical method similar to that described in [8]. In samples B and C, the electron band structure of the wide GaAs QW is modified by the presence of the InAs layer, which acts as an additional narrow and deep QW; thus, the wave function of the electron ground state in the GaAs QW becomes localized at this narrow well. This leads to the following difference: in the reference sample (Fig. 2a), the application of the bias $V = 300$ mV causes a displacement of the wave function to the right (the amplitude at the right-hand interface exceeds that at the left-hand interface by about a factor of 2); in sample B, the wave function is always concentrated near the emitter interface, irrespective of the sign of the applied bias (see Fig. 2b). In sample C (see Fig. 2c), the wave function of the electron ground state is always localized near the center of the GaAs QW and the application of bias voltage has only a minor effect on the wave-function amplitude at both interfaces.

Figure 3a shows, for the case of zero bias, the wave functions of the first two electron states in an 11.2-nm-wide GaAs QW containing an InAs layer inserted near the left-hand barrier. In Fig. 3b, the energies of the first three electron states in this QW are plotted as functions of the position of the InAs layer within the well. Qualitatively, these dependences can easily be understood. The energy of the ground electron state is at its lowest when an InAs layer is placed at the center of the QW. In contrast, the energy of the first excited state remains virtually unchanged by the presence of this InAs layer at the center. It can easily be seen from Fig. 3b that an inserted InAs monolayer only has a considerable effect on the quantum-confinement energy levels in the GaAs QW if the monolayer is located near a maximum (or minimum) of the unperturbed electron wave function in this QW. Thus, by inserting a monolayer of a narrow-gap semiconductor at different positions in the

Current, 10^{-6} A
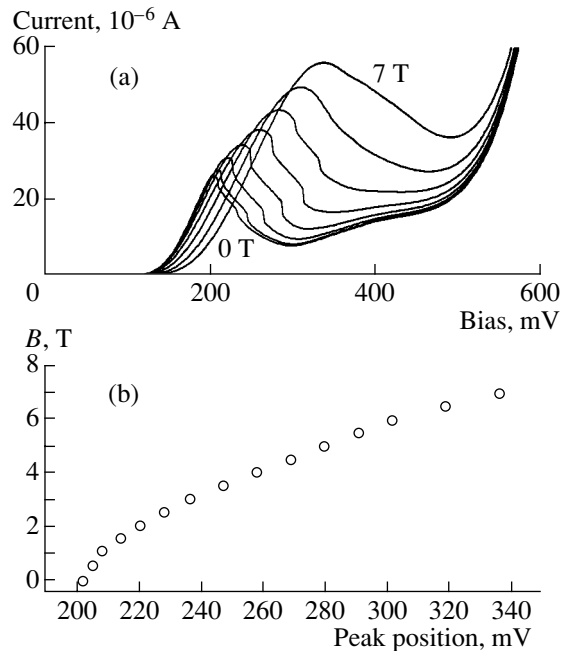
Fig. 4. (a) The *I–V* characteristics of sample B at 4.2 K in a magnetic field perpendicular to the tunneling current. The field was applied in the plane of the QW along the [110] direction and was varied from 0 to 7 T in increments of 1 T. (b) The bias voltage corresponding to the current peak in the *I–V* characteristics of sample B as a function of the magnetic field.

GaAs QW, it is possible to control both the wave functions and the subband energies in this QW in a wide range. We experimentally observed that the ground-state energy in a GaAs QW varies upon the insertion of an InAs layer at different positions within the well. In particular, in sample C (where the InAs layer is located at the center of the QW), the energy of the quantum-confinement level is lower than the Fermi energy in the emitter, which means that, even at zero bias, this level is in resonance with the occupied electron states in the contacts. For sample A (the reference sample) and sample B (where the InAs layer is located near the barrier), the application of a bias voltage of ~100 mV is necessary for the observation of a current resonance corresponding to the tunneling through the ground state in the QW.

3. EXPERIMENTAL

In order to determine the in-plane dispersion relation $E(k_\parallel)$, we used magnetotunneling spectroscopy, a technique described in detail in [3–6, 9, 10]. As a certain bias voltage V_P is applied to a resonance-tunneling diode, electrons in the emitter contact appear to be in resonance with the lowest quantum-confinement level E_1 in the QW and a tunneling-current peak is observed in the diode $I(V)$ curve (Fig. 4a). When a magnetic field B is applied parallel to the QW plane (i.e., normally to the

tunneling current), electrons tunneling from the emitter into the QW over the distance Δs acquire the additional in-plane quasi-momentum $\Delta k_\parallel = eB\Delta s$ in the direction normal both to the current and magnetic field. Since, in the absence of scattering, the quasi-momentum is conserved, the peak in the tunneling current appears at higher bias voltages as the magnetic field is increased, with the resulting shift ΔV_P of the resonance position being proportional to $E(k_\parallel)$. By changing the orientation of the magnetic field in the plane of the QW, we can examine the electron-subband anisotropy in this plane.
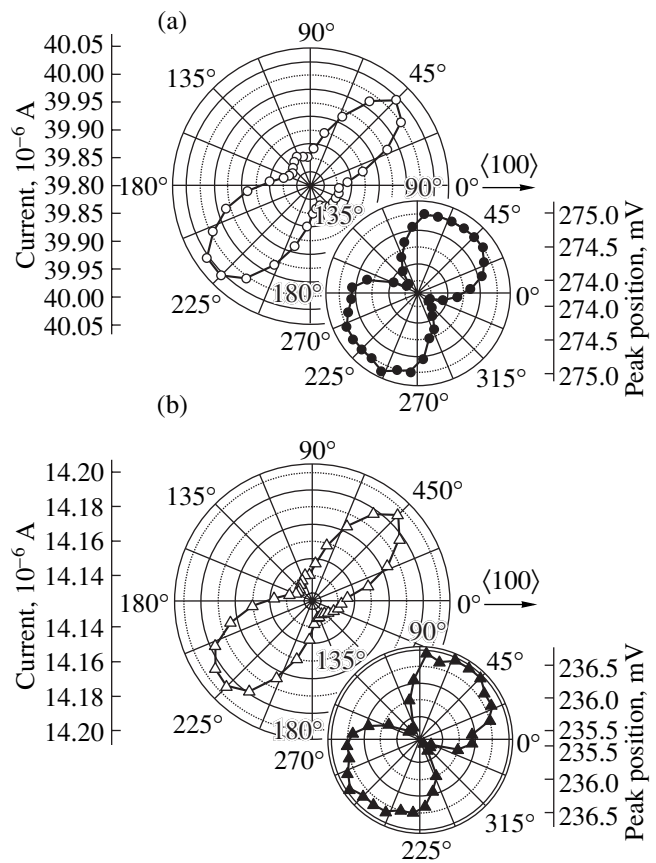
The current–voltage characteristics of sample B when under a magnetic field applied normally to the current are shown in Fig. 4a. The measurements were carried out at the sample temperature of 4.2 K. The field was varied from 0 to 7 T and was oriented in the plane of the QW along the [100] direction. As the magnetic field increases, the resonance-current peak corresponding to tunneling through the quantum-confinement level E_1 broadens and shifts towards higher voltages. The shift ΔV_P of the resonance position varies approximately in proportion to B^2 (see Fig. 4b), in accordance with the parabolic dispersion relation for electrons in the QW, since $\Delta k_\parallel \propto B$ [5, 9]. As the magnetic field is rotated in the QW plane, the peak current I_P and the resonance position V_P change in a correlated manner, i.e., the highest current and largest shift of the resonance position are observed for the same orientation of the field. Note, however, that the peaks in the *I–V* characteristics are strongly broadened in the magnetic field and that the value of the peak amplitude I_P can be measured more accurately than the peak position on the bias-voltage axis [4, 5, 10]. Typical experimental dependences of the current peak amplitude I_P and the resonance position V_P on the orientation of the magnetic field ($B = 5$ T) in the QW plane for reference sample A under forward and reverse biases are shown in Fig. 5. The observed anisotropy of the tunneling current was $\Delta I/I \approx 0.4\%$, and the anisotropy direction changed by 90° as the sign of the bias voltage was changed. The anisotropy in the resonance position V_P, which reflects the effective mass anisotropy of the electrons in the QW, had approximately the same magnitude. In Fig. 5, 0° corresponds to the [100] direction; therefore, the main axes of the observed anisotropy correspond to the $\langle 110 \rangle$ directions. In agreement with [5], the anisotropy axes for the two different polarities of the bias voltage are orthogonal to each other. These experimental results reflect a variation in the electron energy at a constant value of $k_\parallel$ and indicate that the constant-energy surfaces of the electron subbands in the QW are anisotropic. The anisotropy axes correspond to the $\langle 110 \rangle$ directions, which are orthogonal to the planes containing Al–As and Ga–As chemical bonds at opposite interfaces of the QW. As noted above, the electron ground-state
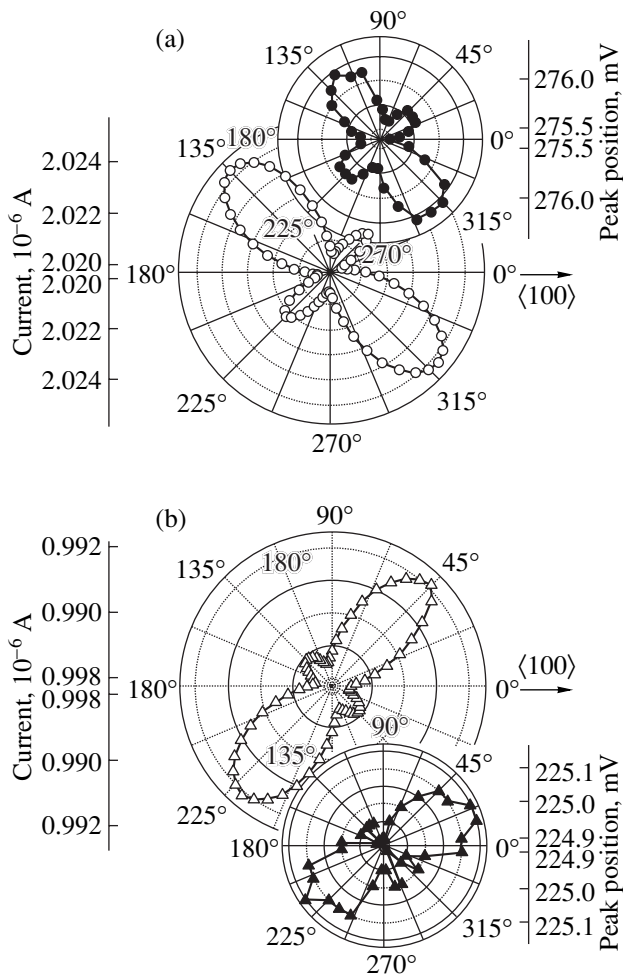
Fig. 5. Dependences of the bias-voltage position and amplitude of the tunneling-current peak associated with the E_1 resonance in reference sample A on the orientation of the magnetic field in the plane of the QW. Diagram (a) corresponds to the forward bias and diagram (b), to the reverse bias. The magnetic field equals 5 T, and the sample temperature is 4.2 K.

Fig. 6. Anisotropy of the bias-voltage position and amplitude of the tunneling-current peak associated with the E_1 resonance in sample B (with an InAs monolayer in the vicinity of the (AlGa)As/GaAs interface) with respect to the orientation of the magnetic field in the plane of the QW. Diagram (a) corresponds to the forward bias and diagram (b), to the reverse bias. The magnetic field equals 5 T, and the sample temperature is 4.2 K.

wave function in the QW is concentrated near one of the interfaces, depending on the sign of the applied bias.

Figure 6 shows the experimental dependences of I_P and V_P on the orientation of the magnetic field in the QW plane for sample B, where the InAs monolayer is grown near the (AlGa)As/GaAs interface in the GaAs QW. In this sample, a pronounced twofold anisotropy was also observed, but the reversal of the sign of the bias voltage did not change the direction of the main anisotropy axis. This result can be qualitatively understood from Fig. 2b. Due to the presence of the InAs layer, the wave function is concentrated near the emitter interface and, thus, is only very weakly affected by the application of positive bias voltages up to 500 mV. For bias voltages in the range of the E_1 resonance, the ground-state wave function in the QW is concentrated near the emitter interface, irrespective of the bias polar-

ity, and, thus, it is this (AlGa)As/GaAs interface that determines the anisotropy. Note, however, that the application of an electric field, which causes the polarization of the chemical bonds, is still necessary for the appearance of the anisotropy.

Figure 7 shows the experimental results for sample C, in which the InAs monolayer is grown at the center of the GaAs QW. In this sample, the energy E_1 of the quantum-confinement level is lower than the Fermi energy in the emitter, which means that, in the absence of a magnetic field, a resonance for this level exists even for a zero bias voltage. However, in a magnetic field of 8 T, the resonance-peak position shifts by about 150 mV. In analogy with the two previous cases, 0° in Fig. 7 corresponds to the orientation of the magnetic field along the [100] direction. Figures 7a and 7b illustrate the anisotropy of the amplitude of the resonance peak in the conductance G with respect to the orientation of the magnetic field in the QW plane, and Figure 7c
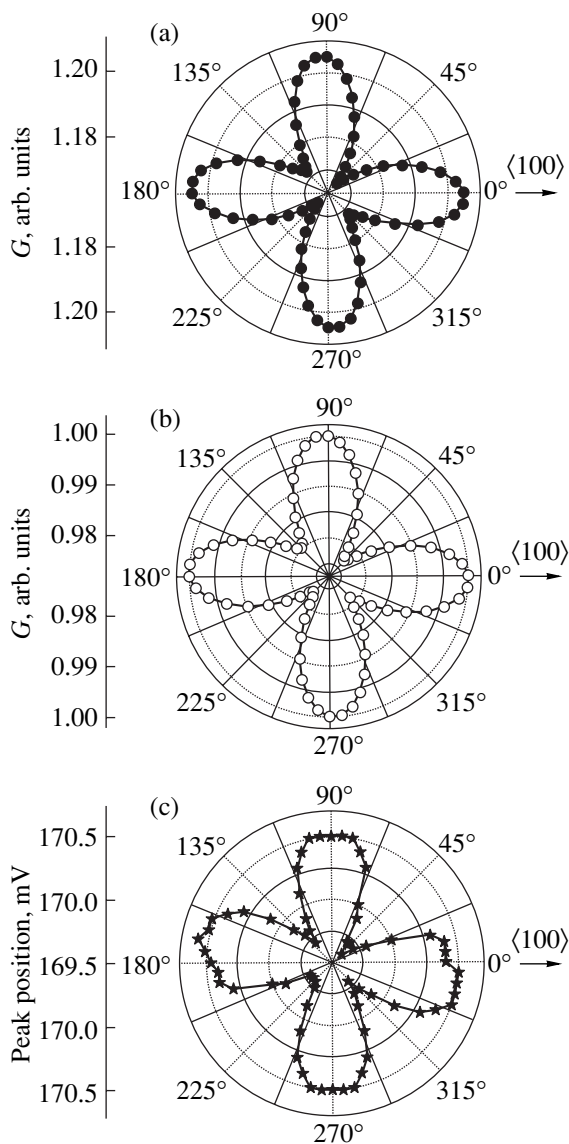
Fig. 7. Anisotropy of the bias-voltage position and the amplitude of the conductance peak in sample C (with an InAs monolayer at the center of the QW) with respect to the orientation of the magnetic field in the plane of the QW. Diagrams (a) and (c) correspond to the forward bias and diagram (b), to the reverse bias. The magnetic field equals 8 T, and the sample temperature is 4.2 K.

illustrates the anisotropy of the bias-voltage position of the E_1 resonance. The magnitude of the effective mass anisotropy for sample C is ~0.5%. One can see three major differences in the anisotropy pattern of this sample in comparison with samples A and B. First, a four-fold rather than a twofold anisotropy is observed. Second, the main axes of the anisotropy correspond to the [100] and [010] directions, instead of to the [110] and [$\bar{1}$10] directions (as is the case for samples A and B). Third, a change in the sign of the bias voltage has no effect on the observed anisotropy.

We believe that the dependence of the anisotropy on the sign of the applied bias voltage disappears due to localization of the wave function of the QW ground state at the center of this QW, as is illustrated in Fig. 2c. It can be seen from Fig. 2c that, even under a fairly high bias voltage (300 mV in this case), there is no large shift of the maximum of the wave function from the center of the QW. Furthermore, comparing Figs. 2a and 2c, it can clearly be seen that the amplitude of the wave function at the QW interfaces in sample C is much smaller than that in sample A. Thus, it can be concluded that the effect of heterointerfaces on the anisotropy in sample C is much less important than in samples A and B. The fourfold symmetry of the anisotropy with the axes normal to the planes of the cubic unit cell is consistent with theoretical views on electron effective-mass anisotropy near the Γ point in bulk GaAs [11]. Therefore, we can conclude that, for the sample with an InAs monolayer located at the center of the GaAs QW, the observed anisotropy of the dispersion relation originates from the anisotropy of bulk GaAs and is completely unconnected to the interfaces. This conclusion is corroborated by the results reported in [12], where magnetotunneling spectroscopy was used to investigate resonance-tunneling diodes without an inserted InAs layer but with a very wide GaAs well (120 nm). In that study, no effect of the interfaces on the anisotropy of the effective mass of the electrons confined in the QW was found, and a fourfold anisotropy with the axes along the [100] and [010] directions (typical of bulk GaAs) was observed.

Along with resonance-tunneling structures grown on (001)-oriented substrates, we investigated those grown on substrates with the (113)B orientation. In recent years, studies of heterostructures grown on high-index surfaces have been the focus of considerable interest. For example, a GaAs (113)B surface was successfully used for growing heterostructures with quantum dots [4, 13, 14], and a two-dimensional hole gas with unprecedentedly high mobility was obtained on a GaAs (113)A surface. The nontrivial properties of high-index surfaces are related both to changes in the band structure and to the conditions of heterostructure growth on these surfaces. Until now, the atomic structure of (113)-oriented surfaces has been poorly understood. In addition, according to one opinion, high-index surfaces grown by MBE are unstable with respect to faceting into low-index planes [15]. However, the data obtained in [16] by scanning tunneling microscopy and low-energy electron diffraction indicate that the GaAs (113)B surface is highly anisotropic and consists of relatively large flat terraces extended along the [$\bar{3}\bar{3}2$] axis, which is one of the principal crystallographic directions on this surface.

We investigated two resonance-tunneling heterostructures grown on GaAs (113)B substrates. The layer
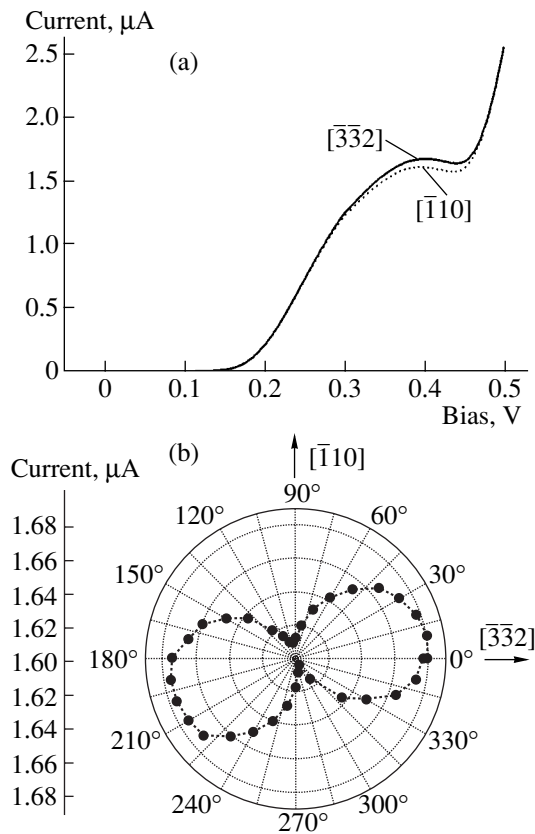
Fig. 8. (a) The current–voltage characteristics of sample D (the reference sample grown on a (113) substrate) at 4.2 K in a magnetic field of 8 T perpendicular to the tunneling current. The field was applied in the plane of the QW along the directions $[\bar{1}10]$ (dotted line) and $[\bar{3}\bar{3}2]$ (solid line). (b) Anisotropy of the tunneling current in a structure of type D.

composition of structure D was the same as that of reference sample A (see table), and structure E was the same as sample C with an InAs layer at the center of the QW. For both types of structures (the reference samples as well as the samples with the InAs monolayer), we observed a twofold anisotropy along the $[\bar{3}\bar{3}2]$ axis, irrespective of the polarity of the applied bias (see Fig. 8). It should be noted that the anisotropy of the tunneling current in the samples grown on the (113)B surface was an order of magnitude higher than in similar samples grown on the (001) surface and amounted to ~5%. However, due to the current lack of understanding of the properties of high-index GaAs surfaces, at this moment, we are unable to conclude whether the observed anisotropy in the tunneling current is related to the interface morphology or to the anisotropy of the conduction band in the QWs on the (113)B surface.

4. CONCLUSIONS

Thus, we investigated electron magnetotunneling in double-barrier GaAs/(AlGa)As structures grown on (001)-oriented substrates. The results obtained provide information on the anisotropy of the electron subbands in GaAs QWs. Insertion of an InAs monolayer at different positions within the GaAs QW was used to modify the electron wave functions and study the nature of the electron subband anisotropy in these QWs. In the reference sample, an anisotropy of the tunneling current along the [110] and [$\bar{1}$10] axes was observed, and the anisotropy direction rotated by 90° as the sign of the bias voltage was reversed. The observed anisotropy can be understood in terms of the difference in the electron-subband mixing [5] at the GaAs/(AlGa)As and (AlGa)As/GaAs interfaces at opposite sides of the GaAs QW. When an InAs layer is placed at the center of the QW, electron localization at the center of the QW increases and, thus, the effect of the interfaces is reduced. The fourfold anisotropy along the ⟨100⟩ axes observed in sample C corresponds to the effective mass anisotropy of Γ electrons in bulk GaAs. When an InAs layer is placed near one of the QW interfaces, the electron wave function is concentrated in the vicinity of that interface, irrespective of the polarity of the bias voltage; thus, we observe a twofold anisotropy along the [110] axis under both positive and negative biases. Finally, we investigated samples similar to those described above but grown on (113)B-oriented substrates. In these structures, we observed a twofold anisotropy along the [$\bar{3}\bar{3}$2] axis, which was independent of the polarity of the applied bias both for the reference samples and for the samples with an InAs monolayer at the center of the QW. The origin of this anisotropy currently remains unclear.

REFERENCES

1. M. P. Lilly, K. B. Cooper, J. P. Eisenstein, *et al.*, Phys. Rev. Lett. **82**, 394 (1999).

2. R. J. Warburton, J. G. Michels, R. J. Nicholas, *et al.*, Phys. Rev. B **46**, 13394 (1992).

3. T. Reker, H. Im, H. Choi, *et al.*, in *Proceedings of International Conference on the Physics of Semiconductors, Osaka, 2000*, Ed. by N. Miura and T. Ando (Springer, Berlin, 2001), p. 827.

4. E. E. Vdovin, Yu. N. Khanin, A. V. Veretennikov, *et al.*, Pis'ma Zh. Éksp. Teor. Fiz. **74**, 43 (2001) [JETP Lett. **74**, 41 (2001)].

5. T. Reker, H. Im, L. E. Bremme, *et al.*, Phys. Rev. Lett. **88**, 056403 (2002).

6. E. E. Vdovin, Yu. N. Khanin, Yu. V. Dubrovskii, *et al.*, Phys. Rev. B **67**, 205305 (2003).

7. J.-Y. Marzin, J.-M. Gerard, A. Izrael, *et al.*, Phys. Rev. Lett. **73**, 716 (1994).

8. H. Tan, G. L. Snider, L. D. Chang, and E. L. Hu, J. Appl. Phys. **68**, 4071 (1990).

9. R. K. Hayden, D. K. Maude, L. Eaves, *et al.*, Phys. Rev. Lett. **66**, 1749 (1991).

10. U. Gennser, V. P. Kesan, D. A. Syphers, *et al.*, Phys. Rev. Lett. **67**, 3828 (1991).

11. U. Rossler, Solid State Commun. **49**, 943 (1984).

12. O. H. Hughes, M. Henini, E. S. Alves, *et al.*, J. Vac. Sci. Technol. **7**, 1041 (1989).

13. E. E. Vdovin, A. Levin, A. Patané, *et al.*, Science **290**, 122 (2000).

14. A. Patane, R. J. A. Hill, L. Eaves, *et al.*, Phys. Rev. B **65**, 165308 (2002).

15. J. Platen, A. Kley, C. Setzer, *et al.*, J. Appl. Phys. **85**, 3597 (1999).

16. J. Marquez, L. Geelhaar, and K. Jacobi, Phys. Rev. B **62**, 9969 (2000).

Translated by M. Skorikov

A Quasi-Hydrodynamic Simulation of Electrical Conductivity in Selectively Doped Submicrometer-Sized Layered Structures and Island Films in High Electric Fields

V. A. Gergel', Yu. V. Gulyaev, V. A. Kurbatov, and M. N. Yakupov^

Institute of Radio Engineering and Electronics, Russian Academy of Sciences, ul. Mokhovaya 18, Moscow, 125009 Russia
^e-mail: yamt@mail.ru
Submitted July 15, 2004; accepted for publication August 9, 2004

Abstract—Mathematical simulation is used to study special features of the high-field drift of electrons that occurs in submicrometer-sized n^+–n–n^+ structures with an appreciable impurity-concentration profile in the their high-resistivity region. A quasi-hydrodynamic description of the electron drift is used. In this description, the dependences of the charge-carrier mobility and energy-relaxation time on the electron temperature, the thermodiffusion component of the electron flow, and the divergence of the electron-temperature flux are taken into account. It is shown that sectioning of the high-resistivity carrier-flight n-type region by additional low-resistivity n^+-type inclusions with submicrometer thickness appreciably reduces the electron-gas temperature and increases the effective mobility of the charge carriers and, consequently, the high-field electrical conductance of the structure owing to a corresponding increase in the drift velocity. © 2005 Pleiades Publishing, Inc.

It was shown in [1] that, in semiconductor structures represented by a series of alternating high- and low-resistivity layers with a thickness on the order of 100 nm, the electrical heating of charge carriers is largely suppressed owing to the effective cooling of the carriers in the low-resistivity interlayers, where the electric-field strength is comparatively low. A corresponding decrease in the electron-gas temperature (compared with the situation in structures with a homogeneous flight region) inhibits thermal degradation of the carrier mobility and ensures both the attainment of drift velocities that appreciably exceed the saturation velocity and a corresponding increase in the electrical conductance of the structure. However, it is worth noting that an analysis of the drift process and the corresponding numerical estimations [1] were performed on the basis of a simplified hydrodynamic description that was initially suggested in [2]. In this description, only the drift component of the current and the convective component of the heat flow are taken into account. It was found that this approximation was justified when applied to the high-resistivity regions of the structures under consideration and yielded the expected appreciable decrease in the electron temperature (as compared to the steady-state value $\sim e\mu\tau E^2$) if the thickness of the high-resistivity regions was much smaller than the so-called thermal length $\mu\tau E$, where μ is the charge-carrier mobility and τ is the energy-relaxation time. However, the applicability of this approximation to the low-resistivity regions, where there is a comparatively low electric field and the expected cooling of the electron gas occurs, is debatable, as it yields an overly optimistic estimate of the thickness of the low-resistivity regions required for efficient cooling of the hot charge carriers.

Since the effect of the ultrafast electron drift under consideration is of much interest from the purely academic and (possibly) application-oriented standpoints, we considered it important to offer a more convincing physical substantiation of this effect in the context of a complete quasi-hydrodynamic model of the charge-carrier drift in a high electric field. This model involves the following power-law (for simplicity) dependences of the carrier mobility μ and the energy-relaxation time on the electron temperature:

$$\mu = \mu_0\left(\frac{T_0}{T}\right)^\alpha, \quad \tau_e = \tau_0\left(\frac{T}{T_0}\right)^{1-\alpha}, \quad (\alpha = 1, 0.5). \quad (1)$$

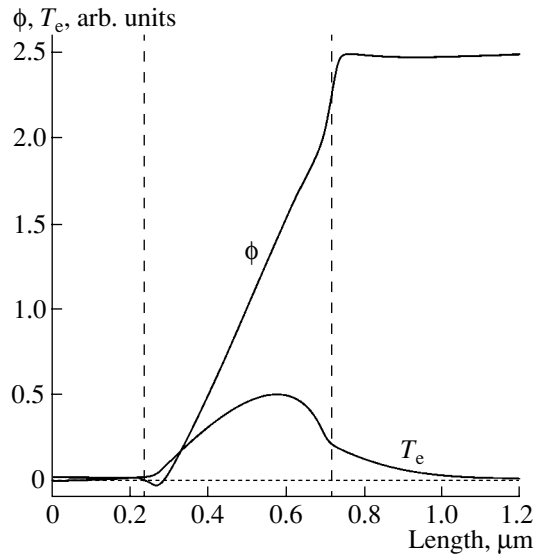In addition, it involves the thermodiffusion component of the electron flow

$$j_n = \mu_\alpha n\left[\frac{d\phi}{dx} - (1-\alpha)\frac{dT}{dx}\right] - \mu_\alpha T\frac{dn}{dx}; \quad (2)$$

and the divergence of the electron-temperature flux

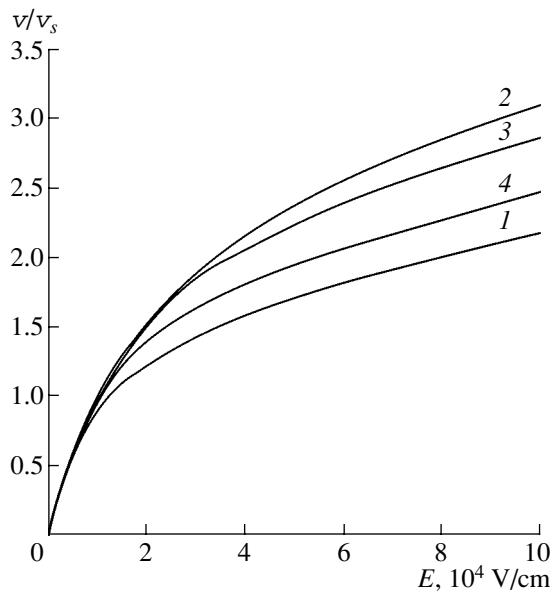$$j_T = \left(\frac{5}{2} - \alpha\right)\left(-\mu_\alpha nT\frac{dT}{dx} + j_n T\right). \quad (3)$$

The corresponding system of model equations (by analogy with the pioneering study by Stratton [3]) can be written as

$$\begin{cases} \dfrac{d^2\phi}{dx^2} = \dfrac{(N_D - n)}{L_D^2}\dfrac{T_0}{N_D^+}, \\[2mm] \dfrac{dj_n}{dx} = 0, \\[2mm] \dfrac{dj_T}{dx} = j_n\dfrac{d\phi}{dx} - \dfrac{n(T - T_0)}{\tau}, \end{cases} \quad (4)$$

Fig. 1. Distributions of the potential ϕ and electron temperature T_e in a reference n^+–n–n^+ structure with $L = 0.48$ μm. The voltage applied to the structure was $V = 2.5$ V.

Fig. 2. Calculated current–voltage characteristics of the structures studied: (*1*) a reference 0.48-μm-thick structure and (*2–4*) structures consisting of three 160-nm-thick n-type layers separated by n^+-type interlayers with a thickness of (*2*) 160, (*3*) 80, and (*4*) 40 nm.

where

$$L_D = \sqrt{\frac{\varepsilon_0 \varepsilon_s T_0}{e N_D^+}}$$

is the Debye length. The model used and the algorithm for its numerical implementation will be described in more detail in our next publication [4]. The latter is

concerned with simulation of the drift process in a conventional n^+–n–n^+ silicon structure with a uniform impurity concentration in the n-type region.

First, we consider the results of simulating the drift process in a reference n^+–n–n^+ structure with the thickness of its uniformly doped ($N_D = 10^{18}$ cm^{-3}) region $L = 0.48$ μm ($N_D^+ = 1.1 \times 10^{19}$ cm^{-3} in low-resistivity contact regions). The distributions of the potential ϕ and electron temperature T_e shown in Fig. 1 and obtained using the numerical procedure developed in [4] correspond to the typical voltage $V = 2.5$ V applied to the structure. These dependences indicate that a significant fraction of the electron thermal energy acquired in the high-resistivity flight region L is dissipated in the lattice in the low-resistivity contact region. Simultaneously, the electron temperature T_e in the high-electric-field region is effectively decreased, which reduces the mobility degradation. As a result, the charge-carrier velocity in the high-electric-field region continues to increase as the voltage increases and does not level off, a fact illustrated by curve *1* in Fig. 2, where the calculated current–voltage (*I–V*) characteristics are shown as plots of the relative mean velocity $v/v_s = j_n/nv_s$ versus the mean field $E = V/0.48 \times 10^4$. *I–V* characteristics *2–4* in Fig. 2 were calculated for the structures that each contained three high-resistivity regions with $L = 160$ nm separated by low-resistivity interlayers with a thickness of (*2*) 160, (*3*) 80, and (*4*) 40 nm.

We now turn directly to a substantiation of the previously suggested [1] sectioning of the flight region as a method for increasing the effective drift velocity. To this end, we divide this region into three parts, each with a thickness of 0.16 μm, by introducing n^+-type interlayers with the same thickness. We assume that an additional cooling of the electron gas in the low-resistivity inclusions brings about an appreciable decrease in the electron temperature and, furthermore, a corresponding increase in both the local electron mobility and effective velocity of the electron flow. The results of a corresponding simulation (see Fig. 2, curve *2*; Fig. 3, curve *2*) clearly indicate that the approach formulated above is reasonable.

In order to assess the required thickness of the separating low-resistivity layers for effective cooling of the electron gas, we performed similar calculations for structures with thinner n^+-type inclusions of 80 and 40 nm (see curve *3*, *4* in Figs. 2, 3). These data show that the mean drift velocity of the electrons remains reasonably high, even in the layered structures with comparatively thin n^+-type interlayers, where the additional thermal energy acquired by the electrons in the high-resistivity layers has no time to relax completely. This circumstance makes it possible to assess the thickness of the "cooling" n^+-type interlayers required to appreciably increase the electron drift velocity at approximately 50–100 nm.

It is clear that a similar increase in the drift velocity of the charge carriers should also take place in island-film structures if the electrical conductivity of the
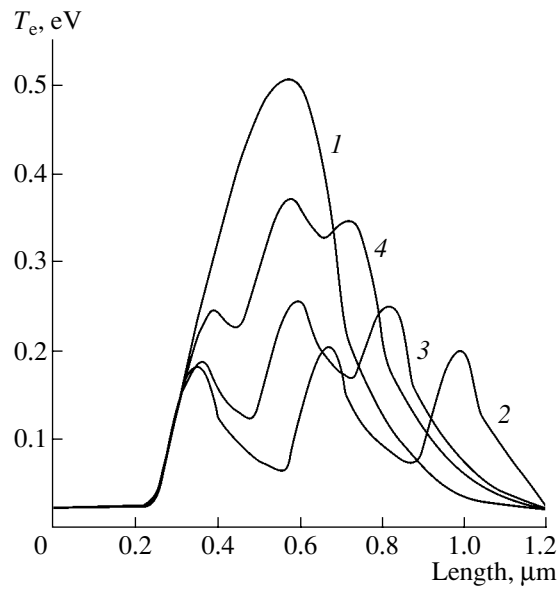
Fig. 3. Typical distributions of the electron temperature T_e at $V = 2.5$ V in test structures *1–4* (see Fig. 2 for details).

islands exceeds that of the matrix as a result of either the additional doping or the given mismatch of the energy bands. We believe that the considered structures with submicrometer-sized high-conductivity inclusions are promising for reducing the response time of field-effect and bipolar transistors.

REFERENCES

1. V. A. Gergel', Yu. V. Gulyaev, A. P. Zelenyǐ, and M. N. Yakupov, Fiz. Tekh. Poluprovodn. (St. Petersburg) **38**, 237 (2004) [Semiconductors **38**, 232 (2004)].
2. V. A. Gergel', V. G. Mokerov, M. V. Timofeev, and Yu. V. Fedorov, Fiz. Tekh. Poluprovodn. (St. Petersburg) **34**, 239 (2000) [Semiconductors **34**, 233 (2000)].
3. R. Stratton, Phys. Rev. **126**, 2002 (1962).
4. V. A. Gergel', Yu. V. Gulyaev, and M. N. Yakupov, Fiz. Tekh. Poluprovodn. (St. Petersburg) (in press).

Translated by A. Spitsyn

LOW-DIMENSIONAL SYSTEMS

The Exciton Photoluminescence and Vertical Transport of Photoinduced Carriers in CdSe/CdMgSe Superlattices

I. I. Reshina^, S. V. Ivanov, D. N. Mirlin, I. V. Sedova, and S. V. Sorokin

Ioffe Physicotechnical Institute, Russian Academy of Sciences, Politekhnicheskaya ul. 26, St. Petersburg, 194021 Russia
^e-mail: reshina@dnm.ioffe.rssi.ru
Submitted September 7, 2004; accepted for publication September 17, 2004

Abstract—The photoluminescence and photoluminescence excitation spectra, phonon-related Raman scattering, and vertical transport of photoinduced carriers and excitons along the growth direction in type I low-strained CdSe/CdMgSe superlattices, which are grown on InAs substrates using molecular-beam epitaxy, are studied for the first time. The studies are carried out at various temperatures and excitation intensities. The vertical transport is studied by a purely optical method involving an enlarged quantum well built in into the superlattice. This well serves as a sink for the excitons and charge carriers tunneled through the superlattice. At 2–150 K, the carriers are preferentially transported by free excitons. However, in superlattices with periods of 5.9 and 7.3 nm, this transport is not of the Bloch type. A comparison of the calculated energies of the band-to-band transitions in the superlattices with the experimental data yields the relative magnitude of the valence-band offset in the range 0.4–0.5. The Raman spectra indicate that the behavior of optical phonons in CdMgSe is bimodal. © 2005 Pleiades Publishing, Inc.

1. INTRODUCTION

In this study, we completed the first examination of the photoluminescence (PL) and photoluminescence excitation (PLE) spectra, vertical transport of charge carriers and excitons, and Raman scattering in CdSe/CdMgSe superlattices (SLs). To our knowledge, the optical and structural properties of type I SLs with CdSe quantum wells (QWs) have not previously been studied because of the absence of corresponding structures. It is known that even thin (thinner than one monolayer) CdSe layers transform into quantum-disc structures of a mixed composition (CdZnSe) during the growth of ZnSe/CdSe heterostructures, due to the existance of a large lattice mismatch (7%) [1]. We have previously studied the PL and Raman scattering in similar quantum-disc structures [2, 3], and the PL of type II QW CdSe/ZnTe structures, grown on a GaAs substrate and ZnTe buffer layer, have also been investigated [4]. It has also been shown that type I low-strained sphalerite CdSe/CdMgSe structures can be grown by molecular-beam epitaxy (MBE) on InAs substrates [5].

Recently, it has been suggested that these materials be a key element of a new type of III–V/II–VI hybrid laser diode for the middle-infrared (IR) spectral region. Such laser heterostructures, which include an active InAs layer between AlAsSb and Cd(Mg)Se layers, have recently been grown by MBE. In these structures, the pulsed generation of light with a wavelength of 2.78 μm was observed at temperatures as high as 100 K [6]. The formation of a perfect heterovalent boundary between InAs and Cd(Mg)Se is the main condition for the fabrication of IR lasers operating at elevated temperatures.

Thus, it is of both academic and practical interest to study the optical properties of the new CdMgSe alloys and CdSe/CdMgSe superlattices grown on InAs substrates and, in particular, the vertical transport of charge carriers and excitons across such superlattices along the growth axis. In this study, we used a purely optical method to examine the vertical transport of charge carriers and excitons that involved a comparison of the intensities of the PL from the superlattice and from the enlarged quantum well (EQW), which was built into the superlattice. This method was suggested for the first time in [7].

2. EXPERIMENTAL

Using the MBE method, we fabricated three CdSe/Cd$_{1-x}$Mg$_x$Se SLs, whose parameters are given in Table 1. The SLs included 40 periods and a CdSe EQW 100 Å wide, which was grown in a central part and served as a sink for the photoinduced carriers transported vertically across the SL.

InAs substrates, which were preliminarily passivated in a Na$_2$S solution, were placed into a III–V MBE chamber, where they were sequentially annealed under an As$_4$ flux at up to 480°C until a pronounced (2 × 4) reconstruction of the surface was attained. Then, the substrates were transported under vacuum into a II–VI growth chamber, where the CdMgSe compounds were grown after their growth had been initiated in the epitaxy mode with an enhanced atomic migration [8]. A CdMgSe layer 0.3 μm thick was grown at 280°C; followed by 40 periods of the CdSe/CdMgSe SL and the CdSe EQW; and, finally, a CdMgSe layer 0.1 μm thick

Table 1. Parameters of the CdSe/Cd$_{1-x}$Mg$_x$Se superlattice (SL), comparison of the splitting energies for the heavy and light excitons, and differences in the calculated energies of the intersubband transitions e–hh and e–lh

SL	d_w, nm/d_b, nm	x	Experimental $E_{lh} - E_{hh}$, meV	Calculated ΔE, E_B					
				Q	ΔE, meV	E_B, meV	Q	ΔE, meV	E_B, meV
1–235	3.65/3.65 (3.4/3.9)	0.23 (0.22)	37	0.40	37.2	25.4	0.3	28.5	31.0
1–106	2.95/2.95 (2.7/3.2)	0.16 (0.175)	34	0.45	32.5	21.4	0.3	20.0	31.2
1–105	1.85/1.85 (1.85/1.85)	0.18 (0.175)	22	0.50	22.8	19.2	0.3	10.7	30.2

Note: The values used in the calculation that yield the best agreement with the experiment are parenthesized. $\Delta E = E(e - lh) - E(e - hh)$, $E_B = E(e - hh) - E_{hh}$. Q is the relative valence-band offset.

and a CdSe layer 50 Å thick. The state of the surface during growth was monitored by reflection high-energy electron diffraction. The SL period, the average Mg concentration in the SL, and the Mg concentration in the cladding layers were determined from X-ray diffraction measurements. As a result, when the Mg concentration in the barriers and cladding layers was identical, we were able to simultaneously determine the layer thickness of the well (d_w) and the barrier (d_b). For two of the SLs with smaller periods, the thicknesses of the well and barrier layers were determined independently using transmission electron microscopy.

The PL and Raman spectra were measured using spectrometers with the double monochromators Jobin Ivon U-1000 and DFS-24, which had a dispersion of 2.4 and 5 Å/mm, respectively. The detection was carried out using cooled photomultipliers in the photon-counting mode, which were based on GaAs and FÉU-79, respectively. The spectra were excited using a He–Ne laser with the photon energy $E_{exc} = 1.96$ eV and an Ar$^+$ laser with the photon energies $E_{exc} = 2.54$ and 2.41 eV.

The PLE spectra were recorded using an SDL-2 setup involving an MDR-23 monochromator with a dispersion of 13 Å/mm to measure the PL and an MDR-12 monochromator with a dispersion of 24 Å/mm to excite the PL. A halogen lamp served as the excitation source. The reflection spectra in the excitonic region were measured using the same setup. In this case, the sample was directly exposed to the focused light of the halogen lamp.

During the measurements, the sample was placed in an evacuated He cryostat in He vapor or in a He cryostat with a copper finger, in which the sample temperature was $T \approx 30$ K.

3. RESULTS AND DISCUSSION

3.1. Luminescence Spectra

The PL spectra of the SLs were measured at temperatures ranging from 2.2 to 100 K at various excitation intensities. The excitation energy was higher than the SL band gap. Figure 1 shows the PL spectrum for an SL with the period $d_w + d_b = 5.9$ nm. At liquid-helium temperature, six peaks were observed in the spectrum.

From the results of measurements at various temperatures, these peaks were identified with the lines of the localized and free excitons in the EQW and the SL, as well as two donor–acceptor bands (D–A). This interpretation is based on the fact that the relative intensity of the peaks attributed to localized excitons and donor–acceptor recombination decreases as the temperature increases. The donor–acceptor peak shifts to higher frequencies and is narrowed as the pump intensity increases. Such behavior is characteristic of donor–acceptor pairs and is associated with the saturation of
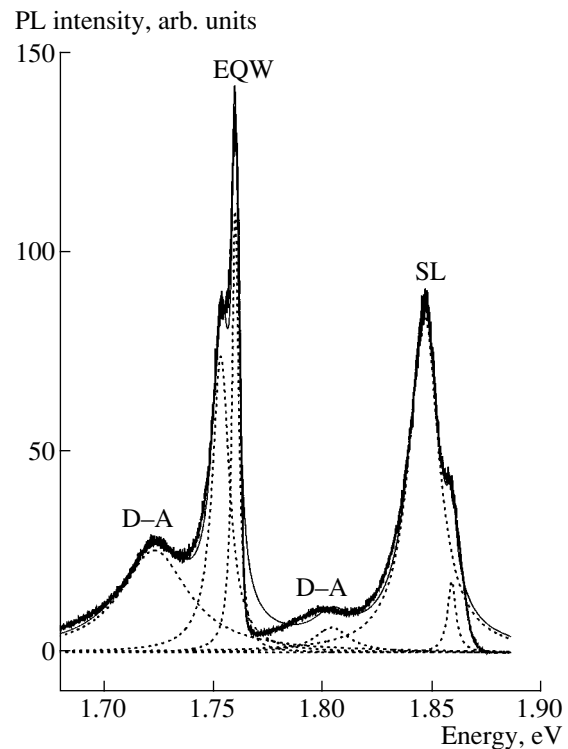
Fig. 1. The photoluminescence (PL) spectrum of the superlattice (SL) (2.95/2.95) nm. $T = 2$ K and $E_{exc} = 1.96$ eV. The dotted curves denote the lines of free and localized excitons in the enlarged quantum well (EQW, region of 1.75 eV) and superlattice (SL, region of 1.85 eV), and the bands of the donor–acceptor pairs (D–A, 1.72 and 1.8 eV). These lines are found by decomposing the spectrum. The thin solid line shows the experimental spectrum.
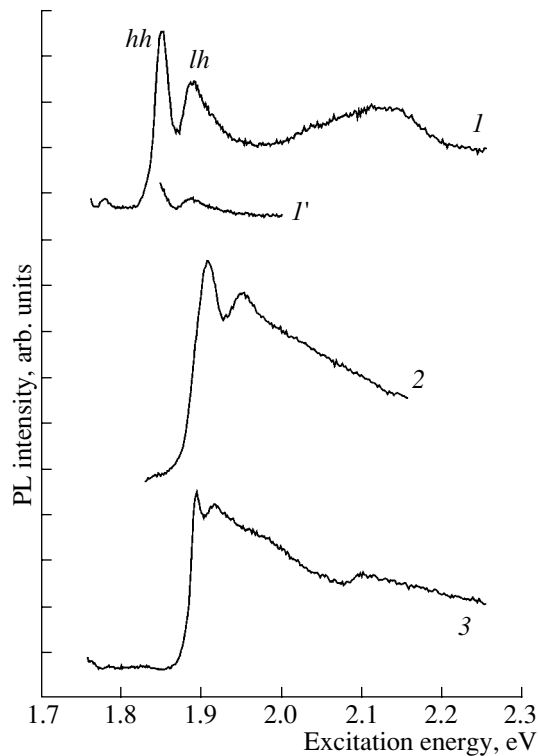
Fig. 2. Photoluminescence excitation (PLE) spectra. $T = 30$ K. (*1*, *1'*) Superlattice (3.65/3.65) nm, (*2*) superlattice (2.95/2.95) nm, and (*3*) superlattice (1.85/1.85) nm. (*1–3*) Detection at the peak of the *hh*-exciton line from the enlarged quantum well (EQW), and (*1'*) detection at the peak of the *hh*-exciton line from the superlattice (SL). For clarity, the spectra are shifted along the ordinate.
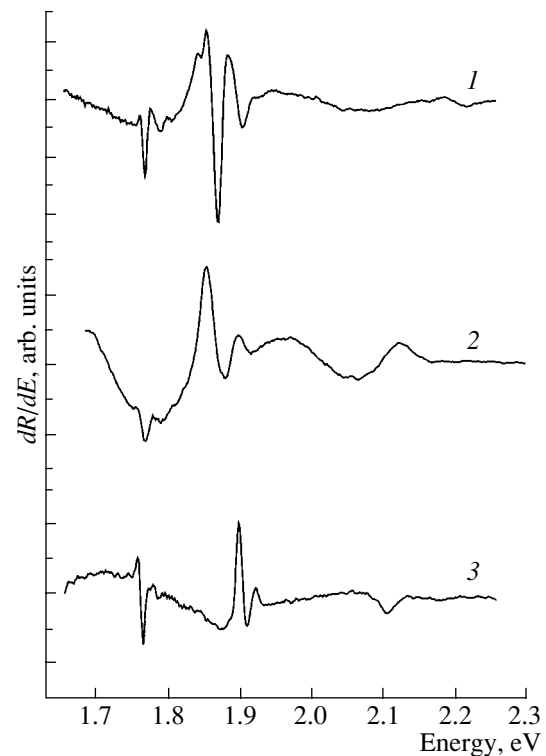
Fig. 3. Reflection spectra differentiated with respect to energy. $T = 30$ K. (*1*) Superlattice (SL) (3.65/3.65) nm, (*2*) SL (2.95/2.95) nm, and (*3*) SL (1.85/1.85) nm.

the remote pairs and a decrease in the average donor–acceptor distance within the pair. At very low pump intensities, additional donor–acceptor peaks emerged. At 77 K, the three peaks remained in the PL spectrum: the most intense peak, attributed to the EQW excitons; a peak attributed to the SL excitons; and a weak peak attributed to the donor–acceptor pairs. The FWHM of the PL peaks attributed to free excitons was ~4 meV for the EQW and ~6 meV for the SL at 2 K.

3.2. Photoluminescence-Excitation Spectra and Reflection Spectra

The PLE spectra are shown in Fig. 2. Curves *1*, *2*, and *3* correspond to the PLE spectra of various SLs detected in the peak of the PL band of the EQW. An abrupt increase in the PL intensity is observed on the excitation of the electron–hole pairs in the SL. The spectrum includes two peaks, *hh* and *lh*, attributed to heavy and light SL excitons, and a broad peak at energies higher than 2 eV. The latter peak apparently corresponds to excitation in the CdMgSe cladding layers. During detection, the peak of a light exciton in the SL is observed in the region of the peak of a heavy exciton in the SL (spectrum *1'*). The *hh* and *lh* peaks are identi-

fied with the peaks of the heavy and light excitons in the SL from measurements of the PLE under the condition of a circular polarization of light. The *hh* peak was more intense for the $\sigma_+\sigma_+$ polarization, while the *lh* peak was more intense for the $\sigma_-\sigma_+$ polarization. The *hh* and *lh* peaks are observed in the PLE spectra at up to ~200 K, i.e., up to a temperature corresponding to the onset of exciton dissociatiation. Thus, it follows from the PLE spectra that the PL from the EQWs is determined by excitons and charge carriers excited in the SL and captured in the EQW after tunneling across the SL. The presence of the pronounced exciton peaks from the SL in the PLE spectrum indicates that the excitons contribute substantially to the vertical transport. We believe that their participation is more dominant than that of free carriers, since the formation time for excitons is usually shorter than the time taken for their emission. Figure 3 shows the derivatives with respect to the energies of the reflection spectra of the SLs *dR/dE*. Resonance peaks corresponding to the heavy and light excitons of the EQWs and SLs, as well as the peaks from the cladding layers of the SLs, can be seen.

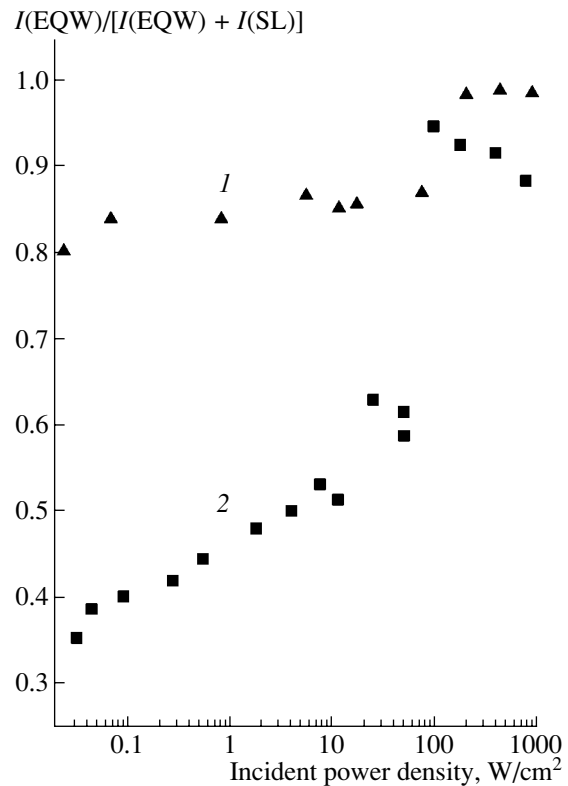### 3.3. Vertical Transport in Relation to Temperature and Pump Density

The efficiency of the vertical transport and, in particular, its temperature dependence can be judged from
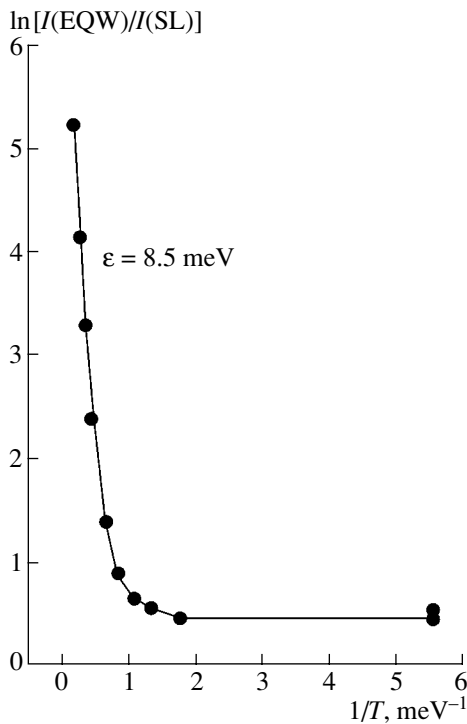
Fig. 4. Temperature dependence of the vertical transport in the superlattice (SL) (1.85/1.85) nm.

Fig. 5. Vertical transport as a function of the excitation intensity. $T = 30$ K and $E_{exc} = 1.96$ eV. (1) Superlattice (SL) (1.85/1.85) nm and (2) SL (2.95/2.95) nm.

the ratio of the integrated intensity of the exciton PL from the EQWs, I(EQW), to the integrated intensity of the exciton PL from the SLs, I(SL) (Fig. 4). In the low-temperature region, the temperature dependence is very weak. From approximately 17 K, this dependence acquires an activation character, which can be explained by delocalization of the excitons. For the SL (1.85/1.85) nm, the activation energy is $\varepsilon = 8.5$ meV, while, for the SL (2.95/2.95) nm, we found the lower energy $\varepsilon = 3.7$ meV. A possible cause of this difference is that the dissociation only starts in the measured temperature range.

The efficiency of the vertical transport, which can be determined as the ratio of the integrated PL intensity from the EQWs to the total intensity from the SLs and EQWs, depends heavily on the pump intensity. Figure 5 shows that, as the pumping intensity increases, this ratio also increases, i.e., the efficiency of the vertical transport increases. This behavior can be attributed to the concentration saturation of the localized excitons in the SL and to an increase in the concentration of free excitons. The vertical transport in the EQWs is realized precisely via free excitons. Measurements carried out for the SLs (1.85/1.85) and (2.95/2.95) nm showed that, for the pump density $W > 1$ W/cm^2, the ratio of the efficiency of the vertical transport to the pump density is virtually independent of W at 30 and 100 K. Thus, at $W > 1$ W/cm^2, only one mechanism of vertical transport is dominant for all the pumping densities. It is our opinion that this mechanism is exciton tunneling.

Figure 5 shows that the efficiency of the vertical transport is substantially higher in the shorter-period SLs. The main differences found in the efficiency of the vertical transport in the SLs studied are apparently associated with the substantial difference in the width of the minibands of heavy holes. Estimations in the effective-mass approximation yield heavy-hole miniband widths of 0.2, 1.4, and 15.8 meV for the SLs (3.65/3.65), (2.95/2.95), and (1.85/1.85) nm, respectively.

The question arises as to which mechanism of exciton transport is occurring: resonance tunneling across the minibands (the Bloch transport) or nonresonant tunneling with the involvement of phonons. It is known that the Bloch transport is impossible if the inhomogeneous broadening of the energy levels, due to fluctuations in the well or barrier widths during the SL growth and to scattering, exceeds the half-width of the miniband. This situation apparently occurs for the miniband of heavy holes in the SL (3.65/3.65) nm. For the SLs (2.95/2.95) and (1.85/1.85) nm, it is possible to verify whether the Bloch transport is realized by studying the vertical transport in a magnetic field, which is applied normally to the SL axis (the Voigt configuration). According to the theory [9], at a certain threshold value of the magnetic field B_{th}, the resonance splits between the energy levels of the neighboring wells in the SL. This phenomenon effectively narrows the miniband

Table 2. Physical parameters of cubic CdSe and MgSe, which were used in the calculation of the energies of the intersubband transitions in the CdSe/Cd$_{1-x}$Mg$_x$Se superlattice (SL)

Parameter	CdSe	MgSe	InAs
a_0, Å	6.077	5.89	6.0583
C_{11}, N m^{-2}	6.67×10^{10} [13]	9.8×10^{10} [5]	
C_{12}, N m^{-2}	4.63×10^{10} [13]	6.27×10^{10} [5]	
a, eV	–3.664 [13]		
a_c, eV	–2.625 [13]		
b, eV	–0.8 [13]		
m_e/m_0	0.11 [12]		
m_{hh}/m_0	0.45 [12]		
m_{lh}/m_0	0.145 [12]		
E_G, eV	1.765 [14]	4.05 [5]	
Δ_0, eV	0.42 [15]		

Note: The quantities m_e/m_0, m_{hh}/m_0, and m_{lh}/m_0 are the values of the relative effective masses for electrons, heavy holes, and light holes, respectively; a, a_c, and b are the values of the deformation potential. The values of E_G are given at $T = 2$ K.

and suppresses the vertical transport. This effect should manifest itself in a magnetic field $B > B_{th}$ as an increase in the PL intensity from the SL. The estimates show that, for the SL (2.95/2.95) nm with a miniband of heavy holes 1.4 meV wide, the threshold magnetic field $B_{th} \approx 7$ T. We carried out the measurements in the range 0–12 T. However, we did not observe an increase in the PL intensity from the SLs. Thus, the vertical transport in this sample is not the Bloch transport. For the SL (3.65/3.65) nm, in a range up to 6.5 T, we also observed no variation in the PL intensity from the SL. In this case, we estimated the threshold field at 2.2 T. No measurements were carried out in a magnetic field for the SL (1.85/1.85) nm, since the threshold field lies in a range that was inaccessible for us (38 T). However, for this SL, the vertical transport is most probably the Bloch transport.

3.4. Calculation of the Intersubband Energy Transitions in the Superlattices and Comparison with the Experiment

Although the SLs studied are low-strained, we took into account the strain-induced variation in the band gaps of heavy and light holes when calculating the energies of intersubband transitions. Then, the quantum-confinement energies were calculated according to the Bastard model [10]. The SL growth was pseudomorphic, i.e., the lattice constants in the layers of wells a_w and barriers a_b were matched to the lattice constant of the substrate a_0. The relative lattice strain in the QW was $\delta_w = (a_0 - a_w)/a_w \approx -0.003$. The lattice strain in the barrier was determined in the same manner. The

changes in the band edges due to hydrostatic and shear stress equal, respectively,

$$\delta E^{hy} = 2a_W\left(1 - \frac{C_{12}}{C_{11}}\right)\delta_w, \tag{1}$$

$$\delta E^{sh} = b_W\left(1 + 2\frac{C_{12}}{C_{11}}\right)\delta_w, \tag{2}$$

where C_{11} and C_{12} are the elastic stiffness constants, and a_W and b_W are the hydrostatic and shear deformation potentials for the QW. Similar expressions are valid for the barriers. The shear strain leads to a shift in the opposite direction for the edges of the band of light and heavy holes, i.e., to the splitting of these bands. The changed values of the band gaps, which are associated with the heavy and light holes, are determined by the following expressions [11, 12]:

$$E_G^{hh} = E_G + \delta E^{hy} - \delta E^{sh}, \tag{3}$$

$$E_G^{lh} = E_G + \delta E^{hy} + \delta E^{sh} + \Delta, \tag{4}$$

$$\Delta = \frac{1}{2}[\Delta_0 - \delta E^{sh} - \sqrt{(\Delta_0 - \delta E^{sh})^2 + 8(\delta E^{sh})^2}], \tag{5}$$

where Δ_0 is the spin–orbit splitting in an unstrained structure.

In the CdSe/CdMgSe SLs grown on the InAs substrates, the wells are compressed while the barriers exprience tension. In the wells, the band gap associated with the heavy holes decreases, while that associated with the light holes increases. The parameters used in the calculation are given in Table 2. It is noteworthy that there is a relatively large spread in the reported physical parameters for CdSe and MgSe, and the values of certain parameters are not known at all. For example, we encountered various values of the effective mass and the band gap E_G for CdSe. The values of E_G for MgSe vary within a wide range, and no values of the effective mass or deformation potential are reported.

We used an experimentally derived formula [5] for E_G in the Cd$_{1-x}$Mg$_x$Se barriers:

$$E_G(\text{Cd}_{1-x}\text{Mg}_x\text{Se}) = xE_G(\text{MgSe}) + (1 - x)E_G(\text{CdSe}) - Cx(1 - x), \tag{6}$$

where $C = 0.2$, $E_G(\text{CdSe}) = 1.765$ eV, and $E_G(\text{MgSe}) = 4.05$ eV. Using the values of the excitonic resonance for the SL cladding layers from the dR/dE spectra and the binding energy for a bulk CdSe exciton of 15 meV, we found the value of x using formula (6). We then used this value to calculate the lattice and elastic stiffness constants for the barriers via a linear interpolation between the values for CdSe and MgSe. The values of the effective mass in the barriers were determined as the values of the effective mass in the well multiplied by the ratio of the band gaps for the barrier and the well. Since the values of the hydrostatic and the shear defor-

Raman intensity, arb. units
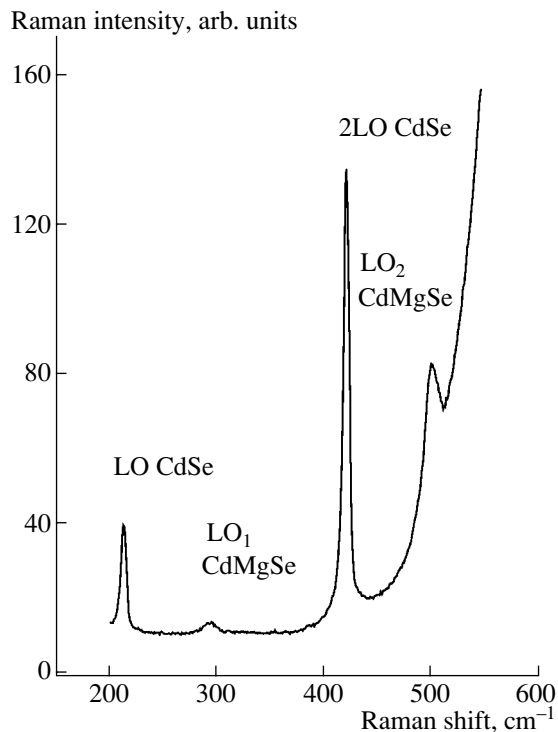
Fig. 6. Spectrum of the Raman scattering by longitudinal optical phonons for the superlattice (SL) (2.95/2.95) nm. $T = 30$ K and $E_{exc} = 1.96$ eV.

mation potentials for MgSe are unknown, we assumed, as the Mg concentration is low ($x < 0.23$), that it is possible to use the same values for the barriers as for the CdSe wells.

The experimental values of the energy difference between a light exciton and heavy exciton, which are found from the PLE spectra, are given in Table 1 (the fourth column). These values are compared with the values of the differences for the transitions $e–lh$ and $e–hh$, which are calculated for two values of the relative valence band offset $Q = \Delta E_V/\Delta E_G$. For various SLs, agreement is satisfactory for $\Delta E_V/\Delta E_G$ to within 0.4–0.5. The value of $\Delta E_V/\Delta E_G = 0.3$ from study [5] leads to appreciable disagreement with the experiment under the assumption that the values of the binding energies for the heavy and light excitons are similar. The binding energy of the heavy exciton E_B, which we estimated as the difference between the calculated energy of the transition $E(e–hh)$ and the experimental energy of the heavy exciton E_{hh} (found from the PLE spectrum), also has more reasonable values for $\Delta E_V/\Delta E_G \approx 0.4$–0.5. It is also noteworthy that this energy decreases for the shortest period SL. Such a result is not unexpected, since this SL approaches the three-dimensional limit.

3.5. Raman Scattering by Optical Phonons

In addition to PL studies, we also studied the Raman scattering in the separate CdSe QWs and in the

CdSe/CdMgSe SLs. We used both nonresonance pumping with a photon energy of 2.41 eV and near-resonance pumping. We observed, for the QW, bands corresponding to longitudinal optical phonons LO and 2LO of the first and second orders and, for the barriers, two bands corresponding to longitudinal optical phonons LO_1 (CdSe-like) and LO_2 (MgSe-like) (Fig. 6). Thus, the $Cd_{1-x}Mg_xSe$ alloy exhibits a two-mode behavior. The measurements for the bulk $Cd_{1-x}Mg_xSe$ layers showed that the variation in the Mg content from $x = 0.06$ to $x = 0.23$ leads to a variation in the frequencies of the LO_1 and LO_2 phonons from 284 to 307 cm^{-1} and from 500 to 509 cm^{-1}, respectively.

4. CONCLUSIONS

We conducted the first studies of the photoluminescence spectra, photoluminescence excitation spectra, Raman scattering by optical phonons, and vertical transport of photoinduced carriers in type I low-strained CdSe/CdMgSe superlattices grown on InAs substrates by molecular-beam epitaxy. The vertical transport across the superlattice at temperatures ranging from 20 to 180 K is effected predominantly by excitons, and its efficiency depends heavily on the superlattice period. Measurements of the photoluminescence from the superlattices placed in strong magnetic fields in the Voigt configuration showed that the vertical transport in the superlattices (2.95/2.95) and (3.65/3.65) nm is not of the Bloch type. We calculated the energies of the intersubband transitions. The binding energy of the exciton in the superlattices and the values of the relative valence band offset were obtained from a comparison with the experiment. The Raman spectra point to a two-mode behavior of the optical phonons in CdMgSe.

REFERENCES

1. N. Peranio, A. Rosenauer, D. Gerthsen, *et al.*, Phys. Rev. B **61**, 16015 (2000).

2. I. I. Reshina, A. A. Toropov, S. V. Ivanov, *et al.*, J. Cryst. Growth **214–215**, 656 (2000).

3. I. I. Reshina, S. V. Ivanov, D. N. Mirlin, *et al.*, Phys. Rev. B **64**, 035303 (2001).

4. F. C. Zhang, H. Luo, N. Dai, *et al.*, Phys. Rev. B **47**, 3806 (1993).

5. V. A. Kaygorodov, V. S. Sorokin, I. V. Sedova, *et al.*, Acta Phys. Pol. A **100**, 443 (2001).

6. S. V. Ivanov, V. A. Kaygorodov, S. V. Sorokin, *et al.*, Appl. Phys. Lett. **82**, 3782 (2003).

7. A. Chomette, B. Deveaud, J. Y. Emery, *et al.*, Solid State Commun. **54**, 75 (1985).

8. S. V. Ivanov, O. G. Lyublinskaya, Yu. B. Vasilyev, *et al.*, Appl. Phys. Lett. **84**, 4777 (2004).

9. A. M. Berezhkovskiĭ and R. A. Suris, Zh. Éksp. Teor. Fiz. **86**, 193 (1984) [Sov. Phys. JETP **59**, 109 (1984)].

10. G. Bastard, Phys. Rev. B **24**, 5693 (1981).

11. G. L. Bir and G. E. Pikus, *Symmetry and Strain-Induced Effects in Semiconductors* (Nauka, Moscow, 1972; Wiley, New York, 1975).

12. V. Pellegrini, R. Atanasov, A. Tredicucci, *et al.*, Phys. Rev. B **51**, 5171 (1995).

13. Yi-Hong Wu, IEEE J. Quantum Electron. **30**, 1562 (1994).

14. C. Guenaud, E. Deleporte, A. Filoramo, *et al.*, J. Cryst. Growth **184–185**, 839 (1998).

15. C. G. Van de Walle, Phys. Rev. B **39**, 1871 (1989).

Translated by N. Korovin

LOW-DIMENSIONAL
SYSTEMS

Resonance Donor States in Quantum Wells

N. A. Bekin

Institute for Physics of Microstructures, Russian Academy of Sciences, Nizhni Novgorod, 603950 Russia
e-mail: nbekin@ipm.sci-nnov.ru
Submitted September 7, 2004; accepted for publication September 30, 2004

Abstract—The energies and wave functions of the resonance states of shallow donors in quantum wells (QWs) are calculated. The calculations are performed in a model of an isolated impurity center using the example of a GaAs/AlGaAs heterostructure. A formula for the probability of a spontaneous emission of polar optical (LO) phonons is derived. It is shown that, in the vicinity of the resonance-state energies, polar electron–phonon interaction is modified. This modification is produced by a hybridization of confinement subbands. Generally, due to hybridization, an electron interacts with phonons simultaneously in two channels (subbands). The absorption cross section for infrared radiation is calculated, taking into account both homogeneous (in the mid-infrared range) and inhomogeneous broadening (in the far-infrared range). The absorption of radiation whose electric field is normal to the heterointerfaces is related to optical transitions to the states near the resonances. Homogeneous broadening of the absorption lines, as well as the LO-phonon scattering rate, depends on the width of the resonance states (the degree of subband hybridization). © *2005 Pleiades Publishing, Inc.*

1. INTRODUCTION

In selectively doped semiconductor heterostructures, there exist additional ways to control the energy spectrum and properties of impurity states, which are of interest both from the fundamental and application-oriented standpoints. In certain regions of the continuous spectrum, a substantial reconstruction of the states occurs: resonance (quasi-localized) states of the impurity centers appear below the upper quantum-confinement subbands [1, 2] as well as below the 3D continuum [3].

Resonance states of the impurities in QWs have been observed in experiments with Raman scattering [4], infrared (IR) radiation absorption [5], and photoconductivity [6]. In addition, certain properties of acceptor resonance states [6] and donor resonance states [1–3, 7–13] have been theoretically studied using a model of isolated impurity centers. In order to find the energy spectrum and wave functions, Dirac's method [8], the variational method [1, 9, 10], and a method of expansion in the wave functions of an electron (hole) in a QW have been used [3, 6, 8, 11–13]. The widths of the resonance levels [1, 3, 7–10, 12, 13], the IR-radiation-absorption coefficient [3, 11–13], the photoconductivity [6], and the probabilities of a spontaneous emission of polar optical (LO) phonons [13] have been calculated.

In this study, we calculate the probability of a spontaneous emission of LO phonons for electron energies in the 2D continuum using the example of GaAs/AlGaAs heterostructures. In contrast to [13], where the corresponding calculations were performed only for the case of narrow resonances, in this study, we derive a formula for the emission probability that can be used for resonances of arbitrary width.

Donor resonance states can be observed in the absorption spectra of IR radiation whose electric field is normal to the quantum-confinement layers [3, 11–13]. In III–V heterostructures, the shape of a homogeneously broadened absorption line for radiation with this polarization is determined by the rate at which the polar scattering of electrons with energies in the vicinity of the resonances occurs. In this study, we calculate the cross section of IR-radiation absorption, taking into account this broadening mechanism.

Due to the presence of an impurity potential in *n*-type heterostructures, the absorption of radiation whose electric field is directed along the quantum-confinement layers is no longer forbidden. The absorption of radiation with this polarization was studied in the region corresponding to optical transitions between localized donor states (for example, in [17]) and to impurity–band transitions [3]. However, in [3] (for the polarization in question), the modification of states in the 2D continuum by the impurity Coulomb potential and the mechanisms leading to a broadening of the absorption lines were disregarded. In this study, when calculating the IR-radiation-absorption cross section, we considered both factors. For the GaAs/AlGaAs heterostructures considered here, the absorption of radiation for this polarization is important only in the far-IR region. We assumed that, for selectively doped heterostructures, the broadening mechanism is related to the dependence of the energy spectrum on the impurity position in the QW.

2. SPECTRUM AND WAVE FUNCTIONS

2.1. Method

The states of shallow donors are described well by the effective-mass approximation. In the absence of an interaction with an impurity ion, we write the Hamiltonian operator as follows:

$$H_0 = -\frac{\hbar^2}{2m_\rho}\left(\frac{\partial^2}{\partial x^2} + \frac{\partial^2}{\partial y^2}\right) - \frac{\hbar^2}{2}\frac{\partial}{\partial z}\frac{1}{m_z(z)}\frac{\partial}{\partial z} + U(z). \quad (1)$$

Here, $m_z(z)$ and m_ρ are the transverse and longitudinal effective masses, respectively. For simplicity, we assume that m_ρ is the same in the QW and in the barrier regions. We seek the solution to the Schrödinger equation containing the impurity Coulomb potential in the form of an expansion in the eigenfunctions of the unperturbed Hamiltonian H_0.

We perform a discretization of the energy spectrum by imposing zero boundary conditions on the electron wave functions at the lateral surface of a cylinder of radius R. We assume that the cylinder axis coincides with the z axis passing through the impurity center and normal to the heterointerfaces. We find the required physical quantities by performing an $R \longrightarrow \infty$ limiting transition. By this discretization of the spectrum, first, we avoid the solution to the integral equation and, second, we naturally resolve the problem of the divergence of the diagonal matrix elements for the basis functions in the Coulomb potential.

Using the polar coordinates ρ, φ, and z, the wave function of a stationary state with a given value of the component L_z of the angular momentum along the z axis can be written as

$$|m, k, n\rangle \approx \sqrt{\frac{\pi k}{R}} J_m(k\rho) g_n(z) \frac{e^{im\varphi}}{\sqrt{2\pi}}, \quad (2)$$

where $J_m(k\rho)$ is a Bessel function of the first kind, $k^2 = 2m_\rho(E - E_n)/\hbar^2$ is the wave number for the longitudinal motion, E is the energy eigenvalue, E_n is the minimum energy of a quantum-confinement subband, and $g_n(z)$ is the normalized wave function for one-dimensional motion in the potential $U(z)$ corresponding to the level E_n. Expression (2) becomes asymptotic as $R \longrightarrow \infty$. In the following formulas, when using the asymptotic expressions, the exact equalities are replaced by approximate ones.

The imposed boundary conditions yield the following set of discrete wave numbers:

$$k_j R \approx \frac{\pi}{2}(m \pm 1) + \frac{\pi}{4} + \pi j; \quad (3)$$

here, j are integers. Using (3), we obtain the following rule for the transition from integration to summation:

$$\frac{R}{\pi}\int dk \longleftrightarrow \sum_k. \quad (4)$$

For roots (3), the Bessel functions satisfy the orthogonality condition

$$\int_0^R J_m(k_l\rho) J_m(k_j\rho) \rho\, d\rho \approx \frac{R}{\pi k_j}\delta_{lj}, \quad (5)$$

where δ_{lj} is the Kronecker delta.

We consider a quasi-two-dimensional case, where the separation between the quantum-confinement subbands (or the separation between the minimum of the lowest subband and the boundary of the 3D continuum) is appreciably greater than the donor binding energy. Such a situation is typical, for example, of GaAs/AlGaAs heterostructures. Furthermore, we are interested in electron energies that are distant from the 3D continuum. Then, we may disregard the contribution of the states of the 3D continuum to the wave function and represent this function in the form of the expansion

$$|m, E\rangle = \sum_{n, j} C_n^{(m, E)}(k_j)|m, k_j, n\rangle, \quad (6)$$

where E is the energy eigenvalue and $C_n^{(m, E)}(k_j)$ are the expansion coefficients. As a rule, in what follows, we omit the superscripts m and E and choose real values of the wave functions $g_n(z)$ and coefficients C_n. From the orthonormality condition for basis functions (2), we find the normalization condition for the expansion coefficients:

$$\sum_{n, j} C_n^2(k_j) = 1.$$

After substituting (6) into the Schrödinger equation, we obtain an infinite system of linear homogeneous equations:

$$C_n(k_j)\left(k_j^2 - \frac{2m_\rho}{\hbar^2}(E - E_n)\right) + \frac{2m_\rho}{\hbar^2}\sum_{l, s} V_{jl}^{ns} C_s(k_l) = 0, \quad (7)$$

where V_{jl}^{ns} is the matrix element of the impurity potential with unperturbed wave functions (2). Expanding the donor Coulomb potential into the Fourier–Bessel series in the interval $0 < \rho < R$, we can obtain the following expression for V_{jl}^{ns}:

$$V_{jl}^{ns} \approx -\frac{\pi^2 e^2}{R^2 \epsilon}\sqrt{k_j k_l}\sum_p G_m(k_j, k_l, k_p, R)$$
$$\times \int_{-\infty}^{+\infty} \exp(-|z - z_0|k_p) g_n(z) g_s(z) dz. \quad (8)$$

Here, k_p are roots (3) for $m = 0$, z_0 is the z coordinate of the impurity center, ϵ is the permittivity, e is the elementary charge, and

$$G_m(k_j, k_l, k_p, R) = \int_0^R J_m(k_j\rho) J_m(k_l\rho) J_0(k_p\rho) \rho \, d\rho. \quad (9)$$

To increase the rate of numerical calculation, we may replace the integral in (9) by its limiting value as $R \longrightarrow \infty$ [14], except for the singular points $k_p = |k_j - k_l|$ and $k_p = k_j + k_l$, where the corresponding limit does not exist.

To solve system (7) numerically, we restrict the calculation to a finite number of equations and choose a cutoff wave number k_{max} and set $C_n(k_j) = 0$ for $k_j > k_{max}$. Then, the problem is reduced to finding the eigenvalues $(E = E_\alpha, \alpha = 1, 2, \ldots, N)$ and eigenvectors ($C_n^{(\alpha)}(k_j)$; $j = 1, 2, \ldots, K$; $n = 1, 2, \ldots, L$; L is the number of subbands in the QW; and $N = LK$) of a finite matrix. The initial value of k_{max} should be chosen so that it is much greater than the inverse Bohr radius a_{3D} of a donor in the bulk semiconductor. Obviously, the radius R of the cylinder must be much greater than a_{3D}. We increase k_{max} and R and repeat the calculations until the convergence and required accuracy are attained.

In the approach used in this study, a number of important factors present in actual heterostructures are disregarded. In particular, we disregard the difference in the permittivities and longitudinal effective masses in the QW and barrier layers. Of course, consideration of these factors results in some corrections to the energies of the localized and resonance donor states; however, qualitatively, the situation does not change [3, 15]. The mutual effect of the impurity centers and other many-particle effects, as well as fluctuations in the composition and thickness of the quantum-confinement layers, appear to be more important. In particular, a model of isolated impurity centers may be applied if the average distance between donors is much greater than the donor Bohr radius, which can be attained by reducing the doping concentration. A consistent discussion of these problems is beyond the scope of this study.

2.2. Classification of States

In the Coulomb potential, stationary states are a superposition of states with different values of k and, generally, contain contributions from all the quantum-confinement subbands and the 3D continuum. Due to the attracting nature of the interaction with the impurity center, a discrete spectrum of states appears, whose boundary is the minimum of the lowest quantum-confinement subband; in addition, a series of quasi-localized (resonance) states appear below the excited quantum-confinement subbands and the 3D continuum [3].

As in [3], for a quantitative characterization of these states, we introduce a quantity $d_n(E, m)$ that describes the degree to which an electron with the energy E and quantum number m is involved in a subband of number n,

$$d_n(E, m) = \sum_j C_n^2(k_j). \quad (10)$$

A quasi-two-dimensional electron whose energy lies sufficiently far from the 3D continuum can be found in states of three types:

(i) *Localized states* receiving contributions from only the upper subbands, so that, for all n, the inequalities $E_n > E$ and $d_n(E, m) \geq 0$ are satisfied.

(ii) *Extended states*. For subband numbers n for which the inequality $E_n < E$ is satisfied, the total contribution $\sum_n d_n(E, m)$ to the formation of the state m is on the order of unity.

(iii) *Hybridized states*. For a certain excited subband n, the quantity $d_n(E, m)$ is on the order of unity and the minimum of this subband lies above the energy of the state under consideration ($E_n > E$). The total contribution of the lower subbands ($E_{n'} < E, n' < n$) to this state is comparable to or much smaller than $d_n(E, m)$. The hybridized state can be associated with the subband in question, and the quantity $d_n(E, m)$ characterizes the probability of electron localization at the impurity center.

In the quasi-two-dimensional case, the dominant contribution to the formation of the hybridized state comes from one or two subbands; for the other two types of states, it comes from only one subband. We must also note that in the presence of the Coulomb potential, the additional degeneracy of the continuous spectrum is conserved, starting from the minimum energies of the excited subbands. In the unperturbed QW, a similar additional degeneracy arises because of the presence of states that have the same energy but belong to different quantum-confinement subbands.

An electron in any of the three types of states is localized inside the QW, irrespective of the position of the impurity center. The donor ion determines only the position of the region of lateral localization in the bound or resonance (in the 2D continuum) state. This fact is specific to the quasi-two-dimensional case, where the main forces acting on an electron in the z direction are related to the heteropotential $U(z)$. Even if the impurity center is located deep in the barrier region, its electron is inside the quantum-confinement layer. However, for electron energies lying close to the boundary of the 3D continuum, there is an exception to this rule: an electron in the resonance states belonging to the 3D continuum can be localized at the donor center when the latter is located in the barrier [3]. Nevertheless, the probability of electron tunneling to the QW remains finite.

Let us discuss the dependence of the expansion coefficients on the wave number qualitatively. A wide domain for the momentum space in which the coefficients are large corresponds to localized states. In con-
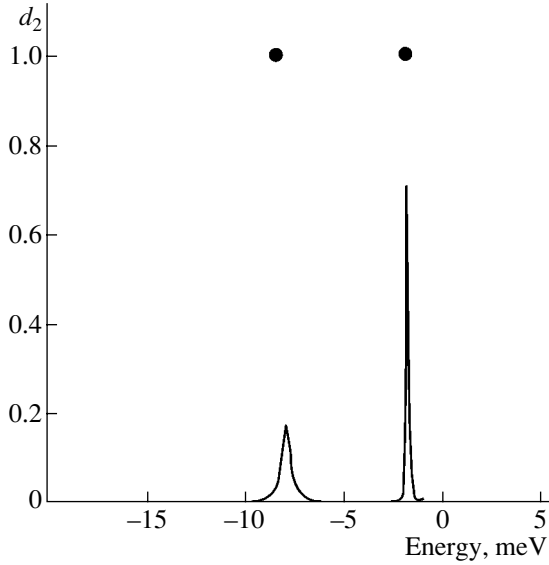
Fig. 1. The energy dependence of the quantity d_2 ($m = 0$). The energy is measured from the minimum of the second subband. The parameters of the heterostructure are as follows: a GaAs layer of 12 nm in width lies between $Al_{0.2}Ga_{0.8}As$ barrier layers, and the donor is located at a distance of 5 nm from the central plane of the quantum well. The circles correspond to the values of d_2 for the two lower discrete levels that arise in the continuous spectrum if the donor is located in the central plane.

trast, for an extended state belonging to a subband n ($d_n \approx 1$), the dependence of the coefficient $C_n(k)$ on k is strong. The wave number k_0, near which the coefficient $C_n(k)$ is relatively large, is determined by the equation $E_n + (\hbar^2 k_0^2)/(2m_\rho) = E$, where E is the energy of the state (for the unperturbed case, $C_n(k_0) = 1$ and $C_n(k) = 0$ for $k \neq k_0$).

The hybridized states belonging to the subband n have two scales of localization. The large scale (in the k space) for the coefficient $C_n(k)$ corresponds to spatial localization in the lateral direction. In contrast, the expansion coefficients for lower subbands depend on k, just as they do for the extended states.

The hybridized states that belong to the nth subband are distinguished by the characteristic energy dependence of quantities (10) in some interval below the minimum of this subband. Figure 1 shows the energy dependence of the quantity d_2 for the states with $m = 0$ in some energy interval below the minimum of the second subband. Everywhere, except for narrow energy intervals, we have $d_2 \ll 1$ ($d_1 \approx 1 - d_2 \approx 1$), which corresponds to the extended states of the first subband. In the vicinity of the resonances, the states are hybridized: the contribution d_2 of the upper (second) subband increases and, accordingly, the contribution d_1 of the lower subband is reduced. The hybridized states corresponding to the maxima in the energy dependence of d_2 are called the resonance states belonging to the second

subband. The resonance states belonging to the nth subband are defined in a similar way. The widths of the maxima in the $d_n(E)$ curve may be identified with the widths of the resonance levels [3].

For symmetric QWs, we can introduce an additional classification of the impurity states based on their symmetry [3]. It is interesting that, when there is high symmetry (the impurity is located in the central plane of a symmetric QW), the admixture of the lower subband to the stationary states is forbidden ($d_1 = 0$). For this reason, the resonance states belonging to the second subband are completely localized and the resonance width is zero.

3. INTERACTION WITH LO PHONONS

Using macroscopic theory [16], we can obtain the following operator for the energy of the interaction of electrons with LO phonons:

$$H_{e-ph} = e\sqrt{\frac{\pi\hbar\omega_{LO}}{\epsilon_p R h_c}} \sum_{m,q,q_z} \frac{\sqrt{q}J_m(q\rho)}{Q}$$
$$\times (b_{mqq_z}\exp(iq_z z + im\varphi - i\omega_{LO}t) \qquad (11)$$
$$+ b_{mqq_z}^+\exp(-iq_z z - im\varphi + i\omega_{LO}t)).$$

Here, $1/\epsilon_p = 1/\epsilon_\infty - 1/\epsilon$; ϵ_∞ and ϵ are the high-frequency and static permittivities; ω_{LO} is the frequency of the LO phonons, which is assumed to be independent of the phonon wave numbers; $Q^2 = q^2 + q_z^2$; $b_{mqq_z}^+$ and b_{mqq_z} are the dimensionless operators of the creation and annihilation of an LO phonon with the component $L_z^{ph} = m\hbar$ of the angular quasi-momentum along the z axis and with the wave numbers q and q_z ($[b_{mqq_z}, b_{mqq_z}^+] = 1$). A cylinder of radius R and height h_c (along the z axis) is chosen as the fundamental volume. Expression (11) is asymptotic as $R \longrightarrow \infty$ and the wave numbers q satisfy Eq. (3) at a fixed m.

In the long-wavelength limit considered, a crystal can understood as an isotropic continuum and phonons can be characterized by projections of the angular quasi-momentum, which is equivalent to choosing crystal lattice vibrations of a certain symmetry with respect to the rotations about the z axis. The electron–phonon interaction conserves the sum of the components of the angular quasi-momenta of the electron and the phonon along the z axis, giving rise to the corresponding selection rules for the matrix elements of operator (11).

We find the probability of the emission of an LO phonon by an electron in the initial state $|m, E\rangle$ using first-order perturbation theory. If the final electron states lie in the continuous spectrum, then, due to its degeneracy in the projections of the angular momentum, the electron can emit a phonon with arbitrary com-

ponents of the angular momentum and the corresponding sum will contain an infinite number of terms. Numerical transition to the limit $R \longrightarrow \infty$ requires high computer power, since the number of final electron states with different components m, for which transitions are possible, is proportional to R.

We can obtain an approximate expression for the probability of the spontaneous emission of an LO phonon if we disregard the modification of the final electron states by the impurity potential (see the Appendix). We have

$$\nu_{m,E}^{spont} = \sum_{s,v} M_{sv},$$

where

$$M_{sv} = \frac{e^2 m_\rho \omega_{LO}}{\epsilon_p \hbar^2} \sum_{j,p} C_s^{(m,E)}(k_j) C_v^{(m,E)}(k_j) A_{sv}^p(k_j), \quad (12)$$

$$A_{sv}^p(k_j) = \int_{-\infty}^{+\infty} \frac{F_{pv}^*(q_z) F_{ps}(q_z) dq_z}{\sqrt{(k_j^2 - k_p^2)^2 + 2q_z^2(k_j^2 + k_p^2)^2 + q_z^4}}, \quad (13)$$

$$F_{ps}(q_z) = \int g_p(z) \exp(-iq_z z) g_s(z) dz, \quad (14)$$

k_p^2 are the roots of the equation

$$E_p + \frac{\hbar^2 k_p^2}{2m_\rho} + \hbar\omega_{LO} = E, \quad (15)$$

and E_p is the energy of the minimum of the subband with the number p.

The probability of the emission of an LO phonon is represented by a convolution of matrix M_{sv} (12) with respect to the subband indices s and v. Each diagonal matrix element of M_{ss} is nonnegative and corresponds to electron scattering from the channel (subband) with the number s. The sign of the off-diagonal matrix elements M_{sv} ($s \neq v$) depends on the overlap (in the k space) of the coefficients $C_s(k_j)$ and $C_v(k_j)$, which correspond to the different channels (subbands) s and v. The sum of all the off-diagonal matrix elements M_{sv} may be interpreted as the interference of the scattering channels in the electron–phonon interaction. The interference's contribution to the frequency ν^{spont} can be negative, which corresponds to the suppression of relaxation by the phonons.

In the quasi-two-dimensional case, one or two channels contribute to quantity (12), depending on the type of initial electron state. As was noted above, if the initial electron state is extended, then it may be considered as belonging to a certain subband n. Therefore, the contribution to the probability ν^{spont} is determined by the dominant channel corresponding to this subband, and the electron scattering does not differ qualitatively from the intrasubband and intersubband relaxation in the unperturbed QW. Generally, for an electron in a hybrid-
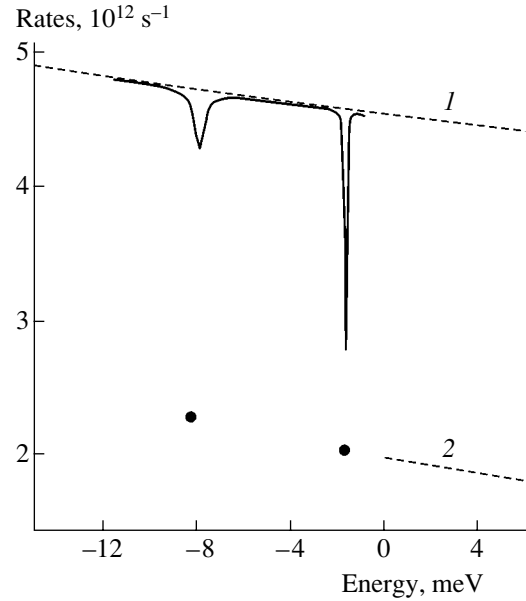
Fig. 2. The dependence of the probability of a spontaneous emission of LO phonons on the energy of the initial electron state with $m = 0$ (solid line). The dashed lines represent the probabilities of LO phonon emission for intrasubband (curve 1) and intersubband (curve 2) transitions. The energy is measured from the minimum of the second subband. The parameters of the heterostructure are listed in the caption to Fig. 1; the impurity center is displaced with respect to the center of the quantum well by 5 nm. The circles correspond to the frequencies of LO phonon emission for the two lower resonance states ($m = 0$) for the donor located at the central plane of the quantum well.

ized initial state, two channels contribute to the phonon scattering. In the quasi-two-dimensional case, the contributions of the diagonal matrix elements M_{ss} are dominant and the interference contribution is very small. This fact is due to the large separation between the subbands, which results in a weak overlap of the expansion coefficients corresponding to the two subbands in the k space that form the hybridized state.

Figure 2 shows the dependence of the probability ν_0 of the spontaneous emission of an LO phonon (12) on the energy of the initial electron state with $m = 0$. The energy interval is limited by the vicinities of the two lower resonances under the second subband. Everywhere, except for in the vicinities of the resonances, ν_0 practically coincides with the rate of intrasubband relaxation for the unperturbed QW. In the vicinity of the resonances, there are dips in the ν_0 curve produced by the hybridization of the subbands. The rate of the spontaneous emission decreases because of the increase in the contribution of the second subband to the hybridized state: the contribution of the slower process of intersubband relaxation increases and the contribution of the faster intrasubband relaxation decreases.

Qualitatively, the plots in Fig. 2 do not change if we take into account the inhomogeneity of the permittivity

(the so-called image force) and the difference in the longitudinal effective masses in the QW and barrier regions. None of these factors can give rise to the dips in the energy dependence of the phonon-emission probability (hybridization of states); they can only change the depth and position of these dips.

If the impurity is located in the central plane of the QW, the widths of the resonances below the second subband are zero and the resonance states are only formed by the upper subbands. For such states, the relaxation by the LO phonons has an "intersubband" character (Fig. 2). If the impurity center is moved deep into the barrier, then, at the energies of the resonance states, probability (12) tends to a quantity corresponding to the intersubband electron transitions with phonon emission in an unperturbed case (not shown in the figure).

4. ABSORPTION OF IR RADIATION

In order to calculate the absorption coefficient of IR radiation in the considered approximation of isolated impurity centers, it is sufficient to know the absorption cross section σ corresponding to a single center. The cross section σ is the ratio of the energy absorbed per unit time to the power density of the radiation. We set the temperature equal to zero.

When calculating the cross section in the mid-IR range, we replace the Dirac delta function that describes the exact energy conservation law in the Fermi "golden rule" by a Lorentzian function,

$$\delta(E_f - E_i - \hbar\omega) \longrightarrow \frac{\Gamma_f/\pi}{(E_f - E_i - \hbar\omega)^2 + \Gamma_f^2}. \quad (16)$$

Here, E_i and E_f are the energies of the initial and final states, respectively, and we assume that the broadening parameter Γ_f depends only on the final state. We set $\Gamma_f = \hbar\nu^{\text{spont}}$, where ν^{spont} is the frequency of the spontaneous emission of an LO phonon (12).

For longer wavelengths (in the far-IR region), we take into account only the inhomogeneous broadening of the absorption lines. We restrict the analysis to the broadening mechanism related to the dependence of the impurity energy spectrum on the impurity spatial position. Then, for a selectively doped heterostructure, the absorption cross section is obtained by averaging over the impurity position [17].

4.1. Absorption of IR Radiation with z Polarization

We consider an electromagnetic wave that has only the z component of the electric field. For this polarization, only optical transitions that conserve the component of the angular momentum along the z axis are possible. The diagonal in m matrix elements of z is

$$\langle m, E'|z|m, E\rangle = \sum_{nn'} z_{n'n} \sum_j C_{n'}^{(m, E')}(k_j) C_n^{(m, E)}(k_j), \quad (17)$$

where $z_{n'n}$ is the matrix element of the z coordinate with the wave functions of one-dimensional motion corresponding to the subbands n' and n.

We consider matrix elements (17) for optical transitions from the ground state. For transitions to the localized and extended states of the lower subband, the matrix elements are small. In the quasi-two-dimensional case, the wave functions of the initial and final states may be approximated by the product of the wave function of the first subband $g_1(z)$ and functions of ρ and ϕ, which are eigenfunctions of the Hamiltonian operator with two lateral degrees of freedom. The more suitable is the approximation in question, i.e., the greater the separation between the subbands and the closer the situation to the two-dimensional case, the smaller the matrix elements of z with these wave functions.

For transitions to the extended states belonging to excited subbands, matrix elements (17) are small because of the weak overlap of the wave functions of the initial and final states corresponding to different scales of localization in the lateral direction. The overlap of the wave functions in the coordinate and momentum spaces is relatively large only for transitions from the ground state to the resonance states. In the quasi-two-dimensional case, matrix element (17) is at its largest for optical transitions to the lower resonance states under the excited subbands. This fact can be explained by the topologically similar k dependence of the expansion coefficients for the initial and final states.

The cross section of the IR-radiation absorption for different positions of the impurity center in the QW is shown in Fig. 3. The maximum of the cross section corresponds to optical transitions to the lowest resonance state below the second subband. For comparison, the absorption cross section for intersubband optical transitions in the unperturbed QW is shown by the dashed line. Both the width of the absorption line and its shift with respect to the absorption maximum for intersubband transitions changes with the impurity position in the QW. The line shift is determined by the difference in the binding energies for the ground state and the lowest resonance state (the binding energy of a resonance state is defined as the difference between the minimum of the nearest upper subband and the energy of the resonance state). Since the main contribution to radiation absorption is made by optical transitions from the ground state to the hybridized states near the lower resonances under each of the subbands, the change in the frequencies of such transitions is equal to the difference of the binding energies. As the distance from the impurity center to the QW increases, this difference tends to zero together with the binding energies, and the position of the absorption line tends to the position of the absorption maximum for the intersubband transitions.

For all the donor positions, the shape of the absorption line is determined by the homogeneous broadening resulting from the interaction with phonons (formula (16)). Depending on the impurity position, the rate of LO

phonon emission changes from 2×10^{12} s^{-1} for a donor located deep in the barrier to 4.3×10^{12} s^{-1} for a donor at a distance of 5 nm from the central plane of the QW (Fig. 2); accordingly, this change affects the line widths.

Experimental detection of such a dependence of the absorption line width on the donor position (the position of the δ-doping layers in the heterostructure) is, however, quite difficult. Typically, absorption lines have a non-Lorentzian shape, and their widths exceed the quantities calculated in the above example. The reason for this circumstance is the presence of several broadening mechanisms that were disregarded in the calculations.

4.2. Normal Incidence of Radiation

We consider a circularly polarized wave $\mathbf{E}_\pm = (E_0 \sin(\omega t), \mp E_0 \cos(\omega t), 0)$ (in the dipole approximation, the coordinate dependence of the electric field $\mathbf{E}_\pm$ is disregarded). We choose the operator of the interaction with the electromagnetic field in the form $V_\pm(t) = e\mathbf{E}_\pm \mathbf{r}$. Commuting this operator with the Hamiltonian operator, we can obtain the following expression for the matrix elements of the coordinate part of the perturbation operator $V_\pm^{abs}$ corresponding to photon absorption:

$$\langle m', E' | V_\pm^{abs} | m, E \rangle = \mp \frac{eE_0 \hbar^2 \langle m', E' | k_\pm | m, E \rangle}{2im_\rho(E_{m'}' - E_m)}; \quad (18)$$

here, the operator $k_\pm$ is given by

$$k_\pm = \mp \exp(\pm i\varphi)\left(\frac{\partial}{\partial \rho} \pm \frac{i}{\rho}\frac{\partial}{\partial \varphi}\right). \quad (19)$$

The matrix elements of the $k_\pm$ operators are nonzero only for optical transitions where m changes by ± 1,

$$\langle m \pm 1, E' | k_\pm | m, E \rangle = \sum_{n, j} C_n^{(m \pm 1, E')}(k_j) k_j C_n^{(m, E)}(k_j). \quad (20)$$

In this expression, we have omitted the terms infinitesimal at $R \longrightarrow \infty$. Sum (20) contains expansion coefficients that are diagonal in subband indices. In the quasi-two-dimensional case, the ground state belongs to the first subband ($d_1 \approx 1$) and, therefore, optical transitions from this state are allowed only to the states for which $d_1 \approx 1$. Therefore, the absorption of IR radiation for a given polarization has an "intrasubband" character: transitions to the localized states and states of the 2D continuum originating from the lower subband are allowed. If the optical transition energy is substantially greater than the donor binding energy, the corresponding matrix element is very small due to a weak overlap in the k space of the factors in sum (20). For this reason, the matrix element for transitions to the resonance states below the second subband is very small. In addition, in the vicinity of these resonances, the quantity d_1 decreases. This corresponds to the dips in the frequency dependence of the absorption cross section. However, if
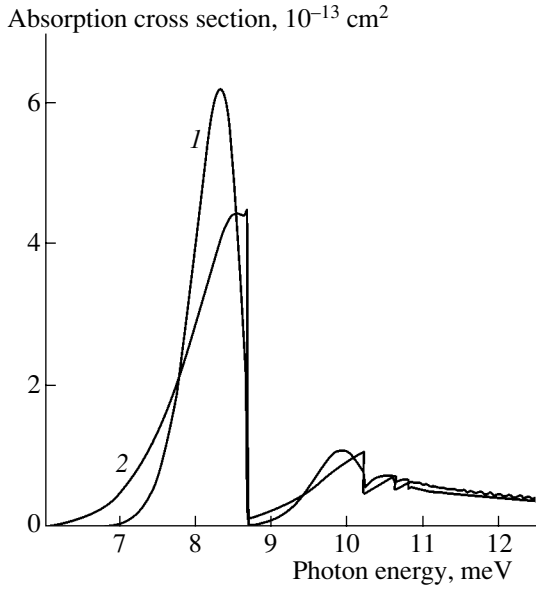

Absorption cross section, 10^{-13} cm^2
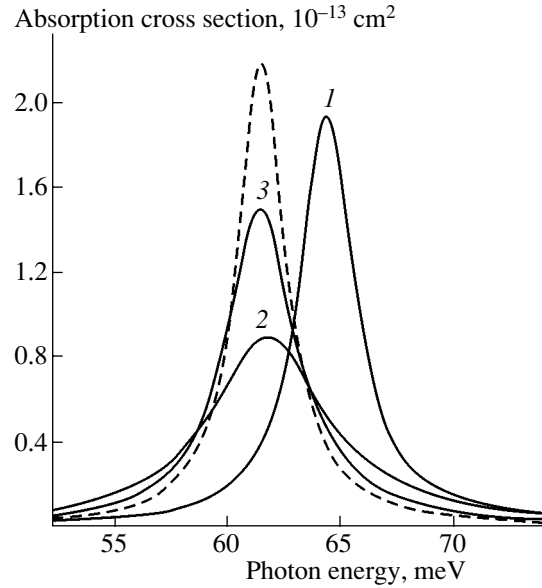
Fig. 3. The absorption cross section for radiation with z polarization. The parameters of the heterostructure are listed in the caption to Fig. 1. The solid lines correspond to absorption cross sections for an impurity center located at the central plane of the quantum well (curve *1*), at a distance of 5 nm (curve *2*) and at a distance of 14 nm from the central plane (curve *3*). The dashed line shows the absorption cross section for intersubband transitions in the unperturbed quantum well.

the different broadening mechanisms are taken into account, such dips are almost unobservable, even for QWs with small intersubband separations (about 15 meV).

Let us consider the mechanism of inhomogeneous broadening related to the dependence of the donor energy spectrum on the donor z coordinate in a QW. Since the z dependence of the difference of the localized state energies may have extrema, Van Hove singularities can arise on the frequency dependence of the absorption coefficient [17]. In the above calculations of the absorption cross section (Fig. 4), these singularities were eliminated by removing the vicinities of the singular points. This procedure is a form of averaging [17], with allowance for the fact that the substitutional impurities are located in certain atomic planes. In the vicinities of the singular points with sizes approximate to a lattice constant, the density of the impurity distribution in the corresponding integrals was taken to be zero.

We assumed that the donors were distributed according to the Gaussian law with a variance of 0.6 and 1 nm. The mean of the distribution was displaced with respect to the center of the QW by a distance of 2 nm. For both cases, the low-frequency maximum of the absorption cross section was due to optical transitions from the ground state to the lowest states with $m = \pm 1$ of the donors located in the vicinity of the maximum of the concentration distribution. The Van Hove singularities manifest themselves as discontinuities on the high-frequency side of the maximum only for a

Absorption cross section, 10^{-13} cm^2

Fig. 4. The absorption cross section for circularly polarized radiation. The parameters of the heterostructure are listed in the caption to Fig. 1. The impurity density corresponds to a Gaussian distribution centered at a distance of 2 nm from the center of the quantum well. Curve *1* corresponds to a variance of 0.6 nm and curve *2*, to 1 nm.

wide impurity distribution, since, near the corresponding singular point (at the center of the QW), the impurity concentration is relatively high. For experimental dependences of the absorption coefficient, such spectral features are smoothed out because of the presence of other broadening mechanisms. Optical transitions to the next excited localized donor states and the 2D continuum yield almost overlapping contributions to the absorption cross section for both distributions.

5. CONCLUSIONS

We showed that, near the energies of resonance states, polar electron–phonon interaction is modified. This modification is due to the hybridization of quantum-confinement subbands. Phonon emission by an electron in a hybridized state is essentially a multichannel process and, in the quasi-two-dimensional case, there are two weakly interfering channels. One channel corresponds to the interaction of a phonon with an electron localized at the impurity center, and the second channel corresponds to an electron leaving the impurity by tunneling to the continuum of the lower subband and to an intrasubband emission of an LO phonon.

The absorption of IR radiation with z polarization is due to optical transitions from the donor ground state to the hybridized states. In contrast, for a normal incidence of radiation, the resonance states do not manifest themselves in the frequency dependence of the absorption cross section. This fact is true for a case in which the separation between the quantum-confinement sub-

bands is much greater than the donor binding energy. In this case, the absorption of radiation at a normal incidence is due to optical transitions between the donor localized states and to impurity–band optical transitions.

APPENDIX

Let us derive formula (12). For the energies and wave functions of the final states, we use expressions corresponding to a QW in the absence of impurities. We use the following computational method. The squared modulus of the matrix element in the Fermi golden rule is a product of two complex conjugate integrals. We change the order of the summation over quantum numbers in the Fermi rule and the integration over coordinates in one of these factors. Then, the frequency of spontaneous emission can be represented as the result of the action of the integral operator on the function of the initial electron state:

$$\nu_{m,E}^{\text{spont}} = \frac{2\pi^4 \omega_{LO} e^2}{R^3 h_c \epsilon_p}$$

$$\times \sum_{is} \sqrt{k_i} C_s(k_i) \int_0^R K_s(\rho) J_m(k_i\rho)\rho\,d\rho. \quad (A.1)$$

Here, the operator kernel is given by

$$K_s(\rho) = \sum_{q, m', q_z, j, v, p, k_f} \frac{q\sqrt{k_j} C_v(k_j) F_{ps}(q_z) F_{pv}^*(q_z)}{q^2 + q_z^2}$$

$$\times J_{m'}(q\rho) J_{m-m'}(k_f\rho)\delta(E - E_p(k_f) - \hbar\omega_{LO}) \quad (A.2)$$

$$\times \int_0^R J_{m-m'}(k_f r) J_{m'}(qr) J_m(k_j r)r\,dr$$

and $E_p(k_f)$ are unperturbed energies of the final states.

We replace the integral with respect to r in (A.2) by its limiting value as $R \longrightarrow \infty$ [14] and sum over m' using the "addition theorem" for the Bessel functions [18]. Using rule (4), we replace the summation over q by integration. The integral is easily calculated if we take the new integration variable θ_2 using the relation $k_p^2 = k_j^2 + k_l^2 + 2k_j k_l\cos\theta_2$.

Next, in kernel (A.2), we pass from summation to integration with respect to the variables k_f and q_z. Formula (12) is obtained after substituting $K_s(\rho)$ into expression (A.1), integrating with respect to ρ, summing over j, and taking into account the orthogonality of Bessel functions (5).

REFERENCES

1. C. Priester, G. Allan, and M. Lannoo, Phys. Rev. B **29**, 3408 (1984).
2. R. L. Greene and K. K. Bajaj, Phys. Rev. B **31**, 4006 (1985).
3. A. Blom, M. A. Odnoblyudov, I. N. Yassievich, and K.-A. Chao, Phys. Rev. B **68**, 165338 (2003).
4. T. A. Perry, R. Merlin, B. V. Shanabrook, and J. Comas, Phys. Rev. Lett. **54**, 2623 (1985).
5. M. Helm, F. M. Peeters, F. DeRosa, *et al.*, Phys. Rev. B **43**, 13983 (1991).
6. V. Ya. Aleshkin, B. A. Andreev, V. I. Gavrilenko, *et al.*, Fiz. Tekh. Poluprovodn. (St. Petersburg) **34**, 582 (2000) [Semiconductors **34**, 563 (2000)].
7. K. Jayakumar, S. Balasubramanian, and M. Tomak, Phys. Rev. B **34**, 8794 (1986).
8. A. Blom, M. A. Odnoblyudov, I. N. Yassievich, and K.-A. Chao, Phys. Rev. B **65**, 155302 (2002).
9. S. T. Yen, Phys. Rev. B **66**, 075340 (2002).
10. S. T. Yen, Phys. Rev. B **68**, 165331 (2003).
11. N. A. Bekin, L. V. Krasilnikova, S. G. Pavlov, and V. N. Shastin, Phys. Status Solidi C **0** (2), 661 (2003).
12. V. Ya. Aleshkin and L. V. Krasil'nikova, in *Proceedings of 11th International Symposium on Nanostructures: Physics and Technology* (St. Petersburg, Russia, 2003), p. 70.
13. V. Ya. Aleshkin and L. V. Krasil'nikova, in *Abstracts of VI Russian Conference on the Physics of Semiconductors* (St. Petersburg, 2003), p. 426.
14. A. P. Prudnikov, Yu. A. Brychkov, and O. I. Marichev, *Integrals and Series. Special Functions* (Nauka, Moscow, 1983; Gordon and Breach, New York, 1986).
15. S. Fraizzoli, F. Bassani, and R. Buczko, Phys. Rev. B **41**, 5096 (1990).
16. M. Born and K. Huang, *Dynamical Theory of Crystal Lattices* (Clarendon, Oxford, 1954; Inostrannaya Literatura, Moscow, 1958).
17. R. L. Greene and K. K. Bajaj, Phys. Rev. B **34**, 951 (1986).
18. N. Ya. Vilenkin, *Special Functions and the Theory of Group Representations* (Nauka, Moscow, 1965; Am. Math. Soc., Providence, 1968).

Translated by I. Zvyagin

AMORPHOUS, VITREOUS,
AND POROUS SEMICONDUCTORS

Special Features of the Electrical Conductivity in Doped α-Si:H Films with Silicon Nanocrystals

S. A. Arzhannikova, M. D. Efremov^, G. N. Kamaev, A. V. Vishnyakov, and V. A. Volodin

Institute of Semiconductor Physics, Siberian Division, Russian Academy of Sciences,
pr. Akademika Lavrent'eva 13, Novosibirsk, 630090 Russia

^e-mail: efremov@isp.nsc.ru

Abstract—The electrical properties of undoped and phosphorus-doped α-Si:H films with Si nanocrystals are studied. The silicon nanocrystals are formed by a solid–solid phase transition resulting from the nanosecond effect of a XeCl excimer laser on an amorphous film. The formation of the nanocrystals in the undoped films is accompanied by an increase in the electrical conductivity by two to three orders of magnitude and a simultaneous decrease in the effective activation energy of the conductivity from 0.7 to 0.14 eV. The nanocrystal sizes range from 2 to 10 nm for various laser treatment modes and are determined from Raman scattering data and high-resolution electron microscopy. The temperature dependence of the Fermi level is obtained by calculating the energies of the localized states of electrons and holes in the nanocrystals. It is shown that, as the temperature decreases, the Fermi level tends to the energy of the states in the Si nanocrystals for a wide concentration range of the dopant. The Fermi level's location close to the states in the nanocrystals is a consequence of the fact that these states are multicharged. It is found that phosphorus effectively transforms into an electrically active state during laser treatment of the doped amorphous Si films, which is an important consideration in the fabrication of shallow p–n junctions and contacts for amorphous Si films. © 2005 Pleiades Publishing, Inc.
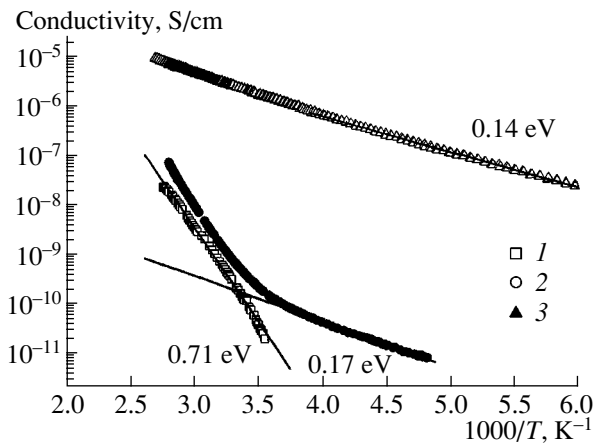
1. INTRODUCTION

Currently, giant microelectronics is one of the most dynamically developing fields of electronics. Developments in this field determine the progress made in the fabrication of planar array devices for information imaging and, in recent times, sensor devices [1]. The main controlling element of active arrays (AAs) is a thin-film transistor (TFT) based on amorphous Si. The ever increasing requirements for the parameters of TFTs have determined the necessity of using polysilicon films as a base material. This problem can be solved via the use of an excimer laser to crystallize amorphous Si films on low-melting substrates [2, 3]. Moreover, the problem relating to the formation of source–drain regions is highly relevant to the development of TFTs based on amorphous Si films. In source–drain regions, p–n junctions can be formed using the radiation from excimer lasers to activate the shallow-level impurity. The advantages of this method are twofold: the formation of shallow p–n junctions and the possibility of combining the crystallizing treatment with the formation of the source–drain regions. However, it is known that nanocrystalline inclusions are formed in an amorphous Si film during low-energy laser treatment [4, 5]. These inclusions can have a discrete energy spectrum and behave as multicharged centers. We can expect that, along with a shallow-level impurity, Si nanocrystals, being electrically active centers, will affect a film's conductivity in an electrically active state.

The aim of this study is to compare the electrical conductivity of doped and undoped amorphous Si films exposed to nanosecond ultraviolet radiation from an excimer laser. For this purpose, we studied the structure and conductivity of nanocrystalline Si films obtained as a result of a pulsed laser effect on amorphous Si films. We also calculated the effect of the Si nanocrystals on the location of the Fermi level in the doped amorphous Si films and estimated the values of the conductivity.

2. EXPERIMENTAL

The amorphous hydrogenated silicon (α-Si:H) films under study were deposited on Corning 7059 glass substrates by a plasma-enhanced chemical vapor deposition at 230°C. The films were 100 nm thick and had a 20% hydrogen content. In order to study the impurity activation caused by the laser treatment, some of the samples were implanted with 60-keV phosphorus ions at a dose of 2×10^{13} cm^{-2}.

The laser treatment was carried out using a XeCl excimer pulsed laser with an emission wavelength of 308 nm. The energy density of the laser emission in the pulse varied from 75 to 100 mJ/cm^2, which is lower than the threshold density needed to form macroscopic regions from the melt of the amorphous Si film [6]. The samples were treated both by single pulses and a series of up to 1000 pulses, with a low energy density to form the higher nanocrystal concentration.
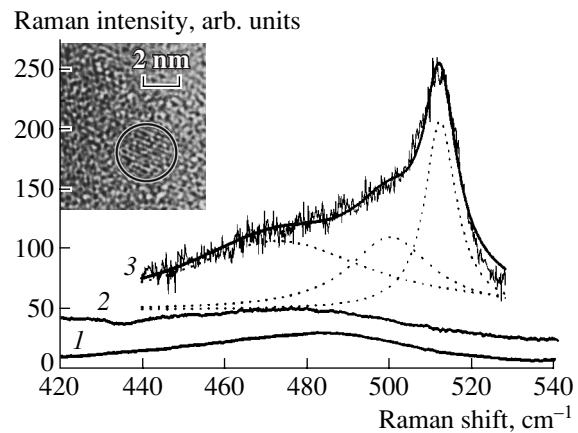
Conductivity, S/cm

Fig. 1. Temperature dependences of the conductivity in (*1*) the initial α-Si:H film and (*2*, *3*) the *a*-Si films with nanocrystals that were 2 nm in size. The nanocrystals were introduced by laser treatment at a dose of 80 mJ/cm², with the number of pulses equal to (*2*) 100 and (*3*) 500.

Raman intensity, arb. units

Fig. 2. Raman spectra for (*1*) the initial α-Si:H film, and (*2*, *3*) the *a*-Si films with nanocrystals that had an average size of 2 nm. The nanocrystals were introduced by laser treatment at a dose of 80 mJ/cm², with the number of pulses equal to (*2*) 100 and (*3*) 500. The HREM data are shown in the inset.

The structure of the obtained films was studied using Raman spectroscopy and high-resolution electron microscopy (HREM). In order to study the electrical properties of the films, we measured the temperature dependences of the dark conductivity of the obtained structures.

3. RESULTS AND DISCUSSION

3.1. The Conductivity of Nanocrystal-Containing Films of Hydrogenated Amorphous Silicon

Figure 1 shows the temperature dependences of the conductivity of the initial α-Si:H film (curve *1*) and the films treated using the excimer laser (ELA) in a mode with 80 mJ/cm² and with the number of pulses equal to 100 (curve *2*) and 500 (curve *3*). The effective activation energy for the conductivity of the initial sample was 0.7 eV, which corresponds to the conventional values for amorphous hydrogenated Si films. The room-temperature conductivity was 1.4×10^{-10} Ω^{-1} cm^{-1}. For samples exposed to 100 pulses of the excimer laser at the energy density 80 mJ/cm², the slope of the dependence of the conductivity changes at temperatures below 285 K and the activation energy becomes equal to 0.17 eV. The slope of the temperature dependence of the conductivity for the film treated with a dose of 80 mJ/cm² × 500 pulses varied over the entire temperature range, and the activation energy of the conductivity for this film was 0.14 eV. The Raman spectra show (Fig. 2) that the average nanocrystal size is 2 nm for this energy density and that an increase in the number of pulses leads to an increase in the number of nanocrystals. According to the Raman data, the total content of the crystalline phase remains at less than 1% for the sample whose temperature dependence is shown by curve *2* in Fig. 1. For the case of curve *3*, the content of the crystalline phase is 35%. The content of the crystal-

line phase and the average crystallite size were estimated on the basis of the Raman data (Fig. 2) using the procedure described in [7–10]. According to the Raman and HREM data, an increase in the pulse energy density leads to an increase in the average size of the nanocrystals formed. For example, as the energy density increases to 100 J/cm², the average size of the introduced nanocrystals increases to 8 nm.

We can assume that the states associated with these Si nanocrystals can both affect the location of the Fermi level, which leads to a variation in the conductivity via the extended states, and be immediately involved in the charge transport in accordance with the hopping mechanism. In this context, the nanocrystals play the role of doping centers [11].

We carried out experiments in order to study impurity activation under laser irradiation and the corresponding variation in the conductivity of the irradiated films. In Fig. 3, we compare the temperature dependences of the conductivity of the initial amorphous film, the film implanted with phosphorus ions, and the P-doped film after the laser treatment. After phosphorus was implanted, the room-temperature conductivity of the films increased by two orders of magnitude, while the activation energy of the conductivity decreased from 0.7 to 0.18 eV. The implanted P concentration was estimated as 2×10^{18} cm^{-3}. However, a considerable part of the dopant was electrically inactive. A subsequent laser treatment at the energy density 80 mJ/cm² × 1000 pulses increased the film's conductivity and decreased the activation energy of that conductivity to 0.15 eV. It seems probable that an increase in the conductivity with a simultaneous decrease in the activation energy indicates that the location of the Fermi level changes due to the fact that a part of the implanted phosphorus becomes electrically active.
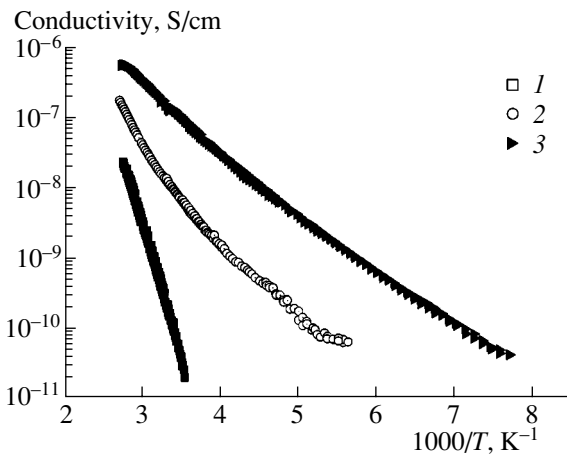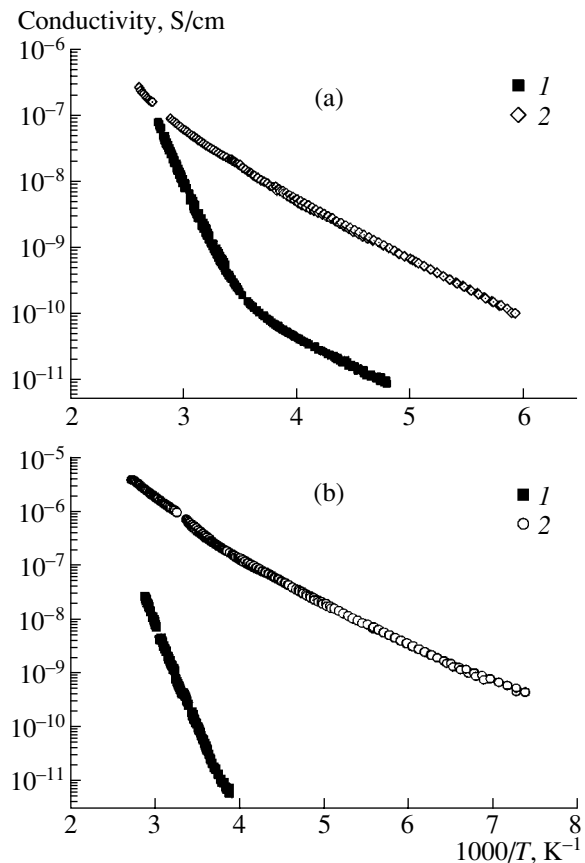
Conductivity, S/cm

Fig. 3. Temperature dependences of the conductivity for (*1*) the initial α-Si:H film, (*2*) the P-implanted α-Si:H film, and (*3*) the P-implanted α-Si:H film treated with an excimer laser.

Figures 4a and 4b show the temperature dependences of the conductivity of the laser-treated films implanted with phosphorus and those without any implantation. The impurity incorporation and the subsequent laser treatment change the film's conductivity by several orders of magnitude. It is noteworthy that this effect becomes more pronounced as the pulse energy density increases. The value of the room-temperature conductivity increased to 10^{-6} Ω^{-1} cm^{-1} (curve *2* in Fig. 4b).

Thus, the experimental value for the conductivity of the α-Si:H films, both doped and undoped, increases after the laser treatment and is accompanied by a decrease in the effective activation energy. A comparison of the experimental data for the doped and undoped films, which were treated under the same conditions, allows us to conclude that the P atoms become electrically active after the laser treatment. Despite the similarity of the results for the incorporation of the shallow-level impurity and the nanocrystals, the mechanisms involved in the increase in the conductivity may be different. To reveal the effect of the nanocrystals on the location of the Fermi level in the amorphous Si films, we carried out the corresponding calculations described below.

3.2. Calculation of the Effect of Nanocrystals on the Location of the Fermi Level in Doped Silicon Films

To estimate the effect of the nanocrystals on the conductivity of the α-Si:H films and the activation energy of that conductivity, we calculated the location of the Fermi level versus the doping level of the film. In these calculations, we took into account the states in the bands, the impurity energy states, and the density of states in the band gap, which is inherent to α-Si:H [12]. The contribution of the nanocrystals was taken into

Conductivity, S/cm

Fig. 4. Temperature dependences of the conductivity of the α-Si:H films treated with 100 pulses of an excimer laser at the energy density of (a) 80 and (b) 100 mJ/cm^2. Curve *2* corresponds to the P-implanted film.

account by introducing multicharged centers into the calculation. The charge state of these centers depends on the number of electrons in the nanocrystal.

We calculated the energy spectrum for nanocrystals of various sizes. The nanocrystal was simulated by a spherical potential well with the potential and mass step at the boundary. It is well known that the problem of a spherical potential well can be reduced to a one-dimensional problem [13], and the zero angular momentum can be determined by solving the following problem for a one-dimensional potential well:

$$\frac{d^2\chi(r)}{dr^2} + \left[\frac{2m}{\hbar^2}(E - U(r))\right]\chi(r) = 0,$$

where $\chi(r)/r$ determines the radial part of the wave function. The condition $\chi(r) = 0$ at $r = 0$ should be satisfied to provide the finiteness of the wave function at the origin. The fulfillment of this condition can be provided by an infinitely high potential wall at $r = 0$. The

nanocrystal radius plays the role of the well width, and the potential has the following form:

$$U(r) = \begin{vmatrix} \infty & \text{at } r = 0 \\ 0 & \text{at } 0 < r < R \\ U_0 & \text{at } r \geq R \end{vmatrix}.$$

The dependences of the energy spectrum of the electrons and holes on the size of the nanocrystals, which were introduced into the a-Si matrix, are shown in Figs. 5a and 5b, respectively.

The contribution of the nanocrystals to conductivity is taken into account by introducing the multicharged centers into the calculation. The energy levels of these centers correspond to discrete levels in the nanocrystal. We assigned numbers from 0 to j to the energy states of the nanocrystal. The index 0 corresponds to the location of the Fermi level below each quantum level in the nanocrystal, i.e., to the absence of valence electrons at quantum-dimensional energy levels. In this case, the total charge of the nanocrystal q_0 is positive and its magnitude is determined by the largest number of holes that can be held in the nanocrystal. The index j thereby corresponds to the number of valence electrons that are located in the nanocrystal. Its charge q in the jth state is given by

$$q_j = q_0 - j \cdot e.$$

The charge density at the multicharged centers can be written as

$$Nq_{mq}(T, E) = Nmq \cdot Q_{mq}(T, E_F),$$

where Nmq and $Q_{mq}(T, E_F)$ are the concentration and charge of the multicharged centers (nanocrystals), respectively. The charge equals

$$Q_{mq}(T, E_F) = \sum_j q_j \cdot fmq_j(T, E_F),$$

where $fmq_j(T, E_F)$ is a distribution function that corresponds to the jth state and is defined as

$$fmq_j(T, E_F) = \frac{g_j \cdot \exp\left(\dfrac{jE_F - E_j}{kT}\right)}{\displaystyle\sum_{j=0}^{J} g_j \exp\left(\dfrac{jE_F - E_j}{kT}\right)}.$$

In this expression, E_j is the energy of the multielecron center with j electrons, and g_j is the degeneracy factor for the center with j electrons. If we know the energies ε_k for the transition of the center from the j state to the $j + 1$ state, we can find the energy of j electrons in the nanocrystal E_j as the sum of the energies of the single-elec-

Fig. 5. The energy spectrum of the (a) electrons and (b) holes for the nanocrystal in the a-Si matrix.

tron states. The values of these energies are determined on a single coordinate scale:
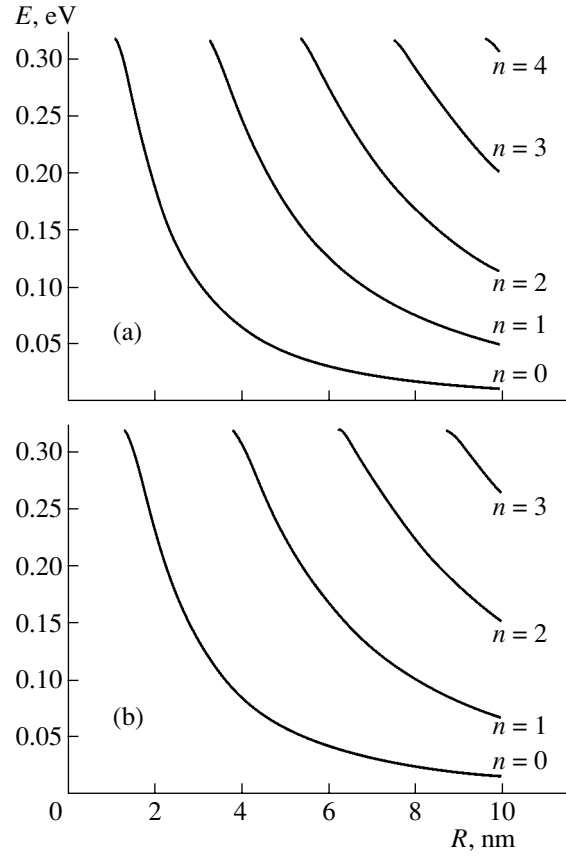
$$E_j = \sum_{k=0}^{j} \varepsilon_k.$$

In the calculations, the concentration of the multicharged centers (nanocrystals) was $Nmq = 10^{17} \text{ cm}^{-3}$. The energy levels were specified for nanocrystals of 8 nm in diameter.

The distribution of the quasi-continuous energy states in the band gap was specified as follows. Let $N_s(\varepsilon)$ be the density of states in the unit energy range. In this case, the concentration of the electrons captured at these states will be equal to

$$n_s = \int_{E_v}^{E_c} f_e(E) N_s(E) dE.$$

The charge density at the states in the band gap will depend on the starting charge of the centers that induce the emergence of the states in the band gap and on the number of captured electrons:

$$\rho_s = q_{s0} \int_{E_v}^{E_c} N_s(E) dE + q_e \int_{E_v}^{E_c} f_e(N) N_s(E) dE,$$

Model parameters for the calculation of the location of the Fermi level

Model parameters	In bands	In the band gap
$Estd_k$, eV	E_v	$E_c - 0.7$
$\Delta Estd_k$, eV	-0.04	-0.15
$Nstd_k$, cm^{-3}/eV	10^{21}	$0.5 \times 10^{14}, 0.5 \times 10^{17}$
$Esta_k$, eV	E_c	$E_c - 0.7$
$\Delta Esta_k$, eV	0.025	0.1
$Nsta_k$, cm^{-3}/eV	10^{21}	$0.5 \times 10^{14}, 0.5 \times 10^{17}$

where q_{s0} is the charge of an unoccupied state in the band gap. The unoccupied donor states have a positive charge, while the acceptor states have a zero charge. The density of states in the band gap was determined from the total density for the donor and acceptor states.

The chosen model of the density of states in amorphous Si implies that we should take into account the additive densities of states, which decrease exponentially from the band edges:

$$Nsd(E) = \sum_k \left(Nstd_k \exp\left(\frac{E - Estd_k}{\Delta Estd_k}v\right)\right),$$

$$Nsa(E) = \sum_k \left(Nsta_k \exp\left(\frac{E - Esta_k}{\Delta Esta_k}v\right)\right).$$

The total charge at the states in the band gap is given by

$$Nqs(T, E_F) = \int_{E_v}^{E_c} Nsd(E)dE$$

$$- \int_{E_v}^{E_c} \left(1 + \exp\left(\frac{E - E_F}{kT}\right)\right)^{-1}(Nsd(E) + Nsa(E))dE.$$

The density of states in the band gap $N_s(E)$ was specified so that its minimum corresponded to the energy $E_c - 0.7$ eV, thus making the model consistent with the experiment. The minimum density of states $Ns_{\min} = 10^{14}$ cm^{-3}.

The table gives the parameters for the exponentially attenuated energy states in the band gap, which were used in the calculations. The band gap E_g was chosen to be equal 1.8 eV, which corresponds to α-Si:H [12]. The location of the Fermi level was found by solving the electroneutrality equation.

The temperature dependences of the Fermi level were calculated for various doping levels. The impurity concentration was varied from 10^{12} to 10^{20} cm^{-3}. In the calculations, phosphorus with $E_d = 0.044$ eV was chosen as the donor impurity and boron with $E_a = 0.045$ eV was chosen as the acceptor impurity.

Figure 6 shows the calculated location of the Fermi level in α-Si:H as a function of the doping level. Without the doping impurity, the Fermi level is located at the midgap. At low temperatures, the introduction of the impurity shifts the Fermi level towards the energy of the impurity state (Fig. 6a). The calculations showed that the nanocrystals profoundly affect the location of the Fermi level (Fig. 6b). Furthermore, at low temperatures, the Fermi level is pinned at quantum levels in the nanocrystals. In this case, the energy depends on the doping level of the film. For Figs. 6a and 6b, the localized states in the band gap were disregarded in the analysis of the effect of the nanocrystalline inclusions themselves.

The results that take into account the localized states are shown in Fig. 6c. It can be seen that the effect of the nanocrystals is less significant in this case. However, at a high impurity concentration and low temperatures, the Fermi level is pinned at the same states in the nanocrystals as mentioned above.
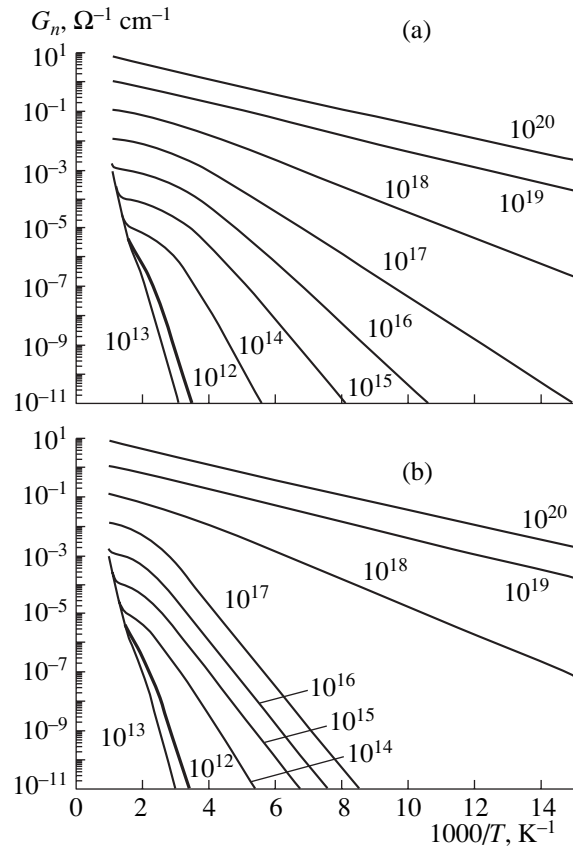
Let us disregard the temperature dependence of the mobility. Then, we can calculate the electrical conductivity of the films with nanocrystals and without them. The results of a calculation for the mobility 1 cm^2/(V s) are shown in Fig. 7. As follows from a comparison of Figs. 7a and 7b, the introduction of the nanocrystals decreases the conductivity through a mobility gap of amorphous Si for concentrations of the shallow-level impurity lower than that of the nanocrystals. Thus, the experimentally observed substantial increase in the conductivity of the undoped laser-treated films (Fig. 1) can not be attributed to a variation in the band conductivity resulting from the introduction of the nanocrystals. The Fermi level shifts as the nanocrystals are introduced. However, by virtue of the fact that the Fermi level tends to the energy of one of the levels in the nanocrystal, which is deeper than the energy level of the shallow-level impurity, the band conductivity decreases while the activation energy correspondingly increases. Thus, in the case of the undoped films, the observed increase in the conductivity and decrease in the activation energy can probably be explained by a variation in the hopping transport rather than by an increase in the band conductivity. This conclusion is confirmed by the fact that the activation energy of the conductivity changes drastically as the temperature decreases for the same sample (curve *2* in Fig. 1), which provides direct evidence that the conductivity mechanism changes. The strong concentration dependence of the conductivity, which is observed for the undoped films (curves *2, 3* in Fig. 1), also confirms the above suggestion that the hopping transport becomes the dominant mechanism on the introduction of nanocrystals with a relatively high concentration. The states in both the nanocrystals and the surrounding matrix, which are located close to the Fermi level, may contribute to the transport. The fact that the Fermi level tends towards the energy levels in the nanocrystals only sim-
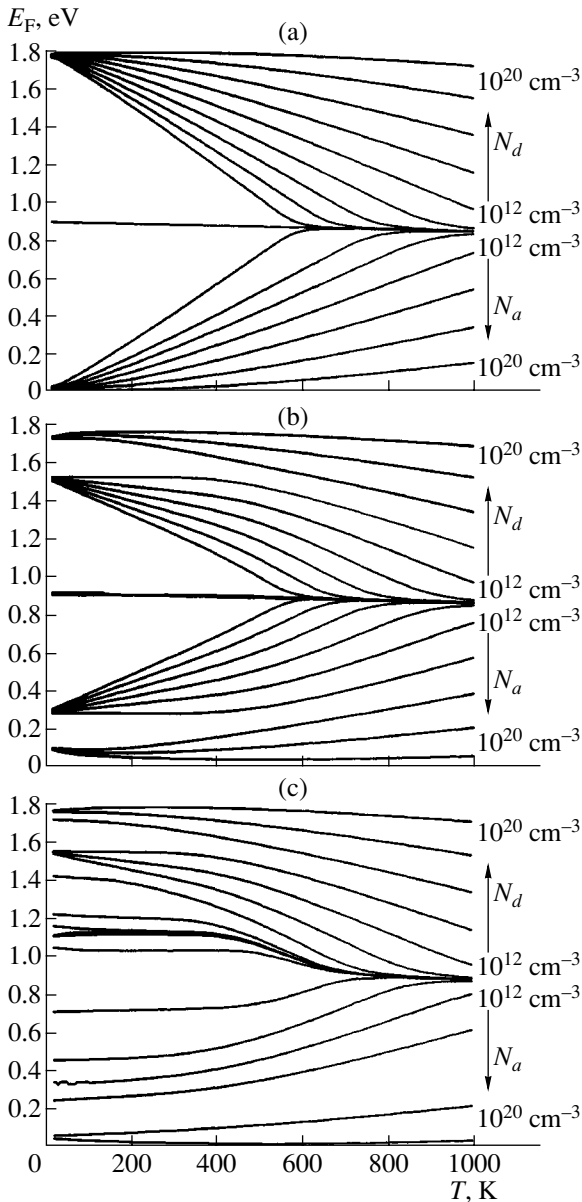
Fig. 6. Temperature dependences of the Fermi level. (a) The shallow-level impurity is taken into account, (b) the shallow-level impurity and the Si nanocrystals $N_{nc} = 10^{17}$ cm^{-3} are taken into account, and (c) the shallow-level impurity, the nanocrystals, and the density of states in the band gap $N_s = 10^{14}$ cm^{-3}/eV are taken into account.

Fig. 7. Temperature dependences of the conductivity of the hydrogenated amorphous Si films ($N_s = 10^{14}$ cm^{-3}/eV) at various doping levels: (a) without nanocrystals, and (b) with nanocrystals. The numbers next to the curves denote the concentration N_d (in cm^{-3}).

plifies the involvement of the nanocrystals in the hopping mechanism.

For the laser-treated doped films, the conductivity increases and the effective activation energy decreases, which superficially resembles the case of the undoped films. However, a direct comparison of these cases under the same laser-treatment conditions proves that the phosphorus atoms become electrically active after the laser treatment. As the energy density of the laser radiation increases, the observed relative difference in

the conductivity is more than three orders of magnitude. In turn, the impurity activation causes the shift of the Fermi level towards the conduction band, which increases the conductivity, with a simultaneous decrease in the activation energy (Fig. 7).

4. CONCLUSIONS

Thus, we showed that Si nanocrystals, which were formed in amorphous Si as a result of laser treatment, increase the electrical conductivity of the films and lead to a simultaneous decrease in the effective activation energy of that conductivity from 0.7 to 0.14–0.17 eV. This increase in the conductivity cannot be described in the context of the conductivity mechanism via the band. The activation energy of the conductivity decreases as the temperature decreases and as the concentration of nanocrystals increases. This phenomenon is attributed to the hopping transport with the involvement of the states in the Si nanocrystals.

Due to the effect of laser radiation with a wavelength of 308 nm and an energy density below the melting threshold, phosphorus atoms become electrically

active in P-doped amorphous Si films. The observed relative difference in the conductivity exceeds three orders of magnitude at room temperature and increases as the temperature decreases, which points to the effective electrical activation of the phosphorus impurity.

ACKNOWLEDGMENTS

REFERENCES

1. L. Zhuravleva, Perspekt. Tekhnol. **10** (7) (2003).
2. W. C. O'Mara, Solid State Technol. **1**, 53 (1992).
3. S. J. Matthews, Laser Focus World **9**, 103 (2001).
4. V. V. Bolotov, M. D. Efremov, L. I. Fedina, *et al.*, in *Abstracts of Spring Meeting of Material Research Society* (San Francisco, 1993), p. A9.54.
5. M. D. Efremov, V. V. Bolotov, V. A. Volodin, *et al.*, J. Phys.: Condens. Matter **8**, 273 (1996).
6. T. Sameshima and S. Usui, J. Appl. Phys. **70**, 1281 (1991).
7. M. D. Efremov, V. V. Bolotov, V. A. Volodin, *et al.*, Fiz. Tekh. Poluprovodn. (St. Petersburg) **36**, 109 (2002) [Semiconductors **36**, 102 (2002)].
8. Z. Iqbal, S. Veptek, A. P. Webb, and P. Capezzuto, Solid State Commun. **37**, 993 (1981).
9. R. Tsu, J. G. Hernandes, S. S. Chao, *et al.*, Appl. Phys. Lett. **40**, 534 (1982).
10. V. Paillard and P. Puech, J. Appl. Phys. **86**, 1921 (1999).
11. M. D. Efremov, V. A. Volodin, L. I. Fedina, *et al.*, in *Abstracts of Spring Meeting of European Materials Research Society* (Strasbourg, 2000), p. O/P24.
12. A. Madan and M. Shaw, *The Physics and Applications of Amorphous Semiconductors* (Academic, Boston, 1988; Mir, Moscow, 1991).
13. L. D. Landau and E. M. Lifshitz, *Course of Theoretical Physics*, Vol. 3: *Quantum Mechanics: Non-Relativistic Theory*, 4th ed. (Nauka, Moscow, 1989; Pergamon, Oxford, 1977).

Translated by N. Korovin

An Electron Spin Resonance Study of Copper–Carbon Systems

B. P. Popov

St. Petersburg Polytechnical University, ul. Politekhnicheskaya 29, St. Petersburg, 195251 Russia
e-mail: popov@tuexph.stu.neva.ru
Submitted July 29, 2004; accepted for publication July 30, 2004

Abstract—The results from electron spin resonance studies of the states of copper intercalated into various carbon hosts, i.e., fullerene (C_{60}), ultradisperse diamond, and amorphous carbon, are considered. The possibility of the occurrence of the copper disproportionation reaction $2Cu^{2+} \longrightarrow Cu^{+} + Cu^{3+}$ is shown. In a system consisting of copper and ultradisperse diamond, a superparamagnetic state is detected in a temperature range of 10–130 K. © *2005 Pleiades Publishing, Inc.*

1. INTRODUCTION

The atomic structure of all the molecular forms of carbon has a unique capability to give rise to various hybridizations of valence orbitals. This circumstance makes it possible to use carbon systems as hosts for the intercalation of metals and metal clusters. However, there is a significant problem to be investigated related to the interaction between a given metal and the carbon host. We studied a series of samples prepared according to the method described in [1–3]. Measurements of the microwave absorptivity, Meissner effect, and temperature dependence of the resistivity showed the existence of superconductivity up to the high critical temperature $T_c = 120$ K in Cu–C_{60} samples [1]. The mechanism of this phenomenon is associated with the formation of macromolecular fullerene clusters, in which copper is incorporated via oxygen bridges [3]. Under the assumption that copper, when in such a system, is an electron donor, the copper disproportionation reaction $2Cu^{2+} \longrightarrow Cu^{+} + Cu^{3+}$ can take place during doping [4]. In this case, the formation mechanism of the superconducting state is associated with the existence of centers with negative effective correlation energy (U^- centers). Copper charge states were studied using the electron spin resonance (ESR) of copper intercalated in various carbon hosts: fullerene (C_{60}), ultradisperse diamond (UDD), and amorphous carbon (α-C:H). The measurements were carried out using a conventional RADIOPAN ESR spectrometer at a frequency of 9.6 GHz in a temperature range of 4–300 K.

2. RESULTS OF ESR STUDIES

The ESR spectrum of the Cu–C_{60} samples (Fig. 1a) consisted of four lines corresponding to the resolved hyperfine structure of copper found in the Cu^{2+} charge state with a *g* factor equal to 1.99 and a narrow line resulting from carbon radicals with $g = 2.003$. First, the ESR spectrum of the polycrystalline samples was observed; then, the samples were ground down to micrometer sizes; and, last, the ESR spectrum of the powders was measured. The ESR spectrum parameters (*g* factor and linewidth) did not demonstrate any significant differences for the polycrystalline and powdered samples. However, the ESR signal intensity from the copper in the powdered samples increased by approximately ten times. This allows us to conclude that the copper in the polycrystalline samples is either in a mag-
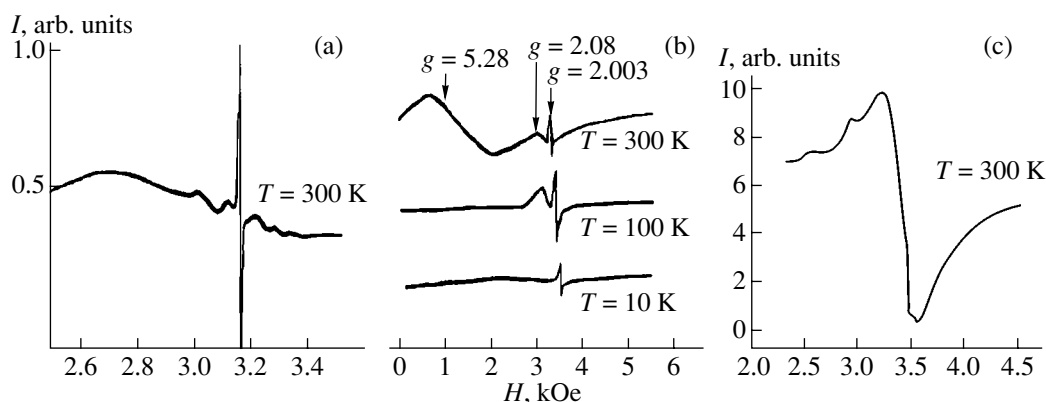

Fig. 1. ESR spectra of the (a) Cu–C_{60}, (b) Cu–UDD, and (c) Cu–α-C:H samples.

Parameters of the ESR spectra

Sample	g factor	ΔH_{pp}, Oe	A_{hpf}, 10^{-4} cm^{-1}	n_{Cu}, cm^{-3} (by spins)
PC Cu–C$_{60}$	1.99	420	131	10^{17}
P Cu–C$_{60}$	1.99	420	131	10^{18}
Cu–UDD	2.08	300	93	10^{19}
Cu–α-C:H	$g_{\parallel}$ = 2.36, $g_{\perp}$ = 1.99 $g_{\parallel}$ = 2.71, $g_{\perp}$ = 1.99	300	93	10^{19}

Note: PC stands for polycrystalline; P, for powder; and UDD, for
ultradisperse diamond.

netic state ($3d^9$) or in one of two nonmagnetic states ($3d^8$ or $3d^{10}$). Furthermore, a deviation from the Curie law was observed in the temperature dependence of the copper ESR signal intensity in the polycrystalline samples. To determine the paramagnetic center concentration, the ESR signal of a Radiopan reference sample (the spin concentration was 5×10^{17} cm^{-3}) was measured simultaneously with the signal of the samples under study. The spin concentration was calculated by comparison with this reference.

The ESR spectra of the Cu–UDD samples, at various temperatures, are shown in Fig. 1b. The ESR spectrum of copper in the $3d^9$ (Cu^{2+}) state with a g factor equal to 2.08 and the linewidth ΔH_{pp} = 400 Oe was observed, as well as a narrow line from carbon radicals with g = 2.003. The characteristic ESR spectrum of the Cu–α-C:H samples is shown in Fig. 1c. We can see that this ESR spectrum is a superposition of wide and narrow lines. The narrow line is characterized by the parameters g = 2.003 and ΔH = 11 Oe and is the well-known ESR spectrum of carbon radicals. The wide component of the spectrum should be considered as a result of the superposition of two spectra from axially deformed copper centers. The parameters of the copper ESR spectrum are listed in the table.

No hyperfine structure was observed in the ESR spectra of the copper in UDD and amorphous carbon. The hyperfine coupling (HFC) constant was estimated using the dipole broadening of an individual transition: $\Delta H_{pp} \approx g\beta S/r^3 \approx g\beta S n_{Cu}$, where g is the copper g factor, β is the Bohr magneton, S = 1/2 is the Cu^{2+} ion spin, and n_{Cu} is the ion concentration. At the experimental ESR linewidth ΔH_{pp} = 100 Oe relating to copper ions, the local Cu^{2+} ion concentration in these samples is $n_{Cu} \approx 10^{19}$ cm^{-3}.
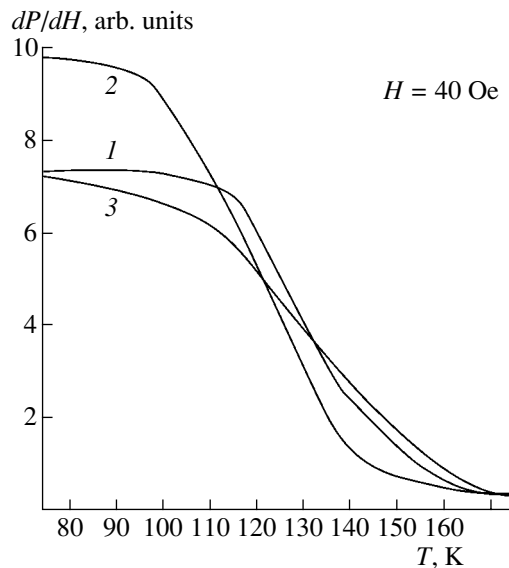
3. RESULTS AND DISCUSSION

Of particular interest is the existence of the resolved HFC and the HFC constant of the copper in the fullerene hosts, A_{hpf} = 131 $\times 10^{-4}$ cm^{-1}. It is known [5] that hyperfine splitting depends on the bond covalence: the stronger the bond ionicity, the larger the splitting. In the case of a covalent bond, electrons transfer to the $4s$ shell of Cu, which decreases the configuration-interaction contribution to the HFC constant within the $3s^23d^9$ configuration. Thus, the copper intercalated in

the fullerene host is in the transition region from the ionic bond (Cu^{2+} region) to the covalent bond (Cu$^+$ + Cu^{3+} region), which exactly maintains the disproportionation reaction. One important factor associated with electron density redistribution as the bond covalence increases is particularly noteworthy: If the Cu–O bond is ionic, the Cu^{2+} ions behave in a similar way to localized $3d^9$ ions. However, as the Cu–O distance decreases, the covalence increases. In this case, the overlap of the copper wave functions with the oxygen orbitals increases, and, in a concentrated system, the electronic levels broaden and transform into impurity bands. When a system is within the ionic bond, the Cu–O–Cu chains are linear. As the bond length decreases during the transition to a covalent bond, the s–p hybridization properties change, which results in an electron density displacement from the bond line. In the region corresponding to disproportionation, the Cu–O–Cu bond takes on a zigzag formation. The existence of oxygen vacancies lowers the coordination number of copper cations. It can be assumed [4] that there exists a transition region of variable copper valence in the copper–fullerene system, where superconductivity takes place.

A study of the microwave absorption (MWA) of the UDD samples intercalated by copper showed the absence of the typical MWA signal for superconducting samples. The linear dependence of the absorbed power on the magnetic field was observed [2]. In the ESR spectra of the Cu–UDD samples, in addition to lines corresponding to Cu^{2+} ions and carbon radicals, a broad line with g = 5.28 was observed. This line is evidently caused by interacting paramagnetic centers (single-domain magnetic clusters) of an unknown nature, but most probably containing copper. As the temperature is lowered, this broad line broadens even more and then disappears, and the manifestation of its g factor shifts to the region of weak fields. At T < 130 K, this line totally disappears. In the region of weak magnetic fields (H = 40 Oe), the dependence of dP/dH on the magnetic field exhibits a slope caused by the nonlinear dependence of the magnetization $M(H)$. The temperature dependence of this slope (Fig. 2) was used to determine the temperature and width of the magnetic phase transition: T_{1c} = 130 K and ΔT = 30 K.

The spectra of the Cu^{2+} ions and carbon radicals did not show drastic changes up to 10 K, which indicates that the C–Cu system is stable. However, as the temperature decreases to T_{2c} = 8–10 K, the ESR line of the Cu^{2+} ions is sharply broadened, so that it becomes almost undetectable. This circumstance could be caused by either a magnetic ordering of the copper not incorporated into the magnetic clusters [6] or a magnetic interaction between the nanoclusters [7]. Such changes in the ESR spectrum are similar to the behavior of superparamagnetic regions. In this case, at temperatures above T_{2c}, an ensemble of macromolecular clusters behaves similarly to a gas composed of paramagnetic molecules with a larger magnetic moment and, at T < T_{2c}, the system transforms into a state of cooperative magnetic ordering. This assumption is confirmed

Studies of copper in films of hydrogenated amorphous carbon indicate the formation of at least two types of centers. These two states emerge due to the different charge and, respectively, magnetic states of copper: the nonmagnetic copper state in the $3d^{10}$ (Cu^+) configuration and the magnetic state $3d^9$ (Cu^{2+}). A copper ion is incorporated into the carbon host via oxygen bridges and forms a Cu^{2+} magnetic state. The influence of hydrogen on the copper charge state manifests itself as a result of its interaction with oxygen atoms leading to the formation of hydroxyl groups. In this case, copper ions transform into the nonmagnetic configuration $3d^{10}$ (charge state Cu^+). Traces of hydroxyl groups were observed in the IR absorption spectra [3]. A model of the formation of the two copper charge states (Cu^+ and Cu^{2+}) in the amorphous carbon host was previously suggested in [3, 8].

4. CONCLUSION

The ESR studies show that copper, when intercalated in carbon hosts, forms two types of centers differing in their magnetic and charge states and with the electronic configurations $3d^9$ (magnetic state) and $3d^{10}$ (nonmagnetic state). These copper states are modified by the direct participation of oxygen, via which copper is incorporated into the carbon host. The large HFC constant of copper ($A_{hpf} = 131 \times 10^{-4}$ cm^{-1}) suggests that the Cu–O bond is in the intermediate region of the transition from the ionic bond (Cu^{2+}) to covalent bond ($Cu^+ + Cu^{3+}+$). Hence, the copper disproportionation reaction $2Cu^{2+} \longrightarrow Cu^+ + Cu^{3+}$ is possible. The results of this study can initiate further comprehensive studies of the physical state of copper–carbon systems.

Fig. 2. Temperature dependences of the ESR signal intensity in a weak magnetic field for the Cu–UDD samples annealed at $T_{ann} = 700, 800,$ and 900 K (curves *1–3*, respectively).
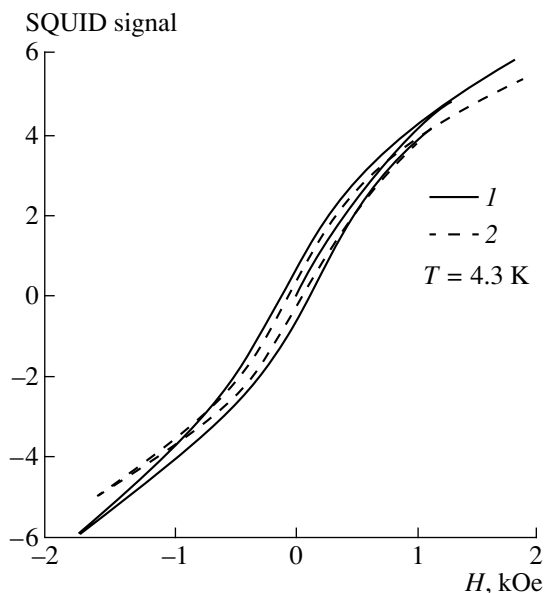
Fig. 3. Magnetization curves measured using a SQUID magnetometer. The solid (*1*) and dashed (*2*) curves correspond to the different samples. The measuring temperature T was equal to 4.3 K.

by measurements of the Cu–UDD samples carried out using a SQUID magnetometer in the temperature range 4–10 K. The magnetization curve $M(H)$ has the shape of the hysteresis loop characteristic of ferromagnets (Fig. 3), which suggests that there is magnetic order in this temperature range. For the Cu–UDD samples, the coercivity determined by this hysteresis loop is $H_r = 40$ Oe. Thus, the C–Cu system prepared on the basis of UDD with copper exhibits two magnetic phase transitions at $T_{1c} = 130$ K and $T_{2c} = 10$ K.

REFERENCES

1. V. F. Masterov, O. I. Kon'kov, A. V. Prikhod'ko, *et al.*, Pis'ma Zh. Tekh. Fiz. **20** (15), 17 (1994) [Tech. Phys. Lett. **20**, 614 (1994)].
2. V. F. Masterov, B. P. Popov, A. Ya. Aleksenskiy, *et al.*, in *Proceedings of International Workshop on Fullerences and Atomic Clusters, IWFAC'-97* (St. Petersburg, Russia, 1995), p. 127.
3. T. K. Zvonareva, V. I. Ivanov-Omskiĭ, B. P. Popov, and K. F. Shtel'makh, Pis'ma Zh. Tekh. Fiz. **26** (24), 56 (2000) [Tech. Phys. Lett. **26**, 1098 (2000)].
4. K. D. Tsendin and B. P. Popov, Supercond. Sci. Technol. **12**, 255 (1999).
5. A. Abragam and B. Bleaney, *Electron Paramagnetic Resonance of Transition Ions* (Clarendon, Oxford, 1970; Mir, Moscow, 1972).
6. I. Ya. Korenblit and E. F. Shender, Usp. Fiz. Nauk **126**, 233 (1978) [Sov. Phys. Usp. **21**, 832 (1978)].
7. P. Allia, M. Coisson, and P. Tiberto, Phys. Rev. B **64**, 144420 (2001).
8. V. I. Ivanov-Omskiĭ and É. A. Smorgonskaya, Fiz. Tekh. Poluprovodn. (St. Petersburg) **32**, 931 (1998) [Semiconductors **32**, 831 (1998)].

Translated by A. Kazantsev

Influence of Pyridine Molecule Adsorption on Concentrations of Free Carriers and Paramagnetic Centers in Porous Silicon Layers

**L. A. Osminkina^, A. S. Vorontsov, E. A. Konstantinova,
V. Yu. Timoshenko, and P. K. Kashkarov**

Moscow State University, Vorob'evy gory, Moscow, 119899 Russia
^e-mail: osminkina@vega.phys.msu.ru
Submitted July 29, 2004; accepted for publication August 19, 2004

Abstract—The influence of adsorption of donor pyridine (C_5H_5N) molecules on free-hole and defect concentrations in porous silicon layers differing in the morphology of composing nanocrystals and pores, as well as in the boron doping concentration, was studied using infrared and electron spin resonance spectroscopy. It was shown that the dependence of the hole concentration on the pyridine vapor pressure is controlled by the initial boron doping level of porous silicon, while the number of defects, i.e., dangling silicon bonds, is almost unchanged during adsorption for all sample types. For samples on substrates with a boron concentration of ~10^{20} cm^{-3}, a decrease in the number of holes at low pyridine pressures is observed and is attributed to hole capture by surface states of adsorbed C_5H_5N molecules. At pyridine pressures close to the saturated vapor pressure, the hole concentration in porous silicon layers increases, which is associated with hole "trap" depopulation due to an increase in the permittivity of the silicon nanocrystal neighborhood under conditions of C_5H_5N vapor condensations in sample pores. © 2005 Pleiades Publishing, Inc.

1. INTRODUCTION

It is known that equilibrium free carriers can exist in porous silicon (*por*-Si) produced by electrochemical etching of silicon single crystals (see, e.g., [1–3]); the carrier concentration can attain rather large values, ~(10^{17}–10^{19}) cm^{-3}, [4–6]. The number of carriers is very sensitive to the state of surface coating and molecular neighborhood of silicon nanocrystals (*nc*-Si) composing *por*-Si [5–7]. This property is due to the fact that a significant fraction of atoms is arranged at the *nc*-Si surface [2]. The developed interior surface accessible to molecules of a surrounding medium makes *por*-Si a convenient model object for studying fundamental features of adsorption processes [8]. Many recent studies were devoted to the influence that adsorbed molecules, which form negative and positive complexes (e.g., NO_2 [5–7], CO_2 [9], NH_3 [10]) on the *nc*-Si surface, have on the electric and optical properties of *por*-Si. Adsorption of such active molecules can change the conductivity of *nc*-Si (NO_2) by several orders of magnitude or even change its conductivity type (NH_3). However, *por*-Si samples with approximately the same doping level were used in all the cited studies, which did not allow us to determine the role of the dopant in interactions of active molecules with the *nc*-Si surface.

In this study, we use pyridine (C_5H_5N) as an adsorbate, since it can be adsorbed as (C_5H_5N)$^+$ complexes on the solid surface [11]. Such charged complexes can arise on the *nc*-Si surface due to hole trapping or the formation of a chemical bond between C_5H_5N mole-

cules and the *nc*-Si surface. In the latter case, adsorbed molecules can be considered a donor-type impurity. The purpose of this study is to identify mechanisms of C_5H_5N adsorption on the *nc*-Si surface. To this end, infrared (IR) spectroscopy and electron spin resonance (ESR) were used to study the influence of C_5H_5N molecule adsorption on the concentrations of free carriers and defects (paramagnetic centers) in *por*-Si with various boron doping levels.

2. EXPERIMENTAL

Porous silicon samples were formed on single-crystal *p*-Si wafers (*c*-Si) with a (100) surface orientation and resistivity ρ ≈ 1–5 and 10–20 mΩ cm, and 10–20 Ω cm (hereafter indicated as samples I, II, and III, respectively, see table) using conventional electrochemical etching [1, 2] in an HF(48%) : C_2H_5OH (1 : 1) solution at a current density of 50 mA/cm². After completing the pore formation, *por*-Si films were detached from the substrate by a short-term increase in the current density to 500 mA/cm². The film thickness was 30–50 μm. The porosity, determined gravimetrically, was 50–70% (see table). The boron concentration in the prepared samples was approximately equal to the substrate doping level [12]. However, the samples differed in *nc*-Si morphology and nanocrystal and pore sizes. The nanocrystal and pore sizes were ~(15–20) nm (sample I), ~(5–6) and <10 nm (sample II), and ~(2–4) and <10 nm (sample III) [3].

Sample parameters

Sample	Substrate resistivity, Ω cm	Porosity, %	N_p in nc-Si in vacuum, cm^{-3}	N_s in nc-Si in vacuum, cm^{-3}	Highest N_p in nc-Si in a C_5H_5N atmosphere, cm^{-3}
I	0.001–0.005	68	2×10^{19}	4×10^{16}	2.3×10^{19}
II	0.01–0.02	50	4×10^{17}	6×10^{16}	5.7×10^{18}
III	10–20	70	$<10^{16}$	9×10^{16}	$<10^{16}$

Freshly prepared *por*-Si layers were studied in vacuum and in a C_5H_5N atmosphere. C_5H_5N molecules were adsorbed on samples exposed to vacuum at a residual pressure of ~10^{-5} Torr. The event of C_5H_5N molecule condensation was monitored by an increase in the He–Ne laser beam reflectance from the *por*-Si surface. Oil-free vacuum equipment of the Varian Company was used in this study.

Infrared transmission spectra were measured using a Perkin-Elmer RX I Fourier spectrometer in the range of 400–6000 cm^{-1} with a resolution of 2 cm^{-1}. The ESR studies were carried out using a PS_100.X spectrometer with an operating frequency of 9.5 GHz and a sensitivity of 5×10^{10} spin/G. To calculate g factors and defect concentrationss, MgO (with Mn^{++} ions) and CuCl$_2 \cdot$ 2H$_2$O reference samples were used, respectively. The experiments were performed at room temperature.

3. RESULTS AND DISCUSSION

Figure 1 shows the typical spectra of the *por*-Si absorptivity, calculated from transmission (T) spectra using the formula $\alpha(\nu) = -\ln(T)/d$, where ν is the frequency and d is the layer thickness. For samples I in vacuum, along with absorption at surface bonds, a component that varied more gradually with frequency and caused by absorption at free carriers (holes) was observed [5]. In contrast to samples I, samples II featured very weak absorption by free holes and, for samples III, such absorption was not detected within the sensitivity of the method. An analysis of absorption at free carriers in samples I and II suggests that the classical Drude model can be applied in this case. The times of hole scattering in nc-Si with characteristic sizes far from the conditions of the quantum-dimensional effect (samples I and II) are close to those for the c-Si substrate used to prepare *por*-Si. Therefore, the free carrier concentration in the system of silicon nanocrystals can be calculated using the formula

$$N_p = N_{c\text{-Si}} \frac{n}{(1-p)n_{c\text{-Si}}} \frac{\alpha}{\alpha_{c\text{-Si}}}, \qquad (1)$$

where $N_{c\text{-Si}}$ is the free-hole concentration in the c-Si substrate; p is the *por*-Si film porosity; and n, α and $n_{c\text{-Si}}$, $\alpha_{c\text{-Si}}$ are the refractive index and absorptivity of *por*-Si and c-Si, respectively. The values of $n_{c\text{-Si}}$ and $\alpha_{c\text{-Si}}$ are known from published data (see, e.g., [13, 14]).

The hole concentrations for freshly prepared samples, calculated using formula (1), are listed in the table. For samples III, the upper limit of N_p was estimated (see table). We note that, although N_p correlates with the boron concentration in the substrate (i.e. was highest for samples I), it was approximately ten times lower than in the substrate. This circumstance can be explained by hole trapping by *por*-Si defects or by an increase in the ionization energy of boron atoms in silicon nanocrystals in comparison with single crystals [5].
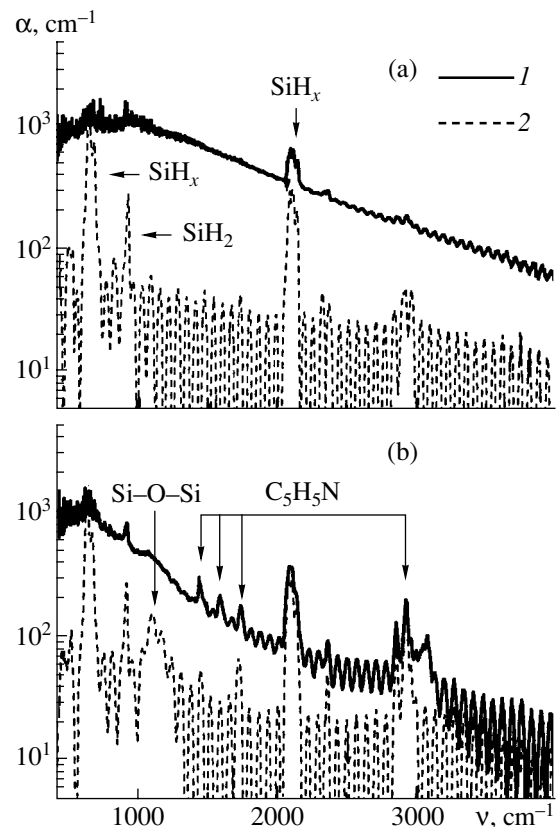
Fig. 1. Absorptivity spectra of sample I under various conditions: (a) in vacuum at a residual pressure of 10^{-5} Torr (*1*) and in pyridine vapor at $P_{C_5H_5N} = 0.1$ Torr (*2*); (b) in pyridine vapor at $P_{C_5H_5N} = 2$ Torr (*1*) and at subsequent pumping out after adsorption (*2*). Arrows indicate the bands corresponding to IR absorption by *por*-Si surface bonds, as well as by adsorbed pyridine molecules.
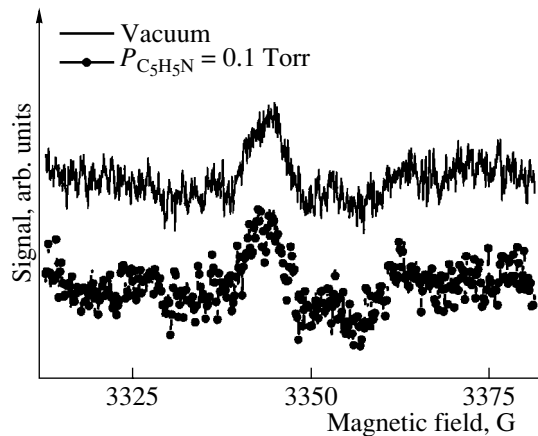
Fig. 2. Electron spin resonance spectra of sample III in vacuum at a residual pressure of 10^{-5} Torr and in an atmosphere of pyridine molecules, $P_{C_5H_5N} = 0.1$ Torr.
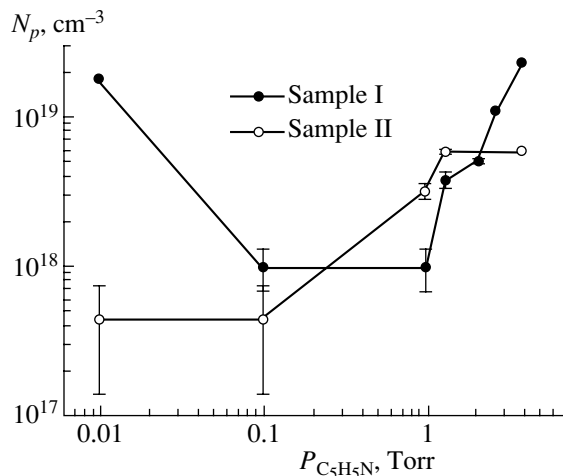
Fig. 3. Dependence of the free carrier concentration on the pyridine molecule pressure for samples I and II.

To clarify this matter, we used ESR to study *por*-Si (Fig. 2). The values of g factors ($g_\perp = 2.0078 \pm 0.0005$ and $g_\parallel = 2.0023 \pm 0.0005$) suggest that detected defects are the P_b centers (defects of the type of dangling silicon bonds at the Si/SiO$_2$ interface) [15]. In freshly prepared *por*-Si, the highest and lowest defect concentrations N_s (recalculated to the nanocrystal volume) were detected in lightly doped sample III and heavily doped sample I (see table), respectively. This means that anticorrelation between the quantities N_p and N_s is observed. This experimental fact can be attributed to hole trapping by *por*-Si defects, which in this case are transformed to a nonparamagnetic state,

$$P_b^0 + h^+ = P_b^+, \qquad (2)$$

where P_b^0, P_b^+, and h^+ represent the defect in the neutral state, defect in a positively charged state, and a free hole in *nc*-Si, respectively.

It was found that pyridine molecule adsorption in samples I at low pressures ($P_{C_5H_5N} < 1$ Torr) results in an irreversible decrease in absorption by free holes in comparison with the freshly prepared sample (cf. curves *1*, *2* in Fig. 1a). For samples II and III, the absorption by free carriers was almost unchanged after adsorption at low pressure $P_{C_5H_5N}$.

An inflow of molecules at higher pressures ($P_{C_5H_5N} > 1$ Torr) for samples I and II was accompanied by an increase in $\alpha(\nu)$ (Fig. 1b, curve *1*). In this case, a reversible change in the absorption by free holes in inflow–evacuation cycles (Fig. 1b, cf. curves *1*, *2*) was observed. Absorption by free carriers in samples III was not detected in a C$_5$H$_5$N atmosphere at all pressures $P_{C_5H_5N}$ used.

Figure 3 shows the free-hole concentrations N_p calculated using formula (1) for *por*-Si layers (samples I and II) in a pyridine atmosphere at various pressures. We can see in Fig. 3 that pyridine molecule adsorption in samples I at low pressures is accompanied by a significant (approximately tenfold) decrease in N_p. This effect can be explained by assuming that charged adsorbed complexes are formed on the *por*-Si surface due to a free hole trapping from the silicon nanocrystal volume. Let us represent this process by analogy with hole trapping by defects (Eq. (2)) as

$$h^+ + C_5H_5N \longrightarrow (C_5H_5N)^+. \qquad (3)$$

Samples II exhibit a low concentrations of free holes (see table), comparable to the lowest value of N_p that can be determined from the $\alpha(\nu)$ spectra. Thus, within the sensitivity of the method, it was impossible to detect changes in N_p during adsorption at low pressures (Fig. 3).

A further increase in an adsorbate pressure resulted in an increase in the free hole concentration in *por*-Si (Fig. 3). This is apparently due to the fact that pyridine is condensed in pores of samples under study at $P_{C_5H_5N}$ close to the saturated vapor pressure. In this case, the effective permittivity of *por*-Si sharply increases, since liquid pyridine has the permittivity $\varepsilon_d = 12.3$ [11]. It is known that filling of pores with a medium with high ε_d ($\varepsilon_d \geq \varepsilon_{Si} = 11.8$, where ε_{Si} is the silicon permittivity) decreases the activation energy of impurity atoms [5], which in turn results in an increase in the free-carrier concentration (holes, in the case under consideration). Indeed, the largest value of N_p is observed in samples I (with the highest boron concentration) (Fig. 3 and table). We note that an increase in N_p with $P_{C_5H_5N}$ in samples II sets in sooner than for samples I (Fig. 3). This fact is explained by the difference in pyridine condensation thresholds, caused by different pore diameters in the samples under study. Indeed, condensation sets in sooner in smaller pores due to the capillary effect. We note that the increase in the free-hole concentration is caused by (along with a decrease in the

activation energy of impurity boron atoms) a decrease in the hole binding energy to traps, i.e., $(C_5H_5N)^+$ complexes and defects (see Eqs. (2) and (3)) during pyridine condensation in *por*-Si pores.

It is noteworthy for comparison that adsorption of donor molecules (by the example of ammonia) on the surface of heavily doped *p*-type *por*-Si was shown to increase the free-electron concentration; i.e., *por*-Si became an *n*-type semiconductor [10]. However, the experimental data we obtained are hardly explained by a conductivity-type change, since an experimentally attainable maximum of N_p increases with the boron doping level of initial *por*-Si. In this case, N_p of samples II becomes close to the doping level of the single-crystal substrate (5.7×10^{18} cm^{-3}). This is caused by small pore diameter in this sample, which results in complete pyridine condensation in pores of the sample.

Since C_5H_5N adsorption significantly affects N_p, the question arises: what is the adsorption form, i.e., whether C_5H_5N molecules are physically sorbed on the *nc*-Si surface or is this a form of chemisorption. This question can be resolved by an analysis of the $\alpha(\nu)$ spectra of absorption bands corresponding to various local surface vibrations. For example, the surface of freshly prepared samples feature Si–H$_x$ bending vibrations with a band peak at 660 cm^{-1}, Si–F bending modes at 866 cm^{-1}, Si–H$_2$ scissor vibrations at 910 cm^{-1}, and Si–H$_x$ ($x = 1, 2, 3$) stretching modes with frequencies of 2070–2170 cm^{-1}. In *por*-Si layers exposed to pyridine molecules at high pressures, absorption at 1430–1757 and 2800–3000 cm^{-1} (Fig. 1b, curve *1*) is observed. These bands correspond to absorption at C–N and C–H stretching vibrations in C_5H_5N molecules [9]. The $\alpha(\nu)$ spectra do not contain lines corresponding to absorption at surface vibrations such as Si–N or Si–C. Thus, analysis of surface chemical bonds and the irreversibility of absorption at free holes at low pressures $P_{C_5H_5N}$ confirms the above conclusion that C_5H_5N molecules are adsorbed with the formation of complexes with charge transfer, but without the formation of covalent bonds with the *nc*-Si surface.

It is noteworthy that the samples were oxidized at high pressure $P_{C_5H_5N}$ (the band corresponding to Si–O–Si bonds at 1050–1100 cm^{-1} [2]). This process seems to be initiated by destruction of *por*-Si pore walls by capillary forces during inflow–evacuation of C_5H_5N molecules at high pressures, which results in oxidation of dangling silicon bonds. Indeed, the ESR experiments showed that the defect concentration remained unchanged in a pyridine atmosphere at low pressures $P_{C_5H_5N}$. However, a certain increase in N_s was observed at higher pressures $P_{C_5H_5N}$, which can be caused by the mentioned oxidation of samples.

4. CONCLUSIONS

As follows from the experimental data obtained, C_5H_5N molecules are adsorbed on the silicon nanocrystal surface in the form of $(C_5H_5N)^+$ complexes without formation of covalent bonds with porous silicon. At low C_5H_5N pressures, the free-hole concentration in the nanocrystal volume decreases due to hole trapping by adsorbed C_5H_5N molecules. At higher pressures, the number of free carriers in porous silicon increases due to a decrease in the activation energy of boron atoms and hole traps on the silicon nanocrystal surface. The defect concentration during pyridine adsorption remained almost unchanged.

REFERENCES

1. A. Uhlir, Bell Syst. Tech. J. **35**, 333 (1956).
2. W. Theiß, Surf. Sci. Rep. **29**, 91 (1997).
3. V. Lehmann, R. Stengl, and A. Luigart, Mater. Sci. Eng. **69–70**, 11 (2000).
4. V. Yu. Timoshenko, Th. Dittrich, and F. Koch, Phys. Status Solidi B **222**, R1 (2000).
5. V. Yu. Timoshenko, Th. Dittrich, V. Lysenko, *et al.*, Phys. Rev. B **64**, 085314 (2001).
6. L. Boarino, C. Baratto, F. Geobaldo, *et al.*, Mater. Sci. Eng. B **69–70**, 210 (2000).
7. L. Boarino, F. Geobaldo, S. Borini, *et al.*, Phys. Rev. B **64**, 205308 (2001).
8. P. K. Kashkarov, E. A. Konstantinova, and V. Yu. Timoshenko, Fiz. Tekh. Poluprovodn. (St. Petersburg) **30**, 1479 (1996) [Semiconductors **30**, 778 (1996)].
9. M. Rocchia, E. Garrone, F. Geobaldo, *et al.*, Phys. Status Solidi A **197**, 365 (2003).
10. M. Chiesa, G. Amato, L. Boarino, *et al.*, Angew. Chem. **42**, 5031 (2003).
11. A. N. Nesmeyanov and N. A. Nesmeyanov, *The Elements of Organic Chemistry* (Khimiya, Moscow, 1974), Vol. 2, p. 298 [in Russian].
12. G. Polisski, G. G. Dollinger, A. Bergmaier, *et al.*, Phys. Status Solidi A **168**, R1 (1998).
13. V. I. Gavrilenko, A. M. Grekhov, D. V. Korbutyak, and V. G. Litovchenko, *Optical Properties of Semiconductors* (Naukova Dumka, Kiev, 1987) [in Russian].
14. H. Hara and Y. Nishi, J. Phys. Soc. Jpn. **21**, 1222 (1966).
15. E. H. Poindexter, P. J. Caplan, B. E. Deal, and R. Razouk, J. Appl. Phys. **52**, 879 (1981).

Translated by A. Kazantsev

PHYSICS OF SEMICONDUCTOR DEVICES

Design and Fabrication Technology for Arrays for Vertical-Cavity Surface-Emitting Lasers

**N. A. Maleev*^, A. G. Kuz'menkov*, A. E. Zhukov*, A. P. Vasil'ev*,
A. S. Shulenkov**, S. V. Chumak**, E. V. Nikitina*, S. A. Blokhin*,
M. M. Kulagina*, E. S. Semenova*, D. A. Livshits*, M. V. Maksimov*, and V. M. Ustinov***

*Ioffe Physicotechnical Institute, Russian Academy of Sciences, St. Petersburg, 194021 Russia
^e-mail: maleev@beam.ioffe.rssi.ru
**Minsk Institute of Radiomaterials, Minsk, 220024 Belarus
Submitted June 28, 2004; accepted for publication July 12, 2004

Abstract—The design and fabrication technology for integrated arrays for vertical-cavity surface-emitting lasers with bottom AlGaAs/GaAs semiconductor and top AlGaO/GaAs distributed Bragg reflectors is suggested. Arrays containing 8×8 lasers with an active region based on two InGaAs quantum wells were produced. Individual emitters with an oxidized aperture of 8–10 μm in diameter demonstrate cw lasing at 960–965 nm at room temperature, with a threshold current of 1.0–2.5 mA, external efficiency of up to 0.4 mW/mA, and a maximum output power of over 2 mW. © 2005 Pleiades Publishing, Inc.

In recent years, semiconductor vertical-cavity surface-emitting lasers (VCSELs) have found wide application in high-speed fiber-optic communication systems, optical sensors, and information processing devices [1]. The principal advantages of VCSELs as compared to standard stripe-type injection lasers is a low angular divergence and symmetric far-field pattern of emission, batch fabrication technology, and the possibility of device testing directly on the wafer. Planar technology of VCSELs allows the formation of 2D arrays with a large number of individually addressed emitters. These array emitters are seen as the most promising emitters for optical commutation of electronic units in future-generation high-power computer systems [2], design of optical vector processors [3], and high-speed multiplexers for neural networks [4].

Distributed Bragg reflectors (DBRs) are used as mirrors that bound vertical Fabry–Perot microcavities in VCSELs. The widespread design includes doped semiconductor DBRs based on alternating quarter-wave $Al_xGa_{1-x}As$ layers of varied composition. In these devices, carriers are injected into the active region by the current flowing directly through the mirrors. In this case, insulating implantation of protons or selective oxidation of buried AlGaAs layers (the formation of the aperture) is used for lateral spatial confinement of the active region in VCSELs [1, 5]. However, the formation of DBRs with low resistance requires using complicated profiles of doping and composition on the layer interfaces, which have to be controlled with high precision [1]. Furthermore, obtaining low stray capacitance in devices with doped reflectors is rather difficult, and this factor can limit their working frequency range; in addition, the large thickness of doped DBRs hinders

heat removal from the active region and complicates etching of the insulating mesa.

In the last few years, the design of VCSELs with nonconducting mirrors has been actively developed. In this type of devices, one or both contacts are made to conducting layers directly adjacent to the active (emitting) region of VCSEL (intracavity-contacted VCSELs, ICVCSELs) [1, 6]. In particular, this approach was successfully employed in the fabrication of VCSELs with the active region based on an array of self-organized quantum dots (QD) [7], where minimum optical loss in the microcavity is required. Furthermore, since both contact pads in this case are located on the face of the structure, ICVCSELs are ideally suited for flip-chip mounting with the emission outlet protruding through the substrate. This configuration is widely used in the integration of array emitters based on VCSELs and digital silicon integrated circuits [5]. However, successful implementation of VCSELs with nonconducting epitaxial mirrors is possible only with high-precision etching of deep multistage mesastructures.

A new interesting approach in ICVCSEL technology is the use of mirrors based on AlGaO/GaAs, which are formed by lateral selective oxidation of $Al_xGa_{1-x}As$ layers with high Al content x in H_2O vapor [8]. A significant difference in the refractive indices of materials for DBR with oxidized layers makes it possible to provide the necessary reflectivity in a wide range of wavelengths, with a significantly reduced number of pairs of quarter-wave layers. At the same time, to provide the prescribed oxidation rates, a thorough calibration of the composition of layers in the epitaxial structure is necessary. This factor is especially critical when oxidized mirrors and current apertures are formed in the same

process, as well as in the production of VCSEL arrays, when a 100% product yield within the array crystal is required. Another serious problem in designing array emitters is ensuring the possibility of flip-chip mounting; for this, all the contact pads must be metallized in such a way that they have the same height. This raises extra demands on the mechanical reliability of mirrors with oxidized layers.

Earlier [9, 10], we developed discrete VCSELs with an active region based on InGaAs quantum wells (QWs), a bottom semiconductor DBR and a top DBR with oxidized layers; these devices demonstrated cw lasing at room temperature with a threshold current of 0.5–1.5 mA, external efficiency of up to 0.5 mW/mA, and a maximum output power of up to 3 mW. Now we present a report on the design and fabrication technology of a VCSEL array with nonconducting mirrors, which contains 8×8 emitters with individual addressing.

Figure 1 shows the design of an individual laser emitter for VCSEL arrays. It is based on the design of aVCSEL with the bottom semiconductor DBR of undoped AlGaAs/GaAs and top AlGaO/GaAs DBR, suggested earlier [9]. The principal distinction as compared to a discrete device is the positioning of the p-contact pad directly on the surface of the AlGaO/GaAs DBR over the active region. In the case of flip-chip mounting, this design improves the heat removal from the active region. Further, in the suggested design the metallization layers of both contact pads lie at the same height, which makes the flip-chip mounting significantly simpler. In this design, etching of the third (insulating) mesa or the insulating implantation is not necessary.

VCSEL structures with active region based on InGaAs QWs were MBE-grown on semi-insulating (001) GaAs substrates in a laboratory Riber 32P machine. A typical epitaxial structure consists of the top undoped DBR, which contains seven pairs of GaAs/$Al_{0.97}Ga_{0.03}As$ layers, an inhomogeneously-doped p-GaAs contact layer, a top p-$Al_{0.98}Ga_{0.02}As$ aperture layer with graded composition on the borders, an undoped active region with two $In_{0.15}Ga_{0.85}As$ QWs in an $Al_{0.15}Ga_{0.85}As$ array, a bottom n-$Al_{0.98}Ga_{0.02}As$ aperture layer with graded composition on the boundaries, a contact n-GaAs layer, and a bottom DBR that contains 19 pairs of $Al_{0.9}Ga_{0.1}As$/GaAs layers. The thickness of the AlGaAs and GaAs layers in the bottom DBR, of the aperture layers, and of the GaAs layers in the top DBR approximately corresponds to 1/4 of the resonance wavelength λ_{Bragg} of the vertical microcavity. The thicknesses of $Al_{0.97}Ga_{0.03}As$ layers in the top DBR are chosen so that, after oxidation, they correspond to $1/4\lambda_{Bragg}$ (taking into account the variation in the refractive index and some mechanical compression after oxidation). The total thickness of the cavity, L_{cav}, approximately corresponds to $5\lambda_{Bragg}$. In several structures, additional $Al_{0.9}Ga_{0.1}As$ and GaAs layers of ~$2\lambda_{Bragg}$ in
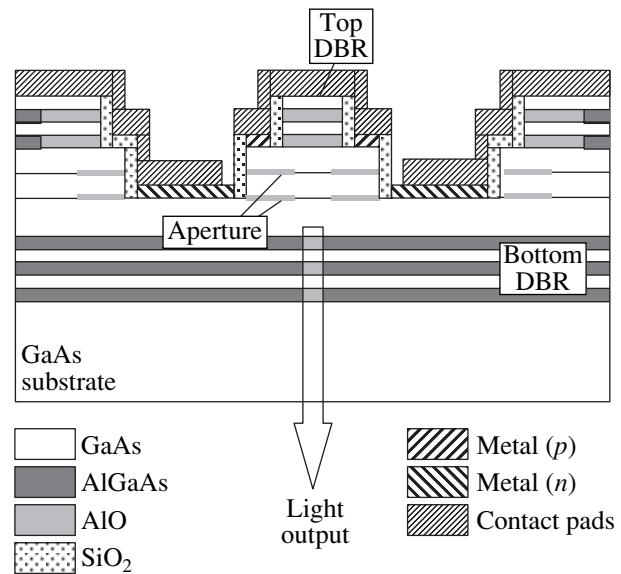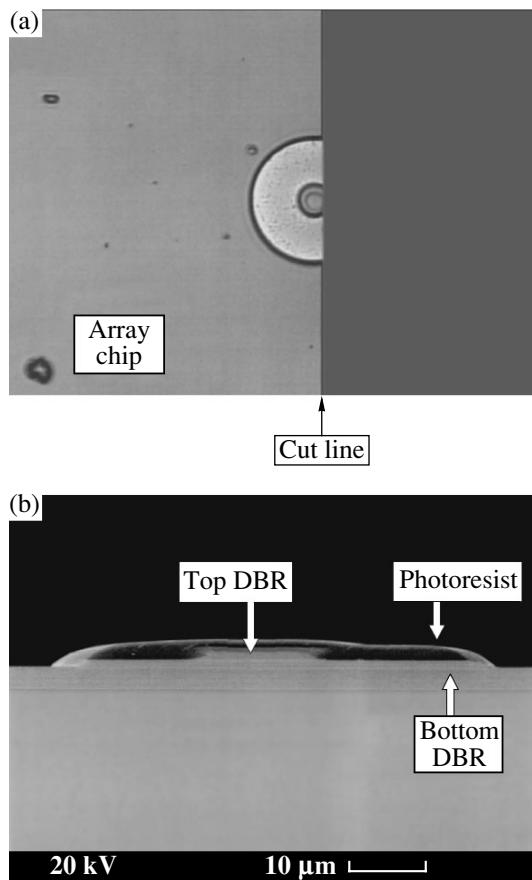

Fig. 1. Cross section of an individual laser emitter with the bottom semiconductor DBR and top DBR with oxidized layers, which is used as a base element for a VCSEL array.

thickness were grown between the substrate and bottom semiconductor DBR; they were used as stop-layers in the chemical etching of through windows in the substrate, destined for the emission output.

The main problem in the epitaxial growth of VCSELs is the necessity of high-precision (not worse than 1%) control of the thickness and composition of layers [1]. Preliminary calibration does not always provide the necessary precision due to possible fluctuations in the growth rate and position of the substrate holder, especially when laboratory-type MBE machines are used. To ensure reproducibility of the prescribed resonance wavelength, the procedure suggested earlier [10] was used, which is the interruption of growth after the formation of the active region, measurement of the reflection spectrum from a partially formed epitaxial structure in the high-vacuum chamber of the MBE machine, and introduction of necessary corrections into the growth modes of the top mirror.
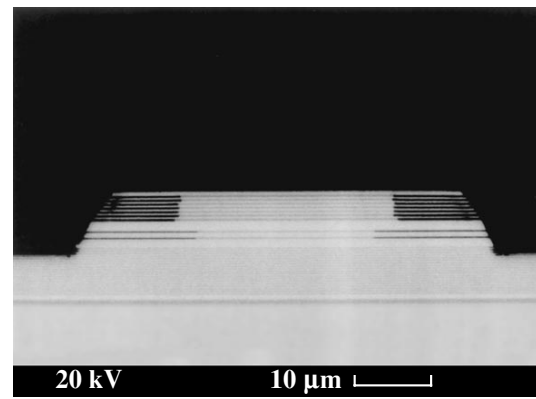
The list of the most critical operations in VSCEL technology includes high-precision etching of multi-step mesastructures and selective oxidation of AlGaAs layers. In this study, we relied on the earlier derived dry etching technique of ion-beam milling with Ar^+ ions [7, 10], which ensures reproducible depth of etching and the prescribed slope of the mesastructure walls. As applied to the technology of array emitters, the most critical is the formation of a stable photoresist mask, which provides a reliable overlapping of a nonplanar profile formed after the etching of the first mesa. Figure 2 shows a micrograph of the surface and a cross-sectional SEM image of a VCSEL mesastructure after the etching of the second mesa. The derived methods of photolithography and dry etching satisfy the claim.

Fig. 3. Cross-sectional SEM image of an optimized VCSEL structure after test etching and selective oxidation.

Fig. 2. VCSEL structure after the formation of a two-step mesastructure by dry etching with Ar^+ ions. (a) Micrograph of the surface; (b) cross-sectional SEM image.

A specific feature of the derived technology for production of VCSEL arrays is the simultaneous formation of oxidized apertures and oxidation of the top reflector layers. Since the aperture diameter must be much less than the size of the top mirror, a careful matching of the oxidation rates in different layers of the epitaxial structure is necessary. A mismatch between the oxidation rates of the aperture layer and top reflector results either in the aperture "collapse" (i.e., total nonoperability of the device), or in a strong "overoxidation" of the top DBR. Overoxidation reduces the reflectivity of mirrors owing to degradation of their morphology, and also impairs the mechanical stability of structure due to extremely strong compression of layers [11]. Therefore, elaboration of technology for array emitters with AlGaO/GaAs DBR is possible only after a thorough comprehensive optimization of the device design and of the parameters of selective oxidation.

The selective oxidation process was calibrated using special test structures and real VCSELs, which allowed a direct measurement of the oxidation rate for DBR and aperture layers. Figure 3 shows the cross-sectional SEM image of an optimized VCSEL structure subjected to selective oxidation for 30 min at 400°C tem-perature. The mesa-structure was etched with a mask in the form of stripes 60 μm in width. Oxidized AlGaAs layers are darker than unoxidized ones. The thickness and composition of oxidized layers were chosen so that the layers of the top reflector were oxidized slower (by a factor of 1.3–1.5) than the aperture layers. Since in the real device the diameter of the top mirror mesastructure is ~30 μm, and that of the aperture mesastructure is ~55 μm, the chosen ratio of the oxidation rates ensures that the oxidation of the top reflector is complete well before the apertures are oxidized to a diameter of 8–10 μm. However, the chosen time of oxidation is not too long as compared to the time of full oxidation of DBR layers, which prevents "overoxidation." It is necessary to stress that the oxidation depth depends not only on the composition of AlGaAs layers, but also on their thickness, which offers an additional degree of freedom in designing an epitaxial VCSEL structure [8]. On the whole, the optimized technology of selective oxidation provides a sufficient reproducibility of the process parameters and a good mechanical stability of VCSEL structures.

After the etching of mesas and selective oxidation, the device structure was passivated with a SiO_2 layer 0.2 μm in thickness, contact windows were opened, *p*- and *n*-type ohmic contacts were formed based on AuZn and AuGe/Nu/Au, respectively, and metallic contact pads based on Cr/Au were produced, with a total thickness of 1 μm. Current–voltage, light–current, and spectral characteristics of the produced VCSEL arrays were measured directly on the wafer in CW mode at room ambient temperature without additional cooling (the emission output through the substrate, without etching of through openings). To measure the far-field pattern of the emission, separate crystals of arrays of laser diodes were mounted onto crystal holders.

Figure 4 shows current–voltage and light–current characteristics of individual laser emitters. The best individual VCSELs with an oxidized aperture of 8–10 μm in diameter demonstrated cw lasing at room temperature with a threshold current of 1.0–2.5 mA, external
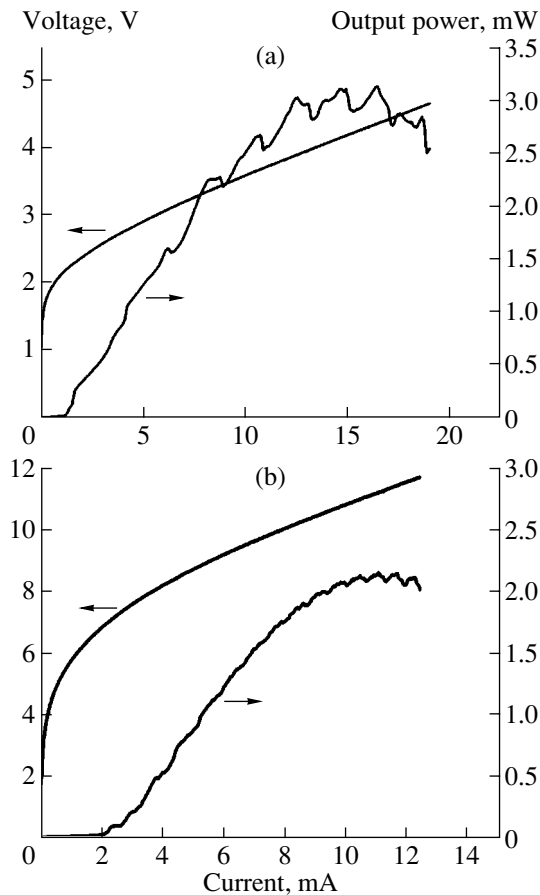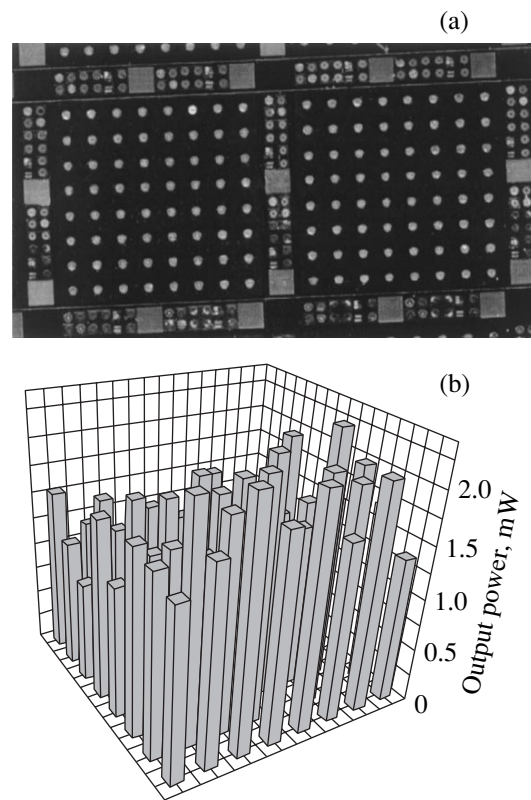
Fig. 4. Current–voltage and light–current characteristics of individual VCSELs: (a) a standard device conforming to the design objectives; (b) a device with higher series resistance.

Fig. 5. (a) Photograph of a crystal with 8×8 array of VCSEL emitters; (b) the distribution of output power of individual VCSELs over the area of one of the produced array emitters.

efficiency of up to 0.4 mW/mA, and a maximum output power of up to 2.5 mW (Fig. 4a). The produced device structures are mechanically stable. Figure 4b shows current–voltage and light–current characteristics of an individual emitter with a high threshold voltage and high series resistance. Poor electrical characteristics are presumably related to too deep etching of the second mesa and/or too weak doping of the contact n-layer in this sample. Nevertheless, even with poor electrical characteristics, this VCSEL yields a cw output power of up to 2 mW (with a dissipated power of over 100 mW), which can be attributed to the presence of a contact metallic layer directly on the top mirror, which facilitates heat removal from the active region.

Figure 5a shows a photograph of crystals with array emitters. Samples of 8×8 laser arrays were produced with a 100% yield, the step between individual VCSELs was 750 μm. Figure 5b shows the distribution of the output power of individual VCSELs over the area of one of the produced array emitters.

The study suggests a design and fabrication technology of VCSEL arrays with combined mirrors (the bottom DBR is based on $Al_{0.9}Ga_{0.1}As/GaAs$, and the top

DBR, on AlGaO/GaAs), and two oxidized apertures. The design of the VCSEL epitaxial structure and technology of selective oxidation are optimized, which makes possible simultaneous oxidation of the aperture layers and DBRs, with the necessary mechanical stability of VCSEL structures ensured. 8×8 VCSEL arrays are produced, with the active region based on InGaAs QWs. Individual emitters demonstrate cw lasing at 960–965 nm at room temperature, with a threshold current of 1.0–2.5 mA, external efficiency of up to 0.4 mW/mA, and a maximum output power of over 2 mW. The derived technology is a promising candidate for developing array emitters for high-speed optical commutation of electronic devices in future-generation computer systems.

REFERENCES

1. *Vertical Cavity Surface Emitting Lasers,* Ed. by L. A. Coldren, H. Temkin, and C. W. Wilmsen (Cambridge Univ. Press, Cambridge, 1999).

2. D. V. Plant, M. B. Venditti, E. Laprise, *et al.*, J. Lightwave Technol. **19**, 1093 (2001).

3. *Optical Processor EnLight256: Publicity of the Lenslet Company* (2003).

4. M. R. Taghizdeh and A. J. Waddie, IEEE Circuits Devices Mag., No. 11, 17 (2002).

5. K. D. Choquette and H. Q. Hou, Proc. IEEE **85**, 1730 (1997).

6. D. L. Huffaker and D. G. Deppe, IEEE Photonics Technol. Lett. **11**, 934 (1999).

7. V. M. Ustinov, A. E. Zhukov, A. Y. Egorov, and N. A. Maleev, *Quantum Dot Lasers* (Oxford Univ. Press, Oxford, 2003).

8. K. D. Choquette, K. M. Geib, C. I. H. Ashby, *et al.*, IEEE J. Sel. Top. Quantum Electron. **3**, 916 (1997).

9. N. A. Maleev, A. R. Kovsh, A. P. Vasil'ev, *et al.*, in *Proceedings of 4th Belarussian–Russian Workshop on Semiconductor Lasers and Systems* (Minsk, 2002), p. 111.

10. N. A. Maleev, A. R. Kovsh, A. E. Zhukov, *et al.*, Fiz. Tekh. Poluprovodn. (St. Petersburg) **37**, 1265 (2003) [Semiconductors **37**, 1234 (2003)].

11. V. A. Haisler, F. Hopfer, R. L. Sellin, *et al.*, Appl. Phys. Lett. **81**, 2544 (2002).

Translated by D. Mashovets

A Study of Carrier Statistics in InGaN/GaN LED Structures

**D. S. Sizov^, V. S. Sizov, E. E. Zavarin, V. V. Lundin, A. V. Fomin,
A. F. Tsatsul'nikov, and N. N. Ledentsov**

Ioffe Physicotechnical Institute, Russian Academy of Sciences, St. Petersburg, 194021 Russia
*^e-mail: Dsizov@pop.ioffe.rssi.ru*
Submitted July 5, 2004; accepted for publication July 12, 2004

Abstract—The carrier statistics in LED structures with ultrathin multilayer InGaN insertions in a GaN matrix was studied. The optical data obtained indicate that an array of quantum dots (QDs) is formed in these structures. The QDs are scattered in size, which leads to an inhomogeneous broadening of the energy spectrum of carriers localized in the QDs. It is shown that, despite the suppressed transport of carriers between QDs, carriers are distributed among the levels of the QD array quasi-statistically at temperatures of about room temperature and higher. This makes it possible to describe the carrier injection and recombination in the device structures studied in terms of quasi-Fermi levels for electrons and holes. © *2005 Pleiades Publishing, Inc.*

1. INTRODUCTION

At present, InGaN/GaN structures are widely used in industry for creating light-emitting devices (LEDs and lasers) for the visible spectral range. Device structures based on gallium nitride are most frequently grown on sapphire substrates because of their comparatively low production cost. The strong lattice mismatch between a sapphire substrate and a growing layer leads to appearance of a large number of threading defects (dislocations, domain boundaries). Being nonradiative recombination channels, these defects adversely affect the optical properties of a structure. However, the influence of defects on the emission efficiency can be diminished by suppressing the carrier transport [1, 2]. It has been shown that, in deposition of thin InGaN layers, the solid solution typically undergoes phase decomposition and there appear layer thickness fluctuations, which leads to formation of quantum dots (QDs) in the structures. A specific feature of heterostructures based on wide-bandgap semiconductor compounds is the high energy of band offsets. In addition, heterostructures based on nitrides of Group-III elements have strong built-in fields at heterointerfaces. For these reasons, the localization depth of an electron–hole pair (i.e., the sum of localization energies of an electron and a hole) may exceed 1 eV. Thus, the strong three-dimensional (3D) localization of carriers on quantum-confined levels in InGaN/GaN QDs suppresses the nonradiative recombination, which makes it possible to obtain high-efficiency light-emitting devices [3] even at a dislocation density of $\sim 10^9$ cm^{-2}. Barriers that confine the lateral motion of carriers (i.e., that in the plane of the InGaN layer) are created by InGaN regions with a lower content of In and a wider band gap as compared to the QDs. The question as to what the height of these barriers is remains insufficiently studied. However, there is evidence that these barriers are high [1].

As the localization depth may exceed severalfold the characteristic value of $k_b T$ (k_b is the Boltzmann constant, and T is temperature) at room temperature, the question of the statistics of carrier distribution over localized levels in QDs remains open. As shown in [4], structures emitting in the UV spectral range show, as temperature increases from 80 to 300 K, a decrease in the relative intensity of the short-wavelength edge of the photoluminescence (PL) line and a considerable decrease in the integral emission intensity are observed. This is indicative of a more intensive thermal escape of carriers from QDs, with their subsequent capture to nonradiative recombination centers. In [5], the influence exerted by an external electric bias on the PL of LED structures that emit in the blue spectral range, i.e., having a stronger localization of carriers than that in the preceding case, was studied. It was shown that the bias affects the intensity only slightly at low temperatures. When temperature is raised to 100 K, the effect of the external bias becomes considerably stronger. These data indicate that carriers are rapidly captured into InGaN QDs at low temperatures, that there are thermally activated, delocalized carriers in the matrix at higher temperatures, and that these carriers are separated by the field of the p–n junction. Application of a negative bias makes the separating field stronger, which leads to depletion of the active region and thereby diminishes the PL efficiency. In [6], a theory that describes the behavior of carriers on levels of QDs and the matrix was developed. This theory takes into account the nonuniform size distribution of QDs (and, therefore, the nonuniformly distributed positions of quantum-confined levels) and the thermal escape of carriers from these levels into the matrix. It was shown that, in the case when temperature exceeds a certain temperature characteristic of a given system, the carrier distribution among the QD levels obeys the Fermi law,
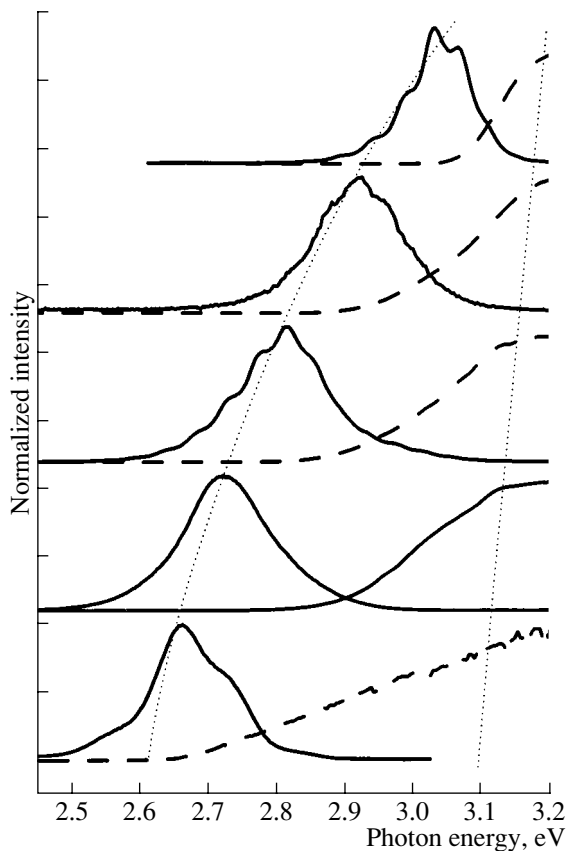
Fig. 1. Spectra of PL (solid lines) and photocurrent (dashed lines) for structures with different average In concentrations in the active region (In concentration increases from top downwards) and different localization energies. $T = 300$ K.

with quasi-Fermi levels considered for the ensembles of electrons and holes. This model has been applied previously for describing the behavior of carriers in QDs formed in the InGaAs/GaAs system by the Stranski–Krastanow mechanism [7]. It was shown, in particular, that raising the temperature in this system leads to an increase in the concentration of delocalized carriers and in the rate of their nonradiative recombination via defects in the matrix. Thus, raising the temperature makes QDs more sensitive to the presence of nonradiative channels in the matrix.

In this study, the carrier statistics in InGaN/GaN QD structures was examined and it is shown that, at temperatures of about room temperature and higher, the rate of thermal activation exceeds that of carrier recombination, which corresponds to the case of a quasi-equilibrium statistical distribution of carriers among the QDs and the residual InGaN quantum well (QW). This fact makes it possible to describe the system in a certain approximation in terms of quasi-Fermi levels. At the same time, a pronounced departure from equilibrium is possible in the case of QDs with a large localization depth. Data pertinent to this problem will be considered in further publications. We also examined the influence

exerted by nonradiative recombination centers on the PL efficiency at various temperatures. In addition, we analyzed in detail the effect of an external bias on the carrier statistics near the active region.

2. EXPERIMENTAL

The structures studied were grown by MOCVD on an AIX 2000-HT machine. The active region of the structures was grown on a GaN buffer layer in the form of several 3-nm-thick InGaN layers separated by Si-doped GaN barrier layers. The structures were studied by PL and electroluminescence (EL) methods and photocurrent spectroscopy. Some of the structures were specially grown to be studied by the PL technique. In these structures, the active region was overgrown with a 50-nm-thick GaN layer and a thin AlGaN layer to prevent current leakage to the surface. In the LED structures, the active region was situated within a *p–n* junction, whose *n*- and *p*-type layers were doped with silicon and magnesium, respectively. The LED structures were also studied by the PL method, with the PL of these structures excited and detected from the outer surface of the structure and an external bias applied via a semitransparent *p*-NiAu contact. The PL was excited with a cw He-Cd laser or a pulsed N_2 laser with a pulse width of 10 ns. The photocurrent was induced with a gas-discharge Xe lamp.

3. RESULTS AND DISCUSSION

Figure 1 shows PL and photocurrent spectra of structures with various In concentrations in the InGaN layers. It is known that raising the In concentration leads to a longer emission wavelength because of the higher energy of carrier localization between QD levels and the GaN matrix. This may, in turn, be due both to an increase in the depth of the InGaN QW and to a rise in the energy of carrier localization between the QD levels and the QW. This energy can be evaluated by analyzing the Stokes shift [8], which is equal in the case in question to the difference between the photon energies corresponding to the emission peak and to the beginning of the gently sloping portion in the curve for the photocurrent (dotted lines in Fig. 1). This consideration is based on the following. At a sufficiently high rate of thermal activation and extraction of electrons and holes photoinduced in the active region (when spontaneous reemission can be disregarded), the shape of the photocurrent spectrum is determined by the product of the density of states in a QD and the overlap integral of wave functions of electrons and holes in the QD. At the same time, in the case of an effective carrier transport caused by thermal activation, QD states with the highest localization energy are occupied (taking into account the quasi-equilibrium statistical distribution). However, in the case when the localization energy exceeds some critical value, the thermal escape from such deeply localized states is unlikely [6], which

leads to some other dependence of the emission peak position and of the shape of the photocurrent spectrum on the electronic spectrum of the structure. Thus, the result obtained in evaluating the localization depth of carriers in QDs by analysis of the Stokes shift depends on the carrier statistics.

In the set of the structures studied, the strongest carrier localization was observed, as expected, in a structure with an emission wavelength of 460 nm: this structure has the longest emission wavelength and the maximum Stokes shift. We studied the optical properties of this structure in order to determine the statistics of capture and escape of carriers. A structure with an identical active region, but no *p–n* junction, was grown for a PL study.

Both structures have the same wavelength and line width of PL. Figure 2 shows photocurrent and PL spectra for the LED and optical structures, respectively. The PL spectra clearly demonstrate a sinusoidal modulation associated with the interference of light in the Fabry–Perot resonator constituted by the heterointerface between the epitaxial layer and the sapphire substrate and by the surface of the epitaxial layer. The modulation is less pronounced in the photocurrent spectra because of the poorer resolution of the corresponding spectrometer. As temperature increases, the photocurrent grows and the PL intensity decreases. This result can be understood in terms of the concept that the concentration of delocalized carriers becomes higher as temperature is increased. On the one hand, this favors capture of carriers by nonradiative traps and thereby makes the nonradiative recombination stronger. On the other hand, delocalization of carriers favors their separation by the field of the *p–n* junction. It is, however, important to note that the shape of the photocurrent edge remains unchanged within the experimental error when the temperature is elevated (whereas the edge itself is shifted to longer wavelengths because of the decrease in the band gap). This indicates that an effective thermal activation occurs in localized states, i.e., an electron–hole pair generated at levels with any localization depth (within the range under study) passes into the matrix to be separated there by the *p–n* junction before recombining. This is the case when the time of radiative recombination is considerably longer than the time of thermal activation or that of phonon relaxation; in other words, this occurs if carriers are quasi-statistically distributed over quantum-confined levels. Another explanation of this phenomenon is the possible tunnel extraction of carriers, which must be temperature-independent. Data useful in explaining the effect observed are considered below.

As already noted, thermal filling of excited states in InGaN QDs enhances carrier transport (including that to nonradiative recombination centers) and makes less steep the short-wavelength edge of the PL spectrum. At a low pumping density (~1 W/cm^2), the occupancy of the levels is low and the system is close to equilibrium in the case of a statistical distribution. If the time of
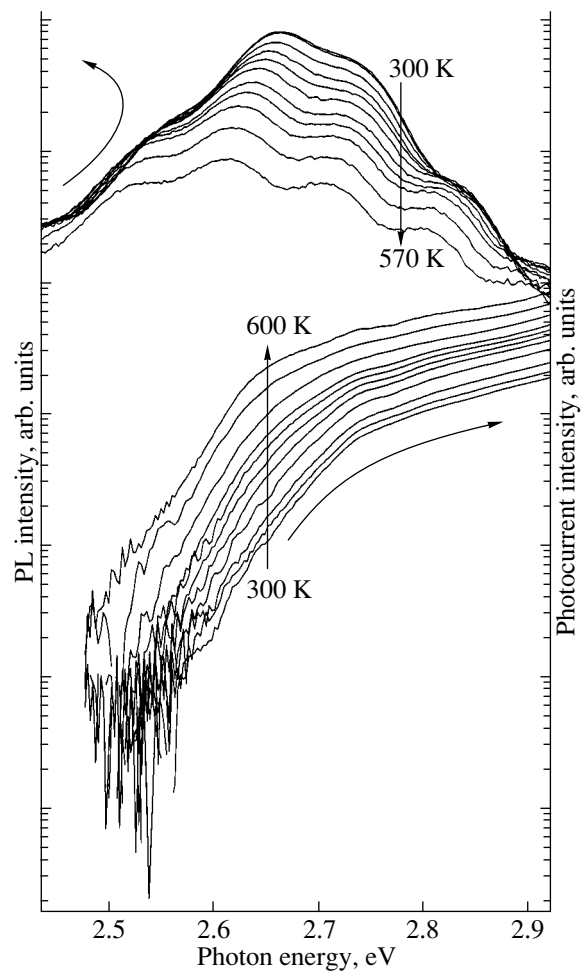
Fig. 2. Spectra of photocurrent and PL for QD structures at room temperature and above. The arrows show the directions in which the photocurrent increases and the PL intensity decreases as temperature is raised.

radiative recombination is assumed in this case to be weakly dependent on the transition energy [9], then the short-wavelength edge of the PL line must be described by the relation $I = Ap(E)\exp(-E/k_bT)$ [4]. Here, I is the emission intensity, A is a constant, and the function $p(E)$ is the ratio between the density of states with corresponding energy E of the electron–hole transition and the radiative-recombination lifetime. The function $p(E)$ can be found in relative units from photocurrent spectra [4, 7]. With the density-of-states function determined in this way, the shape of the short-wavelength edge of PL is indeed close to the calculated one (Fig. 3). This confirms the existence of a statistical distribution of carries in these structures.

To determine the position of quasi-Fermi levels in the active region, PL spectra were measured in relation to the pumping density. As can be seen in Fig. 4, the position of the emission peak remains virtually invariable at comparatively low pumping densities ($\leq$144 W/cm^2). We believe that this case corresponds to
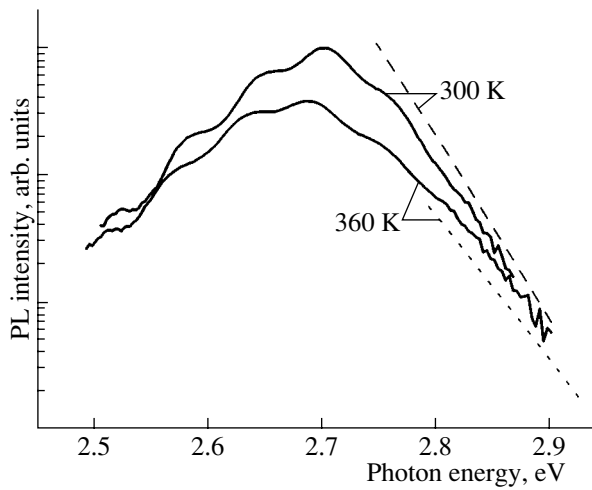
Fig. 3. Comparison of the experimental PL spectra (solid lines) and results of an approximation calculation (dashed lines) at the short-wavelength edge.

Fig. 4. Variation in the shape of the PL spectrum at pumping densities sufficient for filling of the QD levels. Pumping power density: (*1*) 75, (*2*) 144, (*3*) 275, (*4*) 422, and (*5*) 1000 W/cm^2. T = 300 K.

a position of quasi-Fermi levels below (or above, for the valence band) the carrier localization levels in InGaN. As the pumping density is raised to more than 144 W/cm^2, a short-wavelength shift of the line and its broadening are observed. Such a change in the shape of the spectrum is due to occupation of excited levels in QDs and to filling of QD levels with a lower localization depth. In the case of a Fermi distribution of carriers over states in the QD array, the filling of deeply localized states leads to occupation of localized states with a smaller localization depth, with the quasi-Fermi level for electrons going up and that for holes going down. Because the photocurrent, which is proportional to $p(E)$, grows as the transition energy becomes higher, such a shift of the quasi-Fermi levels leads to an increase in the number of states involved in the emission process. The time of radiative recombination for structures of this kind is commonly ~10^{-9} s. If the pumping density at which the shape of the PL spectrum starts to change is known, we can evaluate the density of states in QDs to be about 10^{12} cm^{-2}, in agreement with the data on the density of QDs in structures of this kind, furnished by transmission electron microscopy [1].

We also studied the effect of a reverse bias on the carrier statistics in the active region of an LED structure. For this purpose, the PL was measured for an LED structure to which an external bias was applied. At high temperatures, carriers are separated by the field of the *p–n* junction. The external bias distorts the band diagram of the structure and affects the separation of carriers. Figure 5 shows how the integral PL intensity depends on the applied external bias at different temperatures. A more detailed dependence is presented for room temperature. Three portions can be distinguished in the curve describing this dependence. The first portion corresponds to an exponential decrease in the PL intensity, observed at reverse biases. We attribute this
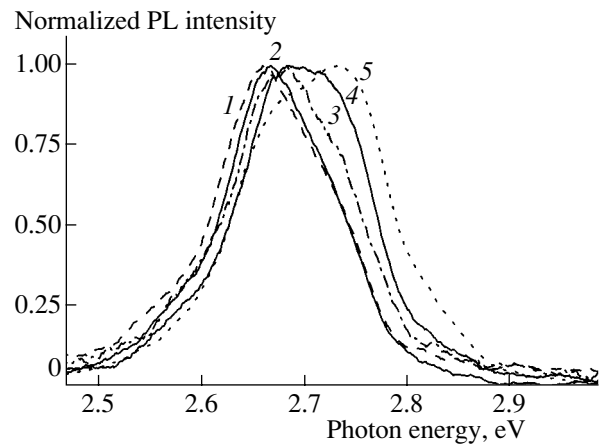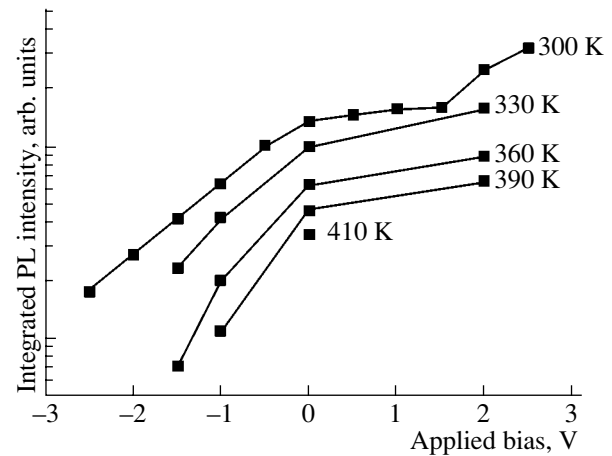
Fig. 5. Effect of bias on the PL intensity at different temperatures.

behavior to an increase in the strength of the separating field of the *p–n* junction. The second portion corresponds to a weak increase in the PL intensity at positive biases lower than 1.5 V. We believe that a bias in this range only slightly distorts the field near the *p–n* junction and has little effect on the carrier separation. At positive biases exceeding 1.5 V, a stronger rise in intensity is observed. The behavior of the PL in the last portion may be due to injection of nonequilibrium carriers into the active region. These carriers are generated in the *p*-region and cannot penetrate into the active region in the absence of a positive bias because of the separating field of the *p–n* junction. This assumption is confirmed by the fact that an exceedingly weak, but detectable EL is observed at positive biases exceeding 1.5 V. Raising the temperature enhances the effect of carrier delocalization and consequently leads to a stronger carrier separation by the field of the *p–n* junction. Despite

the fact that the energies of carrier localization are the same in the structure without a *p–n* junction and in the LED structure, the temperature dependence of the emission intensity in the LED structure is stronger, which is accounted for by an additional channel of non-radiative loss because of the carrier separation by the field of the *p–n* junction.

At a negative bias, the temperature dependence is stronger to an even greater extent (which is equivalent to a stronger dependence of the carrier separation on the reverse bias at higher temperatures). Thus, it may be assumed that the external bias causes carrier depletion (or accumulation) only for statistically delocalized carriers, and an increase in temperature makes their fraction larger, thereby leading to a stronger influence of the bias on the carrier statistics. Further, as the concentrations of localized and delocalized carriers at equal temperatures are interrelated, the effects described affect the emission intensity. If tunnel effects are also involved in these processes, they are temperature-dependent, i.e., particles cannot tunnel directly from the *p*-region of the structure to a localized level in a QD or backwards.

4. CONCLUSIONS

We studied the electronic and optical properties of InGaN/GaN QD structures in the temperature range 300–600 K. It was shown that the rate of thermal activation and relaxation of carriers exceeds the recombination rate in the temperature range studied, which results in a carrier distribution over QD levels that is close to the Fermi distribution.

Owing to the statistical carrier distribution, non-equilibrium carriers occupy the most deeply localized QD states. As a result, a narrow emission line corre-

sponding to transitions between QD levels with the largest localization depth is observed even at a strongly pronounced nonuniformity of the electronic spectrum of QDs. At the same time, the 3D localization of carriers suppresses the lateral transport toward defects, which provides a relatively high temperature stability of devices with a QD-based active region. In our opinion, it is important to take these specific features of the behavior of carriers in the InGaN/GaN system into account in simulation of injection and recombination processes in LED structures.

REFERENCES

1. I. L. Krestnikov, N. N. Ledentsov, A. Hoffmann, *et al.*, Phys. Rev. B **66**, 155310 (2002).

2. S. Chichibu, T. Sota, K. Wada, and S. Nakamura, J. Vac. Sci. Technol. B **16**, 2204 (1998).

3. T. Mukai, M. Yamada, and S. Nakamura, Jpn. J. Appl. Phys. **38**, 3976 (1999).

4. K. L. Teo, J. S. Colton, P. Y. Yu, *et al.*, Appl. Phys. Lett. **73**, 1697 (1998).

5. H. Kudo, T. Tanbe, H. Ishibashi, *et al.*, J. Appl. Phys. **89**, 5779 (2001).

6. L. V. Asryan and R. A. Suris, Semicond. Sci. Technol. **11**, 554 (1996).

7. M. V. Maximov, D. S. Sizov, L. V. Asryan, *et al.*, in *Proceedings of 26th International Conference on the Physics of Semiconductors* (Edinburgh, 2002).

8. R. W. Martin, P. G. Middelton, K. P. O'Donnell, and W. Van der Stricht, Appl. Phys. Lett. **74**, 263 (1999).

9. S. F. Chichibu, T. Azuhata, T. Sota, *et al.*, J. Appl. Phys. **88**, 5153 (2000).

Translated by M. Tagirdzhanov

Interfacial and Interband Lasing in an InAs/InAsSbP Heterostructure Grown by Vapor-Phase Epitaxy from Metal–Organic Compounds

A. P. Astakhova, N. D. Il'inskaya, A. N. Imenkov, S. S. Kizhaev^,
S. S. Molchanov, and Yu. P. Yakovlev

Ioffe Physicotechnical Institute, Russian Academy of Sciences, Politekhnicheskaya ul. 26, St. Petersburg, 194021 Russia
^e-mail: serguie@mail.ru
Submitted July 12, 2004; accepted for publication August 9, 2004

Abstract—Sources of coherent radiation are fabricated on the basis of a double InAs/InAsSbP heterostructure, grown by vapor-phase epitaxy from metal–organic compounds, that includes a thick (3.3 μm) active region. The spectral characteristics of diodes with various cavity lengths are studied, and light polarization is measured. It is established that the modes that compose the spectrum of radiation are controlled by radiative recombination at the heteroboundary and in the bulk of the active region. A new mode with a wavelength of intermediate value, lying between the wavelengths of the aforementioned kinds of radiation, is observed if the current exceeds the threshold value by 30%. This intermediate mode presumably results from an interaction between the modes related to the interfacial and interband radiative recombination, which are present in the cavity at the same time. © 2005 Pleiades Publishing, Inc.

1. INTRODUCTION

Sources of infrared (IR) radiation in the wavelength range λ = 3–4 μm have a large number of applications. It is well known that the molecules of hydrocarbons and other commercial and natural gases (CO, CO_2, H_2S, SO_2, NO, and NO_2) absorb IR radiation in the above spectral range. Gas-analysis methods for controlling technological processes and monitoring the environment are developed on the basis of IR emitters. Sources of spontaneous radiation operate stably at room temperature in the wavelength range under consideration; however, sources with a small-width spectrum (10^{-3}–10^{-2} Å) are necessary for certain applications (for example, high-resolution molecular spectroscopy and coherent methods of signal processing). This paper is a continuation of the previous publications concerned with studying the properties of coherent-radiation sources fabricated on the basis of structures grown by vapor-phase epitaxy from metal–organic compounds (MOVPE).

The electroluminescent properties of lasers based on GaInAsSb/GaAlAsSb heterostructures of types I and II were considered in [1]. The mechanisms of radiative recombination in lasers based on InGaAsSb/InAsSbP heterostructures of types I and II were studied by Aĭdaraliev *et al.* in [2]. The interfacial electroluminescence in light-emitting diodes based on InAs/InAsSbP heterostructures was reported in [3]. In this paper, we report the results of studying the coherent radiation of a laser heterostructure that includes a thick active region (the thickness $h \geq 2$ μm) and is grown by MOVPE.

2. EXPERIMENTAL

The light-emitting structure under consideration was grown by MOVPE in a horizontal reactor at atmospheric pressure. The substrate was positioned on a molybdenum substrate holder equipped with a resistive heater. We used InAs substrates that had a (100) crystallographic orientation and were doped with zinc, yielding a hole concentration as high as $p = (5$–$9.4) \times 10^{18}$ cm^{-3}. The epitaxial part of the structure consisted of a $InAs_{0.53}Sb_{0.15}P_{0.32}$:Zn barrier layer with the hole concentration $p = 2 \times 10^{18}$ cm^{-3}, an undoped InAs active region, and an undoped $InAs_{0.53}Sb_{0.15}P_{0.32}$ barrier layer. The concentration of charge carriers (electrons) was $n = 2 \times 10^{16}$ cm^{-3} in the active region and $n = 1.3 \times 10^{17}$ cm^{-3} in the undoped barrier layer. The thicknesses of the epitaxial layers were as follows: the thickness of the InAs active region was 3.3 μm; the thickness of the lower $InAs_{0.53}Sb_{0.15}P_{0.32}$ barrier layer, 3 μm; and the thickness of the upper $InAs_{0.53}Sb_{0.15}P_{0.32}$ barrier layer, 4 μm. The refractive index in the active region exceeded that in the wide-gap layers by $\Delta n = 0.16$.

An energy-band diagram of the grown structure is shown in Fig. 1. The band gap in the $InAs_{0.53}Sb_{0.15}P_{0.32}$ solid solution amounts to $E_g = 0.610$ eV at the temperature $T = 77$ K. The value of E_g was calculated using the method suggested by Adachi [4] and, in the active region, was determined from the results of measuring the photoluminescence (PL) spectra of the InAs layers, taking into account the expression

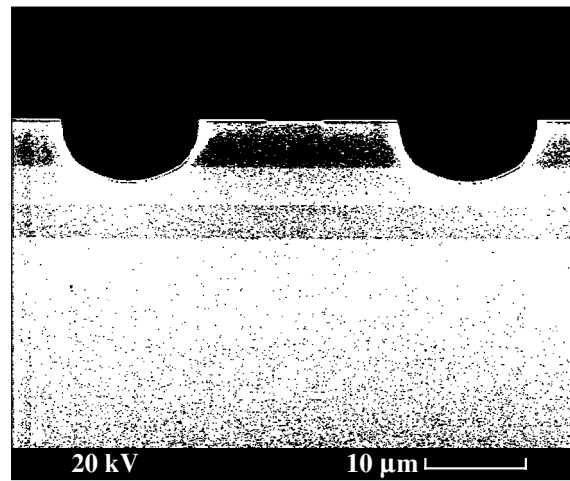$$E_g = h\nu - \frac{1}{2}kT, \qquad (1)$$
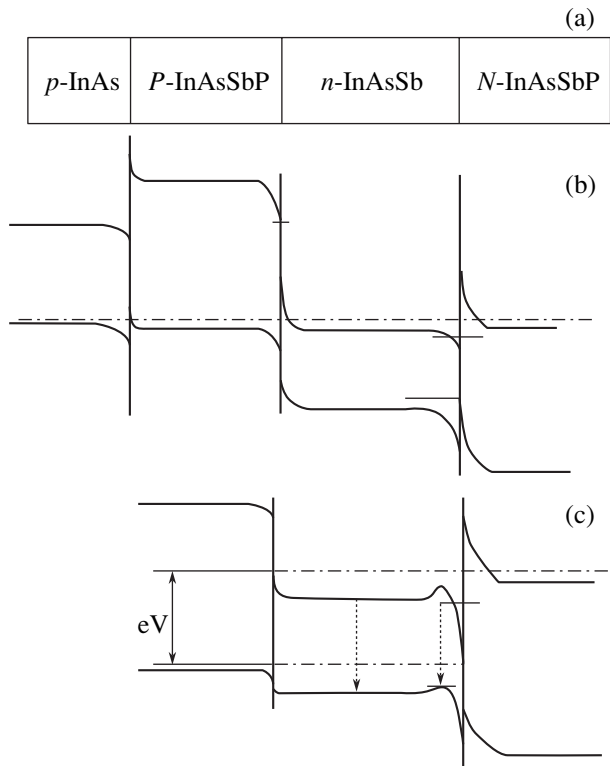
Fig. 1. (a) Schematic representation of the layers' arrangement in the laser structure and (b, c) an energy-band diagram of the structure (b) at a zero bias and (c) under lasing conditions.

Fig. 2. A photograph of the cleaved surface of the laser structure.

where $h\nu$ is the photon energy that corresponds to the peak in the PL spectrum and kT is the thermal energy.

In InAs, $E_g = 0.405$ eV at $T = 77$ K. A heterojunction of type II is formed at the interface between the InAs active region and the $InAs_{0.53}Sb_{0.15}P_{0.32}$ barrier layer; the resulting valence-band offset is $\Delta E_v = -8$ meV and the conduction-band offset is $\Delta E_c = 213$ meV.

We applied photolithography and wet chemical etching to the synthesized structures in order to fabricate radiation sources with a mesa-stripe design using a double-channel scheme. Fabry–Perot resonators were formed in the chips by cleaving and had the length $L = 150$–900 μm. The intergroove spacing was 20 μm. The width of the contact stripe was 5–6 μm (Fig. 2). Ohmic contacts for the p- and n-type regions were formed by thermal deposition of a Cr–Au–Ni–Au multilayered composition in vacuum. We used photoresist, polyamide, and silicon nitride Si_3N_4 as dielectric coatings. The Si_3N_4 thickness was ~(1000–1100) Å. A comparison of the diodes' characteristics showed that the use of Si_3N_4 is preferable.

We studied the spectral characteristics of the diodes at various values of resonator length and measured the polarization of light. The diodes under study were at a temperature of 77 K. The spectral characteristics were measured under conditions in which the diodes were pumped with pulsed current (the pulse width $\tau = 500$ ns and the repetition frequency $f = 2$ kHz). In the measurements of the spectra, the radiation was directed to a grating spectrometer and was detected using an InSb photodiode cooled with liquid nitrogen and installed at the exit from the spectrometer. The radiation intensity was measured using a pulse synchronous detector. As the polarizer, we used a grating formed from fluoroplastic with grooves made of aluminum (1200 groove/mm).

3. RESULTS

We now consider the results of the measurements. In Fig. 3, we show the spectral characteristics of a diode with the resonator length $L = 550$ μm under conditions of spontaneous emission (curve *1*), at the threshold of laser oscillation at the current $I = I_{th}$ (curve *2*), and at a current that exceeds the threshold current by 15% (curve *3*). Coherent radiation appeared at the peak of the spontaneous-emission band ($\lambda = 3.110$ μm). An additional mode ($\lambda \approx 3.087$ μm) is observed at the current $I = 1.15 I_{th}$.
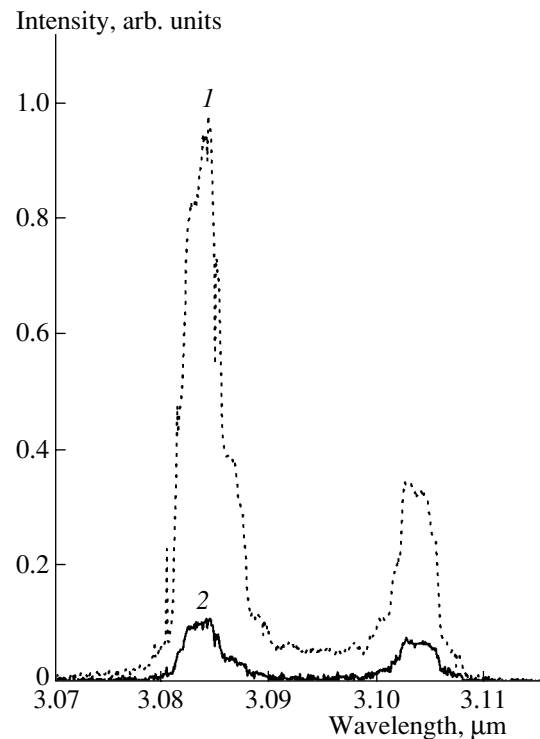
In Fig. 4, we show the spectral dependences of the TE and TM components of the coherent emission from a sample with $L = 350$ μm at the current $I = 0.61$ A. For this diode, $I_{th} = 0.425$ A. The spectrum includes two modes with the wavelengths $\lambda \approx 3.084$ and 3.103 μm. Both of these spectral laser modes preferentially exhibit the TE polarization (the electric-field vector **E** of the wave is parallel to the plane of the p–n junction). The polarization degree σ for each of the modes was determined from the relation $\sigma = (P_{TE} - P_{TM})/(P_{TE} + P_{TM})$, where P_{TE} and P_{TM} are the intensities of radiation with the polarizations TE and TM, respectively. We have $\sigma = 83\%$ for the short-wavelength mode and $\sigma = 45\%$ for the long-wavelength mode. A mode in which the TM polarization was prevalent was not observed.
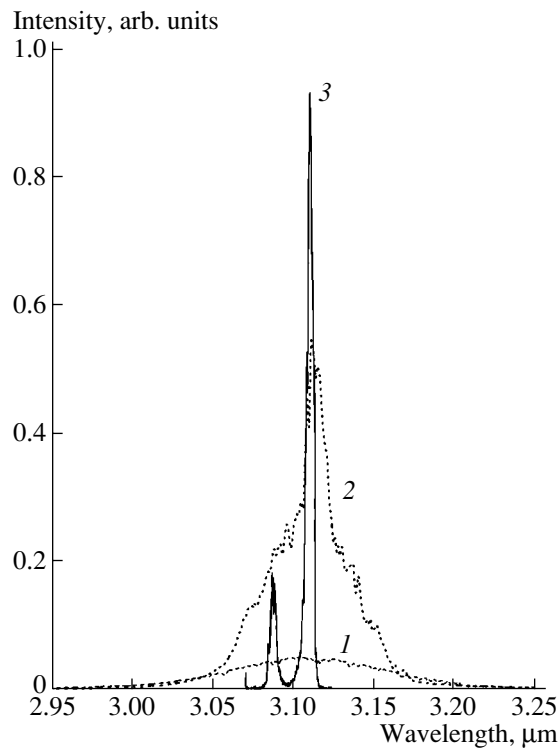
Fig. 3. The emission spectrum of a laser diode with a cavity length of 550 μm at the currents $I = (1)$ 0.465, (2) 0.53, and (3) 0.61 A.


Fig. 4. The spectra of the (*1*) TE and (*2*) TM radiation components of a laser with the cavity length of 350 μm at a current of 0.61 A.

Figure 5 illustrates the effect of the resonator length on the threshold current I_{th} and the radiation wavelength λ at the threshold of the laser oscillation. The value of I_{th} is at its smallest at $L \approx 300$ μm. At $L \leq 175$ μm, lasing was not obtained, although intense electroluminescence was observed. At $L > 300$ μm, I_{th} increases steadily as L increases. The coherent-radiation wavelength λ decreases as L decreases. The dependence $λ = f(L)$ is nearly linear at $L = 350$–750 μm; a drastic decrease in λ as L decreases occurs if $L < 350$ μm.

In Fig. 6, we show the emission spectra of a diode with $L = 350$ μm at various currents. The current dependence of the emission intensity is shown in the inset. The threshold current is $I_{th} = 0.425$ A. The spectrum consists of a single mode with $λ \approx 3.097$ μm at the current $I = 0.51$ A. As the current increases, a mode with $λ \approx 3.087$ μm is also observed and becomes prevalent at the current $I = 0.55$ A. An additional mode with $λ \approx 3.094$ μm emerges at the current $I = 0.73$ A. The current dependence of the emission intensity is steeper (by a factor of 8) in the current range 0.425–0.55 A than in the range 0.55–1.5 A. This observation indicates that the laser's emission efficiency at currents $I < 0.55$ A is higher than its efficiency at $I > 0.55$ A. A decrease in the slope of the current dependence of the emission intensity correlates with the emergence of a laser line at the wavelength $λ = 3.087$ μm. It is noteworthy that the line with a longer wavelength ($λ = 3.097$ μm) is retained.

The emergence of laser lines with an intermediate wavelength $λ = 3.094$ μm is unusual.

4. DISCUSSION

The presence of even a single heterobarrier in the light-emitting structure gives rise to new channels for both radiative and nonradiative recombination. One might expect one of the mechanisms of radiative recombination in the semiconductor structure under study with type-II heterojunctions to be related to interaction between electrons and holes at the n-InAsSbP/n-InAs interface. According to previous studies [5–7], application of a forward-bias voltage that exceeds $V = E_g/e$ (Fig. 1) gives rise to spatially separated self-consistent potential wells for the electrons and for holes in n-InAs in the vicinity of the n-InAs/n-InAsSbP interface. Coherent radiation in such a structure is ensured by the radiative transitions between quantum states in the potential wells.

We observe the emergence of a laser line at the peak of the spontaneous-emission band (Fig. 3) in the diodes under study. According to [8], this observation indicates that the luminescence is related to the interface. In this case, the main contribution to the emission intensity at the lasing threshold is made by a region near the n-InAs/n-InAsSbP interface. The width of this region d is ~200 Å at the given level of doping of the layers [9].
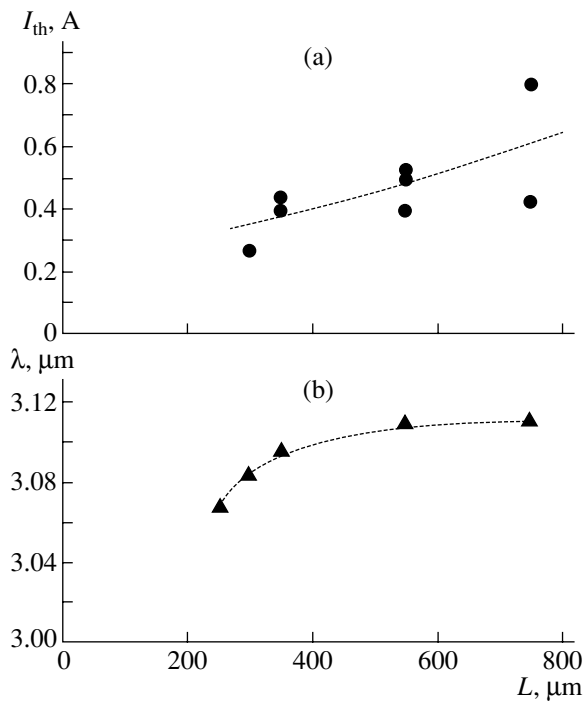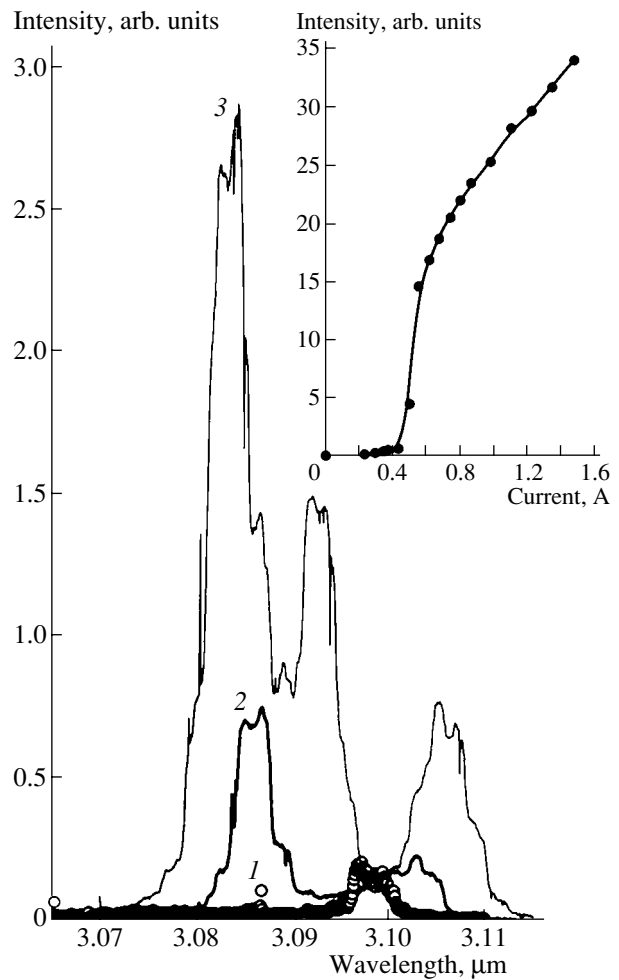
Fig. 5. The dependences of the (a) threshold current and (b) radiation wavelength at the lasing threshold on the cavity length.

Fig. 6. The emission spectrum of a laser with the cavity length of 350 μm at the currents I = (*1*) 0.51, (*2*) 0.55, and (*3*) 0.73 A. The current dependence of the radiation intensity is shown in the inset.

The value of d is much smaller than the thickness of the laser-structure active region (~3.3 μm).

The type of heterojunction affects the polarization of the emitted light. As was shown previously in [10], optical transitions that occur without momentum conservation predominantly exhibit the TM polarization. In the structure under study, the TE polarization is predominant in all the modes (Fig. 4); however, the smaller value of σ for the mode with $\lambda = 3.103$ μm suggests that the long-wavelength portion of the spectrum corresponds to an interfacial radiative recombination. Apparently, the short-wavelength mode with $\lambda = 3.084$ μm corresponds to band-to-band transitions.

In order to ensure laser oscillations in lasers with a small cavity length, it is necessary to increase the voltage applied to the structure, which brings about an increase in the depth of the potential wells and a corresponding rise in the levels in the quantum wells. A rise in the levels means that both the energy spacing between the quantum states and the energy of the coherent-radiation photons increase. Thus, a decrease in L results in an increase in the photon energy and a corresponding decrease in λ (Fig. 5). The absence of lasing at small cavity lengths ($L \leq 175$ μm) is a consequence of the leveling off of the gain, which is characteristic of quantum wells, and indicates that an interface-related channel of radiative recombination exists. The observed increase in the threshold current I_{th} as the cavity length increases at $L \geq 300$ μm shows that there are appreciable internal losses of laser radiation.

The peak of the photoluminescence spectrum of the InAs layer ($E_g = 0.405$ eV) at $T = 77$ K corresponds to the wavelength $\lambda = 3.040$ μm. The emergence of an interband mode with a somewhat larger wavelength, $\lambda = 3.084$–3.087 μm (Fig. 6), is characteristic of lasers that operate by a band-to-band recombination and can be accounted for by the narrowing of the band gap as a result of a high level of excitation in the laser-oscillation mode. As the current is further increased, the shift of the emission peaks corresponding to band-to-band transitions to shorter wavelengths is accounted for by a rise in the quasi-Fermi levels due to an increase in the concentration of free charge carriers in the active region of the structure. A shift of the emission peaks to longer wavelengths is not observed in the case of the band-to-band transitions, which suggests that there is no appreciable increase in temperature in the active region. The fact that the emission peaks corresponding to the interfacial recombination shift to longer wavelengths as the current increases indicates that the origin of the short-

and long-wavelength portions of the spectrum is different and that there is a small increase in temperature during the pulse duration.

As the current increases, the drastic reduction of the increase in the emission intensity at $I > 0.55$ A can be accounted for by the interaction between the modes of interfacial and band-to-band recombination. Thus, it should be recognized that both modes are generated simultaneously. This circumstance differentiates a laser from other sources of optical radiation. As a result of the interaction between the modes, a mode with an intermediate frequency appears; this mode oscillates with the half-difference frequency. The wavelength of the intermediate mode lies between the regions of interfacial and interband amplification; i.e., this wavelength corresponds to the absorption region. As a result, the intermediate mode gives rise to heavy losses of the generated laser radiation, which reduces the slope of the current dependence of the radiation intensity. In general, we can state that a multiband spectrum is undesirable in high-efficiency lasers. However, this multiband situation can be avoided by reducing the role of the band-to-band recombination, e.g., by decreasing the thickness of the narrow-gap layer.

5. CONCLUSION

We fabricated and studied sources of coherent radiation based on an InAs/InAsSbP double heterostructure grown by vapor-phase epitaxy from metal–organic compounds. We studied the spectral characteristics of diodes for various cavity lengths and measured the polarization of emitted light. In the structure under study, all the modes predominantly exhibit the TE polarization. The mode composition of the spectrum is controlled by radiative recombination at the heteroboundary and in the bulk of the active region. Interaction between the modes of interfacial and band-to-band recombination is observed at a current that exceeds the threshold value by 30%. In these conditions, a new mode with an intermediate wavelength, lying between the wavelengths of the previous modes, appears; simultaneously, the current dependence of the total-radiation intensity becomes less steep.

REFERENCES

1. A. N. Baranov, B. E. Dzhurtanov, A. N. Imenkov, *et al.*, Pis'ma Zh. Tekh. Fiz. **13**, 517 (1987) [Sov. Tech. Phys. Lett. **13**, 213 (1987)].

2. M. Aĭdaraliev, N. V. Zotova, S. A. Karandashev, *et al.*, Fiz. Tekh. Poluprovodn. (St. Petersburg) **33**, 233 (1999) [Semiconductors **33**, 200 (1999)].

3. A. Krier and V. V. Sherstnev, J. Phys. D: Appl. Phys. **33**, 101 (2000).

4. S. Adachi, J. Appl. Phys. **61**, 4869 (1987).

5. A. N. Baranov, B. E. Dzhurtanov, A. N. Imenkov, *et al.*, Pis'ma Zh. Tekh. Fiz. **12**, 664 (1986) [Sov. Tech. Phys. Lett. **12**, 275 (1986)].

6. A. N. Baranov, B. E. Dzhurtanov, A. N. Imenkov, *et al.*, Fiz. Tekh. Poluprovodn. (Leningrad) **20**, 2217 (1986) [Sov. Phys. Semicond. **20**, 1385 (1986)].

7. A. N. Baranov, T. N. Danilova, O. G. Ershov, *et al.*, Pis'ma Zh. Tekh. Fiz. **18** (22), 6 (1992) [Sov. Tech. Phys. Lett. **18**, 725 (1992)].

8. T. N. Danilova, A. N. Imenkov, V. V. Sherstnev, and Yu. P. Yakovlev, Fiz. Tekh. Poluprovodn. (St. Petersburg) **34**, 1396 (2000) [Semiconductors **34**, 1343 (2000)].

9. T. I. Voronina, T. S. Lagunova, M. P. Mikhaĭlova, *et al.*, Fiz. Tekh. Poluprovodn. (St. Petersburg) **32**, 215 (1998) [Semiconductors **32**, 195 (1998)].

10. T. N. Danilova, O. G. Ershov, G. G. Zegrya, *et al.*, Fiz. Tekh. Poluprovodn. (St. Petersburg) **29**, 1604 (1995) [Semiconductors **29**, 834 (1995)].

Translated by A. Spitsyn

PHYSICS OF SEMICONDUCTOR DEVICES

Effect of *p*-Doping of the Active Region on the Temperature Stability of InAs/GaAs QD Lasers

I. I. Novikov*^, N. Yu. Gordeev*, L. Ya. Karachinskiĭ*, M. V. Maksimov*, Yu. M. Shernyakov*, A. R. Kovsh**, I. L. Krestnikov**, A. V. Kozhukhov**, S. S. Mikhrin**, and N. N. Ledentsov**

*Ioffe Physicotechnical Institute, Russian Academy of Sciences, St. Petersburg, 194021 Russia
^e-mail: novikov@switch.ioffe.ru
**NL Nanosemiconductor GmbH, 44227 Dortmund, Germany
Submitted September 6, 2004; accepted for publication September 17, 2004

Abstract—A detailed study of the effect of *p*-doping of the active region on characteristics of long-wavelength InAs/GaAs QD lasers is performed. As the doping level increases, the characteristic temperature rises and the range of temperature stability for the threshold current density is broadened. In a laser doped with 2×10^{12} cm^{-2} acceptors per QD sheet, the characteristic temperature of 1200 K is obtained in the temperature range 15–75°C and the differential quantum efficiency is stable in the range 15–65°C. A maximum CW output power of 4.4 W is reached in an optimized structure. © *2005 Pleiades Publishing, Inc.*

1. INTRODUCTION

Quantum dot (QD) semiconductor lasers are now the object of intense study because of the possibility of achieving, with these lasers, device characteristics (threshold current density, its temperature stability, differential quantum efficiency, the factor of line broadening, etc.) considerably exceeding those for quantum well lasers. The ultrahigh temperature stability of the threshold current density was predicted in one of the first theoretical studies devoted to QD lasers [1], and this largely stimulated the interest in their fabrication and study. However, a more detailed consideration has shown that absolute lack of temperature dependence of the threshold current density can be reached only in an ideal situation when all the injection current is expended for radiative recombination in QDs [2]. In real QD lasers, several factors can give rise to the temperature dependence of the threshold current density:

—The inevitable existence of temperature-dependent components in the threshold current density, which are related to radiative and nonradiative recombination of carriers in the waveguide [2].

—the temperature-dependent population of the excited electron and hole states, and recombination via these states.

—Inhomogeneous broadening of the QD array. At high temperatures, carriers within QDs that are not involved in lasing are in quasi-equilibrium with the dots contributing to lasing. The component of the threshold current related to population of dots that are not involved in lasing is temperature-dependent [3];

—violation of charge neutrality gives rise to temperature dependence of the threshold current density component related to generation in QDs [4];

—the temperature dependence of absorption by free carriers.

Due to these effects, temperature stability of the threshold current density depends on the parameters of the QD array, as well as on other parameters of the laser structure, so it can be either high or low. Progress in the technology of QD growth [5] made it possible to produce QD arrays with low scatter in their size and high confinement of the electron and hole ground states in respect to excited states and states in the wide-gap matrix (the waveguide material). A characteristic temperature of 170 K was reached in the temperature range 10–65°C [6]. Several methods were suggested to improve the temperature stability of QD lasers, such as tunnel injection of carriers into QDs [3] and doping of the active region with an acceptor impurity.
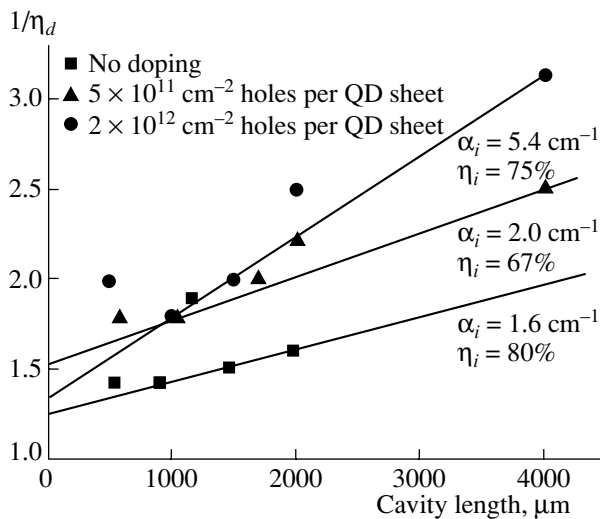
A theoretical study of active region doping as a method for improving semiconductor QD laser characteristics was presented in [7]. It was shown that *n*-doping favors the reduction of the transparency current [7], whereas *p*-doping raises the maximum gain. Recently, a high characteristic temperature ($T_0 = 230$ K in the temperature range from 0 to 80°C) was demonstrated in QD lasers with a *p*-doped active region [8]. However, doping of the active region resulted in a significant decrease in the differential quantum efficiency, which was below 20%.

Therefore, optimization of the doping level in the laser structure is a necessary condition to reach high characteristic temperature without losing high differential quantum efficiency.

This report presents a detailed study of the effect of active region doping on the threshold current density in QD lasers, its temperature stability, differential quantum efficiency, and internal optical loss.

Threshold current density, A/cm^2

- ■ No doping
- ▲ 5×10^{11} cm^{-2} holes per QD sheet
- ● 2×10^{12} cm^{-2} holes per QD sheet
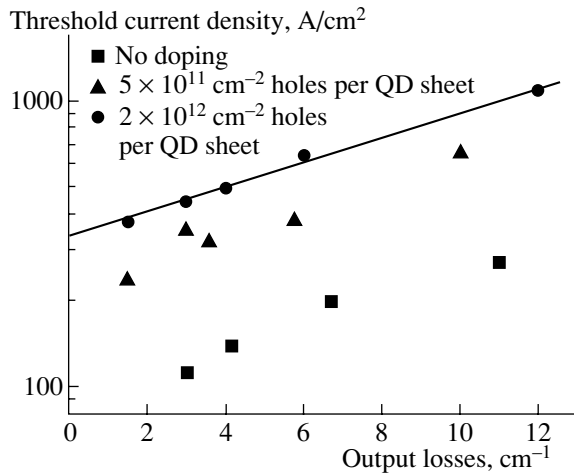
Fig. 1. Threshold current density J_{th} vs. the output loss for the three heterostructures.

$1/\eta_d$

- ■ No doping
- ▲ 5×10^{11} cm^{-2} holes per QD sheet
- ● 2×10^{12} cm^{-2} holes per QD sheet

$\alpha_i = 5.4$ cm^{-1}
$\eta_i = 75\%$

$\alpha_i = 2.0$ cm^{-1}
$\eta_i = 67\%$

$\alpha_i = 1.6$ cm^{-1}
$\eta_i = 80\%$

Fig. 2. The inverse differential quantum efficiency vs. the cavity length for the three heterostructures.

2. EXPERIMENT

Laser structures under study were MBE-grown in the configuration of separate confinement of carriers and the light wave. Three structures were grown: one with an undoped active region ("undoped" structure), and two structures with different degree of doping ("moderately" and "heavily" doped). The waveguide width was 0.4 μm. AlGaAs emitter layers of 1.5 μm in thickness, with an effective Al content of 35%, were doped with Si and C to obtain electron and hole densities of about 10^{18} cm^{-3}. The active region of laser structures contained 10 sheets of InAs QDs separated by 30-nm-thick GaAs spacers. QDs were formed by activated decomposition of InGaAs solution [9]. The central 10-nm-thick portion of each spacer was doped with an acceptor impurity (carbon), with the doping level of

5×10^{11} cm^{-2} acceptors per QD sheet for a moderately doped structure and 2×10^{12} cm^{-2} for a heavily doped one. All three structures emitted in 1.28–1.285 μm range.

Stripe lasers in the shallow mesa configuration, with a stripe width of 100 μm and cavity lengths from 0.5 to 4 mm, were fabricated from the grown structures. The cleaved cavity mirrors were free of antireflection or reflection coating. The samples were soldered with In onto a copper heat sink, with the *p*-contact down. The device characteristics were studied in the temperature range 15–150°C under excitation by current pulses (pulse width 300 ns, repetition rate 1 kHz).

3. EXPERIMENTAL RESULTS

Figure 1 shows the threshold current density as a function of the output loss. The undoped structure demonstrated the lowest threshold current density of 110 A/cm^2 (the laser cavity length was 2 mm), whereas the threshold current density in moderately and heavily doped structures was 233 and 380 A/cm^2, respectively, for the same cavity length.

Figure 2 shows the inverse differential quantum efficiency as a function of the cavity length for the three structures. This dependence allowed us to estimate the internal loss and internal efficiency of stimulated emission. It can be seen that the lowest internal loss of 1.6 cm^{-1} and the highest internal quantum efficiency of about 80% are reached in the undoped structure, whereas the loss in doped structures increases as the doping increases: it is 2 and 5.4 cm^{-1} for moderately and heavily doped structures, respectively. Figure 3 shows temperature dependences of the threshold current density in the semilog scale. The inset shows temperature dependences of the lasing wavelength for the three structures. In the temperature range 17–75°C, the characteristic temperature for the threshold current density is about 70 K for the undoped and 1200 K for heavily doped structure. For a moderately doped structure, it is 550 K in the temperature range 17–55°C. The monotonic, nearly linear run of the dependence of the lasing wavelength shown in the inset to Fig. 3 leads to the conclusion that, in the entire temperature range under study, lasing occurs via the QD ground state. It is noteworthy that the temperature dependence of the threshold current density in the undoped structure is virtually linear, whereas that in doped structures consists of two linear portions (see Fig. 3). The temperature stability of doped structures is impaired at temperatures above 75°C, which is followed by a decrease in the characteristic temperature to 57 and 59 K in moderately and heavily doped structures, respectively. For the undoped structure, the range above 75°C is described by the characteristic temperature of 56 K.

This behavior is manifested also in the temperature dependence of the differential quantum efficiency, shown in Fig. 4. It can be seen that, in the temperature

range 17–55°C, the differential quantum efficiency of doped structures is virtually constant, but it sharply decreases as temperature further increases, whereas in the undoped structure the decrease starts at a much lower temperature.

4. DISCUSSION

Doping of spacer layers allowed us to reach the characteristic temperatures of 550 and 1200 K in moderately and heavily doped structures, respectively. These values demonstrate a significant improvement of the parameters obtained in [8], where the concept of doping of the active region was also applied for QD lasers. As stated in [10], at room temperature and a transition energy of 0.958 eV, the energy spacing between the ground and excited states in QDs is about 88 meV; of these, 75–80 meV is the spacing between the quantum-confinement levels for electron, whereas similar spacing for hole levels is only 8–13 meV. Owing to the small energy spacing between the ground and excited hole states, the injected holes occupy several quantum-well levels even at room temperature, which reduces their density in the ground state. Therefore, in order to reach the threshold gain, additional injection of electron–hole pairs is necessary, which results in increasing lasing threshold as temperature increases. As shown in [11], the increase in the energy spacing between the ground and excited states in QDs opens the way to improving the temperature stability of the threshold current density, owing to lower occupancy of the excited hole states.

An increase in the occupancy of the ground QD state by holes can be reached by means of doping GaAs spacers in the vicinity of QDs with an acceptor impurity. Holes from doped regions are captured by QDs; thus thermal emission of holes from the QD ground state is compensated. Indeed, in the temperature range 17–75°C, the temperature stability of the threshold current density in doped structures is significantly higher than in the undoped one; and the higher the doping level, the better the temperature stability. As can be seen in Fig. 4, *p*-doping also raises the temperature stability of the differential quantum efficiency, which remains virtually constant in doped structures in the temperature range 17–55°C. It is necessary to note that, in discussing the *p*-doping effect, we have disregarded the violation of charge neutrality in QDs [4]; this effect depends on the parameters of a specific laser structure.

At temperatures above 55–75°C (Fig. 3), the structures under study demonstrate a significant increase in the threshold current density, and a decrease in the external differential quantum efficiency (Fig. 4). It is necessary to note also that characteristic temperatures of doped and undoped structures nearly coincide at temperatures above 75°C (Fig. 3). Indeed, at high temperatures the emission of holes from the ground state
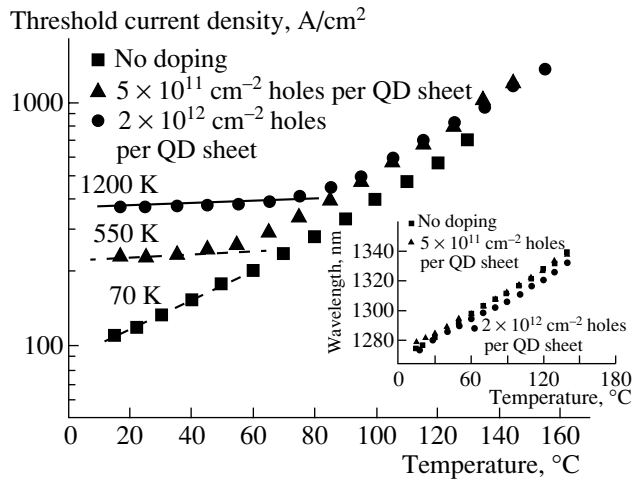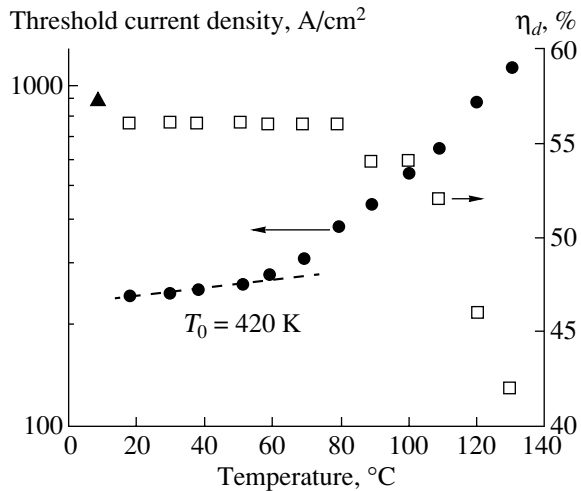

Fig. 3. Temperature dependences of the threshold current density J_{th} for the three heterostructures. Inset: temperature dependences of lasing wavelength. The length of samples was 2 mm for the undoped structure, and 4 mm for doped ones.
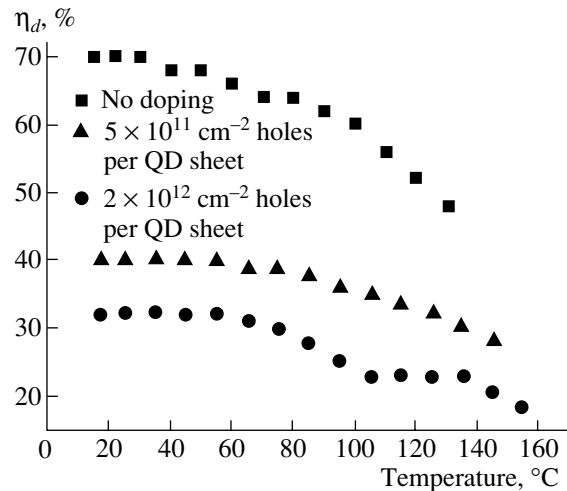

Fig. 4. Temperature dependences of the differential quantum efficiency for the three heterostructures. The length of samples was 2 mm for the undoped structure, and 4 mm for doped ones.

becomes so strong that the positive effect of *p*-doping on the temperature stability is negligible, and an additional injection of electron–hole pairs is necessary to compensate the emission and reach the gain threshold.

Negative effects arising under structure doping are an increase in the threshold current density and decrease in the differential quantum efficiency. These effects are related to a larger loss for absorption by free carriers in doped structures as compared to undoped ones. Therefore, a tradeoff must be made between the objective of raising the characteristic temperature, on the one hand, and a reasonable decrease in the differential quantum efficiency and increasing of the threshold

Threshold current density, A/cm^2

Fig. 5. Temperature dependences of the threshold current density J_{th} and differential quantum efficiency η_d for the optimized structure.
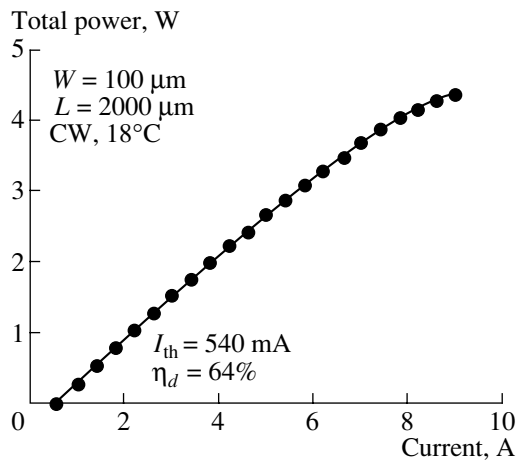
Fig. 6. Light–power dependence in CW mode for the optimized structure. The length of sample was 2 mm.

current density, on the other. Optimization of laser characteristics demands a detailed modeling with due regard for the QD array parameters (density, number of sheets), QD energy spectrum, waveguide thickness, and thickness and doping level of GaAs spacers, and composition and doping of the emitters. We have grown a structure in which the waveguide thickness and the composition and doping of emitters and spacers were optimized. In spacers, two 5-nm-thick GaAs layers were doped, with a 13-nm-thick GaAs layer in between them (the total thickness of the spacer was 33 nm). This structure has demonstrated a high differential quantum efficiency of 56%, with its value remaining constant in the temperature range 15–80°C, and high enough char-

acteristic temperature of 420 K in the temperature range 15–60°C (Fig. 5). Maximum power of CW optical emission from this structure was 4.4 W (Fig. 6), which, to our knowledge, is the highest value reached for long-wavelength QD lasers.

5. CONCLUSION

Semiconductor laser heterostructures with a *p*-doped active region have been studied. In a laser doped with $\sim 2 \times 10^{12}$ cm^{-2} acceptors per QD sheet, the characteristic temperature of 1200 K is reached in the temperature range 15–75°C. It is expected that further optimization of structures will make it possible to raise the characteristic temperature to an even greater extent and to broaden the range of high temperature stability of laser operation, with simultaneous retention of high differential quantum efficiency and low threshold current density.

REFERENCES

1. Y. Arakawa and H. Sakaki, Appl. Phys. Lett. **40**, 939 (1982).
2. L. V. Asryan and R. A. Suris, Semicond. Sci. Technol. **11**, 554 (1996).
3. L. V. Asryan and L. Luryi, IEEE J. Quantum Electron. **37**, 905 (2001).
4. L. V. Asryan and R. A. Suris, IEEE J. Sel. Top. Quantum Electron. **3**, 148 (1997).
5. V. A. Shchukin, N. N. Ledentsov, and D. Bimberg, *Epitaxy of Nanostructures* (Springer, Berlin, 2003), ISBN 3.540-67817-4, Springer Ser. Nanosci. Technol.
6. A. R. Kovsh, N. A. Maleev, A. E. Zhukov, *et al.*, Electron. Lett. **38**, 1104 (2002).
7. K. J. Vahala and C. E. Zah, Appl. Phys. Lett. **52**, 1945 (1988).
8. O. B. Shchekin, J. Ahn, and D. G. Deppe, Electron. Lett. **38**, 712 (2002).
9. M. V. Maximov, A. F. Tsatsul'nikov, B. V. Volovik, *et al.*, Phys. Rev. B **62**, 16671 (2000).
10. O. B. Shchekin and D. G. Deppe, Appl. Phys. Lett. **80**, 3277 (2002).
11. O. B. Shchekin, G. Park, D. L. Huffaker, and D. G. Deppe, Appl. Phys. Lett. **77**, 466 (2000).

Translated by D. Mashovets

Temperature Dependence of the Effective Coefficient of Auger Recombination in 1.3 µm InAs/GaAs QD Lasers

**I. I. Novikov^, N. Yu. Gordeev, M. V. Maksimov, Yu. M. Shernyakov, E. S. Semenova,
A. P. Vasil'ev, A. E. Zhukov, V. M. Ustinov, and G. G. Zegrya**

Ioffe Physicotechnical Institute, Russian Academy of Sciences, St. Petersburg, 194021 Russia
^e-mail: novikov@switch.ioffe.ru
Submitted September 27, 2004; accepted for publication October 12, 2004

Abstract—Semiconductor laser heterostructures containing five and ten sheets of InAs/GaAs QDs on GaAs substrates, with an emission wavelength of ~1.3 µm, have been studied. Dependences of the nonradiative lifetime and effective Auger coefficient in QDs are obtained from an analysis of temperature and current dependences of the efficiency of spontaneous radiative recombination. The zero-threshold Auger recombination channel in QDs is shown to dominate at low (below 200 K) temperature, whereas at higher temperatures the quasi-threshold channel becomes dominant. The effective 3D Auger coefficient is estimated in the approximation of a spherical QD, and a good agreement with the experimental data is obtained. © *2005 Pleiades Publishing, Inc.*

1. INTRODUCTION

Quantum dot (QD) semiconductor lasers attract much attention because of their vast potential for modern optoelectronics [1]. In this context, a detailed understanding of physical processes defining the electrical and optical properties of QD lasers is very important. One of the first theoretical studies of the Auger recombination in QDs predicted the suppression of the Auger recombination rate due to the large confinement energy for an electron in a QD [2]. However, further studies of the Auger recombination in QDs have shown that the presence of a heterointerface lifts the limitations imposed on the electron–electron interaction by the energy and momentum conservation laws. Hence, new Auger recombination channels, zero-threshold and quasi-threshold, appear in heterostructures [3]. Namely, these channels were shown to be responsible for the increase of the Auger recombination efficiency as the dimension of structure decreases. Thus, the Auger recombination efficiency in QDs [4] and quantum wires [5] is significantly higher than in a bulk semiconductor. Since QDs represent the limiting case of spatial confinement of carriers, a rise in the Auger recombination efficiency in respect to quantum wells and quantum wires can be expected. The emission characteristics of long- (1.3 µm) and short-wavelength (0.98 µm) QD lasers were analyzed in [6]. It was shown that the Auger recombination in long-wavelength QD lasers is more important than in short-wavelength ones, and at room temperature the contribution of the Auger process to the threshold current can reach 70% [6]. Therefore, due regard for the impact of the Auger processes on the threshold characteristics and efficiency becomes especially important for long-wavelength QD lasers. This report presents an analysis of the temperature dependence of the effective Auger recombination coefficient and nonradiative lifetime of carriers in QD lasers. A simple model is constructed, which allows the estimation of the effective lifetime for the nonradiative recombination (monomolecular recombination) and effective Auger recombination coefficient from the dependence of the spontaneous recombination intensity on the driving current.

2. THEORETICAL MODEL

The measured dependence of the integral intensity on current was analyzed in terms of the model described below. We assumed the total rate of spontaneous radiative recombination in the active region of the volume V to be expressed by [7, 8]:

$$L = VBn^2, \qquad (1)$$

where n is the carrier density, and B, the coefficient of spontaneous radiative recombination, which is considered independent of the carrier density below the transparency current. Further, we assume the existence of two main channels of nonradiative recombination. The first is related to nonradiative recombination, which depends linearly on the carrier density, the second is the Auger recombination, which is significant in long-wavelength lasers [9]. Then the total rate of nonradiative recombination can be expressed by

$$K = V\left(\frac{n}{\tau_{nr}} + Cn^3\right), \qquad (2)$$

where τ_{nr} is the time of the Shockley–Read nonradiative recombination, and C the effective coefficient of the Auger recombination. We assume that recombination
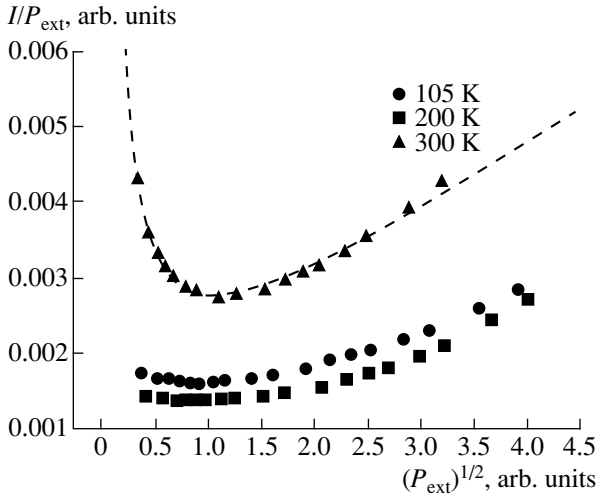
Fig. 1. Inverse efficiency of spontaneous emission at different temperatures vs. the detected power for the heterostructure with ten QD sheets. Dashed line, the approximation of the experimental dependence with Eq. (5).

outside of the active region is negligible. Then the total current can be expressed by

$$I = e(L + K), \qquad (3)$$

where e is the elementary charge. A precise determination of the carrier density or total output power L in the experiment is very difficult. However, the use of a linear photodetector and the stability of the experimental conditions allow a relatively simple measurement of the fixed portion of the emitted power; i.e., the power can be expressed by

$$P_{ext} = RL, \qquad (4)$$

where P_{ext} is the measured power, and R, the proportionality factor between the measured and real power. Using Eqs. (1)–(4), the equation for the inverse efficiency of the spontaneous radiative recombination is easily obtained:

$$\frac{I}{P_{ext}} = \frac{e}{R} + \left(\frac{e^2 V}{R}\right)^{1/2}\left(\frac{1}{\tau_{nr}^2 B}\right)\left(\frac{1}{P_{ext}}\right)^{1/2}$$
$$+ \left(\frac{e^2}{R^3 V}\right)^{1/2}\left(\frac{C}{B^{3/2}}\right)(P_{ext})^{1/2}. \qquad (5)$$

Therefore, the measurement of the dependence of output integral intensity of spontaneous emission on the driving current and further approximation of the obtained dependence by a curve in form (5) allows us to calculate the time of nonradiative recombination, τ_{nr}, and the effective coefficient of the Auger Recombination, C.

3. EXPERIMENT

Laser heterostructures for experiment were grown by MBE. The active region consisted of five or ten

sheets of InAs/GaAs QDs formed by activated decomposition of InGaAs [10]; the emission wavelength was in the range 1.25–1.29 μm. The details of the laser heterostructure design are presented in [11]. Stripe laser diodes with a stripe width of 100 μm were fabricated. Samples were soldered with In onto a copper heat sink, with the epitaxial layer down. The device characteristics were studied under excitation by current pulses (pulse width 500 ns, repetition rate 1 kHz), the emission power was measured using a Ge photodiode. In the experiment, we used samples fabricated from structures with 10 and 5 QD sheets, with a cavity length of 100 and 75 μm, respectively. This length provided high emission output loss and strongly reduced reabsorption.

4. RESULTS AND DISCUSSION

Figure 1 shows the inverse efficiency of spontaneous recombination as function of the square root of optical power at different temperatures. For further analysis and for calculating the temperature dependence of the coefficient of spontaneous radiative recombination B we used the relation [12]

$$B(T) = \frac{4}{3}(\sqrt{2}\pi^{3/2})\alpha\sqrt{\varepsilon}\frac{1}{T^{3/2}}\frac{m_{chh}^{3/2} + m_{clh}^{3/2}}{m_c^{3/2}m_v^{3/2}}E_g\left(\frac{P_k}{c}\right)^2, \quad (6)$$

where $m_v^{3/2} = m_{hh}^{3/2} + m_{lh}^{3/2}$; $m_{chh} = m_c m_{hh}/(m_c + m_{hh})$; $m_{clh} = m_c m_{lh}/(m_c + m_{lh})$; m_c, m_{lh}, and m_{hh} are the effective masses of electron and light, and the heavy hole, respectively; α, the fine structure constant; c, the velocity of light in free space; ε, the dielectric constant; E_g, the effective bandgap (here, the energy of the spontaneous emission peak was used); T, temperature (in eV); and P_k, the Kane parameter, which is calculated from the expression

$$P_k^2 = \frac{1}{2}\hbar^2 E_g\frac{E_g + \Delta}{E_g + (2/3)\Delta}\frac{1}{m_c}, \qquad (7)$$

where Δ is the spin-orbit splitting. In the calculation, we used the following parameters for InAs: $m_c = 0.023m_e$; $m_{hh} = 0.41m_e$; $m_{lh} = 0.026m_e$; $\Delta = 0.41$; $\alpha = 1/137$; $\varepsilon = 12$; m_e, the free electron mass, $m_e = 0.911 \times 10^{-27}$ g. The typical size of a QD was 15–20 nm at the base and 5–7 nm in height [13], so in the calculation we assumed the volume of a QD to be $V = 2 \times 10^{-18}$ cm^3.

Figure 2 shows temperature dependences of the nonradiative recombination time calculated using the above-described method. It can be seen that these dependences for different structures are similar: they exhibit a maximum at about 200 K. In an earlier study of these structures [14], we showed that this temperature corresponds to the boundary between the ranges of nonequilibrium and equilibrium carrier distribution in QDs. Below 200 K, the distribution is nonequilibrium [15]: the occupancy of QD states is determined by the probability of carrier trapping by a QD of a specific size, rather

Nonradiative time τ_{nr}, ns
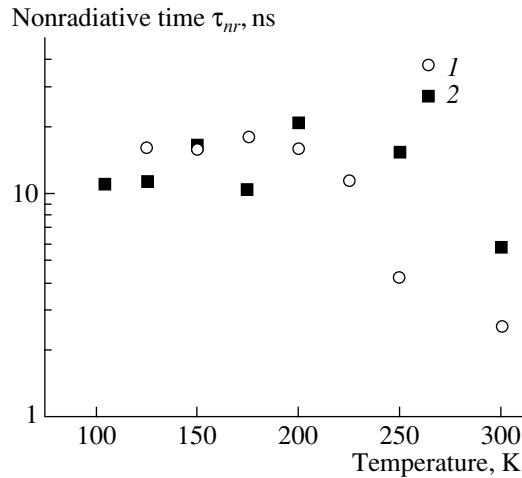
Fig. 2. Temperature dependence of effective nonradiative lifetime for two structures: (*1*) with five sheets of QDs; (*2*) with ten sheets.

Auger coefficient C, cm^6/s
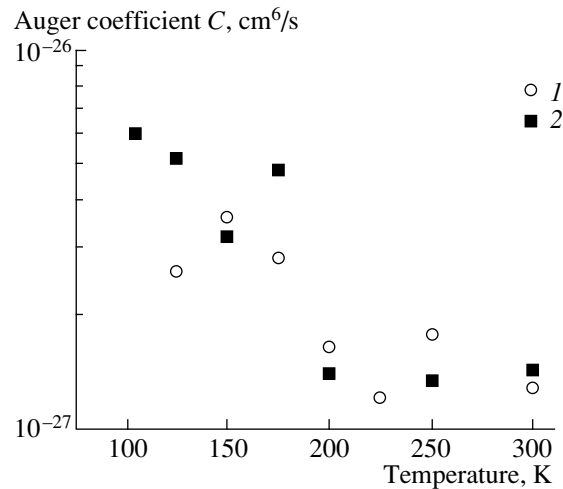
Fig. 3. Temperature dependence of effective coefficient of the Auger recombination for two structures: (*1*) with five sheets of QDs; (*2*) with ten sheets.

than by the Fermi distribution. We believe that the observed temperature dependence of the nonradiative recombination time can be attributed, namely, to the modification of the type of distribution of nonequilibrium carriers in QDs. It is necessary to note the good agreement of the estimated time of nonradiative recombination with the estimate made in [16], where temperature-independent time of nonradiative recombination of ~10 ns was also obtained from the analysis of the efficiency of spontaneous recombination.

Figure 3 shows calculated temperature dependences of the effective coefficient of Auger recombination in QDs. It can be seen that, at temperatures below 200 K, in all structures this coefficient decreases as temperature increases; above 200 K, it increases slightly or remains unchanged. Noteworthy is the unusual behavior of this coefficient and its value. As mentioned above, the study of Auger recombination in quantum-well heterostructures had shown that the presence of a heterointerface lifts the limitations imposed on the electron–electron interaction by the energy and momentum conservation laws. In this case, new Auger recombination channels, zero-threshold and quasi-threshold, appear in heterostructures [3]. At low temperatures, the zero-threshold channel, in contrast to the quasi-threshold one, becomes an effective channel of nonradiative recombination, and for narrow quantum wells with high carrier density it dominates over the phonon-assisted Auger recombination. The presence of a zero-threshold matrix element of the electron–electron interaction has a significant influence also on the phonon-assisted Auger recombination. This process becomes a resonant one, and it is strongly enhanced as compared to the 3D phonon-assisted Auger process [4]. Similar behavior was also predicted theoretically for quantum wires [5]. Therefore, taking into account that a QD represents the limiting case of quantum confinement, we

can expect an increase in the probability of the Auger recombination as compared to quantum wells, quantum wires, and bulk semiconductors.

We believe that the studied characteristics in the low-temperature (below 200 K) range are related to the zero-threshold mechanism, in which a large momentum is transferred to an excited carrier. At higher temperatures, above 200 K, the quasi-threshold process becomes dominant, and it turns into a 3D threshold Auger process in the limit of an infinitely large effective size of a QD [4, 5]. Indeed, the zero-threshold process is related to carrier scattering on the interface, whereas the quasi-threshold one depends on the degree of carrier confinement [3]. At low temperatures, carriers are more strongly localized in QDs—i.e., the effective QD radius is smaller than at elevated temperature; in this case, the probability of scattering on the heterointerface increases, and, consequently, the zero-threshold process dominates over the quasi-threshold one. The temperature rise results in carrier delocalization (the effective radius of the wave function increases), which results in the domination of the quasi-threshold process over the zero-threshold one.

The temperature dependence of the effective Auger recombination coefficient in QDs was determined in [17] from the dependence of the optical pulse delay in respect to the exciting pulse; in this case, the effective Auger recombination coefficient decreased as temperature increased, from 8×10^{-29} cm^6/s at 100 K to 4×10^{-29} cm^6/s at 300 K. The decreasing of the Auger coefficient was attributed to the influence of the excited states in QD and to the temperature dependence of the rate of electron–hole scattering, which is one of the mechanisms responsible for the elimination of the threshold in the Auger process [3].

The formalism of microscopic theory of Auger recombination in QDs in the approximation of a spher-

ical QD was presented in [18, 19]. In the limit of strong electron localization ($\hbar^2/2m_c a^2 \ll V_c$, where a is the effective radius of QD, and V_c, the height of the heterobarrier in the conduction band), the probability (inverse time) of the Auger transition is expressed by

$$G = 10^7 \left(\frac{1\ \text{eV}}{E_g}\right)^{5/2} \left(\frac{1}{m_c/m_e}\right)^{3/2} \frac{V_c}{E_g} \left(\frac{5 \times 10^{-7}\ \text{cm}}{a}\right)^5, \quad (8)$$

where E_g is the transition energy. In our case, the condition $\hbar^2/2m_c a^2 \ll V_c$ is valid, because for a QD size of ~10–15 nm, we obtain 8–20 meV in the left-hand side, whereas $V_c \approx 260$ meV [20]. To estimate the effective 3D Auger coefficient C_{eff}^{3D}, (8) must be multiplied by the cubed surface area of the heterobarrier, $(4\pi a^2)^3$. Then we obtain

$$C_{\text{eff}}^{3D} = G(4\pi a^2)^3 = 3.4759 \times 10^{-26}\ \text{cm}^6\ \text{s}^{-1} \quad (9)$$

at a QD radius of $a = [(3/4\pi)V]^{1/3} \approx 8$ nm, and $E_g = 1.0248$ eV, which corresponds to the wavelength of the spontaneous emission peak for the heterostructure with ten QD sheets at 200 K, i.e., at the temperature at which the zero-threshold Auger recombination dominates in both structures. The effective coefficient of Auger recombination, obtained from an analysis of the experimental data, is 1.35×10^{-27} and 1.39×10^{-27} cm^6 s^{-1} for heterostructures with five and ten QD sheets, respectively. It can be seen that the these values agree well with estimate (9) for both structures. A slight discrepancy is easily explained by using the spherical approximation and the necessity of due corrections for the nonspherical shape of real QDs.

5. CONCLUSION

We studied semiconductor laser heterostructures with an emission wavelength of ~1.3 μm with five and ten sheets of InAs/GaAs QDs, grown on GaAs substrates. Estimates of the temperature dependence of the nonradiative lifetime and effective Auger recombination coefficient in QDs were obtained from an analysis of the dependence of the integral intensity of electroluminescence on the driving current. The zero-threshold Auger recombination channel is shown to dominate at low (below 200 K) temperatures, whereas at higher temperature the quasi-threshold channel becomes dominant. The effective 3D Auger coefficient is estimated in the approximation of a spherical QD, and a good agreement with the experimental data is obtained.

REFERENCES

1. N. N. Ledentsov, IEEE J. Sel. Top. Quantum Electron. **8**, 1015 (2002).
2. J. L. Pan, Phys. Rev. B **46**, 3977 (1992).
3. G. G. Zegrya and V. A. Kharchenko, Zh. Éksp. Teor. Fiz. **101**, 327 (1992) [Sov. Phys. JETP **74**, 173 (1992)].
4. A. S. Polkovnikov and G. G. Zegrya, Phys. Rev. B **58**, 4039 (1998).
5. E. B. Dogonkin, G. G. Zegrya, and A. S. Polkovnikov, Zh. Éksp. Teor. Fiz. **117**, 429 (2000) [JETP **90**, 378 (2000)].
6. I. P. Marko, A. D. Andreev, A. R. Adams, *et al.*, IEEE J. Sel. Top. Quantum Electron. **9**, 1300 (2003).
7. K. R. Poguntke and A. R. Adams, Electron. Lett. **28**, 41 (1992).
8. K. Mukai, Y. Nakata, K. Otsubo, *et al.*, IEEE J. Quantum Electron. **36**, 472 (2000).
9. M. I. Dyakonov and V. Yu. Kachorovskii, Phys. Rev. B **49**, 17130 (1994).
10. M. V. Maximov, A. F. Tsatsul'nikov, B. V. Volovik, *et al.*, Phys. Rev. B **62**, 16671 (2000).
11. S. S. Mikhrin, A. E. Zhukov, A. R. Kovsh, *et al.*, Fiz. Tekh. Poluprovodn. (St. Petersburg) **36**, 1400 (2002) [Semiconductors **36**, 1315 (2002)].
12. B. L. Gel'mont, Zh. Éksp. Teor. Fiz. **75**, 536 (1978) [Sov. Phys. JETP **48**, 258 (1978)].
13. A. R. Kovsh, N. A. Maleev, A. E. Zhukov, *et al.*, J. Cryst. Growth **251**, 729 (2003).
14. I. I. Novikov, M. V. Maksimov, Yu. M. Shernyakov, *et al.*, Fiz. Tekh. Poluprovodn. (St. Petersburg) **37**, 1270 (2003) [Semiconductors **37**, 1239 (2003)].
15. A. E. Zhukov, A. Yu. Egorov, A. R. Kovsh, *et al.*, Fiz. Tekh. Poluprovodn. (St. Petersburg) **31**, 483 (1997) [Semiconductors **31**, 411 (1997)].
16. D. G. Deppe, D. L. Huffaker, Z. Zou, *et al.*, IEEE J. Quantum Electron. **35**, 1238 (1999).
17. S. Ghosh, P. Bhattacharya, E. Stoner, *et al.*, Appl. Phys. Lett. **79**, 722 (2001).
18. G. G. Zegrya and A. S. Polkovnikov, in *Abstracts of 2nd Russian Conference on the Physics of Semiconductors* (1996), Vol. 1, p. 95.
19. E. B. Dogonkine, V. N. Golovatch, A. S. Polkovnikov, *et al.*, in *Proceedings of 8th International Symposium on Nanostructures: Physics and Technology* (St. Petersburg, 2000), p. 399.
20. J. He, B. Xu, and Z. G. Wang, Appl. Phys. Lett. **84**, 5237 (2004).

Translated by D. Mashovets